HOLOCENE CHRONOSTRATIGRAPHY OF DUNE FIELDS IN SOUTHERN UTAH: GEOMORPHIC RECORD OF PAST ARIDITY IN THE CENTRAL COLORADO PLATEAU

by

Harriet S. Cornachione

A dissertation submitted in partial fulfillment
of the requirements for the degree

of

DOCTOR OF PHILOSOPHY

in

Geosciences

Approved:

_____ Tammy Rittenour, Ph.D. Major Professor	_____ Patrick Belmont, Ph.D. Committee Member
_____ Joel Pederson, Ph.D. Committee Member	_____ Paul Grossl, Ph.D. Committee Member
_____ Dennis Newell, Ph.D Committee Member	_____ D. Richard Cutler, Ph.D. Vice Provost of Graduate Studies

UTAH STATE UNIVERSITY
Logan, Utah

2022

ABSTRACT

Holocene Chronostratigraphy of Dune Fields in Southern Utah:

Geomorphic Record of Past Aridity in the Central Colorado Plateau

by

Harriet S. Cornachione, Doctor of Philosophy

Utah State University, 2022

Major Professor: Dr. Tammy Rittenour
Department: Geosciences

The Southwestern United States has a semi-arid climate and is currently in a hydrologic drought that exceeds in magnitude and duration any period of drought in at least five centuries. Evidence of past migrations by Indigenous communities and the appearance/rise of other cultural adaptations in the archaeological record during previous episodes of aridity provide warning of similar disruption in modern times. This is especially of concern given that climate models predict conditions of aridity in this region will be exacerbated in the future due to anthropogenic climate change. Better understanding of the natural variability of hydroclimate will inform both adaptive strategies for future climate change and improved climate forecasts. While instrumental records only span the last <100 years, paleoclimate archives (i.e., tree-rings, sediment deposits) can provide longer duration records that provide a baseline for the frequency and magnitude of past aridity.

This dissertation investigates two dune fields on the central Colorado Plateau in southern Utah. A chronostratigraphic record of eolian activity is developed to determine periods of dune-field activation as an indicator of hydroclimate conditions during the Holocene. Methods and datasets used in this research include geomorphic mapping, descriptions of stratigraphy and

sedimentology, optically stimulated luminescence and radiocarbon dating, geochemical analysis of sediments and analysis of regional wind data.

The Kanab dune field in southwestern Utah is a largely stable dune field with parabolic dunes of 2-15 m in height. The dune field is oriented roughly west to east. Chronostratigraphic records were used to identify five periods of dune-field wide eolian activity: K0 (~9.2-7.8 ka), K1 (~6.8-5.6 ka), K2 (~4.4-3.3 ka), K3 (~2.2-1.2 ka) and K4 (~0.7-0.4 ka). Activity events occur at millennial intervals, and coincide with Bond events and other global climate records, suggesting a climate driver. The San Rafael dune field in east central Utah contains thin (2-6 m tall), east-northeast trending dune forms, partially stabilized with soil biocrusts and xeriphytic shrubs, with sections of currently active parabolic dunes and smaller barchan dunes and dune fields. Seven episodes of eolian activity were determined from chronostratigraphy in the dune field: SR0 (~17 – 16.2 ka), SR1 (~12.4 – 11.2 ka), SR2 (~9.7 – 7.4 ka), SR3 (~4.7 ka), SR4 (~3.4-2.5 ka), SR5 (~2.0-1.6 ka) and SR6 (~1.1 – 0.4 ka). Thin deposits and discontinuities in the record suggest an erosion-dominant landscape. Results from both dune field indicate three periods of coeval dune activation in the two dune fields at ~9.5-7.5 ka, ~2-1.5 ka, and ~1-0.5 ka. These are interpreted to record periods of regional aridity. Records of mobile dune activity from other sites across the Colorado Plateau suggest at least three and as many as five periods of regional dune activity interpreted to be related to regional aridity.

Analysis of weather station data indicate that modern wind regimes are consistent with dune field orientation, suggesting they are a useful analog for Holocene winds. Analysis of dune sediment geochemistry using K/Rb-K/Ba suggests that the sediment source material did not change between periods of dune activation. This result supports interpretation of a climate driver for dune field (re) activation events and not changes in sediment supply.

(239 pages)

PUBLIC ABSTRACT

Holocene Chronostratigraphy of Dune Fields in Southern Utah:

Geomorphic Record of Past Aridity in the Central Colorado Plateau

Harriet S. Cornachione

The southwestern United States is characterized by dry climate, and droughts are common. The region is currently in an extreme drought that began in 2000 CE and has lasted longer than any previous drought in at least 500 years. Models predict greater future climate extremes under human-caused climate change. Understanding of the natural range of climate variability is important to put these changes in context. Sedimentary archives of past sand dune activity can help extend the available instrumental observations (last century) and tree-ring records (last millennium).

Sand dunes are landforms that are sensitive to aridity and decreased vegetation cover. They can reactivate and migrate downwind during periods of aridity leaving behind a sediment record of past dune field activity. Research goals were to reconstruct past dune activity the Kanab and San Rafael dune fields in southern Utah. This was accomplished by mapping the dune forms and sampling for age control and sediment character. Modern wind data were compared to the orientation of the older dune forms to determine if wind directions have changed.

The Kanab dune field, in southwestern Utah, was found to have been active five times over the last 10,000 yr. The data indicate 1000 yr-long periods of activity separated by similar duration periods of stability. The San Rafael dune field, in east central Utah contained records of seven episodes of eolian activity from late Pleistocene (~17,000 years ago) to the present. Dunes are active today in this dune field with thinner dune deposits and sparser vegetation suggesting greater wind erosion than in the Kanab dune field. Comparing records between the two dune

fields indicates three time periods when they were both actively migrating, suggesting regional aridity ~9,500-7,500, 2000-1500 and 1000-500 years ago. Expanding this comparison to existing sand dune records across the Colorado Plateau suggests at least these three periods, and as many as five periods of regional aridity, may have occurred in the last 10,000 years. Wind and geochemical data indicate similar wind and source sediments have been active over the history of the dune fields.

Harriet S. Cornachione

ACKNOWLEDGMENTS

I am indebted to Dr. Tammy Rittenour for taking me on as a non-traditional student, and providing support, guidance and encouragement throughout this endeavor. I also deeply appreciate my committee members, Joel Pederson, Dennis Newell, Patrick Belmont and Paul Grossl for their wisdom, wit and assistance as well as their tenacity throughout this project. I am especially grateful to my husband and field manager (Michael), my sons and technical support crew (Matthew, Adam and Egan), and my granddaughter and first field assistant (Jade), and daughters-in-law (Kristen and Allison) for inspiration and counsel during challenging moments . I thank my siblings and in-laws (Catherine, Thom, Penny, John, Sherry, Jerry and Noreen) for forbearance with missed family Zoom-meets during COVID. Without the unflagging support of my family, I could not have made this lifelong goal a reality. Finally, but not least, I treasure the collegiality, affirmation, and technical savvy provided by new colleagues and friends formed during my extended USU journey (Kerry, Rob, Alex, Coleman, Natalie, Nick, Heather, Will, Dominique, Alison, Aidan, Carlie, Michelle, Michael, Carol, Kelly) as well as the support of all of the Geosciences Department faculty and staff.

Finally, I am deeply appreciative of the support from these organizations that enabled me to conduct and accomplish this research, including access to Bureau of Land Management public lands, and financial support from the National Science Foundation, EarthScope, the Geological Society of America, the Colorado Scientific Society and the Association of Women Geoscientists. I especially want to thank the USU Geosciences Department for awarding me the Patrick McKinney Scholarship, the J. Stewart Williams Graduate Fellowship, and for providing opportunities to work as both a research and teaching assistant. Truly, it takes a village to stay the course and complete the journey and I am profoundly grateful for the remarkable village who helped me reach my destination.

CONTENTS

LIST OF TABLES

Page

LIST OF FIGURES

Page

CHAPTER 1
INTRODUCTION

The Colorado Plateau region in the southwestern United States straddles the Four Corners area where the states of Utah, Colorado, New Mexico and Nevada meet. Despite arid and semi-arid conditions, there is a long record of human occupation in this high plateau region. Early Holocene (10-8 ka) migratory hunter-gatherers responded to changes in climate with shifting subsistence patterns. Abandonment of ancestral Puebloan communities, developed between ~ 2000 to 500 years ago, may have been linked with decadal-scale drought (e.g., Smith and McFaul, 1997; Benson et al, 2002; Cook et al, 2011; Betancourt and Guiterman, 2016). Modern land-use centered around agriculture and grazing is in competition with sensitive native ecosystems, tourism and recreation on public lands. Economic benefits from tourism on public lands are important to the regional economy (Cullinane-Thomas et al, 2018; Powell et al, 2021).

Both the Colorado Plateau and the Colorado River that bisects it are highly sensitive to aridity, with adverse impacts on natural and economic systems (i.e., streamflow, forests, agriculture) occurring in the 20th century as a result of multi-annual to multi-decadal drought (Bentz et al, 2010; Howitt et al, 2015; Fettig et al, 2019). Annual to multi-annual droughts in late 1990's gave way to the ongoing multi-decadal drought that started in the early 2000's and exceeds any drought experienced in the past 500 years (Williams et al, 2022). Understanding landscape response to climate variability is increasingly urgent as models predict more frequent extremes in regional temperature and aridity in the western United States (Cook et al, 2015; Papalexiou et al, 2018). Anthropogenic climate change will be overprinted on and is exacerbating the underlying natural variability in this region (Woodhouse et al, 2016; Williams et al, 2022).

While the instrumental record provides climate data for the past 70-100 years, climate proxies such as tree rings (dendrochronology) can extend the instrumental record. Tree ring

records from the region indicate decadal-scale periods of aridity not observed in historic times (Gray et al 2004; Meko et al 2007). However, dendrochronology can only extend the record 1000-2000 years. Lake sediments and speleothems can further expand the record (e.g., Polyak and Asmerom, 2001) but are rare within the Colorado Plateau.

Eolian sand dunes mobilize and stabilize following a threshold response to changes in vegetative cover, soil moisture, sediment supply and wind strength. Found across much of the central and southern Colorado Plateau, dunes can provide a record of landscape response to change in hydroclimate. Although tree rings, speleothem records, and lake sediments can provide annual records of moisture variability, sand dunes respond biogeomorphically to climate perturbations and reflect summative response to hydroclimate perturbations on decadal to centennial timescales. Due to their preservation of the landscape, records of sand dune activity can fill spatial and temporal gaps in modern instrumental and longer-term paleoclimate records (e.g. Lancaster, 1997). Improved understanding of natural hydroclimate variability can inform development of adaptive strategies for future climate change and may contribute to improved predictive modeling of landscape and ecosystem response to future drought.

The goals of this research are to reconstruct sand dune activity through time in two dune fields in southern Utah, an area of the central Colorado Plateau largely lacking other paleoclimate records. The second chapter reports the investigation of eolian activity in the Kanab dune field in southwestern Utah, while the third chapter is focused on the San Rafael dune field Holocene activity. Chapter 4 explores records of wind regime and trends in geochemistry.

The chronostratigraphy of the Kanab dune field in southern Utah identified five periods of Holocene eolian activity with millennial-scale pulsing suggestive of a climate driver. A significant contribution of this chapter is the outline of a tiered mapping and sampling approach that allows dune-field wide reactivations to be identified and durations of events to be better quantified than opportunistic sampling from a few sites, as employed in past studies. The research questions addressed in this chapter include: What are the dune morphologies present in

the dune field and how are they distributed? What is the timing of eolian activity in individual dune sites? Is there evidence for dune-field wide activity? Does regional eolian activation occur? How does dune activation timing compare with tree ring and other hydroclimate records? This manuscript is being prepared for submittal to the journal *Quaternary Science Reviews.*

Chapter 3 used a similar systematic approach to reconstruct a chronostratigraphic record of eolian activity in San Rafael dune field in east-central Utah, comparing results to other regional records from mobile dunes in the Colorado Plateau region to develop a region-wide dune activation record. The research objectives in this chapter seek answers to the following questions: What are the type and distribution of dune morphologies in the San Rafael dune field, and what geomorphic processes predominate the development of the landscape? What is the timing of eolian activity in individual dune sites? Is there evidence for dune-field wide activity? How do the two Utah dune fields compare geomorphically? Is there evidence of coeval dune activation in both dune fields and/or in other region-wide dune activation records? Does eolian activity vary with dune morphology? This manuscript is being prepared for submittal to the journal *Arid Environments*.

Chapter 4 reports the results of analysis of modern wind records and dune sediment geochemistry, to contribute depth to understanding the dune field development and history in southern Utah. Bagnold's (1941) seminal research in desert dune fields provided fundamental information on thresholds required for sand dune activity. Fryberger (1979) developed a method to compare wind potential to transport sand in different regions and environments. Muhs (2017) compared dune sediment geochemistry and source sediment geochemistry, successfully differentiating dune sediment provenance, using K/Rb and K/Ba ratios present in feldspar grains. Research questions for Chapter 4 are: Can modern wind records from portable analog wind stations be evaluated for drift potential according to the method developed by Fryberger (1979), and can these modern wind records be used as analogs for Holocene winds at the study dune fields? Can the source rock for Kanab and for San Rafael dune fields be identified using readily

available geochemistry obtained for each study dune field chronology? Is there geochemical evidence for change in the source rock geochemistry of Kanab and/or San Rafael dune field through the Holocene? Components of this research may provide future research questions and student research.

Chapter 5 provides a summary of the studies contained in this dissertation, reviews the major conclusions and provides a discussion of future directions for this research. Through these chapters the history of sand dune activity in the Colorado Plateau is presented, and the implications for hydroclimate variability are discussed.

References

Bagnold, RA, 1941. The physics of wind-blown sand and desert dunes. Methuen, London, 265 (10)

Benson, L., Kashgarian, M., Rye, R., Lund, S., Paillet, F., Smoot, J., Kester, C, Mensing, S, Meko, D. and Lindstrom, S, 2002. Holocene multidecadal and multicentennial droughts affecting Northern California and Nevada. Quaternary Science Reviews, v. 21 (4-6), p. 659-682

Bentz, B.J., Régnière, J., Fettig, C.J., Hansen, E.M., Hayes, J.L., Hicke, J.A., Kelsey, R.G., Negrón, J.F., Seybold, S.J., 2010, Climate Change and Bark Beetles of the Western United States and Canada: Direct and Indirect Effects , BioScience, Volume 60, Issue 8, 1 September 2010, Pages 602–613

Betencourt, J.I., Guiterman, C.H., 2016. Revisiting human-environment interactions in Chaco Canyon and the American Southwest, PAGES v. 24 (2), p 64-65

Cook, B.I., Ault, T.R., Smerdon. J.E., 2015. Unprecedented 21st century drought risk in the American Southwest and Central Plains. Science Advances. 1(1)

Cook, B.I., Seager, R., Miller, R.L., 2011. The impact of devegetated dune fields on North American climate during the late Medieval Climate Anomaly, Geophys. Res. Lett., 38, L14704

Cullinane Thomas, C., Koontz, L. and Cornachione, E., 2018. 2017 national park visitor spending effects: Economic contributions to local communities, states, and the nation. Natural Resource Report NPS/NRSS/EQD/NRR—2018/1616. National Park Service, Fort Collins, Colorado.

Fettig, C.J., Mortenson, L.A., Bulaon, B.A., Foulk, P.B., 2019, Tree mortality following drought in the central and southern Sierra Nevada, California, U.S., Forest Ecology and Management, 432, 164-178

Fryberger, S.G, 1979, Dune Forms and Wind Regimes. In A Study of Global Sand Seas; McKee, E.D., Ed.; U.S. Geological Survey: Reston, VA, USA, 1979; pp. 137–169

Gray, S.T., Graumlich, L.J., Betancourt, J.L., Pederson, G.T., 2004. A tree-ring based reconstruction of the Atlantic Multidecadal Oscillation since 1567 A.D. Geophys. Res. Lett., 31, L12205.

Howitt, R.E., MacEwan, D., Medellín-Azuara, J., Lund, J.R., Sumner, D.A., 2015. "Economic Analysis of the 2015 Drought for California Agriculture". Center for Watershed Sciences, University of California – Davis, Davis, CA, 16 p.

Lancaster, N., 1997, Response of eolian geomorphic systems to minor climate change: examples from the southern Californian deserts: Geomorphology, v. 19, p. 333–347

Meko, D. Woodhouse, C.A., Baisan, T., Knight, J.J., Lukas, M.K., Hughes, J., Salzer, M.W., 2007. Medieval drought in the upper Colorado River Basin, Geophys. Res. Lett., 34, L10705

Muhs, D.R., 2017. Evaluation of simple geochemical indicators of aeolian sand provenance: Late Quaternary dune fields of North America revisited. Quaternary Science Reviews, 171, pp.260-296.

Papalexiou, S.M., AghaKouchak, A., Trenberth, K.E., and Foufoula-Georgiou, E., 2018, Global, Regional, and Megacity Trends in the Highest Temperature of the Year: Diagnostics and Evidence for Accelerating Trends: Earth's Future, v. 6(1), p. 71–79

Powell, J., Rumore, D. and Smith, J., 2021. The GNAR Initiative: Empowering gateway communities through collaboration. Vaugeois, N., Phillips, M., Arbogast, D. & Twilley, D.(Eds.).(2021). Innovative and promising practices in sustainable tourism. Nanaimo, BC: VIU Publications.

Polyak, Victor J., Asmerom, Y., 2001. Late Holocene Climate and Cultural Changes in the Southwestern United States, Science, vol. 294, no. 5540, 2001, pp. 148–151

Smith, G.P and McFaul, M. 1997, Paleoenvironmental and geoarchaeologic implications of late Quaternary sediments and paleosols: north-central to southwestern San Juan Basin, New Mexico, Geomorphology 21 (1997) 107-138

Woodhouse, C.A., Pederson, G.T., Morino, K., McAfee, S.A., and McCabe, G.J., 2016, Increasing influence of air temperature on upper Colorado River streamflow: Geophysical Research Letters, v. 43, p. 2174–2181

Williams, A. P., Cook, B I., Smerdon, J. E., 2022, Rapid intensification of the emerging southwestern North American megadrought in 2020-2021. Nature Climate Change, v.12, n.3, p.232-234.

CHAPTER 2

EOLIAN ACTIVITY IN THE KANAB DUNE FIELD, SOUTHWESTERN UTAH: A PALEOCLIMATE PROXY FOR HYDROCLIMATE VARIABILITY DURING THE HOLOCENE

Abstract

The semi-arid Colorado Plateau and Four Corners region of the southwestern United States is rich with human history, sensitive desert ecological systems, public lands, and natural resources, including water supply from the Colorado River. Impacts from increasing population pressures and future climate change are a concern for land and water managers. Past mega-droughts have affected this region, and it is currently experiencing one of the most severe droughts on historic record. This study investigates eolian sediments in southern Utah to extend the short instrumental and tree-ring climate records beyond the last 100-1000 years and into the mid and early Holocene (last 10,000 years (10 kyr)). A record of eolian activity was produced using geomorphic mapping, sediment and stratigraphic analysis with age control from radiocarbon (^{14}C) (n=3) and optically stimulated luminescence (OSL) (n=35) analyses.

Four episodes of eolian activity are determined for the Kanab dune field, 15 km north of Kanab in southern Utah. Periods of dune activity include episodes K1 (~6.8-5.6 thousand years ago (ka)), K2 (~4.4-3.3 ka), K3 (~2.2-1.2 ka) and K4 (~0.7-0.4 ka), each identified at multiple individual sites within the dune field. These intervals are interpreted as dune field-wide eolian activity. There is also evidence for early Holocene eolian activity, denoted K0 (~9.2-7.8 ka). We compare these results to climate records and find early Holocene eolian activity, K0 and K1 consistent with western Pacific Ocean warming and changes in North Atlantic thermohaline circulation. Episodes K2, K3 and K4 are contemporaneous with increased intensity of El Niño Southern Oscillation (ENSO) events, and match other records of aridity from the region, suggesting a linkage to monsoonal precipitation patterns and their drivers.

1.0 Introduction

The Colorado Plateau (CP) straddles the Four Corners region of southwestern United States where the borders of Utah, Colorado, New Mexico and Arizona meet. The CP is characterized by vistas of erosional escarpments, natural resources and diverse human history. Readily accessible recreational opportunities on vast areas of public lands have attracted increasing visitation since the mid-20th century, escalating stress on unique and sensitive ecosystems and public infrastructure with both growing tourist and local populations (Poudyal et al, 2016; Culliane-Thomas et al, 2018). The Colorado River, providing water to over 40 million people and irrigating almost 5.5 million acres (USBR, 2012), dissects the region. Water supply and distribution are regulated via water-rights compact agreements and managed through an extensive reservoir system. However, this vital resource has been impacted by extended drought over the last two decades in the US southwest (California, Nevada, Utah, Colorado, New Mexico and Arizona) (Cook et al, 2021). Rising population growth and climate change contribute to uncertainty in the sustainability of utilizing the available water supply to meet municipal and agro-industrial demands while maintaining healthy ecosystems needed to help combat continued climate change (i.e., Udall and Overpeck, 2017; USBR report, 2021).

Climate models predict increasing temperature across the region, leading to concerns that megadroughts could become more common (Woodhouse et al, 2010; Cook et al, 2015; Papalexiou et al, 2018). Precipitation is largely bi-modal with winter precipitation modulated by El Niño-Southern Oscillation (ENSO) activity and late summer precipitation derived from North American Monsoon (NAM) coming from Baja California (e.g., Menking and Anderson, 2003; Schwinning et al, 2008; Anderson, 2012; Jones et al, 2015). Records of past hydroclimate variability can provide context for natural climate dynamics and improve understanding of the range of future climate change (Copeland et al, 2017; Woodhouse and Pederson 2018). However,

the instrumental (<120-year) and tree-ring records (<1200 years) are too short or dispersed to provide climate context for past drought regimes.

While tree-ring and sediment records for paleoclimate reconstruction are found in other parts of the southwestern US, such records are limited in the CP. Eolian dune systems provide an important indication of landscape response to climate because they record a threshold response to sustained changes in effective moisture and are prevalent on the arid and semi-arid CP. Previously stabilized dunes can remobilize under threshold conditions of adequate loose sediment availability, low soil moisture (≤ 4%) and sufficient wind strength (≥ 6 m/s) (Bagnold, 1941; Logie, 1982; Tsoar, 2005; Lancaster, 2008).

Geomorphic thresholds for sand dune activation were initially identified in a landmark study by R.J. Bagnold (1941). Subsequent work investigated the role of sediment supply and availability, defining sediment state relative to sand availability (i.e., Lancaster 1994, Kocerak and Lancaster, 1999). Dune activity is controlled by interlinked biogeomorphic processes and thresholds that lead to hysteresis (lagged non-linear response) of the system to changes in hydroclimate (Hugenholtz and Wolfe, 2005; Viles, 2008; Wolfe and Hugenholtz, 2009; Barchyn and Hugenholtz, 2013).

The purpose of this study is to extend the record of dune field activity as a proxy for aridity (natural hydroclimate variability) in the central CP region utilizing a dune field north of the city of Kanab in southern Utah, here called the Kanab dune field (KDF) (Figure 2.1). Results indicate five episodes of dune activity, linked to regional periods of aridity. These periods of eolian activity are millennial-scale in pacing, with decreasing intervals between episodes during the late Holocene. This record is consistent with other records of reduced effective moisture across the region and with atmospheric circulation during the Holocene.

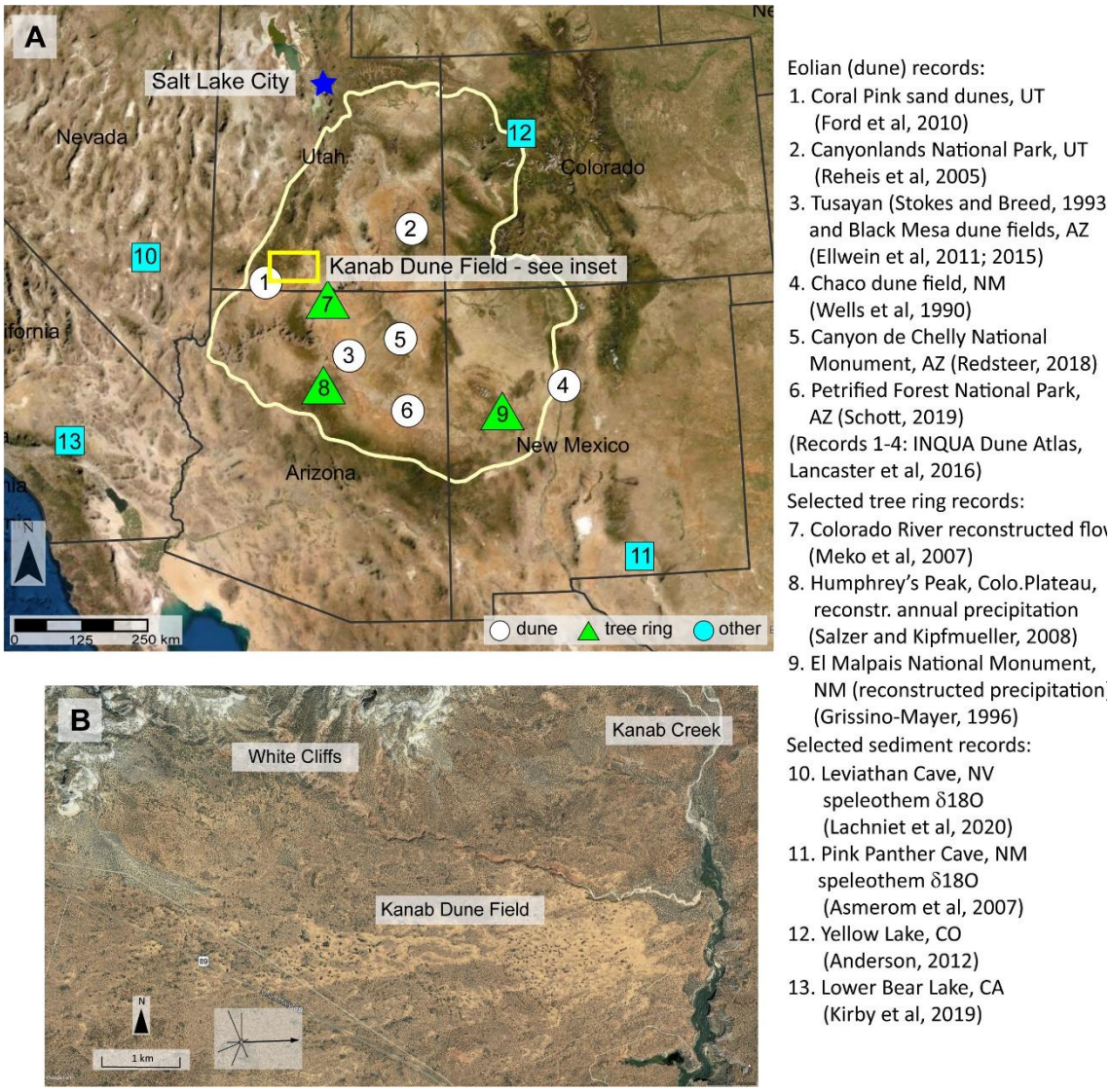

Figure 2.1. Project vicinity map. A. Project site location and selected paleoclimate records for southwestern United States shown within central Colorado Plateau referenced. Numbered circles (1-6) correspond to dune activity records. Numbered triangles (7-9) are selected tree ring records and numbered squares (10-14) are regional sediment records. B. Inset is aerial image of project area showing the White Cliffs escarpment, Kanab Dune Field and Kanab Creek (eastern boundary).

2.0 Physiographic Setting

The Colorado Plateau is a high elevation (750 –3840 meters above sea level (masl)), largely undeformed part of the intermontane physiographic province in North America, bounded by the Rocky Mountain ranges to the north and east and the Basin and Range province to the

west. The Colorado River and its tributaries dissect the Colorado Plateau. These drainage routes were established following integration of the Colorado River to the Gulf of Baja ~ 5 (million years ago (Ma)) (Figure 2.1, vicinity of Lee's Ferry, green triangle labelled #7) (Lucchitta, 1972; Dorsey et al, 2007; Karlstrom et al, 2014). Climate and vegetation of the CP varies with elevations ranging from semi-arid sage scrublands to forested and alpine conditions at higher elevations.

The Kanab dune field is located approximately 15 km north of the town of Kanab, Utah within the Grand Staircase geomorphic province of the west-central Colorado Plateau. The Grand Staircase is an erosional landscape that steps back from the Grand Canyon, so-named for the bench-and-step landscape formed by differential erosion of the Mesozoic to Cenozoic bedrock units (Dutton, 1882). The dune field is composed of stabilized and partially stabilized parabolic dunes that are 2-15 m in height and is oriented roughly west-east along the base of the White Cliffs, a steep exposure (~2190 masl) of Jurassic Navajo Fm. sandstone (Figure 2.1B). Elevations in the dune field range from ~1650 – 1830 masl, decreasing to the east and south. The eastern downwind edge of the dune field borders Kanab Creek, a north-south oriented tributary to the Colorado Rier in the Grand Canyon.

Vegetation within the dune field consists primarily of xeric shrubs and grasses typical of a sage-steppe ecosystem. Dominant shrubs include species of rabbitbrush (*chrysothammus nauseosa* and *chrysothamnus viscidiflorus*), ephedra, desert gooseberry and sagebrush (*Artemesia arbuscula* and *Artemesia tridentata*). Grasses, annual forbs, yucca and cactus varieties are also prevalent. A few Ponderosa pine trees (*Pinus ponderosa*) occur in the central part of the dune field, primarily in low-lying interdune scours where bedrock is sometimes exposed. Utah juniper (*Juniperus osteosperina*) are distributed across the dune field. Vegetative cover is denser in the western half of the dune field and the flanking mixed eolian-alluvial deposits to the north and south, as well as interdune areas. Biological soil crusts (biocrusts) occur in the dune field,

generally in areas of lower surface relief and where dune morphology is muted or absent, typically on the western (upwind) end of the dune field.

Climate is semi-arid or steppe in the Koeppen-Geiger climate classification system, with hot, dry summers and cold, dry winters. Mean annual precipitation is 342 mm (Table 2.1), delivered through bimodal, seasonal weather systems. Winter precipitation is driven by a southward dip of the Polar Jet Stream while precipitation from late summer monsoons is primarily convective thunderstorms occurring due to advection of moist air from the south during summer months (Mock, 1996). The North American Monsoon (aka Mexican Monsoon) provides precipitation via convective storms while winter storms generate precipitation from the western Pacific (Schwinning et al, 2008; Metcalf et al, 2015). Summary climate records for the period December, 1899 – June, 2016 from the Kanab Cooperative Observer Network (COOP) weather station are shown in Table 2.1. The station is located approximately 15 km south of the dune field in the town of Kanab.

Table 2.1 Summary climate records. (Kanab Cooperative Observer Network (COOP))

Precipitation (mm)		Temperature (^{o}C)	
Mean annual precipitation	342.6	Mean annual temperature	21.0
Monthly maximum (January)	38.9	Monthly minimum (January)	8.6
Monthly minimum (July)	8.6	Monthly maximum (June)	33.8

(Source: https://wrcc.dri.edu/cgi-bin/cliMAIN.pl?ut4508)

Wind data from the Kanab MesoWest (KKNB) climate station, located about 15 km south of the dune field (2003-2018), indicate a bimodal character to seasonal wind speed and direction. Wind velocities required for sand erosion and transport represent a fundamental threshold system. Pioneering work on thresholds for sand transport in air is attributed largely to Major Ralph Bagnold (1941). This landmark work, based on laboratory studies supplemented by extensive field experiments and observations in deserts, forms the basis for understanding complex relationships between particle size, wind speed and mechanism of transport and

deposition that are characteristic of dune formation and migration processes. Typically, wind velocity > 6 m/s and soil moisture < 4% thresholds must be attained for erosion of sand-sized particles (0.062 – 2 mm) to occur (e.g., Bagnold,1941; Logie, 1982; Kocerak and Lancaster, 1999; Tsoar, 2005). With the availability of Landsat imagery and reliable surface wind records, Fryberger (1979) developed a method of comparison of wind energy regimes and dune forms that could be applied to dune fields globally. The sand-moving capacity of wind as is defined as drift potential (DP), based on relative amount of sand migration produced by a wind velocity measured at standard height of 10 m (33 ft), determined for 16 standard compass-based wind directions. This relationship is shown in Equation 1, below

$$DP = \sum q = \frac{u^2(u-u_t)}{100} t \qquad \text{(Eq 1)}$$

where DP is drift potential, q is the rate of sand drift, u is wind velocity (knots), u_t is threshold velocity (knots) and t is percent of time wind blew above threshold velocity (%) (Fryberger, 1979; Tsoar, 2005). Drift potential, rather than wind velocity, may better reflect conditions during dune activations, since vegetation cannot establish when sand is entrained (Siegal, 2013).

During the winter and fall, threshold winds (>6 m/s) are predominantly from the NNW, shifting to dominantly SW during the spring and summer. Resultant drift direction (RDD) and resultant drift potential (RDP) are the vector sum of annual drift potential for the 16 compass directions. In Kanab, annual RDD is 88^o (E) and RDP is 550, or “high”, following the methods of Fryberger (1979). Orientation of individual dunes varies between ENE and ESE, with general eastward trend of Kanab dune field (Figure 2.1B). Dune field orientation is broadly consistent with RDD (88^o) determined from the modern wind records.

3.0 Previous regional work

Regional and extra-regional records have been used to reconstruct paleoclimate of the Colorado Plateau (Figure 2.1). Tree rings, lake sediments and speleothems can provide high-resolution, annual to centennial proxy records for climate. Records of ring-width in trees growing in stressed conditions with respect to water and temperature can be used reconstruct past climate conditions. Tree ring records can extend instrumental records to ~ 1000 years or longer in specific settings with old trees or good preservation of remnant wood. Lake sediment can reflect annual variability in climate and lake sediment characteristics, coeval plant material and chemistry contribute information on precipitation and temperature. Speleothems (carbonate precipitation in caves) can also record annual variability in temperature and precipitation, measured through changes in isotope chemistry. While lower resolution, sediment records from sand dunes can extend throughout the Holocene (> 10 kyr). In this section previous paleoclimate reconstructions from the region are described.

3.1 Tree ring records

Tree ring records from across the Colorado Plateau and Four Corners region extend the instrumental climate record back about one millennium. Tree ring records from the Upper Colorado River Basin (UCRB) indicate that there were multiple decadal-scale periods of low flow in the Colorado River over the last 1200 years (Meko et al, 2007). One of the most significant dry intervals occurred from ~900 – 840 years ago, characterized by a 13-year interval where flows were ~16-20% below normal (observed mean flow, 1906-2004 CE). Reconstructed temperature and precipitation using tree ring records from ecological boundary zones (lower forest and sub-alpine) in north-central Arizona indicate variable climate over the past 1-2 kyr (Salzer and Kipfmueller, 2005). The longest periods of warm/dry conditions were identified at 874-866 years ago, and 67-48 years ago, with reconstructed temperatures during these periods revealing cooler temperatures than those of the 20th century. A reconstruction of mean annual

precipitation for El Malpais National Monument in west-central New Mexico identified six decadal or greater-duration drought over the past 1000 years (Grissino – Mayer, 1995). The most severe drought identified was from 454-412 years ago. These tree-ring studies also reveal significant variability in late Holocene hydroclimate on seasonal (annual) to decadal or greater scales.

3.2 Eolian records

Sand dunes are threshold systems limited to reduced vegetative cover typically associated with drought (reduced effective moisture). Sediment supply is also a limiting factor for sand dune activity in certain places. Previously stabilized (vegetated) sand dunes reactivate in response to changes in moisture and temperature conditions that lead to devegetation (destabilization) of the dune sediment. Loose sediment supply becomes vulnerable to transport by deflationary action (scour), which may partially or wholly remove existing records of prior activation.

Records of eolian activity and aridity from mobile dunes in the CP region are summarized in Figure 2.2 (see Figure 2.1 for locations). Eolian records from the Coral Pink dune field 6 km southwest of Kanab dune field indicate active sand movement at ~4.1, 2.8 and 0.51 ka (Ford et al, 2010). Eolian and alluvial deposits with intercalated paleosols in Canyonlands, in east-central Utah find early to middle Holocene dune activity occurred at ~8.6 – 6.8 ka, episodic eolian activity at ~4.2 and 3.8 ka, and late Holocene dune activity ~ 1.8 - 1.0 ka. Wetter, cooler climate conditions are interpreted at ~6 to ~2 ka based on site stratigraphy (Reheis et al, 2005).

Dune fields in northern Arizona and New Mexico have been investigated more extensively than in central Colorado Plateau. Early Holocene dune activity is identified between ~10-7 ka (falling dunes linked to sediment supply), ~5-2 ka and late Holocene <0.5 ka in the Tusayan and Black Mesa area (; Stokes and Breed, 1993; Ellwein et al, 2011, 2015). Occurrences of dune activity in parabolic dunes are documented between ~ 6.5-2.7 ka and ~2.2-1.2 ka, overlying older dune deposits >10 ka in Chaco dune field, New Mexico (Wells et al,1990). Eolian

records from Canyon de Chelly, Arizona indicate Holocene dune activity ~5.3 ka, 3.9 ka, 2.9-2.2 ka and 1.5 ka (Manning, 2010). Eolian activity records from Petrified Forest National Park in northeastern Arizona indicate eolian activity ~2.3, 1.7-1.5, 0.9-0.4 ka (Schott, 2019).

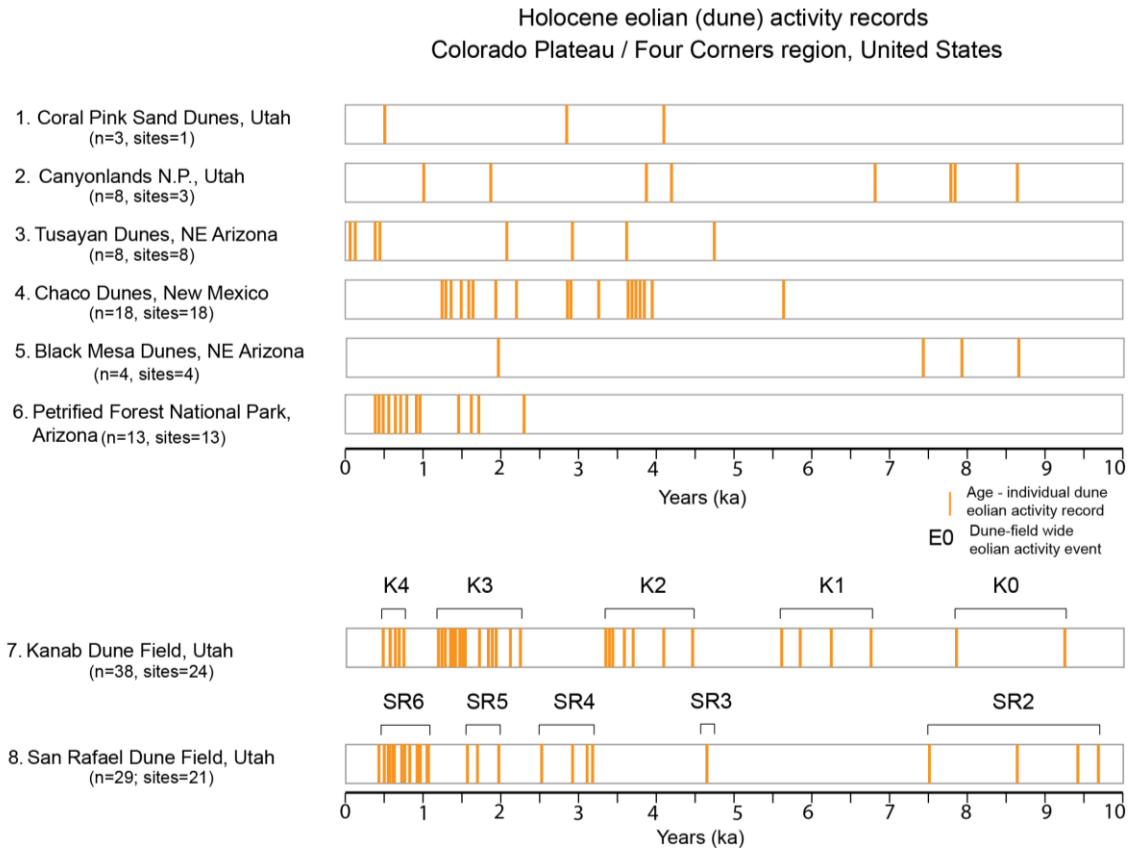

Figure 2.2. Regional dune activity. Records of Holocene dune activity for the Colorado Plateau and Four Corners regions, obtained using luminescence dating of mineral grains from eolian sediments (sites 1-3, 5-7) or radiocarbon ages of charcoal or archaeological materials in dune sediment (sites 4, 7). Number refers to study sites in Figure 3: 1-Ford et al, 2010; 2-Reheis et al, 2005; 3- Stokes and Breed, 1993; 4-Wells et al, 1990; 5- Ellwein et al, 2011, 6-Schott, 2019; 7-Ch. 2, this study, Kanab dune field, Ch.2; 8- Ch. 3, this study, San Rafael dune field. Dune ages (orange bars) reflect ages of individual samples. Interpreted eolian events are identified with brackets, labeled "E0" where "E" is the event, identified by the letter(s) of the dune field name, and "0" is the number, increasing with decreasing age.

3.3 Eolian system thresholds

The spatial variability of temporally equivalent dune activation suggests that dune response to hydroclimate perturbation is complex and multi-faceted. Sediment supply and wind components likely also contribute to regional variability in spatial distribution of contemporaneous dune activation records, as well as local differences in antecedent conditions

(e.g., Lancaster, 2008). Landmark research in desert dunes identified limits for eolian transport via sand saltation at thresholds in wind speed (≥ 6 m/s), soil moisture (≤ 4%) and sediment availability (Bagnold, 1941). In a case study of the Coachella Valley, California, where threshold wind conditions prevail, vegetation was the primary control on sediment availability with precipitation controlling vegetation and thus dune mobility at both modern and millennial timescales (Lancaster, 1997). Sediment supply and sediment state also impact dune accumulation and distribution patterns (Kocurek and Lancaster, 1999; Lancaster, 2008). However, eolian system response to perturbations is complex, and is characterized by a biogeomorphic (lag) response to these threshold conditions (e.g. Lancaster, 1988; Wolfe et al, 2000; Wolfe and Hugenholtz, 2002). Dune mobility indices attempt to quantify the response, incorporating concepts of both moisture, using precipitation to evapotranspiration ratios (P/PE) and wind velocity (Muhs and Maat, 1993; Lancaster, 1997). Thresholds for dune drift potential (DP) were developed to qualitatively categorize dune activation response as high (>400 VU), medium (200-400 VU) or low (<200 VU) (where VU denotes a dimensionless unit) for global comparison of sand dune mobility (Fryberger, 1979).

Vegetative cover typically stabilizes dunes, but vegetation establishment can be difficult due to high infiltration rates of precipitation in combination with high wind speeds (Tsoar, 2005, 2009). A conceptual model of the biogeomorphic response of dune mobility and stabilization developed by Hugenholtz and Wolfe (2005a) shows dune reactivation lagging a disturbance (i.e. change in moisture conditions) that destabilizes the dune (i.e. loss of vegetation) and a similar lag response when climate conditions change again, leading to stabilization of the dune. Specific external variables influencing the lag have been identified as rainfall variability, antecedant moisture and wind power and intrinsic factors including a hysteresis effect (Viles et al, 2008). Thus, studies of dune activity should address the uncertainty induced by the known but unquantified biogeomorphic response both in research design and interpretation of results.

OSL ages collected from the Kanab dunes are expected to post-date the onset of aridity due to the lag in devegetation needed to mobilize a dune. A similar lag in stabilization is expected after the return to wetter conditions that promote dune vegetation growth and dune stability.

The International Quaternary Association (INQUA) Dune Atlas compiles global records of dune ages (Lancaster et al, 2016). A series of contributions to this work summarize our increased understanding of eolian depositional processes and paleoclimate globally, from North (Halfen et al, 2016) and South America (Tripaldi and Zárete, 2016) to Africa (Thomas and Burrough, 2016; Bristow and Armitage, 2016), Arabia (Duller, 2016), Australia (Hesse, 2016) and China (Li and Yang, 2016; Liu et al, 2016). One outcome of this synthesis, which recognizes limitations common to dune studies (i.e., uneven spatial and temporal coverage, dune record heterogeneity from stochastic processes, analytical challenges from age uncertainties), is a call for systematic approaches to eolian dune investigations. The following section details the methodology used in this study to reduce the impact of sampling bias and address record heterogeneity.

4.0 Methods

The goal of this study is to establish a record of eolian activity for the Kanab dune field in southern Utah. A systematic, hierarchical approach is used to first establish breadth (spatial) and depth (temporal) parameters for dune activity. Individual dune reactivation can occur through short term triggers that act to destabilize dunes, such as fire, animal or human disturbance, insect infestation or local changes to water/precipitation delivery. One or more of these events may induce vegetation loss on an older stabilized dune, leaving the unbound sediment susceptible to reactivation under threshold wind and soil moisture conditions. Within the dune field, these local trigger events are expected to be limited in areal extent to a few adjacent dunes, and not observed throughout the dune field. Co-eval activity of multiple dunes, spatially distributed throughout the dune field is interpreted as evidence for dune field-wide activation. While reactivation of the

dune field could be due to a localized event (such as a fire) it is likely that such events are triggered by hydroclimate change leading to vegetation loss and dune activation (mobility) in a semi-arid region.

4.1 Geomorphic mapping

To identify major reactivation event(s) in the dune field, rather than isolated blow-outs or individual dune movement, a systematic approach is needed to obtain representative samples of dune activity. The self-cannibalizing nature of dune mobilization is expected to leave an incomplete record. Soils and horizons that record periods of dune stability can be removed or obscured through subsequent dune reactivation processes. A targeted approach to site selection, coupled with in-field adjustment for site conditions (i.e., bioturbated sediments) facilitated a systematic investigation of past dune field activity. First, the dune field was mapped into geomorphological units using best available imagery (Google Earth historical imagery; National Agriculture Imagery Program (NAIP)).

Geomorphic map units were defined using surficial characteristics and three types of landforms: bedrock, alluvium, dune (see Figure 2.3). Vegetation type and density, and color intensity (hue) of surficial sediments were used to define the current state of surface (sediment) stability (i.e., stabilized, partially stabilized, active). Dune morphology (i.e., sand sheet, short parabolic, large parabolic) and relative age (i.e., younger in active, lighter Munsell hue, downwind sediment / dune) were used to further refine geomorphic units. Sample sites (n=24) were then selected for characterization of soils, sediments, stratigraphy and age of deposition using observed dune morphology to provide representative coverage ($n \geq 4$) in each mapped dune unit.

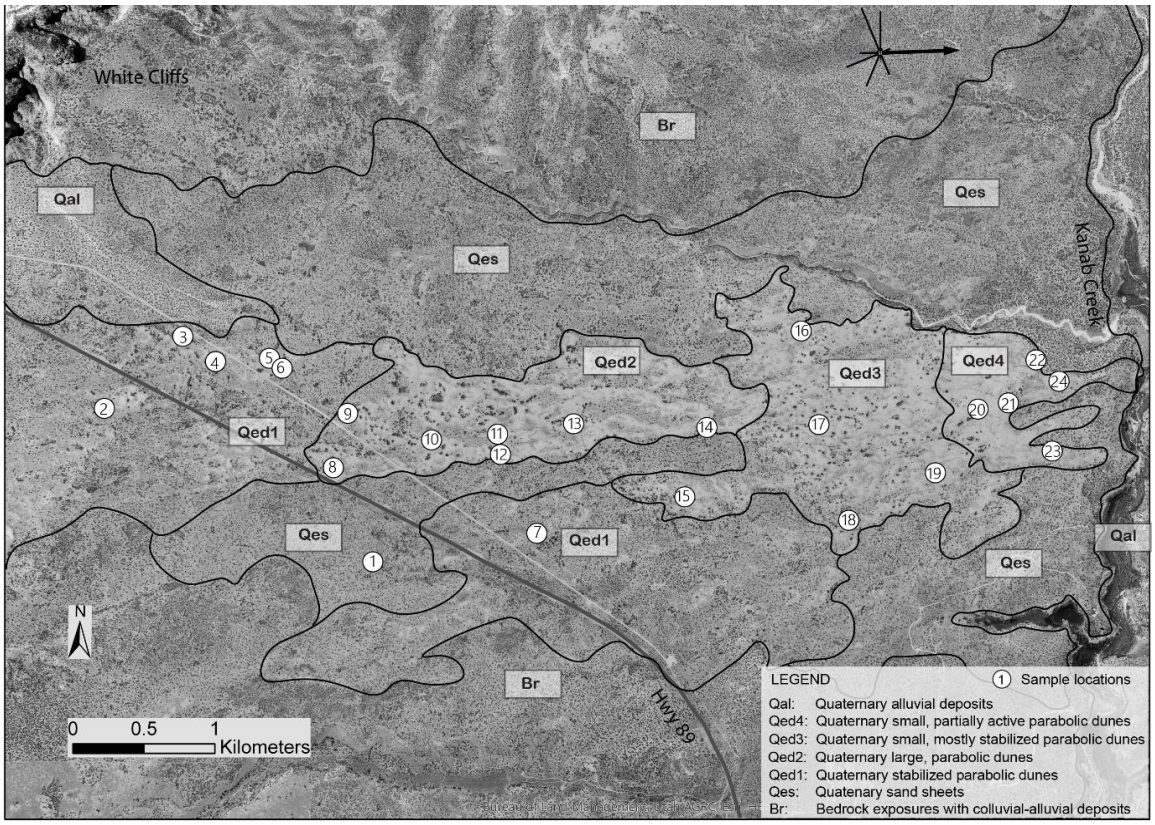

Figure 2.3. Kanab dune field geomorphic map. Map units include bedrock (Br), exposed southward of the field, and vegetated, stabilized sand sheets (Qes) surrounding a series of dune units (Qed1-4 -older to younger) become younger, sparsely vegetated and more active eastward and downwind, toward Kanab Creek. Dune forms include parabolic and long, curvilinear parabolic (center of field). Sand rose (upper right) indicates drift potential binned to 16 compass directions (data source: MesoWest KKNB station, 2009-2018) (methods: Fryberger, 1979). Arrow indicates resultant drift direction (RDD). Locations for study sample sites study indicated on map.

4.2 Field investigation and sampling

Samples from 24 stabilized or partially active dune sites in the Kanab dune field were collected across a dune field area approximately 6.5 km E-W and 2 km N-S to obtain a representative distribution of mapped dune units (n≥4 each unit) (Figure 2.3 and Table 2.2 Field Sites). A hand auger was used where natural exposures (i.e., stream cuts) were not available and in sensitive areas of the dune field requiring minimally invasive sampling. Surficial materials were excavated to depths of 20-30 cm to form a platform for augering. A minimum target depth for samples was 60 cm, to reduce the potential for surficial contamination through bioturbation, and to avoid sampling modern (recently transported) sediments. Sediment and soil descriptions

including grain size, sorting, color, and texture were noted at each site. Samples for grain size, organic content and isotope geochemistry were collected at regular intervals (~20-30 cm). Field observations and sediment descriptions were used to guide sampling for age control. Where encountered, charcoal samples were collected for radiocarbon (^{14}C) dating (n=3). Samples for optically stimulated luminescence (OSL) dating (n=35) were obtained following standard protocols for trench / natural exposure or for coring with a hand auger system (Nelson et al, 2015; 2019). Field sampling methodology is further detailed in Appendix A.

Table 2.2 Field site summary.

Site	Map Unit	Sample ID	Latitude *(dd)*	Longitude *(dd)*	Elev *(km)*	Depth *(m)*	Site Description
1	Qes	USU-3331	37.16113	-112.59753	1.795	3.00-3.15	E-W parabolic limb, with biocrust, adjacent deflation area
2	Qed1	USU-2647	37.17021	-112.61926	1.856	1.80-2.00	dune ridge, ^{14}C - 370 ± 20 *(yr BP)*
2	Qed1	USU-2648	37.17021	-112.61926	1.856	3.30-3.55	dune ridge
3	Qed1	USU-1530	37.17501	-112.61301	1.846	0.8	below dark soil
4	Qed1	USU-3325	37.17362	-112.61033	1.795	0.90-1.15	interdune behind nose stabilized parabolic, strat break ~1.8 m
4	Qed1	USU-3327	37.17362	-112.61033	1.795	2.70-2.95	interdune behind nose stabilized parabolic, below strat break ~1.8 m
5	Qed1	USU-1526	37.17379	-112.60576	1.836	3.35	blow out dune outcrop
6	Qed1	USU-1528	37.17343	-112.60538	1.827	1.65-1.80	center of dune, vertical core sample
7	Qed1	USU-3328	37.16313	-112.58447	1.785	1.20-1.45	below root / vfU in thick eolian package
8	Qed2	USU-1155	37.16688	-112.60091	1.83	2.00-2.15	core from between 2 dune forms
9	Qed2	USU-1156	37.17041	-112.59982	1.839	1.50-1.65	north arm large parabolic, strat break ~1.8 m
9	Qed2	USU-1157	37.17041	-112.59982	1.829	2.55-2.60	north arm lg parabolic, below charcoal horizon. ~1.8 m
10	Qed2	USU-1154	37.16875	-112.59312	1.810	2.00-2.10	sample above ashy layer in dune - site 1; ^{14}C age: 2135 ±15 *(yr BP)*
11	Qed2	USU-2589	37.16921	-112.58804	1.907	0.55-0.85	deflation center, stabilized parabolic dune
12	Qed2	USU-2623	37.16789	-112.58764	1.803	1.75-2.00	older dune, vegetated
13	Qed2	USU-2628	37.16998	-112.58200	1.801	1.75-2.00	dune, ridge top in swale
13	Qed2	USU-2629	37.16998	-112.58200	1.801	3.25-3.50	dune, ridge top in swale, strat break ~2.0-2.3 m
14	Qed2	USU-2630	37.17003	-112.57156	1771	1.80-2.05	dune top, mid-long parabolics
14	Qed2	USU-2631	37.17003	-112.57156	1.771	3.30-3.55	dune top, mid-long parabolics, strat break ~2.6 m
15	Qed3	USU-2634	37.16540	-112.57312	1.761	1.75-2.00	dune ridge, older with ripple marks, med veg to ~0.9 m
15	Qed3	USU-2635	37.16540	-112.57312	1.761	3.25-3.50	dune ridge, older with ripple marks , strat break ~2.3 m
16	Qed3	USU-2576	37.17605	-112.56400	1.748	2.85-2.90	side ridge between blowouts, partially stabilized dune
17	Qed3	USU-2653	37.17018	-112.56236	1.714	1.80-2.05	center of dune ridge, small parabolic
17	Qed3	USU-2654	37.17018	-112.56236	1.714	3.30-3.55	center of dune ridge, small parabolic
18	Qed3	USU-2632	37.16407	-112.55997	1.704	1.75-2.00	small dune ridge NE of deflation dune, long parabolic
18	Qed3	USU-2633	37.16407	-112.55997	1.704	3.25-3.50	small dune ridge NE of deflation dune, long parabolic, ^{14}C 2010±20 *(yr BP)*
19	Qed3	USU-2651	37.16720	-112.55338	1.732	1.75-2.00	dune, small parabolic, low veg cover
19	Qed3	USU-2652	37.16720	-112.55338	1.732	3.25-3.50	dune, small parabolic, low veg cover
20	Qed4	USU-2650	37.17111	-112.54986	1.869	3.30-3.55	dune crest between hummocks, Qed3 unit @ depth
21	Qed4	USU-2626	37.17170	-112.54747	1.687	1.80-2.05	active dune, sparse vegetation
22	Qed4	USU-3388	37.17456	-112.54521	1.675	0.80-1.10	nose of parabolic dune
23	Qed4	USU-2587	37.16868	-112.54369	1.866	1.50-1.75	small parabolic, partially stabilized, below crest
23	Qed4	USU-2588	37.16868	-112.54369	1.866	3.25-3.35	small parabolic, partially stabilized, below strat break ~2.2 m
24	Qed4	USU-2624	37.17318	-112.54340	1.667	1.80-2.05	active foredune
24	Qed4	USU-2625	37.17318	-112.54340	1.667	3.10-3.35	foredune at depth, below strat break - charcoal horizon

4.3 Analytical approach

Field observations and laboratory analyses were used in conjunction with OSL and ^{14}C ages to develop dune-field chronostratigraphy. Sediment samples were analyzed for grain size using a Malvern Mastersizer 2000 laser particle analyzer. Selected sediment samples were also analyzed for total organic content (TOC), and percent carbon (%C) using an isotope ratio mass spectrometer (IRMS). Select sediment samples were also analyzed for chemical composition using inductively coupled plasma mass spectrometry (ICP-MS). Analytical methods for sediment and chronology are further detailed in Appendix B.

Individual sediment packages and paleosols representing periods of partial dune stabilization were identified from the field descriptions and laboratory analyses. Particle-size analyses were used in conjunction with field descriptions to identify changes in sorting and trends in mean grain-size or silt addition. Paleosols (periods of stabilization) were identified using field observations and corroborated where possible with increased organic carbon content. Figure 2.4 shows the example stratigraphic sequence for Site 23, with particle size, color, $\delta^{13}C$ reflecting similar increases at a buried soil horizon at ~250 cm depth, above the lower OSL (dune) sample. Dune stability / soil formation are suggested by increased clay and silt fraction appearing at about 230-285 cm depth, reflected in the increases in very fine and fine sand component. Munsell soil color (value) and %C support the evidence (here exhibited graphically) of a hiatus in dune activity with development of an erosional (soil) horizon above the lower OSL sample (USU2588). Similar reconstructed stratigraphic columns depicting the graphical results from 20 sample sites can be found in Appendix C.

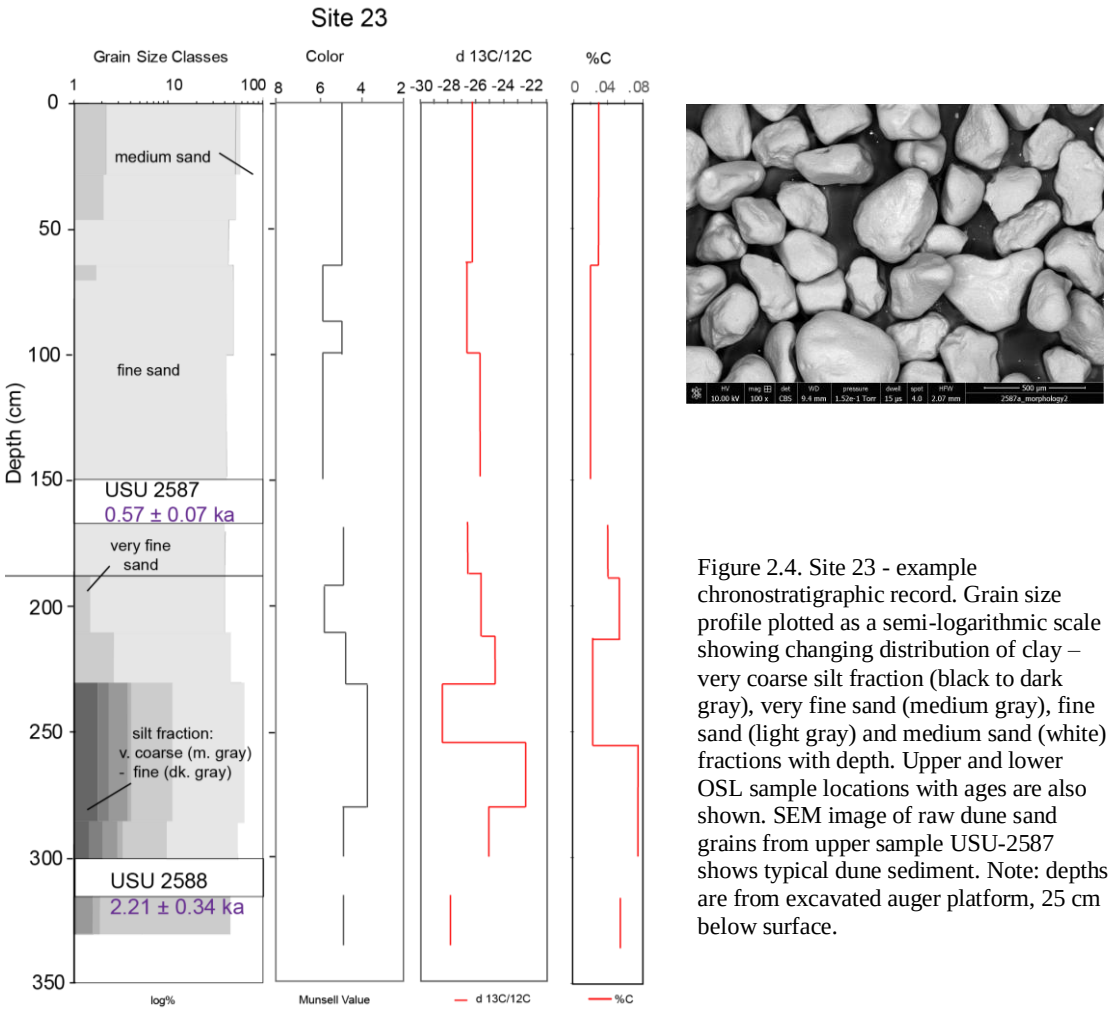

Figure 2.4. Site 23 - example chronostratigraphic record. Grain size profile plotted as a semi-logarithmic scale showing changing distribution of clay – very coarse silt fraction (black to dark gray), very fine sand (medium gray), fine sand (light gray) and medium sand (white) fractions with depth. Upper and lower OSL sample locations with ages are also shown. SEM image of raw dune sand grains from upper sample USU-2587 shows typical dune sediment. Note: depths are from excavated auger platform, 25 cm below surface.

4.4 Age Control

Research in geomorphic processes and landscape evolution has been transformed with the application of luminescence dating to sedimentary deposits (Aitken, 1963, 1989; Huntley et al, 1985; Rhodes, 2011). Luminescence dating determines the last time a mineral grain was previously exposed to light or heat. This technique uses the charge that has accumulated in a crystal lattice due to exposure to ionizing radiation in the surrounding sediments and incoming cosmic dose acquired after burial. This tool allows researchers to resolve the age of sediment deposition and is invaluable in deposits that have limited material for radiocarbon (i.e., fluvial-alluvial, glacial and eolian).

Age control for Kanab dune activity is obtained primarily from optically stimulated luminescence (OSL) dating, (Huntley et al, 1985). Thirty-five samples for OSL dating were collected from 24 sites, either using a soil auger with coring capability (n=32) or from hand-dug or natural exposure (n=3). Accelerated mass spectrometry (AMS) radiocarbon dating of charcoal samples (n=3) provided additional age control.

4.4.1 Radiocarbon Analysis

Charcoal samples greater than 1 mm size (n=3) were dated using radiocarbon to provide age control for periods of dune activity. Samples were analyzed using accelerated mass spectrometry (AMS) at University of California at Irvine Center Accelerator Mass Spectrometry (n=1) and the Center for Applied Isotope Studies at University of Georgia (n=2). Cleaned samples were converted to graphite, then $^{14}C/^{13}C$ isotope ratios were measured using AMS, and compared with the ratio measured from the Oxalic Acid I (NBS SRM 4990). Sample $^{13}C/^{12}C$ ratios were measured separately using a stable isotope ratio mass spectrometer and expressed as $\delta^{13}C$ with respect to PDB, with an error of less than 0.1‰. Uncalibrated ages are reported in radiocarbon years before 1950 (years BP), using the ^{14}C half-life of 5568 years and corrected for isotope fractionation. Laboratory-reported ages were calibrated using INTCAL20 and are reported to a datum of BP_{2020} to allow for direct comparison with OSL ages that also have a datum of CE 2020.

4.4.2 Optically Stimulated Luminescence

Optically stimulated luminescence (OSL) provides an age estimate of last time sediment was exposed to light (or heat) and has been shown to provide reliable ages up to 200,000 years ago or more in most settings ((Huntley et al,1985; Rhodes, 2011). Luminescence dating is based on the loss of stored charge (electrons) from defects (traps) in a mineral lattice when exposed to

sunlight or heat (200-400^{o}C), a process known as “bleaching” or “zeroing”. A gradual reacquisition of charge begins after the grain is buried and exposed to ionizing radiation in the surrounding sediments, and from exposure to cosmic radiation. The environmental dose rate (D_R) is determined from the sediments surrounding the sample and an estimate of the incident cosmic radiation, based on the depth and geospatial location of the sample (Aitken, 1998). The effective D_R includes attenuation by interstitial water so an estimate of the water content of the sample is made, typically from a sample collected from the surrounding sediments. The equivalent dose (D_E) of radiation the sample received during burial (or last exposure to light or heat) is calculated using the luminescence response of individual aliquots or grains, to laboratory doses of radiation. The age of the sample is determined by dividing the D_E by the D_R (Aitken, 1998). Measurements are in SI units of Grays (Gy, where 1 Gy = 1 Joule/kg). D_R is reported in Gy yr-1.

Obtaining successful results from OSL dating, regardless of the application, is dependent upon three main factors. First, the sample must be collected with careful regard to preserve sample integrity (i.e., avoid exposure to light or heat, sample surrounding materials for dose rate determination, preserve stratigraphic integrity). Second, post depositional disturbance such as bioturbation from animals, root growth or mechanical processes including soil creep or frost heave, collectively termed pedoturbation, should be avoided, as these processes introduce foreign grains above and below the OSL target (e.g., Bateman et al, 2003, 2007 a, b; Rink et al., 2013). Third, sampling should target depositional environments conducive to adequate sun exposure. Optimal luminescence properties are developed through frequent dosing and resetting of the luminescence signal, such as repeated sediment cycling on the Earth’s surface (Rhodes, 2011).

OSL samples were processed and analyzed at the Utah State University Luminescence Laboratory in Logan, Utah. Sediment cores and sample tubes were processed under dim amber light (~590 nm) to isolate the quartz mineral fraction. Outer sediment from the tubes and cores was discarded to remove grains potentially exposed to light, and the remainder of each sample was wet-sieved to a target particle size between 150 and 250 µm (Appendix B). The sample was

then treated with hydrochloric acid to dissolve carbonates, bleach or peroxide to remove organic material, separated from higher density minerals using sodium polytungstate (2.7 g/cm^3), followed by concentrated hydrofluoric and hydrochloric acid treatments to remove feldspars, etch the outer surface of the grains, and prevent formation of fluorite precipitates (e.g., Wintle, 1997).

Representative subsamples of sediment for dose rate determination were analyzed using ICP-MS and ICP-AES analyses for concentrations of radioelements K, Rb, Th, and U. In-situ gravimetric moisture content was measured on all samples (Appendix B). Given the variation in moisture conditions over the sampling seasons, an average of 5±2% was used as the moisture content in dose rate calculations for all samples. Dose-rate calculations include conversion factors from Aitken (1989) and Guérin et al. (2011), the influence of water attenuation, cosmic contribution by using sample depth, elevation, and longitude/latitude following Prescott and Hutton (1994), and uncertainty in elemental measurements.

Luminescence measurements were performed on two Risø TL/OSL Model DA-20 readers equipped with blue-green light emitting diodes (LED) (470±30 nm) (Bøtter-Jensen et al., 2003). OSL ages were obtained from the quartz sand (150-250 μm) fraction using the single aliquot regenerative (SAR) dose protocol of Murray and Wintle (2000). Aliquot size was 2 mm and contained ~60-80 grains per disk. A dose recovery test (Appendix C) was used to optimize temperature settings for regenerative preheat (220^o C) and test dose preheat (cutheat) (220^o C) settings, and an optical bleach was used to remove remaining charge buildup between dose cycles (Wintle and Murray, 2006). Dose response curves were fit within linear and saturating-exponential fits to calculate D_E values.

D_E values were calculated from more than 15 accepted aliquots using the central age model (CAM) of Galbraith and Roberts (2012) (Appendix B). Rejection criteria included evidence of feldspar contamination, recycling ratio <0.7 or >1.3, natural D_E greater than the highest regenerative dose given, large (>100%) D_E error and/or $D_E \leq 0$ Gy. Errors on D_E and age

estimates are reported at 1-sigma standard error and include errors related to instrument calibration, and dose rate and equivalent dose calculations and were calculated in quadrature using the methods of Aitken and Alldred (1972) and Guerin et al. (2011).

5.0 Results

The orientation of the dune field is largely west-east, dominated by parabolic dunes that are mostly stabilized on the west end of the dune field, and partially active to the east. Elevations in the dune field decrease from ~1.9 to ~1.6 km, west to east and ~1.75 to 1.63 km, north to south. Slopes vary across the dune field, from ~2-6% in the west and south, and vary to extremes of up to ~35% in the center of the field. Downwind (east) elevations and slopes decrease near Kanab Creek.

Sand sheets comprised dominantly of eolian deposits, including relict dunes with some alluvial sediments, surround the dune field and are more densely vegetated than the sand dunes. Dunes appear to progressively young to the east. Soils in the dune field are thin and poorly developed throughout the dune field. Biological crust development is evident across approximately the western one-third of the dune field, mostly in the eolian sand sheets. Dune sediment is mainly fine to medium-grained, sub-rounded to rounded, quartz sand grains, with reddish color (typically Munsell 5 YR 5-6/8 ranging to 2.5 YR 6/6-8) with minor amounts of feldspar, heavy minerals, and lag gravels. Most dunes contain some grass cover and shrubs or root mounds, primarily sage or rabbitbrush. Sample sites were chosen to minimize disturbance from vegetation and avoid evidence of bioturbation (Bateman et al, 2007b; Rink, et al, 2013). Interdune areas are more consistently vegetated, with pinion pine and juniper. In the central to south-central dune field, Ponderosa pine (*Pinus ponderosa*) is established and some scrub oak (*Quercus turbinella*) is present.

5.1 Geomorphic mapping

Four geomorphic dune units were mapped in Kanab dune field, identified as Quaternary eolian dune unit 1 (Qed1), Quaternary eolian dune unit 2 (Qed2), Quaternary eolian dune unit 3 (Qed3) and Quaternary eolian dune unit 4 (Qed4) from oldest to youngest (Figure 2.3). Sand sheets of mixed eolian and alluvial sediment (Qes) are mapped to the north and south. This unit onlaps bedrock exposures (undivided map unit Br) and merges with alluvial-colluvial debris shed from the White Cliffs to the north and small bedrock knobs exposed to the south of the main dune field. An alluvial fan developed from a small ephemeral drainage in the northwest corner of the study site is mapped as Quaternary alluvium (Qal).

The geomorphically oldest dune unit mapped, Qed1, is characterized by stabilized small parabolic dunes, ~50-250 m in length and ~3-5 m in height, moderately well vegetated with Utah juniper (*Juniperus osteosperina*), sagebrush (*Artemesia arbuscula*) and various grasses predominant. Soils of the Pinepoint-Parkwash and Dune-Pinepoint complex are mapped here, the latter more sparsely vegetated (Soil Survey Staff, 2021). Biological soil crust is developed on some dunes and interdunes in this unit particularly where the surface is not disturbed by human activity (i.e., OHV trails or grazing). Two spatially distinct areas are mapped as Qed1, one west of Hwy 89 and another south of the main dune field, separated by undifferentiated eolian sand sheets (Qes) that are well vegetated (see Figure 2.3). Vegetation in Qes is primarily shrubs (i.e., sage, rabbitbrush, gooseberry) with grasses and forbs, and sparse occurrences of juniper trees.

Map unit Qed2 is a long, narrow unit located in the central portion of the dune field. It is comprised of large, long parabolic dunes ~200-500 m in length and 5-15 m in height. Dune limbs are sparsely vegetated with grasses, forbs and occasional small shrubs such as gooseberry or rabbitbrush. Soils are mapped as Dune-Pinepoint complex (Soil Survey Staff, 2021). Trees, including Ponderosa pine (*Pinus ponderosa*) and scrub oak (*Quercus turbinella*) groves are found in interdune areas where deflation has exposed bedrock.

The dune field expands to the north and south at the eastern (downwind) side of the long parabolic dunes, marking the western boundary of a new map unit, Qed3 (Figure 2.3). Small parabolic dunes, ~50-150 m in length and ~4-8 m in height that are partially active to the north and east characterize unit Qed3. Dunes in map unit Qed3 are typically vegetated with shallow-rooted vegetation (sparse grasses, with some sagebrush, rabbitbrush and some forbs), covered with a thin, sometimes ripple-marked layer of loose sediment. Junipers (*Juniperus osteosperina*) and piñon pine (*Pinus edulis*)are common in interdune areas.

The easternmost dune unit, Qed4, is comprised of partially active to active small parabolic dunes, <100 m in length and ~2-5 m in height. Three fingers of active eolian sediment extend from the eastern edge of the dune field into Kanab Creek. These deposits cross a stabilized eolian sand sheet that is vegetated with low-lying shrubs, grasses and some forbs.

5.2 Results of sediment analysis

Samples for sediment analysis were obtained from 24 sites in the Kanab dune field. Site locations, descriptions, sample depths and interpreted eolian events are shown in Table 2.4 and depicted on the geomorphic map of Kanab dune field (Figure 2.3). Results of sediment and organic content analysis (particle size, color, %C) are graphically compiled in stratigraphic columns in for 20 augered sample sites in Appendix C. Sedimentary structures were not recovered from sites that were hand-augered, due to mixing of the sediment.

The dune sediment is dominated by medium to fine and very fine sand that is well-rounded to rounded, well sorted, non-calcareous and frosted (Figure 2.4). A minor fraction of the sand is coarse sand, typically limited to the upper 20-30 cm of sediment. Dune sediment is primarily quartz with minor amounts of feldspar, mica or other minerals. Kanab dune sediment is similar in both physical properties and mineralogy to the Jurassic Navajo Formation, which outcrops along the northern border of the dune field (Uyghar and Picard, 1980; Beitler et al, 2003; Parry et al, 2007; Fossen et al, 2011). There are only minor proportions of silt and clay size

fractions in the Kanab dunes, concentrated in the western side of the dune field, reported at sites 1, 2, 4, 8, 9, 11, 12 and 23. These size fractions are typically associated with soil formation (e.g., Reheis et al, 2005; Ellwein et al, 2018) and reflect periods of cessation of dune activity (dune stability). Figure 2.4 shows the stratigraphic sequence for Site 23 with particle size, color, and %carbon (%C) reflecting similar increases at a soil horizon.

Increased carbon typically occurs during soil formation, and is another indicator used to identify buried soil horizons (Buol et al, 2011). In all cases, the carbon content of the sediments or soils is less than 1%. These %C results from loss on ignition (LOI) and elemental combustion analysis (ECS) are similar to measurements in arid dune deposits (i.e., Muhs and Maat, 1993) using the Walkley Black method (Walkley and Black, 1934). Carbon content of Kanab dune sediment measured in 114 sediment samples, spatially and temporally distributed across the dune field, ranged between 0.006% and 0.076%, with an error range of 0.47% to 32.3% of the reported value (±0.00003 – 0.025%). Error for calibration of instrumentation is reported by the laboratory at ±0.5%. Analytical results are graphically depicted in Appendix C for all sites analyzed. Nitrogen content did not exceed 0.008%, with most samples registering instrumental baseline (0.0-0.002%) and therefore not used in further interpretation. Tabulated results of the TOC analyses are presented as Appendix D.

Stratigraphic evidence for multiple periods of dune activity was seen at several sites. Stratigraphic sequences obtained from sites 4, 9, 13 and 23 in map units Qed1, 2 and 4 provide evidence of hiatus through a combination of field observations and sediment analysis. The primary indicator of a hiatus in eolian activity at these sites is the presence of an interval, about 60 – 80 cm thick, containing an increased fine fraction (very fine sand and silt particle sizes). Smaller particles, especially silts and clays, act to reduce moisture loss from dune sands by infilling pore spaces, which supports establishment of vegetation and over time, soil development (Buol et al, 2011). Darker color (Munsell value) and/or increased %C result from soil development processes in the stratigraphic sequence. OSL and radiocarbon ages add chronologic

evidence. Figure 2.4 shows the graphical stratigraphic analysis for Site 23, where a depositional hiatus occurs between 3.25 m (2.21±0.34 ka) and 1.75 m (0.57±0.07 ka). Dune activity is separated by 1.25 m of sediment. Using similar methods, evidence for depositional breaks occur at site 4 between 2.7 m (5.59±0.69 ka) and 0.9 m(3.55±0.53 ka), site 9 between 2.55 m (4.38±0.49 ka) and 1.5 m (1.69±0.21 ka) and site 13 between 3.0 m (1.65±0.35 ka) and1.5 m (0.67±0.26 ka). Detailed chronostratigraphy for these and other sites can be found in Appendix C.

5.3 Results of age analysis

Radiocarbon ages are reported for three charcoal samples collected from dune sediment (Table 2.3). Ages are consistent with OSL results (Table 2.4) for samples from sites 10 and 18. The age of the charcoal sample collected at site 2 is an age inversion relative to the OSL results (Table 2.4; Appendix C). This sample was likely displaced from the sidewall sediment above the upper OSL sample, during the sample collection process, and recovered during collection of the sediment below the age sample. While the age of the charcoal sample is not useful for stratigraphic interpretation at this site it does record a fire event in the dune field.

Table 2.3 Radiocarbon ages. Charcoal samples recovered in Kanab dune field

Lab Code[1]	**Sample Site**	**Depth** *(m)*	**^{14}C Age** (yr BP) *± 1 sigma*	**Median Age**[2] *cal yr BP ± 2 sigma*	**Age** (BP_{2020}) *(kya) ± 2 sigma*
UCIAMS - 113993	10	2.7	2135±15	2111 63 38	2.18±0.05
UGAMS - 44599	18	2.3	2010 ± 20	1951 62 45	2.02±0.05
UGAMS - 44600	2	1.8	370 ± 20	444 17 50	0.51±0.03

[1] UCIAMS is the lab ID for the University of California Irvine Accelerator Mass Spectrometry Lab; UGAMS is the lab ID for the University of Georgia Accelerator Mass Spectrometry Lab.
[2] The calibrated median age was calculated with CALIB Execute Version 8.2html (Stuiver et al, 2021) and the IntCal20.14c calibration curve (Reimer et al, 2020). Ages are reported in years before 1950 (cal yr BP).

Age results from the OSL analyses are presented in Table 2.4 organized numerically by sample site as shown on the geomorphic map (Figure 2.3) with additional information on dose

rate chemistry and calculation available in Appendices B and E. Dune sediments typically respond well to OSL dating due to full sun exposure during transport. However, Kanab dune sediment produced unexpectedly low sensitivity, from ~2-160 counts/Gy, thus requiring as many as 50 aliquots to acquire the target accepted number of 18-20 aliquots to determine age of burial. Low quartz sensitivity can reflect temperature of crystallization from the original source rock and can also indicate limited sediment cycling (Sawakuchi et al, 2011). The Jurassic Navajo Formation, interpreted as erg sediments, is the likely provenance for Kanab dune sands, thus expected to have a higher sensitivity than was observed (Doelling et al, 2017; Beitler et al, 2003). Low sensitivity of Kanab sands may result from limited sediment transport distances and sediment cycling prior to burial. Low radiation exposure during burial could also be a factor for low sensitivity of the sands. Equivalent dose radial plots are available in Appendix F. Ages are discussed here, organized by map unit, Qes to Qed4, and in approximate order of sample site west to east. Appendix C contains detailed information for each dune site discussed below.

Table 2.4. Optically stimulated luminescence ages. Kanab dune field.

Site	Map Unit	Depth (m)	USU No.	Number of Aliquots[1]	Dose rate (Gy/kyr)	Equivalent Dose ± 2σ (Gy)	Age ± 1σ (ka)	Eolian Event
1	Qes	3.00-3.15	USU-3331	22 (22)	1.01±0.05	9.29±0.72	**9.19±0.85**	K0
2	Qed1	1.80-2.05	USU-2647	21 (29)	0.50±0.04	1.83±0.22	**3.34±0.39**	K2
2	Qed1	3.30-3.55	USU-2648	16 (26)	0.50±0.04	1.67±0.36	**3.35±0.50**	K2
3	Qed1	0.80	USU-1530	22 (25)	1.02±0.05	3.67±0.29	**3.60±0.34**	K2
4	Qed1	0.90-1.15	USU-3325	20 (35)	0.55±0.04	1.95±0.42	**3.55±0.53**	K2
4	Qed1	2.70-2.95	USU-3327	24 (34)	0.51±0.04	2.86±0.40	**5.59±0.69**	K1
5	Qed1	3.35	USU-1526	21 (28)	0.52±0.04	2.1±0.27	**4.04±0.48**	K2
6	Qed1	1.65-1.80	USU-1528	20 (27)	0.52±0.04	3.48±0.32	**6.75±0.76**	K1
7	Qed1	1.20-1.45	USU-3328	20 (34)	0.60±0.04	0.78±0.21	**1.30±0.22**	K3
8	Qed2	2.00-2.15	USU-1155	17 (38)	0.96±0.05	5.58±0.83	**5.82±0.66**	K1
9	Qed2	1.50-1.65	USU-1156	20 (31)	0.65±0.04	1.10±0.18	**1.69±0.21**	K3
9	Qed2	2.55-2.60	USU-1157	25 (40)	0.63±0.04	2.78±0.34	**4.38±0.49**	K2
10	Qed2	2.00-2.10	USU-1154	14 (27)	0.89±0.05	1.78±0.31	**1.99±0.25**	K3

Table 2.4. Optically stimulated luminescence ages, Kanab dune field, continued.

Site	Map Unit	Depth (m)	USU No.	Number of Aliquots[1]	Dose rate (Gy/kyr)	Equivalent Dose ± 2σ (Gy)	Age ± 1σ (ka)	Eolian Event
11	Qed2	0.55-0.85	USU-2589	24 (32)	0.69±0.04	5.37±0.91	**7.84±1.00**	K0
12	Qed2	1.75-2.00	USU-2623	14 (29)	1.10±0.05	6.88±0.75	**6.25±0.62**	K1
13	Qed2	1.75-2.00	USU-2628	17 (59)	0.52±0.04	0.32±0.10	**0.67±0.26**	K4
13	Qed2	3.25-3.50	USU-2629	24 (50)	0.53±0.04	0.71±0.20	**1.65±0.35**	K3
14	Qed2	1.80-2.05	USU-2630	15 (46)	0.65±0.04	0.42±0.07	**0.65±0.08**	K4
14	Qed2	3.30-3.55	USU-2631	18 (40)	0.61±0.04	0.43±0.13	**1.60±0.35**	K3
15	Qed3	1.75-2.00	USU-2634	18 (36)	0.67±0.04	0.50±0.13	**0.74±0.12**	K4
15	Qed3	3.25-3.50	USU-2635	21 (38)	0.56±0.04	0.80±0.17	**1.42±0.20**	K3
16	Qed3	2.85-2.90	USU-2576	17 (29)	0.48±0.04	0.89±0.31	**1.86±0.38**	K3
17	Qed3	1.80-2.05	USU-2653	24 (39)	0.64±0.04	0.85±0.19	**1.32±0.19**	K3
17	Qed3	3.30-3.55	USU-2654	20 (44)	0.64±0.04	0.88±0.29	**1.38±0.26**	K3
18	Qed3	1.75-2.00	USU-2632	17 (24)	0.65±0.04	1.23±0.15	**1.88±0.21**	K3
18	Qed3	3.25-3.50	USU-2633	19 (25)	0.74±0.04	1.57±0.21	**2.12±0.24**	K3
19	Qed3	1.75-2.00	USU-2651	18 (28)	0.63±0.04	0.74±0.22	**1.18±0.21**	K3
19	Qed3	3.25-3.50	USU-2652	27 (42)	0.61±0.04	0.87±0.22	**1.42±0.22**	K3
20	Qed4	3.30-3.55	USU-2650	23 (41)	0.58±0.04	1.07±0.38	**1.84±0.37**	K3
21	Qed4	1.80-2.05	USU-2626	17 (48)	0.58±0.04	0.69±0.24	**1.20±0.24**	K3
22	Qed4	0.80-1.10	USU-3388	16 (23)	0.72±0.04	1.06±0.31	**1.47±0.25**	K3
23	Qed4	1.50-1.75	USU-2587	21 (44)	0.66±0.04	0.38±0.07	**0.57±0.07**	K4
23	Qed4	3.25-3.35	USU-2588	18 (29)	0.72±0.04	1.58±0.4	**2.21±0.34**	K3
24	Qed4	1.80-2.05	USU-2624	19 (31)	0.66±0.04	0.30±0.11	**0.46±0.09**	K4
24	Qed4	3.10-3.35	USU-2625	16 (36)	0.58±0.04	1.94±0.49	**3.32±0.52**	K2

[1] Number of aliquots used in age calculation and number of aliquots analyzed in parentheses.
[2] Dose rate is derived from radioelemental concentrations by conversion factors from Guérin et al. (2011). Radioelemental concentrations determined using ICP-MS and ICP-AES techniques.
[3] Equivalent dose (D_E) calculated using the Minimum Age Model (MAM) Galbraith and Roberts (2012).
[4] Optically stimulated luminescence (OSL) age analysis using the single-aliquot regenerative-dose procedure of Murray and Wintle (2000) on 2mm small-aliquots of quartz sand. Equivalent dose (D_E) calculated using the Central Age Model (CAM) Galbraith and Roberts (2012), unless otherwise noted.

One location within the Qes map unit and six sites in Qed1 were sampled and described during the initial field investigation. OSL ages span early to late Holocene (9.19±0.85 to 1.30±0.22 ka) (Figure 2.3, Table 2.3; Appendix A). Evidence of a stratigraphic break is observed at site 4, with an influx of very fine sand and coarse silt at ~2.0 m. The break separates two different age samples, 3.55±0.53 ka (0.9 m) and 5.59±0.69 ka (2.7 m) respectively (Appendix C).

Map unit Qed2 was sampled and observed at seven sites. OSL ages span middle to late Holocene and range from 7.84±1.00 to 0.65±0.08 ka (Figure 2.3, Table 2.3; Appendix A). Millennial-length chronologic breaks are observed in OSL ages between the upper and lower age samples at sites 9, 13 and 14. A stratigraphic break is observed at site 9 based on increased fine particle sizes occurring ~1.8 m depth, immediately below the upper OSL sample. Significant carbonaceous content and more poorly sorted sediment mark a stratigraphic break ~2.0 m depth at site 13. A color change at ~2.6 m depth is a weak indication of a stratigraphic break above the lower OSL age sample at site 14.

Five sites were sampled from map unit Qed3 in the east-central portion of the dune field (Figure 2.3). OSL ages are late Holocene, ranging from 2.12±0.24 to 0.74±0.12 ka (Figure 2.3, Table 2.3; Appendix A). A chronologic break occurs between the upper and lower age samples at site 15, with weak evidence (color change and sediment sorting) of a stratigraphic break ~2.3 m depth observed.

Map unit Qed4 is the farthest east and downwind. Five sites were sampled from this map unit. Like map unit Qed3, OSL ages are all late Holocene. Ages range from 3.32±0.52 to 0.46±0.09 ka, in the upper and lower OSL samples obtained at site 24 (Figure 2.3, Table 2.3; Appendix A). A stratigraphic break is clearly evident at site 23 (Figure 2.4) with changes in grain size, color and carbon content marking a horizon of stabilization between the upper and lower OSL samples at ~ 2.0 m depth. The chronologic break is ~1.4 kyr between the samples.

The oldest record of dune activity is identified at site 1 – 9.19±0.85 ka (3.0 m), obtained from a dune limb stabilized with biocrust, within the Qes map unit southwest of the main dune field. Youngest dune activity is identified at site 24 – 0.46±0.09 (1.8 m). Records of early to mid-Holocene ages were obtained in the western half of the dune field in units Qes, Qed1 and Qed2, with one record at the east end of the field in site 24, lower sample. Records from late Holocene were identified in units Qed2, Qed3 and Qed4 in the eastern 2/3 of the dune field. These ages are

consistent with the geomorphic map interpretation that dunes generally are younger downwind (east). The results also suggest dune field-wide activation has occurred throughout the Holocene.

6.0 Discussion

6.1 Temporal and spatial age distribution

To establish episodes of eolian activity groups of ages that were both temporally segregated (i.e., separated by a gap in the OSL records) and spatially distributed (i.e., occurred at multiple sites within the dune field) and also separated by stratigraphic breaks, were identified. Sediment analyses in combination with field observations were used to identify stratigraphic breaks between periods of eolian activity at individual sites with two or more age samples (Appendix C). Temporal distribution of age records for the Kanab dune field indicates five periods of eolian activity from early to late Holocene, K0 (9.2-7.8 ka), K1 (6.8-5.6 ka), K2 (4.4-3.3 ka), K3 (2.2-1.2 ka) and K4 (0.7-0.4 ka) (Figure 2.5). The probability density function shows a normal distribution for episodes K1 and K4. Episodes K2 and K3, identified in 7 and 18 records respectively, demonstrate a positive skew while K0, identified in only two records, exhibits a slight negative skew. The positive skew occurs due to more records being obtained at the end of the interpreted eolian interval than at the start.

Eolian response to changes in geomorphic thresholds is biogeomorphic, lagging the onset of threshold attainment (i.e., Hugenholtz and Wolfe, 2005a,b; Viles et al, 2008). Thus, while a change in effective moisture, or in sediment supply might lead to dune activation, dune activity lags the onset of that change (ie., decreased moisture and/or increased sediment supply). If records of eolian activity from OSL dating further lag the onset threshold condition, positive skew would likely be observed toward post-event (younger) ages. For instance, if sediment supply exceeds threshold conditions, initiation of eolian activity will occur (when wind speed and effective moisture thresholds are met or exceeded). Initial eolian response might involve only the uppermost loose, dry sediment, but as winds continue to scour the surface, moisture in the lower

sediments will be lost through evaporation and additional sediment will likely become available, effectively ramping up the eolian activity until an equilibrium state is attained for the locale and the deposits reach their maximum thickness. Records obtained will therefoe likely be greatest from the period of maximum sediment accumulation, at some time after activity is initiated.

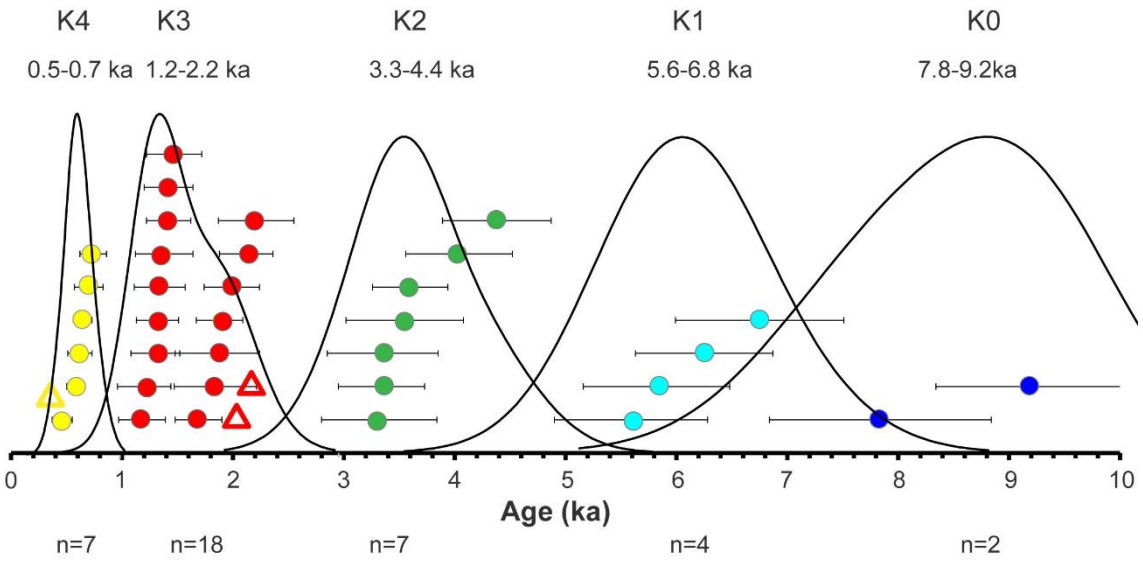

Figure 2.5. Kanab dune field activity records. Individual dune activity records are shown as dot-and-error bar plots. Five episodes of Holocene eolian activity are identified by chronostratigraphy, with probability distribution function (pdf) curves. Episodes are identified as: K0 (~9.2-7.8 ka), K1 (~6.6-5.6 ka), K2 (~4.4-3.3 ka), K3 (~2.2-1.2 ka) and K4 (~0.7-0.5 ka).

Spatial distribution of eolian activity periods is shown in Figure 2.6 and further discussed here. Ages at the southwestern edge (unit Qes) (9.2±0.85 ka) and center (unit Qed2) (7.8±1.0 ka) of the dune field reveal early Holocene eolian activity, denoted as K0. This episode is interpreted to represent a significant period of eolian activity, due to the preservation of these older deposits. Preservation of stratigraphic records is inversely correlated with age (Sadler, 1981; Schumer et al 2016). K0 records are separated by approximately a millennium from the K1 eolian activity episode (Figure 2.6, top panel). These results are interpreted as an early Holocene interval of

eolian activity (~9.2 – 7.8 ka). However, it is possible that they reflect localized, shorter-term eolian activity within the Kanab dune field.

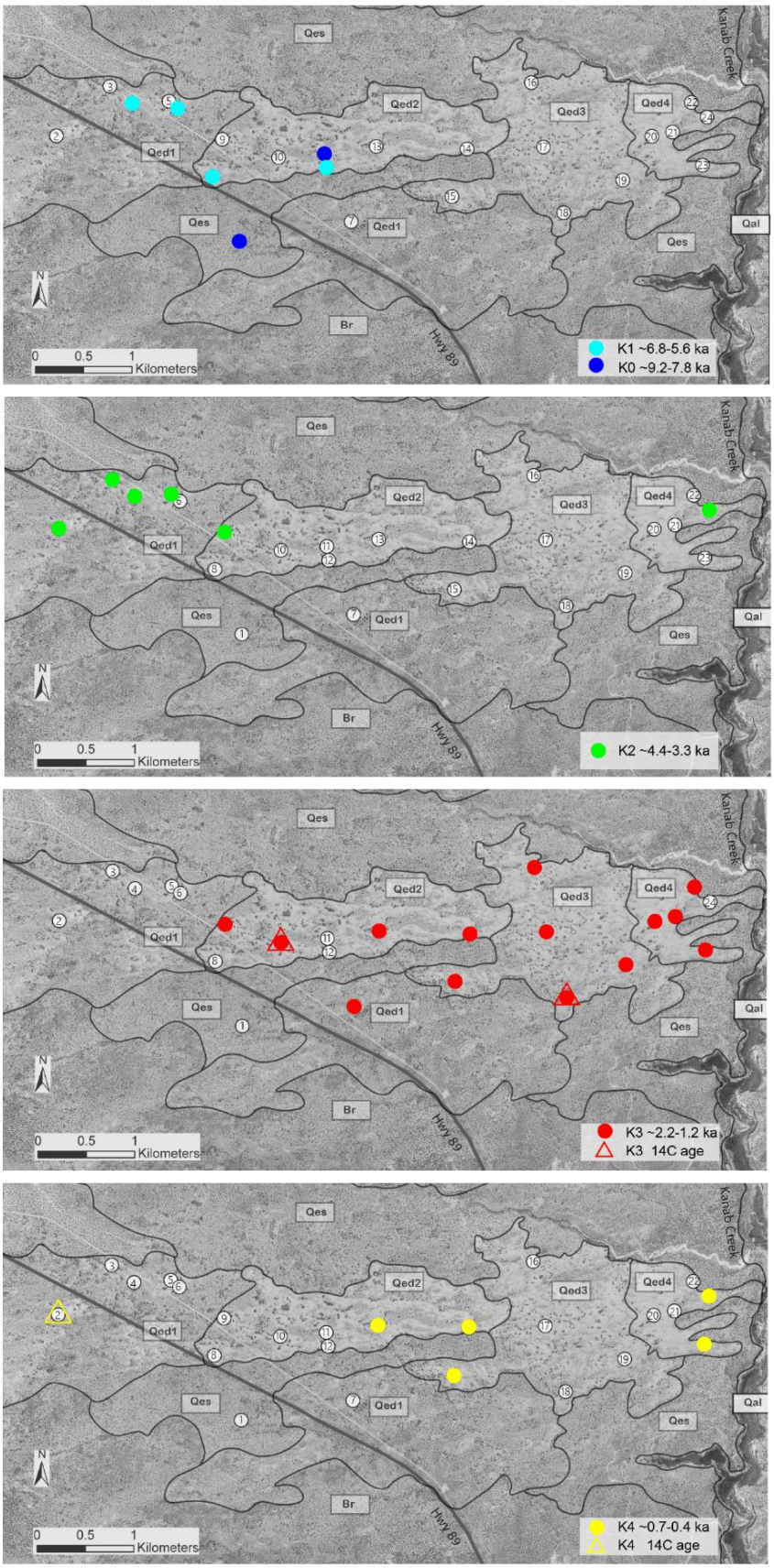

Figure 2.6. Spatial distribution of OSL ages. Intervals of eolian activity from individual dunes sampled within the dune field are plotted in order of decreasing age from upper to lower panel. Events K0 (dark blue) and K1 (cyan) in top panel are early and early mid-Holocene, respectively. K2 (green) is mid-Holocene activity. Records are not captured from the center of the dune field, but recorded at the western 1/3 and eastern edge of the dune field. Dune field-wide activity is apparent in K3 (red) during late Holocene. Latest Holocene activity (yellow) is observed in records from the central and eastern edge of the dune field, as well as recorded in a charcoal sample at the western edge of the dune field.

Evidence for mid-Holocene eolian activity (6.75±0.76 to 5.59±0.69 ka) was found at four sample sites distributed across the western half of the dune field (map units Qed1 and Qed2). These records are interpreted as widespread eolian activity in the dune field at that time and identified as event K1 (Figure 2.6, top panel). Sample site 4, located at the northwest end of the dune field (map unit Qed1), produced ages of eolian activity in this early mid Holocene K1 event (5.59±0.69) and also contained a younger, mid-Holocene age (3.55±0.53 ka) above this sample. Evidence of a hiatus is identified between these periods (Appendix C). This suggests two episodes of dune activity occurred at site 4.

Evidence for a later-mid Holocene (4.38±0.49 to 3.32±0.52 ka) eolian activity is indicated by ages obtained at six sample sites. Samples capturing sediments from the K2 period of eolian activity are widespread across the western side of the dune field in units Qed1 and Qed2, and also found in a deeper sample at the eastern edge of the dune field in unit Qed4 (Figure 2.6, K2 panel). The magnitude of this dune field reactivation period can also be seen within individual sample sites. For example, at site 2 ages for both the upper (1.8 m – 3.34±0.39 ka) and lower sample (3.3 m – 3.35±0.50 ka) are equivalent, signifying migration of the entire dune (at least 3.6 m) occurred during this event (Table 2.3 and Appendix C). Age control and stratigraphic evidence from this site is interpreted as evidence that the sediment package was deposited by the migration of a dune.

Evidence for late Holocene, (2.21±0.34 to 1.18±0.21 ka) eolian activity during period K3 is recorded within the chronostratigraphy at 14 sample sites spatially distributed across the entire dune field in map units Qed2, Qed3 and Qed4. Age control for this period comes from upper and lower samples from sites 17, 18 and 19 where documented ages occur within the interval. Site 18 contains a chronostratigraphic sequence from lower to upper ages of 2.12±0.24 ka (3.3 m) (OSL) to 2.02±0.54 ka (2.3 m – ^{14}C) to 1.88±0.21 ka (1.8 m) (OSL), suggesting movement of an entire dune during this event. Spatial distribution of sites dating to this 2.2-1.2 ka interval (Figure 2.6, K3 panel) suggests dune-field wide involvement during this event.

The youngest period of eolian activity (0.74±0.12 to 0.46±0.09 ka) is identified from ages in six sites, including ages from both OSL (n=5) and ^{14}C (n=1). Sites containing sediment dating to the K4 period of eolian activity are found in sites within the eastern portion of the dune field, in map units Qed1, Qed2 and Qed4 (Figure 2.6, K4 panel). Similar aged sand units are missing from the intermediate map unit Qed3 likely due to limited sampling with a bias toward sampling stabilized dunes at minimum depth of 60 cm for this study. The concentration of younger ages to the east is consistent with geomorphic mapping of younger and less well vegetated dunes in the east, and reflective of eastward sand transport from threshold winds producing resultant drift direction between ENE and ESE.

6.2 Episodes of dune activity and stability

This project used a hierarchical approach to best capture periods of dune activity and stability in the dune field, by initially identifying and mapping geomorphic units. This process helped target sites to obtain a representative, systematic sampling of the dune field from multiple sample sites, spatially distributed, within each geomorphic unit. Units mapped as eolian dunes were interpreted to become younger downwind (eastward). Age and sedimentologic evidence collected at each site was combined to capture spatial (breadth) and temporal (depth) resolution at the scale of the dune field, and used to infer periods of dune field activity and stability. Working from the concept that a single sample age represents one local event, multiple ages (here $n \geq 4$) from different sites are interpreted as regional activation of the dune field.

Five millennial-scale periods of eolian activity are identified in the Kanab dune field during the middle to late Holocene, separated by gaps in the record that are inferred as periods of stabilization. Periods of dune field-wide activity are K0 (~9.2-7.8 ka) (n=2), K1 (~6.8-5.6 ka) (n=4), K2 (~4.4-3.3 ka), (n=7), K3 (~2.2-1.2 ka) (n=18) and K4 (~0.7-0.4 ka) (n=7). Periods of inferred dune stability are ~5.6-4.4 ka, ~3.3-2.2 ka, ~1.2-0.7 ka. Duration of intervals of dune

activity and stability are approximately millennial (~1.1 ka) in duration until latest Holocene. The duration between events K3 and K4 is less, ~ 0.5 kyr.

Sample population increases with younger ages, likely due to erosion and removal of older deposits from scour associated with mobile dune reactivation. Sample bias inherent within the study (i.e., auger depth limit of 4 m) may also contribute to this trend. Preservation of the early Holocene eolian records suggests significant eolian activity at that time, despite the limited number of records obtained in this study. Early mid-Holocene records from events K1 and K2 are well represented in the western half of the dune field and one record from the K2 event was obtained at the farthest eastern boundary of the dune field. Although the millennial-scale temporal spacing and the spatially distributed records suggest dune-field wide activity, the limited number of records obtained from events K0 and K1 could also represent destabilization of small portions of the dune field. The spatial distribution of event K2 is less readily explained as local vegetation die-off, but still possible. Evidence of paleosol development is absent at sample sites to suggest additional stratigraphic breaks at closer intervals, however, than the millennial-scale temporal distribution.

Event K3, in late Holocene, is identified field-wide. It is possible that this event records a local destabilization of the dune field. One possible local cause is fire, which might be argued based on the finding of the two charcoal samples, recording the start of the K3 event, ~2.1 ka, although wildfire is also linked to climate forcing. Records suggest the latest Holocene event starts after a shorter period of stability than earlier eolian events. This may reflect the better preservation of later records. If so, it seems likely that previous events were also separated by shorter periods of stabilization. However, it may also reflect the influence of climate on destabilization of this dune field. This study targeted older dune activity events, so the lack of records younger than ~500 years is not interpreted as definitive evidence of eolian event K4 cessation.

In summary, the dune records reflect progressively younger dune activity to the east, similar to mapped dune units on the geomorphic map. Two exceptions are eolian activity late Holocene (event K4) identified at site 2 based on radiocarbon dating of a charcoal sample and apparent age inversion, and early Holocene age recovered at site 11, from a shallow dune limb adjacent to exposed bedrock. Eolian events identified in this study suggest millennial-scale duration of eolian reactivation, separated by millennial or multi-centennial periods of stabilization. Stratigraphic evidence to identify or suggest events of shorter duration did not occur in sites from this study (Appendix C).

6.3 Comparison with regional records of eolian activity

To assess the magnitude and regional extent of Holocene periods of aridity, we compare the record of Kanab dune field activity to other regional studies reporting eolian activity in mobile sand dunes. Early Holocene dune activity (K0 – 9.2-7.8 ky) in the Kanab dune field is also seen in other records from the Colorado Plateau (Figure 2.2). In Canyonlands National Park, two OSL ages coeval with K0 were obtained and interpreted as eolian activity during an arid period between 8-6 ka, following a cooler wetter period at the Pleistocene-Holocene transition (~12-8 ka) (Figure 2.2, study 2) (Reheis et al, 2005). In Tusayan-Black Mesa dune field in northeastern Arizona (Figure 2.2, study 3), ages between 10 and 7 ka are from mesa-top eolian deposits in sand sheets, interpreted in that study to record localized, limited extent eolian activity during an otherwise mostly stable period (Ellwein et al, 2011; 2015). The Kanab dune field eolian records suggest K0 may represent a millennial period of aridity, consistent with the pattern of younger records obtained this study. This interpretation is broadly consistent with the interpretation of eolian activity during drier climate conditions in the Canyonlands NP vicinity east and north of the study site. Recovery of these early Holocene records of eolian activity suggests significant extent of hydroclimate conditions at or exceeding threshold for dune activity may have existed regionally. While more records from regional (mobile) dune fields might constrain this temporal

activity and provide additional detail, limited preservation of older (i.e., early Holocene) records is likely.

Evidence for episode K1 (6.8-5.6 ka) in Kanab dune field is sparsely represented in other regional records. An age of 6.8 ka reported in Canyonlands (southeastern Utah) (Reheis et al, 2005) and an age of 6.5 ka reported in Chaco dunes, New Mexico (Wells et al, 1990) fall within this episode. These records of eolian activity, while limited in number, suggest very limited eolian activity during part of the K1 interval, but do not alone indicate significant regional eolian activity.

Eolian activity at Coral Pink Sand dunes (Figure 2.2, site 1) is documented at ~4 ka and ~2.9 ka (Ford et al, 2007) co-eval and following episode K2 (4.4-3.3 ka) in the nearby Kanab dune field. Evidence of eolian activity between 4.5 and 3.5 ka is also documented in southern Colorado Plateau, at New Mexico's Chaco Dune field (Wells et al, 1990) in multiple sites and Tusayan dunes, Arizona in two sites along linear dune crests (Stokes and Breed, 1993). Only from Chaco dune field, a compilation of datasets with radiocarbon ages determined from samples of both sediment and artifacts, does record abundance approach that of the Kanab dune field, and these records suggest at least partial coeval regional activation during K2.

Additionally, Chaco dune field records (Wells et al, 1990) are coeval with episode K3 (2.2-1.2 ka) in the Kanab dune field. Other regional records within this eolian event occur in northeast Arizona at Tusayan (linear) dunes (n=2) and Petrified Forest National Park (n=3) and in Canyonlands National Park, southeastern Utah (n=2). Records falling within the most recent episode, K4 (0.7-0.5 ka), also occur at other sites in the Colorado Plateau. Coeval eolian records are reported in Petrified Forest National Park (n=5) and in Coral Pink sand dunes (n=1). These suggest conditions favoring dune activation existed at several locations in the CP during at least portions of the K2, K3 and K4 episodes identified in the Kanab dune field activity record.

Eolian activity is also reported elsewhere on the CP between eolian events identified in Kanab dune field. Eolian records are reported in Arizona (Tusayan dunes, (n=1)) between Kanab

eolian events K1 and K2 (~5.6 – 4.4 ka). Overlapping eolian activity records also occur during the K2-K3 hiatus (~3.3-2.2 ka) in Utah (Coral Pink sand dunes, (n=1)), New Mexico (Chaco dune field, (n=3)) and Arizona (Tusayan dune fields, (n=1)) (Figure 2.2). Between the K-3 and K-4 Kanab events, eolian activity is reported in Arizona (Petrified National Forest, (n=3)) and Utah (Canyonlands National Park, (n=1)).

Eolian activity records from previous dune field or eolian sediment studies in this region are typically fewer in number, often obtained as supplemental or corroborative evidence in site investigations, rather than studies of dune field-wide studies to obtain eolian activity chronologies. This study used a systematic approach and multiple eolian activity records to investigate temporal and spatial eolian activity at the scale of both dunes and dune-field wide. While limited coincidental records of dune ages from other mobile dune sites in the Four Corners region are documented, the five, millennial-scale eolian activity events identified in this study are not consistently represented in these other mobile dune records. There are also instances of overlap between other eolian records and the inter-eolian events identified in the present study. These inconsistencies reflect, in part, sampling/study biases, but also suggest complex, spatially variable landscape responses to may occur in response to changes in threshold (effective moisture, sediment supply, wind) conditions for eolian activity (i.e., dune reactivation).

6.4 Comparison with dendochronology records

This section examines selected tree-ring records of hydroclimate variability from the Colorado Plateau, in comparison with the record of eolian activity in the Kanab dune field (Figure 2.7). The tree ring data reflects the extreme annual variability that is characteristic of the Holocene, moderated by using the 30-yr running mean of each record. Individual dune activity (OSL and ^{14}C ages) (this study, orange circles and triangles, respectively) are plotted for comparison above the tree ring records. Most OSL ages reported for the Kanab dune field in the

late Holocene lag aridity onset in these tree ring records and do not link directly with aridity intervals observed in tree ring records from the broader Colorado Plateau region.

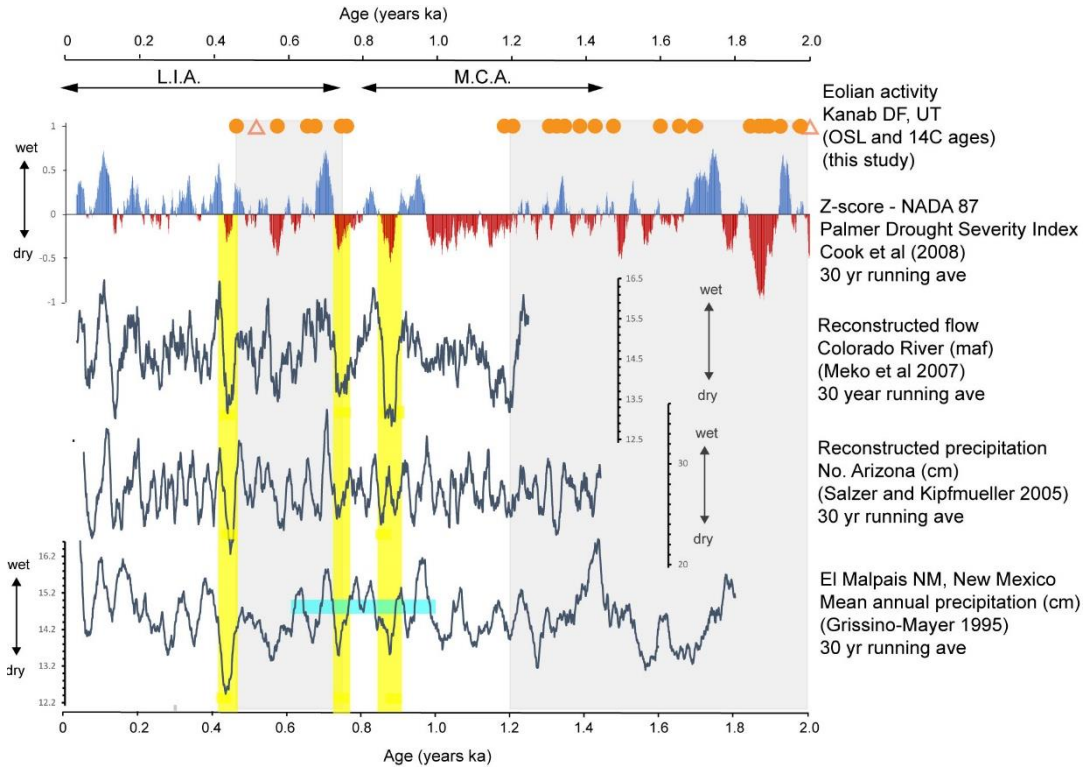

Figure 2.7. Reconstructed hydroclimate records from tree-rings. Selected studies in the Colorado Plateau and Four Corners region using tree ring records of millennial-scale hydroclimate reconstructions are presented (lower to upper): Reconstructed precipitation, El Malpais NM, New Mexico (Grissino-Mayer, 1995); Northern Arizona reconstructed precipitation (Salzer and Kipfmueller, 2005); Reconstructed stream flow for Colorado River at Lee's Ferry, AZ (Meko et al, 2007).; Palmer Drought Severity Index z-score at the NADA-87 grid point (Cook et al, 2008). Selected intervals of inferred multidecadal aridity are highlighted (yellow columns) (Meko et al, 2007). Gray shading represents interpreted periods of eolian activity in Kanab dune field, K3 (2.2-1.2 ka) and K4 (0.7-0.5 ka) (this study). Blue bar is period of inferred long term above normal precipitation (Grissino-Mayer, 1995). Orange circles are individual OSL records, and orange triangles are radiocarbon records.

While in broad agreement for reconstructed periods of aridity, spatial and temporal differences within the four tree-ring records presented are evident as slight offsets to the onset, relative magnitude and duration of dry episodes. This is expected as the records reflect specific conditions from differing climate regions. Yellow bars focus on selected multi-decadal aridity events identified in each record, centered ~860, ~750, and ~430 years ago. Included is a 23-year period of flow (~850 ka) reduced to ~84% of normal in the Colorado River (Meko et al, 2007). These and other decadal to multi-decadal events are clearly visible in all four tree ring records.

The blue bar indicates an interval identified as a prolonged period (>100 years) of above-normal precipitation in the El Malpais region interrupted by two short term pulses of aridity (<50 years, multi-decadal events) which serves as a reminder of the complex nature of climate and climate reconstructions (Grissino-Mayer and Swetnam, 1997).

Multi-decadal gaps occur in the K3 eolian event (n=18) records (i.e., ~1.8-1.7 ka and ~1.6-1.5 ka). During the K3 event, multiple wet and dry periods, multi-annual to multi-decadal are documented in the NADA-87 (red shading indicates drier and blue shading wetter climate) and El Malpais tree ring records (shown as 30-year running averages). Gaps in the OSL records (orange circles) during the K3 event coincide with one or more pulses of drier periods indicated by the tree ring records. Gaps typically end at the start of a wetter period. Dune activity is observed following each gap. Following the K3 event (gray bar), a period of prolonged aridity lasting approximately 400 years occurs, during the latter portion of the Medieval Climate Anomaly (MCA). Along with some wetter pulses, this interval includes two multidecadal droughts in the 12th century (i.e. Meko et al, 2007; Woodhouse et al, 2010). Eolian activity resumes with the K4 event and continues through several intervals of prolonged wetter climate that is recorded in these tree-rings.

Sand dunes and trees both inform as hydroclimate proxies, although on different scales. Trees respond relatively rapidly to changes in effective moisture, providing annual/seasonal hydroclimate records. Sand dunes respond (actively form or migrate) with a lag between the onset of a climate or other threshold perturbation (i.e., effective moisture, sediment supply) and provide records of a multi-decadal or greater scale. Thus, direct correlation between these two different types of records, responding on different temporal scale, can be elusive, although both records are providing evidence of hydroclimate variability.

The pattern of multi-annual to multi-decadal or greater aridity (drought) that is observed in the Colorado Plateau tree ring records occurs through both the K3 and K4 eolian activity periods, and also occurs during the inter-eolian period between these events. While the

hydroclimate (low effective moisture) during these periods of aridity likely is at or even below thresholds for dune activity, if winds are sufficient, dune activity would subside without adequate sediment supply. The wetter periods (i.e., blue on the NADA-87 record) likely promote erosion and sediment transport, thus increasing or renewing sediment supply. With subsequently reduced effective moisture, eolian activity is likely to resume. The pattern of gaps within and between the K3 and K4 suggest a response pattern of activity showing records during an apparent wetter period following a period of aridity. The end of the K4 event is marked by a multi-decadal period of aridity, however the lack of eolian activity observed in OSL records following K4 may not be the true end of the event. Instead the lack of OSL records represents inherent sampling bias within the study, which preferentially targeted non-modern dune sediments and thus is not interpreted as a hiatus of eolian activity.

In summary, dune destabilization during an arid interval appears to be followed by a moister interval that may deliver additional sediment to the dune field, which would the sediment supply available for dune activity during periods when threshold conditions of effective moisture and wind are attained. This landscape response pattern is suggested in the Kanab dune field during the late Holocene (Figure 2.7).

6.5 Comparison with Holocene paleoclimate records

Other selected Holocene paleoclimate records from outside the Colorado Plateau region provide a broader foundation to evaluate potential climate linkages of Kanab eolian activity periods. Early Holocene, post-younger Dryas (~9-10ka) is expected to be the driest part of past 10 ka due to maximum summer insolation at this time (i.e., Berger and Loutre, 1991; Asmerom and Polyak, 2007; Steponaitis et al, 2015; Routson et al, 2019; Lachniet et al, 2020). The semi-quantitative Aridity Index (Figure 2.8a, red line) averaging a wide variety (i.e., pollen, lake) of southwestern U.S. hydroclimate records, mirrors the summer insolation variability (Lachniet et al, 2020). Episode K0 (~9.2-7.8 ka) in Kanab dune field, bracketed by two records, suggests

potential for a millennial event during the early Holocene, following this insolation maximum. Aridity is also observed in a 13.4 kyr speleothem $\delta^{18}O$ record from Leviathan Cave, NV (Figure 2.8a) indicates warmer, drier conditions prevailed from ~8.5-7.5 ka (Lachniet et al, 2020). This period also coincides with Bond event 5 (Figure 2.8b). Bond events are a series of millennial-scale records of ice-rafted sediment linked with cooler sea surface temperatures (SST) in the North Atlantic Ocean (Bond et al, 1997, 2001; Obrachta et al, 2014).

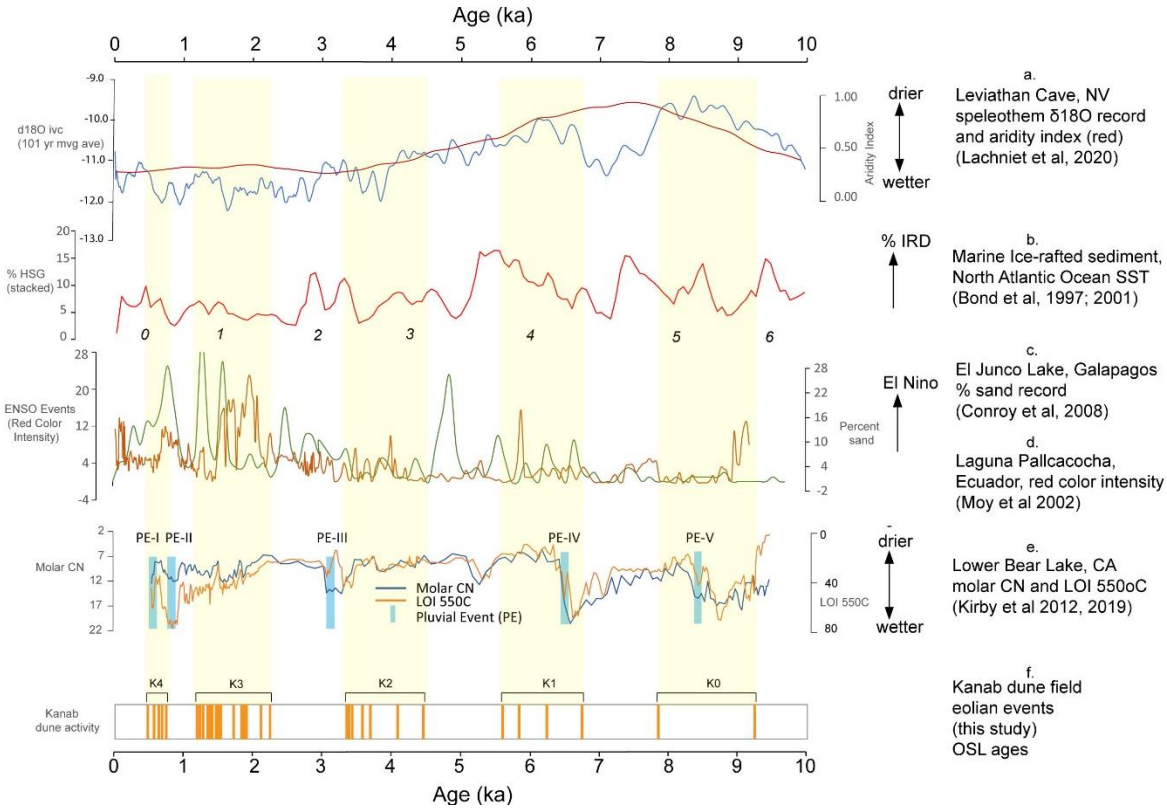

Figure 2.8. Millennial-scale hydroclimate records. Duration and timing of Kanab dune activity events is compared with selected millennial-scale records, extra-regional. From top to base: a) Leviathan Cave speleothem $\delta^{18}O$ record (blue) with Aridity Index (red) - synthesis of multiple paleoclimate records (Lachniet et al, 2020); b) millennial scale variability in marine ice-rafted sediments (Bond events 0 – 6 shown here) mark cooler SST in North Atlantic Ocean (Bond et al, 1997, 2001); c) Percent sand (brown) increases directly with El Niño events (Conroy et al, 2008); d) Red color intensity in lake sediment (green) increases with El Niño events (Moy et al, 2002); e) Lower Bear Lake, CA sediment records (molar C/N and LOI 550ºC) pluvial pulses with long aridity intervals; (Kirby et al, 2012,2019); f) millennial-scale eolian activity events (yellow bars) from individual dune activity records (this study).

Episode K1 (6.8-5.6 ka) is the oldest well-defined event of Kanab dune field activity. The Leviathan Cave speleothem record (Figure 2.8a) indicates excursion to arid conditions from ~6.7 – 5.7 ka, following a cooler, wetter period (~7.8-6.8) (Lachniet et al, 2020). The K1 eolian episode also corresponds with Bond event 4 (Figure 2.8b) (Bond et al, 2001; Obrachta et al, 2014). Records of El Nino-Southern Oscillation (ENSO) (Figure 2.8c) indicate a slight increase in ENSO activity that coincides with K1 (Moy et al, 2002; Conroy et al, 2008). A connection between increased ENSO activity and hydroclimate variability in southwestern U.S. has been identified in previous work (e.g., Cole and Cook, 1998; Moy et al, 2002; Conroy et al, 2008; Anderson, 2012; Cai et al, 2015; Jones et al, 2015; Jimenez-Moreno et al, 2021). An aridity event observed a sediment record from Lower Bear Lake, CA (~6.5-5.7 ka) (Figure 2.8d) is coeval with the latter part of episode K1 (Kirby et al, 2019).

Kanab dune activity episode K2 (4.4-3.3 ka) is a well-defined millennial-scale interval, with increasing concentration of dune activity records at the younger end of the interval. A period of aridity is recorded at Lower Bear Lake (Figure 2.8e) during K2, and higher aridity occurs in the early K2 period as indicated in the Leviathan Cave speleothem record (Figure 2.8a). A period of increased El Niño activity following the K2 eolian activity (Figure 2.8c,d) corresponds with the inter-eolian period of inferred stability between events K2 and K3. Bond event 3 occurs early in the K2 event and, while both are millennial-scale, are temporally offset. The Lower Bear Lake sediment record from southern California and a period of reduced El Nino records are temporally consistent with the K2 interval.

Eolian activity during Kanab event K3 (~2.2-1.2 ka) is well-defined spatially and temporally as dune-field wide activation (Figures 2.6 and 2.8f). Records indicate highly variable, but generally increased El Niño activity during this interval (Figure 2.8c, d) and a mixed record at Lower Bear Lake, with increased carbon and variable C/N ratio during this period. This suggests a change from initial drier climate to a wetter climate condition nearing the end of the interval. A

decreased $\delta^{18}O$ in the Leviathan Cave speleothem record occurs and Bond event 1 also occur during the latter half of the K3 episode.

The most recent episode of dune activity in Kanab, K4 (~0.7-0.5 ka) is likely abbreviated due to sample bias. However, records from Lower Bear Lake indicate a brief pulse of aridity during this event, and a decrease in El Nino events occurs during the latter K4 period. Bond event 0 is identified at the end of K4, and Leviathan Cave speleothem records indicate increasing aridity marking the late K4.

The millennial-scale periodicity observed in various hydroclimate records outside the Colorado Plateau region is also observed in the eolian activity events identified from the individual dune activity records from Kanab dune field. Events K0 – K4 record millennial-scale dune activity interpreted as dune-field wide, that is involving most or all of the dune field. Dune-field wide activity may occur in response to local events (i.e., stream relocation, wildfire, insect or disease leading to devegetation), particularly in a small dune field such as Kanab (~13 km^2). However, dune-field wide activity may also result from forcing due to changes in climate and impact thresholds for dune activity. While the response of individual eolian activity records provides an imprecise correspondence with some millennial records (i.e., tree-ring records, Figure 2.7), significant overlap of aridity is observed in both lake and speleothem records (Figures 2a,2d and 2e) with Kanab eolian events (Figure 2f).

The Kanab events also correspond with other records such as ice-rafted debris (IRD) and increased El Niño activity. Records of increased El Niño and IRD have been linked with climate events impacting the southwestern United States, including both winter and summer storms (North American Monsoon) (e.g., Moy et al, 2002; Conroy et al, 2008; Barron and Anderson, 2011; Obrachta et al, 2014; Steponaitis et al, 2015; Routson et al, 2019). The strong millennial scale pulsing evident in the Kanab dune field thus appears likely in at least partial response to extra-regional climate forcings. Sediment supply is a limiting threshold condition for dune activity. Wetter climates can promote erosion and also deliver sediment, which is mobilized

during more arid climate periods. Dune activity will occur during periods of aridity, but is also responsive to sediment influx as well as dune destabilization as sediment sources. Thus, landscape response in dune fields is not likely to respond as a direct correlation to changes in a single climate variable, such as precipitation or temperature, on a seasonal or annual basis. Instead, dune records provide evidence of complex landscape response at millennial or greater scales to hydroclimate variability. A systematic approach to evaluate dune field-wide activity is important to inform the dune field history and landscape evolution, particularly to inform regional and extra-regional influences and impacts.

7.0 Summary of regional paleoclimate records

Both spatial and temporal variability is evident in hydroclimate conditions obtained from paleoclimate records across the southwestern U.S. Although low effective moisture is a threshold condition for sand dune activity, dune activation may not solely reflect aridity. To address the question of whether the millennial-scale Kanab dune activity events reflect periods of aridity, maps showing records of hydroclimate were constructed for periods of events K0-K4, and periods between events (Figure 2.9). A site key to the paleoclimate records shows the spatial distribution and lists the proxy used (i.e., tree ring, lake sediment, dune). Kanab eolian events are mapped as records of aridity (red circles) and framed in red, plotted in decreasing order of age. Inter-eolian periods are plotted in decreasing order of age, framed in white, below the site key in the left column. Records indicating wet or pluvial climate conditions are indicated with a blue circle. Records that do not indicate a change or are otherwise indeterminate for the period are indicated with a white circle.

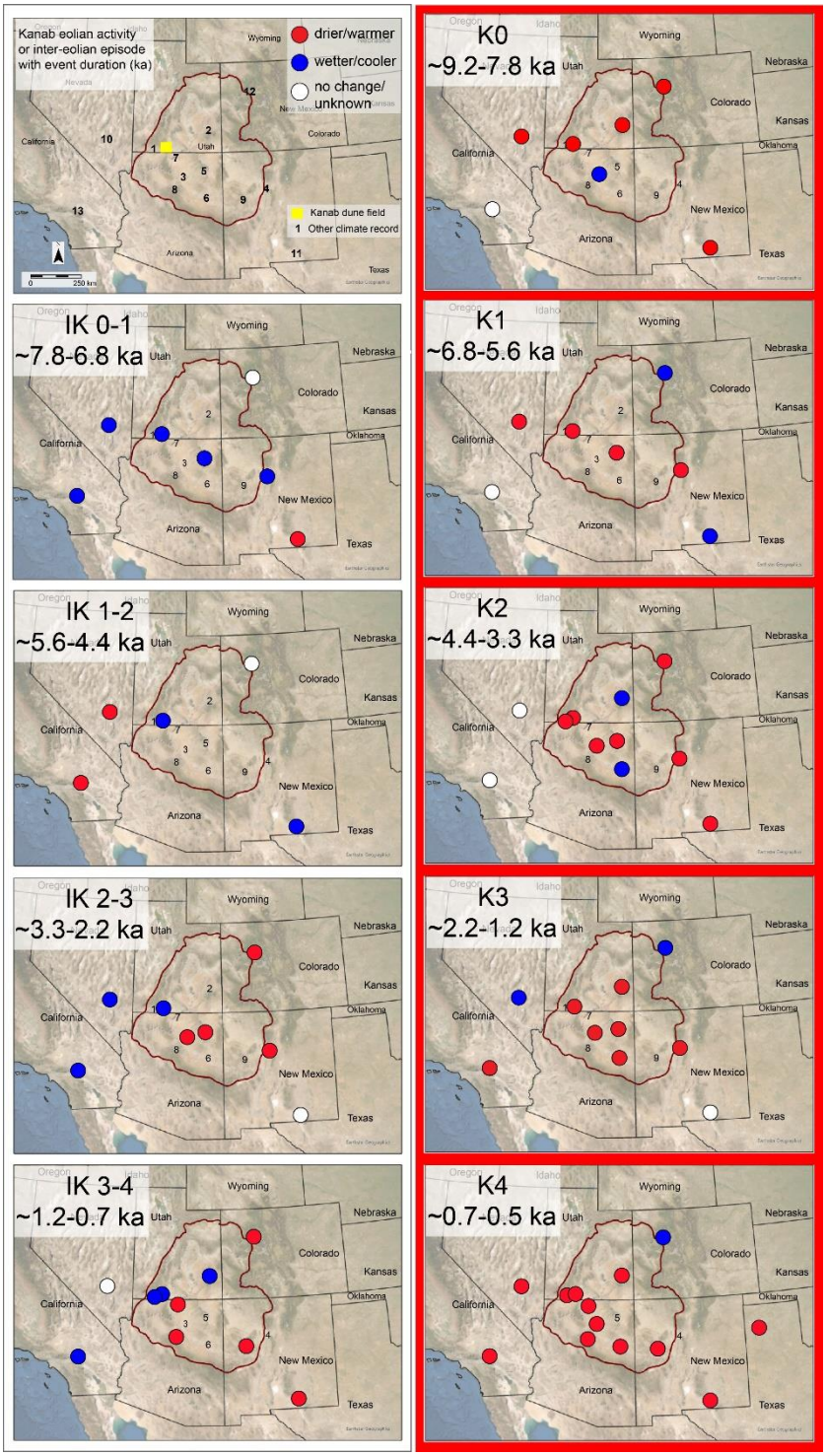

1-Coral Pink dunes, UT (Ford et al, 2010)

2-Canyonlands Nationl Park, UT (Reheis et al, 2005)

3-Tusayan dunes , AZ (Stokes and Breed, 1993) and Black Mesa dunes, AZ (Ellwein et al, 2015)

4-Chaco dunes , NM (Wells et al, 1990)

5-Canyon de Chelly, AZ (Manning, 2010 unpub)

6-Petrified Forest National Park, AZ (Schott, 2019)

7-Colorado River reconstructed flow (Meko et al, 2007)

8-Humphrey's Peak, AZ (Salzer and Kipfmueller, 2008)

9- El Malpais, NM (Grissino-Mayer, 1995)

10-Leviathan Cave, NV (Lachniet et al, 2020)

11-Pink Panther Cave, NM (Asmerom and Polyak, 2007)

12-Yellow Lake, CO (Anderson, 2012)

13-Lower Bear Lake, CA (Kirby et al, 2019)

Figure 2.9. Holocene hydroclimate distribution. Hydroclimate records from southwestern United States are shown during and between interpreted eolian episodes in Kanab dune field. Site key (upper left) shows locations of cited studies (right). Records corresponding to timing of Kanab eolian events K0-K4 (this study) in right column (red frame) in descending order, early to latest Holocene. Records from inter-eolian periods shown in left column (white frame) below site key in descending order, (IK) 0-1, 1-2, 2-3, and 3-4.

Eolian event K0 (~9.2-7.8 ka) occurs within the Greenlandian stage, early Holocene that began ~11.7 ka (before 2000 CE) following the Younger Dryas cold event (Walker et al, 2019). K0 also falls within the Northgrippian Stage, or middle Holocene that starts with a brief but global climate event, the 8.2 ka event (Walker et al 2019). Climate cooling that lasts a few centuries is followed by a period of rising temperatures in early Holocene, sometimes referred to as the Holocene Climate Optimum. Drier and/or warmer climate is indicated in regional selected lake and speleothem records, and eolian records in southern Utah. The blue record is from a sand sheet, and may represent a period of stability. Largely the K0 records suggest aridity prevailed across the central Colorado Plateau during this period.

The hiatal interval in Kanab (IK ~7.8-6.8 ka) following K0 is a wetter /colder period in other regional records as well (Figure 2.9), with the exception of a record of aridity in a speleothem in southern New Mexico (Asmerom and Polyak, 2007). Individual dune activity records from northeastern Arizona and northwestern New Mexico within the Colorado Plateau/Four Corners region(south and east of KDF) also suggest periods of stability. Records to the west of KDF, a speleothem from eastern Nevada and a lake sediment record from southern California, indicate wetter conditions prevailed at those locations during this interval.

Kanab event K1 (~6.8-5.6 ka) is a time of drier and/or warmer climate in the central Colorado Plateau and southwestern regional records as well, but suggests a divergent pattern to the north and south. A high elevation lake record in Colorado interpreted as a cooler climate interval or reflection of high snowpack/low precipitation period (Anderson, 2012). The Pink Panther Cave speleothem in southern New Mexico also indicates wetter conditions (Asmerom and Polyak, 2007).

The hiatal interval (IK ~5.6-4.4 ka) following K1 is mixed, with wetter and cooler climate conditions in the dune field and to the south where the Pink Panther speleothem also records a wetter interval. Lake and speleothem records north and west of the Colorado Plateau are

either mixed or indicate warmer/drier climate and suggest different climate conditions (i.e., hotter and drier) prevailed to the west of the Colorado Plateau.

Kanab eolian event K2 (~4.4-3.3 ka) occurs during upper/late Holocene, in the Meghalayan Stage, which begins with the 4.2 ka climate event marked by reduced rainfall (Walker et al, 2019). Spatial variability increases regionally in the selected hydroclimate records during this period. Wetter and/or cooler climate is indicated in a dune record from east central Utah (Reheis et al, 2005) and in dune records from Petrified Forest National Park in northern Arizona. The remaining records indicate arid conditions prevailed. While records indicate aridity dominated the central Colorado Plateau during this episode, some spatial variability is evident.

The hiatal interval (IK ~3.3-2.2 ka) following K2 is divided along a northwestern trend that extends through the western portion of the Colorado Plateau including the Kanab dune field. To the south and east records indicate dry conditions prevailed. The spatial pattern is similar to the previous hiatal interval with the dry and wet regions reversed. The following hiatal interval (ID ~1.2-0.7 ka) maintains this general pattern, however, with wetter and cooler climate conditions to the west and north, and drier/warmer conditions to the south and east. In these three hiatal intervals (mid to late Holocene) the ratio of wet/cool to dry/warm records is nearly even.

Drier and/or warmer climate predominates the maps during the most recent eolian events, K3 and K4. Wet/cool climate is indicated during K3 in a high-elevation lake record in the northeast boundary of the Colorado Plateau (Anderson, 2012) and in the Leviathan Cave speleothem in eastern Nevada (Lachniet et al, 2020). During the most recent event, K4, only the high elevation lake indicates a wet/cool condition.

While spatial variability is apparent in the selected records, the other regional records predominately (i.e., spatially and $n \geq 50\%$) reflect aridity during the five millennial eolian events identified in this study. Records indicating dry/warm conditions increase significantly (nearly double) during the K3 and K4 event periods. Spatial variability in the mid-Holocene hiatal (i.e.,

gaps in eolian activity in Kanab) periods appears to follow a northeast/southwest trend aligned within the western boundary of the Colorado Plateau.

8.0 Conclusions

Holocene eolian activity is reconstructed for Kanab dune field in southern Utah using a systematic approach to achieve a breadth and depth of records obtained in this mostly stabilized dune field. Eolian units were first identified through geomorphic mapping. Sediments from multiple sites in each unit were obtained from natural exposures or by hand auger for physical and chemical analysis and for age analyses. Study results extend the instrumental record and are interpreted to reflect natural hydroclimate variability for the central Colorado Plateau into early Holocene. Ages of eolian activity range from ~9.19 to ~0.46 ka.

Five major millennial-scale chronostratigraphic units are identified by multiple age and stratigraphic records obtained from individual sand dunes spatially distributed across the dune field. The five units, denoted as eolian events, are here reported as K0 (9.2±0.85 and 7.8±1.0 ka), K1 (6.75±0.76 to 5.59±0.69 ka), K2 (4.38±0.49 to 3.32±0.52 ka), K3 (2.21±0.34 to 1.18±0.21 ka), and K4 (0.74±0.12 to 0.46±0.09 ka). Whole dune field activation is interpreted in multiple vertical sequences where contemporaneous ages were obtained in multiple records within a vertical sequence from an individual dune site.

Comparison of late Holocene eolian activity records units with tree ring records from the Colorado Plateau indicates a lag between aridity onset and eolian activity. Dune response does not link directly with drought periods interpreted from these regional tree ring records. Eolian activity has been shown to lag both onset and cessation of hydroclimate perturbation (Hugenholtz and Wolfe, 2005; Viles et al, 2008).

However, the millennial-scale events identified in Kanab correspond with other millennial Holocene hydroclimate records. Events K0 through K5 correlate with drier periods identified in speleothem records from Leviathan Cave in Nevada and lake sediment records from

Lower Bear Lake in southern California (Kirby et al, 2019; Lachniet et al, 2020). They are consistent with ENSO trends seen in paleoclimate records (Moy et al, 2002; Conroy et al, 2008) during early and mid-Holocene. Kanab events K4, K3, K2, K1 and K0 correlate with Bond events 0, 1, 3, 4 and 5, identified from ice-rafted debris in the North Atlantic Ocean (Bond et al, 1997; 2001; Obrachta et al, 2014). Later Holocene eolian activity events in Kanab correlate with periods of regional aridity linked to winter and summer monsoon precipitation (Anderson, 2012; Kirby et al, 2019). V, both regional and in broader teleconnections.

Kanab eolian activity records suggest a landscape response to hydroclimate variability that is dune-field wide, and reflected in millennial-scale climate records at both regional and broader teleconnections. Eolian activity records obtained in systematic investigations of mobile dune fields as in this study may contribute to our understanding of the natural hydroclimate variability in the Colorado Plateau and the southwestern U.S. generally, by providing a deeper time record for areas where other paleoclimate records are scarce.

9.0 References

Aitken, M.J. 1998: An Introduction to Optical Dating: The dating of Quaternary sediments by the use of photon-stimulated luminescence. New York, Oxford University Press, 267 p.

Aitken, M.J., 1989. Luminescence dating: A guide for non-specialists. Archaeometry 31: 147-159

Aitken, M.J., 1983, (INVITED) Recent Advances in Thermoluminescence Dating, Radiation Protection Dosimetry, v. 6, i. 1-4, p. 181–183.

Aitken, M.J. and Alldred, J.C., 1972. The assessment of error limits in thermoluminescent dating. Archaeometry, 14(2), pp.257-267.

Anderson, L., 2012. Rocky Mountain hydroclimate: Holocene variability and the role of insolation, ENSO, and the North American Monsoon, Global and Planetary Change, Volumes 92–93, pp. 198-208

Asmerom, Y., Polyak, V., Burns, S. and Rassmussen, J., 2007. Solar forcing of Holocene climate: new insights from a Holocene speleothem record, southwestern United States. Geology, v.35, n.1, p.1-4

Ault, T.R., J.E. Cole, J.T. Overpeck, G.T. Pederson, and D.M. Meko, 2014: Assessing the Risk of Persistent Drought Using Climate Model Simulations and Paleoclimate Data, J. Climate, 27, 7529–7549

Bagnold, RA, 1941. The physics of wind-blown sand and desert dunes. Methuen, London, 265 (10)

Bateman, M.D., Frederick, C.D., Jaiswal, M.K., Singhvi, A.K., 2003. Investigations into the potential effects of pedoturbation on luminescence dating. Quat. Sci. Rev. 22, 1169-1176

Bateman, M.D., Boulter, C.H., Carr, A.S., Frederick, C.D., Peter, D., Wilder, M., 2007a. Preserving the palaeoenvironmental record in Drylands: bioturbation and its significance for luminescence-derived chronologies. Sediment. Geol. 195, 5K19

Bateman, M.D., Boulter, C.H., Carr, A.S., Frederick, C.D., Peter, D., Wilder, M., 2007b. Detecting post-depositional sediment disturbance in sandy deposits using optical luminescence. Quat. Geochronol. 2, 57e64

Barchyn, T.E., and Hugenholtz, C.H., 2013, Reactivation of supply-limited dune fields from blowouts: A conceptual framework for state characterization: Geomorphology, v. 201, p. 172–182

Barron, J., Anderson, L., 2011. Enhanced late Holocene ENSO/PDO expression along the margins of the eastern North Pacific, Quaternary International 235 (2011) 3K12

Beitler, B., Chan, M., and Parry, W.T., 2003, Bleaching of Jurassic Navajo sandstone on Colorado Plateau Laramide highs: evidence of exhumed hydrocarbon supergiants? Geology; v. 31; no. 12; p. 1041–1044

Berger, A. and Loutre, M.F., 1991, Insolation values for the climate of the last 10 million years. Quaternary Science Reviews, 10(4), pp.297-317.

Bond, G., Showers, W., Cheseby, M., Lotti, R., Almasi, P., DeMenocal, P., Priore, P., Cullen, H., Hajdas, I. and Bonani, G., 1997, A pervasive millennial-scale cycle in North Atlantic Holocene and glacial climates. *science*, *278*(5341), pp.1257-1266.

Bond, G., Kromer, B., Beer, J., Muscheler, R., Evans, M.N., Showers, W., Hoffmann, S., Lotti-Bond, R., Hajdas, I. and Bonani, G., 2001, Persistent solar influence on North Atlantic climate during the Holocene. *Science*, *294*(5549), pp.2130-2136.

Bøtter-Jensen, L., McKeever, S.W.S, and Wintle, A.G., 2003, Optically Stimulated Luminescence Dosimetry, Elsevier, 374 pp.

Bristow, C.S. and Armitage, S.J., 2016, Dune ages in the sand deserts of the southern Sahara and Sahel, Quaternary International, v. 410, Part B, pp. 46-57.

Buol, S.W., Southard, R.J., Graham, R.C. and McDaniel, P.A., 2011. Soil genesis and classification. John Wiley & Sons.

Cole, J.E. and Cook, E.R., 1998. The changing relationship between ENSO variability and moisture balance in the continental United States. Geophysical Research Letters, 25(24), pp.4529-4532.

Conroy, J., Overpeck, J.T., Cole, J.E., Shanahan, T.M., Steinitz-Kannan, M., 2008. Holocene changes in eastern tropical Pacific climate inferred from a Galapagos Lake sediment record, Quaternary Science Reviews, 27, 1166-1180

Cook, B. I., Mankin, J. S., Williams, A. P., Marvel, K. D., Smerdon, J. E., & Liu, H, 2021, Uncertainties, limits, and benefits of climate change mitigation for soil moisture drought in southwestern North America. Earth's Future, 9, K2021EF002014.

Cook, B.I., Ault, T.R., Smerdon. J.E., 2015. Unprecedented 21st century drought risk in the American Southwest and Central Plains. Science Advances. 1(1)

Cook, E.R., Seager, R., Heim Jr, R.R., Vose, R.S., Herweijer, C. and Woodhouse, C., 2010. Megadroughts in North America: Placing IPCC projections of hydroclimatic change in a long-term palaeoclimate context. Journal of Quaternary Science, 25(1), pp.48-61.

Copeland, S.M., Bradford, J.B., Duniway, M.C. and Schuster, R.M., 2017. Potential impacts of overlapping land-use and climate in a sensitive dryland: a case study of the Colorado Plateau, USA. Ecosphere 8(5):K01823.10.1002/ecs2.1823

Cullinane Thomas, C., Koontz, L. and Cornachione, E., 2018. 2017 national park visitor spending effects: Economic contributions to local communities, states, and the nation. Natural Resource Report NPS/NRSS/EQD/NRR—2018/1616. National Park Service, Fort Collins, Colorado.

Dorsey, R.J., Fluette, A., McDougall, K., Housen, B.A., Janecke, S.U., Axen, G.J., and Shirvell, C.R., 2007, Chronology of Miocene-Pliocene deposits at Split Mountain Gorge, Southern California: A record of regional tectonics and Colorado River evolution: Geology 35, 57-60.

Duller G.A.T. 2006. Single grain optical dating of glaciogenic deposits. Quat. Geochronol. 1:296–304

Duller, G.A.T., 2016, Challenges involved in obtaining luminescence ages for long records of aridity: Examples from the Arabian Peninsula: Quaternary International, v. 410, p. 69–74

Dutton, C.E., 1882. The physical geology of the Grand Cañon district. US Government Printing Office.

Ellwein, A.L., Mahan, S.A. and McFadden, L.D., 2011, New optically stimulated luminescence ages provide evidence of MIS3 and MIS2 eolian activity on Black Mesa, northeastern Arizona, USA. *Quaternary Research*, *75*(3), pp.395-398.

Ellwein, A.L, Mahan, S.A., and L. D. McFadden, 2015, Impacts of climate change on the formation and stability of late Quaternary sand sheets and falling dunes, Black Mesa region, southern Colorado Plateau, USA, Quaternary International 362 (2015) 87-107

Ellwein, A.L., McFadden, L.D., McAuliffe, J.A., and S.A. Mahan, 2018, Late Quaternary Soil Development Enhances Aeolian Landform Stability, Moenkopi Plateau, Southern

Colorado Plateau, USA, Geosciences 2018, 8(5), p. 146

Ford, R.L., Gilman, S.L., Wilkins, D.E., Clement, W.P. and Nicholl, K., 2010. Geology and Geomorphology of Coral Pink Sand Dunes State Park, Utah *in* Sprinkel, D.A, Chidsey, R.C. Jr., and Anderson, P.B., eds, Geology of Utah's Parks and Monuments, Utah Geological Association Publication 28 (3rd ed), p 371-398

Fossen, H., Schultz, R.A., and Torab, A., 2011, Conditions and implications for compaction band formation in the Navajo Sandstone, Utah, Journal of Structural Geology, v. 33: 10, pp. 1477-1490

Fryberger, S.G, 1979, Dune Forms and Wind Regimes. In A Study of Global Sand Seas; McKee, E.D., Ed.; U.S. Geological Survey: Reston, VA, USA, 1979; pp. 137–169

Galbraith, R.F. and Roberts, R.G., 2012. Statistical aspects of equivalent dose and error calculation and display in OSL dating: an overview and some recommendations. Quaternary Geochronology, 11, pp.1-27.

Grissino-Mayer, H.D., 1995. Tree-ring reconstructions of climate and fire history at El Malpais National Monument, New Mexico, University of Arizona, dissertation, http://hdl.handle.net/10150/191192

Grissino-Mayer, H.D., and Swetnam, T.W., 1997. Multi-century history of wildfire in the Ponderosa pine forests of El Malpais National Monument, New Mexico Bureau of Mines and Mineral Resources, Bulletin 156

Guérin, G., Mercier, N., and Adamiec, G., 2011, Dose-rate conversion factors: update, Ancient TL v. 29, n.1

Halfen, A., Hesse, P., Roskin, J., Singhvi, A., Tsoar, H., Tripaldi, A., Yang, X., Zárate, M., 2016. The INQUA Dunes Atlas chronologic database, Quaternary International, v. 410, Part B, pp. 3-10

Halfen, A.F., Lancaster, N., Wolfe, S., 2016. Interpretations and common challenges in aeolian records from North American dune fields, Quaternary International, v. 410, 75-95.

Hesse, P., 2016, How do longitudinal dunes respond to climate forcing? Insights from 25 years of luminescence dating in the Australian desert dunefields, Quaternary International, v. 410, 11-29

Hugenholtz, C.H., Wolfe, S.A., 2005a. Biogeomorphic model of dunefield activation and stabilization on the northern Great Plains. Geomorphology, 70(1), p 53-70.

Hugenholtz, C.H., Wolfe, S.A., 2005b. Recent stabilization of sand dunes on the Canadian prairies and relation to recent climate variations. Geomorphology, 68(2005), p 131-147.

Hugenholtz, C.H., Whitehead, K., Brown, O.W., Barchyn, T.E., Moorman, B.J., LeClair, A., Riddell, K. and Hamilton, T., 2013. Geomorphological mapping with a small unmanned aircraft system (sUAS): Feature detection and accuracy assessment of a photogrammetrically-derived digital terrain model. *Geomorphology*, *194*, pp.16-24.

Huntley, D.J., Godfrey-Smith, D.I., Thewalt, M.L.W., 1985. Optical dating of sediments. Nature 313: 105-107.

Jiménez-Moreno, G., Anderson, R.S., Shuman, B.N. and Yackulic, E., 2019. Forest and lake dynamics in response to temperature, North American monsoon and ENSO variability during the Holocene in Colorado (USA). Quaternary Science Reviews, 211, pp.59-72.

Jones, M.D., Metcalfe, S.E., Davies, S.J., Noren, J. 2015. Late Holocene climate reorganisation and the North American Monsoon, Quaternary Science Reviews, v. 124, pp. 290-295.

Karlstrom, K., Lee, J., Kelley, S. *et al.* 2014, Formation of the Grand Canyon 5 to 6 million years ago through integration of older palaeocanyons. Nature Geosci 7, 239–244.

Kirby, M.E.C.; Patterson, W.P.; Lachniet, M.; Noblet, J.A.; Anderson, M.A.; Nichols, K.; and Avila, J., 2019, Pacific southwest United States Holocene droughts and pluvials inferred from sediment ^{18}O (calcite) and grain size data (Lake Elsinore, California), Frontiers Earth Sci. 7:74.

Kirby, M.E., Zimmerman, S.R.H., Patterson, W.P., and Rivera, J.J., 2012. A 9170-year record of decadal-to -multi-centennial scale pluvial episodes from the coastal Southwest United States: a role for atmospheric rivers? Quaternary Science Reviews, V 46, p.57-65.

Kocurek, G.; Lancaster, N., 1999, Aeolian system sediment state: Theory and Mojave Desert Kelso dune field example. Sedimentology, 46, 505–515.

Lachniet, M. S., Asmerom, Y., Polyak,V., & Denniston, R., 2020, Great Basin paleoclimate and aridity linked to Arctic warming and tropical Pacific sea surface temperatures. Paleoceanography and Paleoclimatology, 35, K2019PA0037

Lancaster, N., 1994. Controls on aeolian activity: some new perspectives from the Kelso Dunes, Mojave Desert, California. Journal of Arid Environments, 27(2), pp.113-125.

Lancaster, N., 1997, Response of eolian geomorphic systems to minor climate change: examples from the southern Californian deserts: Geomorphology, v. 19, p. 333–347.

Lancaster, N., 2008, Desert dune dynamics and development: Insights from luminescence dating. Boreas, 37, 559–573.

Lancaster, N., Wolfe, S., Thomas, D., Bristow, C., Bubenzer, O., Burrough, S., Duller, G., Halfen, A., Hesse, P., Roskin, J., Singhvi, A., Tsoar, H., Tripaldi, A., Yang, X., Zárate, M., 2016, The INQUA Dunes Atlas chronologic database, Quaternary International, v. 410, Part B, pp. 3-10.

Logie, M, 1982. Influence of roughness elements and soil moisture on the resistance of sand to wind erosion. In Acidic soils and geomorphic processes: proc. International Conference International Society Soil Science Jerusalem Israel, Mar 19-Apr 4, 1981/DH Yaalon, ed.

Li, H. and Yang, X., 2016, Spatial and temporal patterns of aeolian activities in the desert belt of northern China revealed by dune chronologies, Quaternary International, v. 410, 58-68.

Liu, S.W., Lai, Z.P., Wang, Y.X., Fan, X.L., Tian, M.Z., Jiang, Y.D. and Zhaog, H., 2016, Growing pattern of mega-dunes in the Badain Jaran Desert in China revealed by luminescence ages, Quaternary International, v. 410, 111-118.

Lucchitta, I., 1972, Early history of the colorado river in the basin and range province: Bulletin of the Geological Society of America 83, 1933-1948.

Manning, J., 2010. OSL age information, Canyon de Chelly, Arizona, USGS-Flagstaff, NNLP, unpublished report, used with permission.

Meko, D., Woodhouse, C.A., Baisan, T., Knight, J.J., Lukas, M.K., Hughes, J., Salzer, M.W., 2007. Medieval drought in the upper Colorado River Basin, Geophys. Res. Lett., 34, L10705.

Menking, K.M. and Anderson, R.Y., 2003, Contributions of La Niña and El Niño to middle Holocene drought and late Holocene moisture in the American Southwest. *Geology*, *31*(11), pp.937-940.

Metcalfe, S.E., Barron, J.A., Davies, S.J., 2015. The Holocene history of the North American Monsoon: 'known knowns' and 'known unknowns' in understanding its spatial and temporal complexity, Quaternary Science Reviews, v. 120, pp. 1-27.

Mock, C.J., 1996. Climatic controls and spatial variations of precipitation in the western United States. Journal of Climate, 9(5), pp.1111-1125.

Moy, C.M., Seltzer, G.O., Rodbell, D.T. and Anderson, D.M., 2002, Variability of El Niño/Southern Oscillation activity at millennial timescales during the Holocene epoch. Nature, 420(6912), pp.162-165.

Muhs, D.R. and Maat, P.B., 1993. The potential response of eolian sands to greenhouse warming and precipitation reduction on the Great Plains of the USA, Journal of Arid Environments 25: 351-361.

Murray, A.S. and Wintle, A.G., 2000. Luminescence dating of quartz using an improved single-aliquot regenerative-dose protocol. Radiation measurements, 32(1), pp.57-73.

Nelson, M.S., Gray, H.J., Johnson, J.A., Rittenour, T.M., Feathers, J.K., and Mahan, S.A., 2015. User guide for luminescence sampling in archaeological and geological contexts, Advances in Archaeological Practice 3(2), 2015, pp. 166–177.

Nelson, M., Rittenour, T. and Cornachione, H., 2019. Sampling methods for luminescence dating of subsurface deposits from cores. Methods and Protocols, 2(4), p.88.

Obrochta, S.P., Crowley, T.J., Channell, J.E., Hodell, D.A., Baker, P.A., Seki, A. and Yokoyama, Y., 2014. Climate variability and ice-sheet dynamics during the last three glaciations. Earth and Planetary Science Letters, 406, pp.198-212.

Parry, W.T., Forster, C.B., Evans, J.P., Bowen, B.B., and Chan, M.A., 2007, Geochemistry of CO2 sequestration in the Jurassic Navajo Sandstone, Colorado Plateau, Utah, Environmental Geosciences, v. 14: 2, pp. 91–109.

Poudyal, N.C., Elkins, D., Nibbelink, N., Cordell, H.K., and Gyawali, B., 2016, An exploratory spatial analysis of projected hotspots of population growth, natural land loss, and climate change in the conterminous United States, Land Use Policy, 51, p 325–334.

Polyak, Victor J., Asmerom, Y., 2001. Late Holocene Climate and Cultural Changes in the Southwestern United States, *Science*, vol. 294, no. 5540, 2001, pp. 148–151.

Prescott, J.R. and Hutton, J.T., 1994, Cosmic ray contributions to dose rates for luminescence and ESR dating: large depths and long-term time variations, Radiation Measurements v. 23: 2–3, pp. 497-500.

Redsteer, M. H., 2020, Sand Dunes, Modern and Ancient, on Southern Colorado Plateau Tribal Lands, Southwestern USA *in* Inland Dunes of North America ed. by Lancaster, N. and Hesp, P., pp. 287 – 310.

Reheis, M.C.; Reynolds, R.L.; Goldstein, H.; Roberts, H.M.; Yount, J.C.; Axford, Y.; Cummings, L.S.; Shearin, N., 2005, Late Quaternary eolian and alluvial response to paleoclimate, Canyonlands, southeastern Utah. GSA Bull., 117, 1051–1069.

Reimer, P.J., Austin, W.E., Bard, E., Bayliss, A., Blackwell, P.G., Ramsey, C.B., Butzin, M., Cheng, H., Edwards, R.L., Friedrich, M. and Grootes, P.M., 2020. The IntCal20 Northern Hemisphere radiocarbon age calibration curve (0–55 cal kBP). Radiocarbon, 62(4), pp.725-757.

Rhodes, E.J., 2011. Optically Stimulated Luminescence Dating of Sediments over the Past 200,000 Years, Annu. Rev. Earth Planet. Sci. 2011. 39:461–88.

Rink., W.J., Dunbar, J.S., Tschinkel, W.R., Kwapich, C., Repp, A., Stanton, W., Thulman, D., 2013. Subterranean transport and deposition of quartz by ants in sandy sites relevant to age overestimation in optical luminescence dating. Journal of Archaeological Science, 40: 2217-2226.

Routson, C.C., McKay, N.P., Kaufman, D.S., Erb, M.P., Goosse, H., Shuman, B.N., Rodysill, J.R. and Ault, T., 2019. Mid-latitude net precipitation decreased with Arctic warming during the Holocene. *Nature*, *568*(7750), pp.83-87.

Sadler, P.M., 1981. Sediment accumulation rates and the completeness of stratigraphic sections. *The Journal of Geology*, *89*(5), pp.569-584.

Salzer, M.W., Kipmueller, K.F., 2005. Reconstructed temperature and precipitation on a millennial timescale from tree-rings in the southern Colorado Plateau, USA, Climatic Change 70: 465–487.

Sawakuchi, A.O., Blair, M.W., DeWitt, R., Faleiros, F.M., Hyppolito, T. and Guedes, C.C.F., 2011. Thermal history versus sedimentary history: OSL sensitivity of quartz grains extracted from rocks and sediments. Quaternary Geochronology, 6(2), pp.261-272.

Schott, A.F., 2019, Eolian Landscape History and Prehistoric Dune Farming in Petrified Forest National Park: A Geoarchaeological Approach to Understanding the Long-Term Use of a Marginal Landscape, downloaded, 10/30/2020, http://hdl.handle.net/10150/634273.

Schumer, R., Taloni, A. and Furbish, D.J., 2016, December. Geomorphic Transport Laws and the Statistics of Topography and Stratigraphy. In AGU Fall Meeting Abstracts (Vol. 2016, pp. EP13B-1025).

Schwinning, S., Belnap, J., Bowling, D.R. and Ehleringer, J.R., 2008. Sensitivity of the Colorado Plateau to change: climate, ecosystems, and society. Ecology and Society, 13(2).

Siegal, Z., Tsoar, H. and Karnieli, A., 2013. Effects of prolonged drought on the vegetation cover of sand dunes in the NW Negev Desert: field survey, remote sensing and conceptual modeling. Aeolian Research, 9, pp.161-173.

Soil Survey Staff, Natural Resources Conservation Service, United States Department of Agriculture. Web Soil Survey. Available online at the following link: http://websoilsurvey.sc.egov.usda.gov/. Accessed [April/26/2021].

Steponaitis, E., Andrews, A., McGee, D., Quade, J., Hsieh, Y.T., Broecker, W.S., Shuman, B.N., Burns, S.J. and Cheng, H., 2015. Mid-Holocene drying of the US Great Basin recorded in Nevada speleothems. Quaternary Science Reviews, 127, pp.174-185.

Stokes, S., and Breed, C.S., 1993 A chronostratigraphic re-evaluation of the Tusayan Dunes, Moenkopi Plateau and southern Ward Terrace, northeastern Arizona. In The dynamics and Environmental Context of Aeolian Sedimentary Systems; Pye, K., Ed.; Geological Society: London, UK, 75–90.

Straub, K.M. and Foreman, B.Z., 2018. Geomorphic stasis and spatiotemporal scales of stratigraphic completeness. Geology, 46(4), pp.311-314.

Thomas, D.S. and Burrough, S.L., 2012. Interpreting geoproxies of late Quaternary climate change in African drylands: implications for understanding environmental change and early human behaviour. Quaternary International, 253, pp.5-17.

Tripaldi, A. and Zárate, M.A., 2016. A review of Late Quaternary inland dune systems of South America east of the Andes. Quaternary International, 410, pp.96-110.

Tsoar, H., 2005. Sand dunes mobility and stability in relation to climate, Physica A: Statistical Mechanics and its Applications, v. 357 (1), pp. 50-56.

Tsoar, H., Levin, N., Porat, N., Maia, L.P., Herrmann, H.J., Tatumi, S.H., and Claudino-Sales, V., 2009, The effect of climate change on the mobility and stability of coastal sand dunes in Ceará State (NE Brazil): Quaternary Research, v. 71, p. 217–226.

Udall, B. and Overpeck, J., 2017. The twenty-first century Colorado River hot drought and implications for the future. *Water Resources Research*, *53*(3), pp.2404-2418.

U.S. Bureau of Reclamation, 2012, Colorado River Basin Water Supply and Demand Study, 95 pp., https://www.usbr.gov/lc/region/programs/crbstudy/finalreport/Study%20Report/CRBS_Study_Report_FINAL.pdf.

U.S. Bureau of Reclamation, 2021, Review of the Colorado River Interim Guidelines for Lower Basin Shortages and Coordinated Operations for Lake Powell and Lake Mead, 56 pp.,

https://www.usbr.gov/ColoradoRiverBasin/documents/7.D.Review_FinalReport_12-18-2020.pdf.

Uyghar, K. and Picard, M.D.,1980, Reservoir Characteristics of the Navajo Sandstone, Utah Geological Association: Henry Mountains Symposium.

Viles, H.M., Naylor, L.A., Carter, N.E.A., Chaput, D., 2008, Biogeomorphological disturbance regimes: progress in linking ecological and geomorphological systems, Earth Surf. Process. Landforms 33, 1419-1435.

Walker, M., Head, M.J., Lowe, J., Berkelhammer, M., BjÖrck, S., Cheng, H., Cwynar, L.C., Fisher, D., Gkinis, V., Long, A. and Newnham, R., 2019. Subdividing the Holocene Series/Epoch: formalization of stages/ages and subseries/subepochs, and designation of GSSPs and auxiliary stratotypes. Journal of Quaternary Science, 34(3), pp.173-186.

Walkley, A. and Black I.A., 1934. An examination of the Degtjareff Method for Determining Soil Organic Matter, and a proposed Modification of the Chromic Acid Titration Method. Soil Science, 37(1): 29-38.

Wells, S.G., McFadden, L.D. and Schultz, J.D., 1990. Eolian landscape evolution and soil formation in the Chaco dune field, southern Colorado Plateau, New Mexico. In: P.L.K. Knuepfer and L.D. McFadden (Editors), Soils and Landscape Evolution. Geomorphology, 3:517-545.

Wintle, A.G., 1997. Luminescence dating: laboratory procedures and protocols. Radiation measurements, 27(5-6), pp.769-817.

Wintle, A.G. and Murray, A.S., 2006. A review of quartz optically stimulated luminescence characteristics and their relevance in single-aliquot regeneration dating protocols. Radiation measurements, 41(4), pp.369-391.

Wolfe, S.A. and Hugenholtz, C.H., 2009. Barchan dunes stabilized under recent climate warming on the northern Great Plains. Geology, 37(11), pp.1039-1042.

Woodhouse, C.A., Meko, D.M., MacDonald, G.M., Stahle, D.W., and Cook, E.R., 2010, A 1,200-year perspective of 21st century drought in southwestern North America: Proceedings of the National Academy of Sciences, v. 107, p. 21283–21288.

Woodhouse, C.A. and Pederson, G.T., 2018. Investigating runoff efficiency in upper Colorado River streamflow over past centuries. Water Resources Research, 54(1), pp.286-300.

CHAPTER 3

HOLOCENE SAND DUNE ACTIVITY RECORDS FROM THE SAN RAFAEL DESERT DUNE FIELD, EAST-CENTRAL UTAH

Abstract

A multi-decadal and on-going drought beginning in the early 2000's CE has impacted much of the western United States, and resulted the first ever water restrictions of Colorado River water supply to Arizona, Nevada and Mexico. Mitigation and adaptive strategies will be crucial to populations reliant on this vital resource. Understanding past hydroclimate variability and landscape response is increasingly important for improving predictive capability for future impact of changing climate on the dry American southwest. Paleoclimate records can extend the relatively short instrumental record and provide perspective on the magnitude and duration of natural hydroclimate variability. This perspective is important for the development of adaptive management strategies in light of growing population and changing climate.

Sand dunes are geomorphic systems responsive to changes in aridity, capable of reactivation from a stable (vegetated) state when threshold conditions are exceeded. In order to identify past episodes of eolian activity in the San Rafael dune field, a chronostratigraphic record of sand dune activity was developed using a systematic approach. A geomorphic map of the San Rafael dune field was first constructed and five eolian map units were identified. Sediment samples were collected from the 22 sites targeted for field investigation. Physical properties, Munsell soil color, and analyses of grain size, total organic carbon (TOC) and $\delta^{13}C$ for the sediments were used to develop site stratigraphy. Ages from 33 samples were obtained using optically stimulated luminescence (OSL) dating and a chronostratigraphic record was developed for the dune field. Seven episodes of millennial-scale, eolian activity were identified: SR0 (~17 –

16.2 ka), SR1 (~12.4 – 11.2 ka), SR2 (~9.7 – 7.4 ka), SR3 (~4.7 ka), SR4 (~3.4-2.5 ka), SR5 (~2.0-1.6 ka) and SR6 (~1.1 – 0.4 ka). Of these, three intervals are less well-defined, due to limited samples intercepting these time periods. Episodes SR0 and SR1 are probably significant, considering the preservation potential of older deposits. Episode SR3 likely has greater preservation potential and would likely be encountered by additional sampling effort.

Three millennial San Rafael dune field eolian episodes were found to correspond statistically with three millennial events identified in the Kanab dune field, using similar research methods. Early Holocene episodes SR2 (~9.7-7.4 ka) and K0 (9.2 and 7.8 ka) were found to correspond, as did late Holocene episodes SR5 (~2.0-1.6 ka) and K3 (2.2-1.2 ka), and SR6 (~1.0 - 0.4 ka) and K4 (0.7 - 0.5 ka). Existing records of mobile dune activity on the Colorado Plateau report coeval dune activity during SR 2 (Canyonlands National Park, UT), SR5 (Petrified Forest National Park, Tusayan/Black Mesa, and Canyon de Chelly, AZ and Chaco, NM) and SR6 (Petrified Forest National Park and Tusayan/Black Mesa, AZ) suggesting at least three episodes of regionally extensive aridity.

1.0 Introduction

Periods of aridity in the Colorado Plateau can be multi-decadal or greater in duration, but were typically multi-annual or less after the mid-1900's CE. The southwestern US is in an ongoing drought that began in the early 2000's CE and its magnitude has exceeded records from at least 500 years (Williams et al, 2022). This drought and increased water demands has resulted in water shortages in the Colorado River system, leading to the implementation of water delivery reductions due to inadequate water supply to meet Colorado River Compact allocations (Fleck and Castle, 2021).

Climate models suggest increased temperatures and aridity are likely in the Colorado Plateau and the Colorado River Basin (e.g., Vano et al, 2014; Udall and Overpeck, 2017; Overpeck and Udall, 2020). Climate records that extend the historic (instrumental) record and

document spatial and temporal variability across the region are important to inform land and water resource management strategies to address changing conditions (i.e., Copeland et al, 2017; Woodhouse et al 2018; Overpeck and Udall, 2020). Tree-ring records and some sediment records (i.e., speleothems and lake deposits) can provide high-resolution (annual) records of climate and extend the short instrumental record but are sparse on the Colorado Plateau. Sand dune-records, in contrast, are plentiful and archive changes in hydroclimate by activating under threshold conditions of reduced moisture, and stabilize during wetter conditions (e.g., Lancaster, 1997; Tsoar, 2005, 2009).

The San Rafael desert is located in east-central Utah, in the central Colorado Plateau within the Upper Colorado River Basin. Bounded to the southwest and northeast by tributaries to the Colorado River, this region is rich in eolian deposits, including sand dunes. This study investigates eolian activity in the San Rafael desert to extend the record of natural hydroclimate variability in east-central Utah, focusing on Holocene eolian activity (Figure 3.1). Records of dune activity from this study are compared with records from the Kanab dune field, to the southwest, and with other regional hydroclimate records (Figure 3.1) to identify periods of coeval or overlapping eolian activity in southern Utah and the Colorado Plateau region. Implications for natural variability of hydroclimate are discussed.

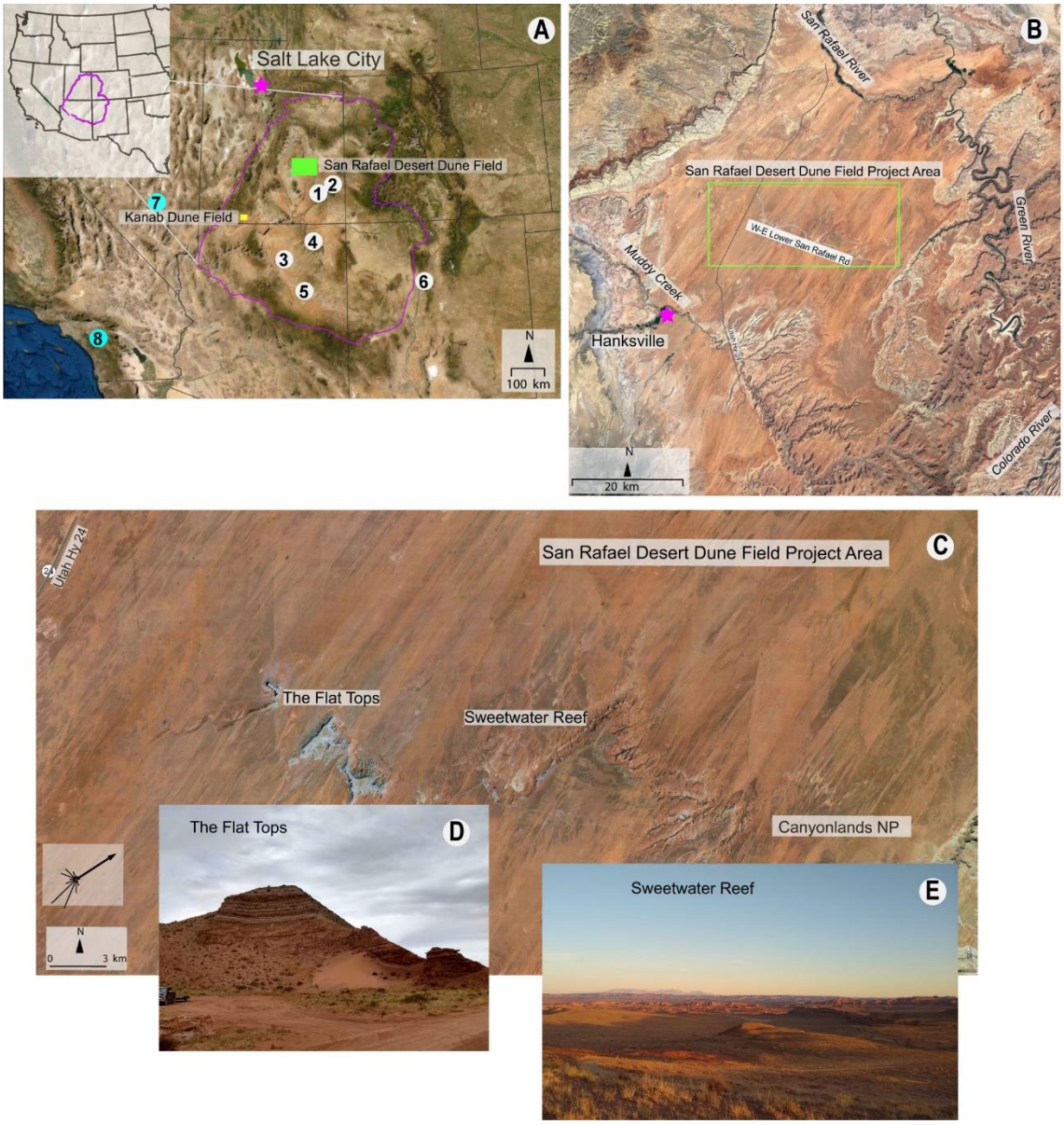

Figure 3.1. Project vicinity map. A. Locations of selected eolian activity records (Four Corners Region) and paleoclimate records. The Colorado Plateau (magenta outline), San Rafael desert dune field and project study area with nearby Kanab dune field study site (yellow rectangle, this study, Chapter 2). Locations of paleoclimate records shown in Figures 3.2 and 3.7 are in numbered circles: 1 – Canyonlands National Park (Reheis et al, 2005); 2- Canyonlands National Park (Reheis et al, 2018); 3- Tusayan and Black Mesa dunes (Stokes and Breed, 1993; Ellwein et al, 2011, 2015); 4- Canyon de Chelly (Manning, unpubl.2010); 5- Petrified Forest National Park (Schott, unpubl. 2019); 6 – Chaco Dunes (Wells et al, 1990). (Dune records 1-4 from INQUA Dune Atlas, Lancaster et al, 2016).Selected paleoclimate records: 7 – Lehman Cave speleothem $\delta^{18}O$ record, relative precipitation (Steponaitis et al, 2015); 8 – Lake Elsinore, CA (Kirby et al, 2019). B. Project location map for San Rafael Desert Dune Field (SRD) project area with local access roads. C. Aerial view of project area with locations of major bedrock exposures, and vicinity of Canyonlands National Park. Sand rose diagram from records at Hanksville climate station. D. Inset photograph of The Flat Tops exposure of Jurassic bedrock. E. Inset photograph of Sweetwater Reef, Jurassic bedrock.

2.0 Physiographic Setting

The San Rafael desert is located in east-central Utah, within the Colorado Plateau physiographic province, encompassing about 3000 km^2 in Emery, Wayne and Grand counties. The desert occupies the area between the San Rafael Swell to the northwest, the Green River to the east and the Colorado River to the southeast, the San Rafael River to the northeast and Muddy Creek borders the southwestern edge of the desert. The northwestern side is bounded by the San Rafael Reef, the northeast-southwest trending boundary of geologic monoclinal fold of largely Mesozoic strata. Elevations reach a maximum of ~1900 m to the south along the mesa-topped exposures of bedrock, decreasing to the north and to the southwest to a low of ~1400 m in the stream valleys (Figure 3.1). Steep slopes ~35% are typical along exposed bedrock ridges and canyons, abruptly flattening to a gentle range of 2-8% across most of the project area. This high desert region is predominantly public land, managed by various state and federal agencies, primarily as rangeland and for recreation. Ready access to active sand dunes, dark-sky parks and unique rock formations ranging from hoodoos to slot canyons and archaeologic sites, attract year-round tourism to the San Rafael desert. Close proximity to multiple national parks and designated wild and scenic areas likely has enhanced visitation in recent decades (Cullianne-Thomas and others, 2018; U.S. Bureau of Land Management, 2020).

San Rafael desert dune field (SRDF) is located east of east of Utah Hwy 24 and northeast of Hanksville, Utah, (see Figure 3.1B). SRDF contains a variety of dune morphologies, as well as Jurassic and Quaternary bedrock exposures, and encompasses approximately 2000 km^2. The study area includes both bedrock exposures and observed dune forms in a contiguous area of approximately 600 km^2, in the center of the dune field (Google Earth; National Agriculture Imaging Program (NAIP); Doelling et al, 2015). The dune field is composed of active and stabilized to partially stabilized parabolic and barchan sand dunes and barchanoidal (transverse) ridges about ~ 3-10 m in height and ~ 50 m (barchan) – 2 km (parabolic) in length. Linear ridges from ~2 – 20 km in length and <1-2 km in height, are visible in satellite imagery (see Figure

3.1C). Linear ridges and arms of parabolic and barchan dunes are oriented southwest-northeast, approximately N40E. The Flat Tops, a series of mesa-capped outcrops comprised of bedrock formed by the Jurassic San Rafael group (Carmel, Entrada, Curtis and Summerville Formations) occur in the central part of the project area, along West Lower San Rafael Road (Doelling et al, 2015) (see Figure 3.1C). These are mesas comprised of loosely consolidated strata, predominantly siltstones and sandstones. The Salt Wash member of the Jurassic Morrison formation caps the mesas. The San Rafael Reef is a prominent monoclinal bedrock structure exposed northwest of the dune field forming the eastern boundary of the San Rafael Swell, comprised primarily of Jurassic Navajo and Wingate Formation sedimentary layers. Further east a prominent ridge of exposed Jurassic bedrock is the Sweetwater Reef. This geologic feature is comprised primarily of Jurassic Entrada formation sandstones and siltstones.

Vegetation within the project area is sparse, typically comprised of xeriphytic species that are associated with the sand-desert shrub-zone assemblage (Harris, 1983). Larger vegetation consists primarily of sagebrush and other sage-steppe shrubs (i.e., *Artemisia filifolia, Ephedra torrevana, Yucca hatrimaniae*) and Utah juniper (*Juniperus osteosperina*), with sparse grasses and forbs (Davidson, 1996). Biological soil crusts (biocrusts) are common within the project area, acting as a stabilizing cover along with the sagebrush shrubs, to inhibit erosion by wind or water. Soil mapping project area is limited to northern Wayne County in the southern portion of the field area. Major soil units include the Begay, Sheppard, Factory and Mido sand and loamy fine sands. Slopes are 2-8%, depth to water table generally exceeds 80 cm and soils are typically excessively drained (Soil Survey Staff, 2021).

Climate is semi-arid (steppe in the Koeppen-Geiger climate classification system) with hot, dry summers and cold, dry winters. Average annual precipitation is ~109-250 mm (Source: PRISM group 1971-2000, average annual normal). Late summer monsoonal precipitation brings the greatest amounts of precipitation as convective thunderstorms occurring due to advection of moist air from the south during summer months. The North American Monsoon (aka Mexican

Monsoon) provides precipitation via late summer thunderstorms, while winter storms generate precipitation from the western Pacific (Metcalfe et al, 2015; Schwinning et al, 2008). Summary climate records for the period December, 1899 – June, 2016 from the Hanksville Cooperative Observer Network (COOP) weather station are shown in Table 3.1.

Table 3.1 Summary climate records. (Hanksville Cooperative Observer Network (COOP) station (1910-2016))

Precipitation (mm)		Temperature (^{o}C)	
Average Annual	143.8	Average Annual	11.9
Monthly Maximum (August)	19.3	Monthly Maximum (July)	36.8
Monthly Minimum (February)	6.9	Monthly Minimum (January)	-11.7

(Source: https://wrcc.dri.edu/cgi-bin/cliMAIN.pl?ut3611)

Wind data records from the Hanksville (KHVE) and the San Rafael River near Green River (SRFU1) MesoWest climate stations indicate concentration of modern threshold winds (> 6 ms^{-1}) in WSW to SSW direction across the San Rafael desert (Figure 3.3). Modern wind data is consistent with orientation of both stabilized and active dunes in San Rafael dune field, generally aligned SSW-NNE. All mapped dune morphologies (linear sand ridges, barchan, barchanoid ridges, and parabolic dunes, both stabilized and active) are similarly oriented, broadly aligned SSW –NNE. This suggests a consistent wind pattern throughout the Holocene, with threshold winds generating a resultant drift direction approximately SSW.

3.0 Previous regional work

Eolian dune systems provide extensive information on Late Quaternary hydroclimate variability in western North America (e.g., Muhs, 1985; Muhs and Holliday, 1995; Lancaster, 1988, 1997; Forman et al, 2001, 2008; Mayer and Mahan, 2004; Halfen et al, 2013; Rich et al, 2015; Halfen et al; 2016; Wolfe and Hugenholtz, 2017). Paleoclimate records such as tree rings and sedimentary strata (i.e., lake deposits) provide high-resolution records of hydroclimate that can be used to extend instrumental records of natural variability. Sand dunes are threshold

systems which are (re) activated in response to reduced vegetative cover and soil moisture, in the presence of sufficient wind velocity and sediment supply. Sediment supply is a limiting factor for eolian activity, linked both to influx and soil cover of the sediment present in a landscape (Lancaster, 1992; Kocurek and Ewing, 2005). While records of eolian activity provide a sensitive archive of changes in effective moisture, they are rarely continuous. Records of dune reactivation often contain temporal gaps due to the scouring of previous sediment layers as dunes reactivate and migrate downwind. Incomplete or apparently discontinuous profiles can occur as a result of geologic record fading due to reduced preservation of older deposits (Sadler, 1981). Lower resolution is also inherent due to the biogeomorphic (lag) response to changing climate conditions (driving forces). Thus, a systematic, high-density approach to field sampling is particularly important in eolian landscapes (Lancaster et al, 2016; Halfen et al., 2016).

3.1 Eolian records

Several studies have identified dune or dune field activity on the Colorado Plateau and in the Four Corners region. Late Pleistocene (~17.1-16.2 ka) and earliest Holocene (~13.8-12.2 ka) eolian activity is documented in eolian sand deposits interspersed with paleosols, in Canyonlands National Park (NP) in east-central Utah, southeast of the project area (Reheis et al, 2005). Early to middle Holocene eolian activity at ~8.6, 7.7, and 6.8 ka, and during the late Holocene at ~1.8 and 1.0 ka was also reported at that site. The Canyonlands record was interpreted to reflect a Pleistocene-Holocene transition from warmer wetter local conditions with alluviation episodes to drier conditions in the mid-Holocene (~8.5-6ka), cooling from ~6 to ~3 ka, with episodic eolian deposition (~4.2 and 3.8 ka) and drier conditions predominant through modern times, with persistent localized dune mobilization. Loess deposits near Canyonlands National Park and in Mesa Verde National Park in southwest Colorado suggest enhanced dust deposition during late Pleistocene (~17.1 ka), early Holocene (~10.4 ka), middle Holocene (7.6-4.5 ka) and late Holocene (3.6-1.4 ka) (Reheis et al, 2018).

In southeastern Utah near the Arizona border, five episodes of millennial scale dune activity are reported (~9.2-7.8 ka, ~6.8-5.5 ka, ~4.6-3.3 ka, ~2.2-1.2 ka and ~0.8-0.4 ka) in the Kanab dune field in southeastern Utah (see Ch 2). Eolian records from the Coral Pink dune field, in close proximity to Kanab dune field, indicate active sand movement at ~4.1, 2.8 and 0.51 ka (Ford et al, 2010). Within the project area eolian activity is reported from a spring mound archaeological site in vertical sequence at ~2.1 and ~1.4 ka (Byers, 2013).

Dune fields in northern Arizona and New Mexico, southwestern Colorado Plateau have been investigated more extensively than in central Colorado Plateau (Figure 3.1.A). Linear dune activity is recorded at ~4.7, 3.5-2, and 0.4 ka in the Tusayan dunes in north-central Arizona (Stokes and Breed, 1993). The record suggests that only the dune crests were mobilized, and that potential for deeper time records of eolian activity remains undisturbed by the late Holocene dune activity. Early Holocene eolian activity from ~10.9 - 7.4 ka is identified in stable sand sheets of Black Mesa dune field, with renewed deposition in late Holocene recorded at ~2 ka (Ellwein et al, 2011, 2015). Sand sheets are likely stabilized by soil development during wetter, cooler conditions. Increased sediment supply occurs during Late Holocene, resulting in sand accumulation.

In Chaco dune fields, located in northwestern New Mexico parabolic dunes are documented at ~ 5.6-2.7 ka and ~2.2-1.2 ka, developed on older dune deposits >10 ka (Wells et al,1990). Periods of stability are marked by paleosol development >5.6 ka, and 2.7-2.2 ka, with soil profile less well-developed during the latter period. Little evidence of soil development after ~1.2 ka is identified, suggesting ongoing eolian activity to the present. Records from Canyon de Chelly, Arizona indicate Holocene falling dune activity ~5.3 ka, 3.9 ka, 2.9-2.2 ka and 1.5 ka (Manning, 2010, unpubl.). Falling dunes represent records of significant sediment deposition, and often protect sediments from subsequent erosional removal of the depositional record that accompanies mobile dune response to changing threshold conditions (Redsteer, 2020). Eolian records from Petrified Forest National Park in northeastern Arizona indicate two episodes of dune

activity, late Pleistocene to earliest Holocene (~18 – 13 ka) and late Holocene (~2.3-0.8 ka) (Schott, 2019). Earlier activity is found in upland deposits, in stable linear dune deposits, while late Holocene activity is recorded in low elevation deposits that reflect reworking of older Pleistocene dune sediments. These studies are important to capture the history of eolian activity and aridity in the Colorado Plateau region.

3.2 Eolian system thresholds

The timing of dune activity is not uniform across the region, and instead varies spatially. Thresholds for eolian activity via saltation in sand are linked to wind speed, soil moisture and sediment availability (e.g., Bagnold, 1941; Tsoar, 2005). However, eolian-system response to perturbation is complex, following processes related to biogeomorphic (lag) response to threshold conditions (e.g. Lancaster, 1988; Wolfe et al, 2000; Hugenholtz and Wolfe, 2005b). A dune mobility index used effective moisture (precipitation to evapotranspiration ratio (P/PE)) and wind velocity to predict eolian response to changing climate conditions (Muhs and Maat, 1993; Lancaster, 1997). A spatially-independent metric to compare sand dune activation response, or drift potential (DP) was developed based on threshold wind velocity expressed as a baseline (dimensionless) vector unit (VU) (Fryberger, 1997). Three categories are defined: high (>400 VU), medium (200-400 VU) or low (<200 VU). These and other modeling efforts to characterize, quantify or compare threshold conditions in individual dune fields or between dune fields provide a context for evaluating the landscape response in eolian systems.

Vegetative cover typically stabilizes dunes, but establishment can be hindered by high infiltration rates of precipitation in combination with high wind speeds (Tsoar, 2005). When dunes are destabilized, largely through removal of vegetative cover there is an observed lag in reactivation response of the dune and similarly, a lag in response to a change in hydroclimate, wind regime and sediment supply, leading to revegetation and stabilization of the dune (Hugenholtz and Wolfe, 2005a,b; Wolfe and Hugenholz, 2009; 2013). The non-linear reaction

response of a natural system to a geomorphological disturbance was conceptually modelled as a complex response characteristics to different factors (i.e. ecological change) (Bull et al, 1991; Allen, 2008). Specific external variables influencing the lag in eolian systems have been identified as rainfall variability, antecedant moisture and wind power and intrinsic factors including a hysteresis effect with regard to wind thresholds and dune stabilization (Tsoar, 2005; Viles et al, 2008; Yizhaq and Ashkenazy, 2016). In biological systems, hysteresis refers to a non-linear response lag to stimulus that is observed when a threshold forcing event contains multiple stable states. The coexistence of active (devegetated) and stabilized (vegetated) proximal dunes is an example of hysteresis observed in eolian systems (Li et al, 2005). Asynchronous dune states (stable and active) are documented, both intra- and inter-dune field in a study of four dune fields in China that experienced similar climate (monsoon) perturbations, over the past 12,000 years (Xu et al, 2020). Dune state response is hysteretic, suggesting local conditions may preferentially influence dune state rather than climate conditions.

Uncertainty induced by the complex biogeomorphic response in dune activity to perturbations (physical, ecological, human or other) is not readily quantified, and serves as a cautionary note for interpreting the relationship between dune activity ages and climate, specifically aridity. Qualitative understanding from model simulations of dune development from flat ground and time to stabilization by vegetation (i.e. climate change from dry to wet conditions) found speed of stabilization correlated to equivalent sediment thickness (available sediment), dune size, and dune spacing (Barchyn and Hugenholtz, 2009, 2012). Simulations showed extended stabilization time correlated with extension of parabolic arms when parabolic dunes developed in the model simulation. Another study modelled landscape evolution pathways using various combinations of ecologic, geomorphic and climatic variables, and successfully replicated real-world dune fields (Nield and Bass, 2008). A field study of blowout development in vegetated, supply-limited dune fields described four conceptual states based on amount of vegetation and sediment supply: stable, blowout-dominated, reactivating, and disturbance-

susceptible (Barchan and Hugenholtz, 2013). The study included field tests of simulated blowouts in a vegetation-stabilized dune field in Canada and found a minimal effect on eolian activity, with revegetation quickly stabilizing the exposed sediments. Similar rapid (within a few years) revegetation occurred in similar studies in the Netherlands (Arens et al, 2006, 2013). These results show the feasibility of modeling spatial aspects of dune landscape evolution but indicate inherent uncertainty with regard to temporal resolution.

Mobile sand dunes in San Rafael dune field are expected to exhibit a characteristic biogeomorphic response to a geomorphic disturbance such as a change in climate conditions (ie. effective moisture change). Figure 3.2 is a diagrammatic sketch showing a lag in activation of both dune activity and dune de-vegetation response, following the onset of a decrease in effective moisture. Similarly, a lag in response to a subsequent increase in effective moisture is expected to occur prior to return to dune stabilization (vegetation). Dune mobility is expected to decrease as stability increases, likely at a different rate. OSL age distribution obtained from dune records is likely to reflect a lag following the onset of the reduction in effective moisture, with more records (ages) during the time the dune is fully mobilized. With a return to wetter conditions, a similar lag response is anticipated in a significant reuction of OSL records (ages) obtained. Fading of the records with time may exacerbate this predicted age distribution, further exaggerating the apparent low (lag) response to the climate event onset.

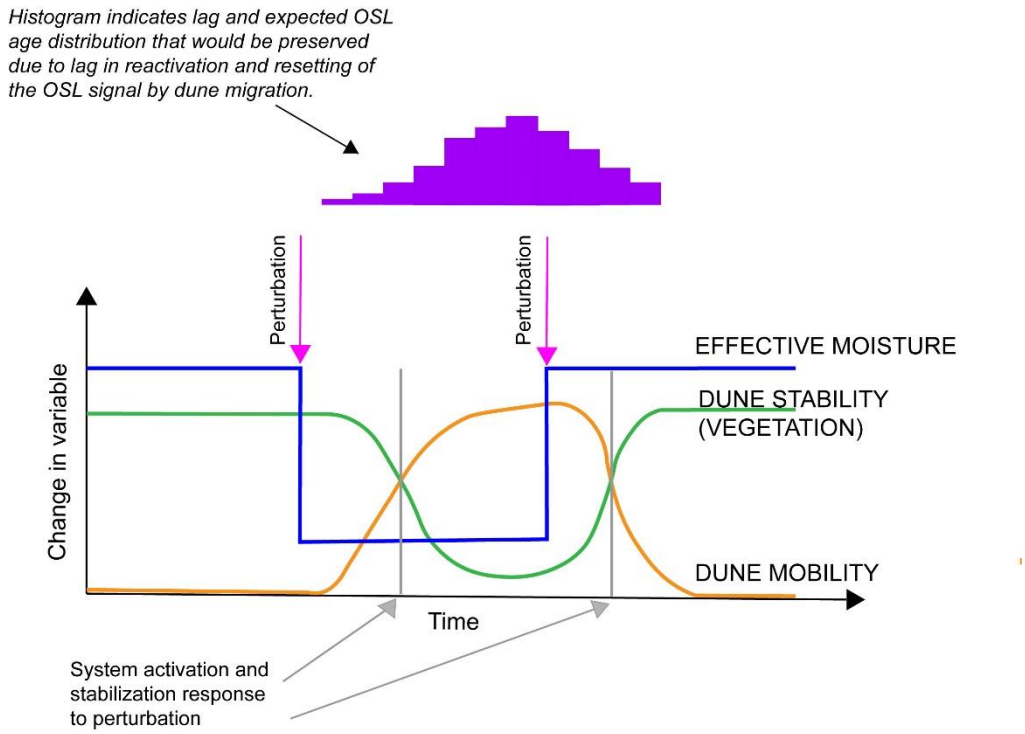

Figure 3.2. Schematic showing biogeomorphic and OSL response. Lag in response to climate perturbations and likely impact on distribution of OSL records. (Adapted from Hugenholtz and Wolfe, 2005a).

4.0 Methods

Research objectives of this study are to investigate dune activity in the SRDF. Satellite imagery was used to identify a representative project area within the dune field, approximately 40 km E-W and 15 km N-S. The project area is readily accessed in the northwest corner via State Road 24 turnoff to West - East Lower San Rafael Road (Figure 3.1). Migrating (active) dunes are a hazard at several locations along the road. A preliminary geomorphic map was then developed of this project area, used to plan a systematic field site investigation with a goal to identify breadth (spatial) and depth (temporal) of dune activity within the SRDF. A tiered approach to the investigation aims to obtain representative dune activity records in each of the eolian (dune) map units with samples from several (≥3) locations, seeking two or more vertical samples where possible.

Records of co-eval dune activity spatially distributed in the project area within or across multiple dune map units are interpreted as dune field-wide activation. Events of this magnitude are likely to be triggered by changing climate conditions (e.g., reduced P/PE) leading to dune mobilization in a semi-arid region such as San Rafael desert, rather than a local event. Short term triggers such as fire, animal or human disturbance, insect infestation or change to moisture delivery systems can act to destabilize one or a few dunes that are vegetated or soil-covered, in a localized portion of a dune field.

4.1 Geomorphic mapping

Remobilization (dune activity) is expected to result in an incomplete stratigraphic record due to removal of soils and horizons that record periods of dune stability. A geomorphic map was constructed for the study area using imagery from Google Earth and the National Agriculture Imagery Program (NAIP)). Geomorphic map units were based on surficial characteristics and landforms (i.e., bedrock, alluvium, dune) as well as existing geologic mapping (Doelling et al, 2015) (see Figure 3.3). Vegetation type and density, and color intensity (hue) of surficial sediments also help define the current state of dune stability (i.e., stabilized, partially stabilized, active). Dune morphology (i.e., sand ridge, parabolic, barchanoid) and relative age (i.e., younger in active, lighter Munsell hue, downwind sediment / dune) were used to further refine geomorphic units. Sample sites for characterization of soils, sediments, stratigraphy and age of deposition were then selected using observed dune morphology to provide representative coverage of each mapped dune unit to systematically capture representative records in each map unit.

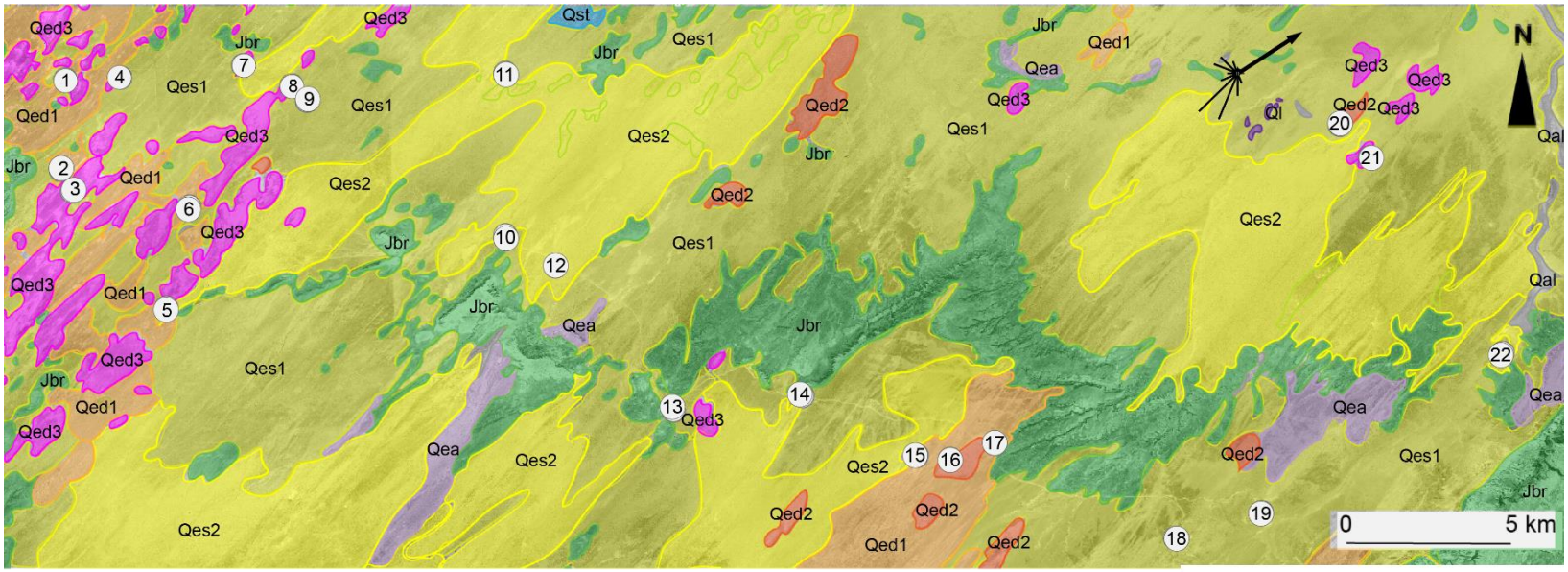

Figure 3.3. Geomorphic map of San Rafael project. Map units include bedrock (Br), exposed in the Flat Tops and along north to northeast trending "reef" structures broadly aligned with monoclinal folds of the San Rafael Swell to the east. Two sand sheets (Qes1 and Qes2) comprise much of the project area, characterized by moderate to sparse sage and juniper shrub vegetation, linear features comprised of sand ridges and mixed alluvial-eolian sediments with coppice dunes and relict dune limbs, partially eroded. Qes1 is typically darker in hue on the imagery, with denser vegetation, and abundant areas of cryptobiotic soil covering. Qes2 appears less densely vegetated and the vegetation contains more grasses, while the sand ridges appear lighter in hue with little vegetative cover.

Three dune units are identified (Qed1-3) are differentiated by dune morphology and abundance of vegetation. Qed1 includes low relief parabolic dunes and apparent abandoned limbs of parabolic dune, stabilized with vegetative or biocrust cover. Qed2 includes barchan dunes and barchanoid or transverse ridges, partially stabilized typically with sage-steppe shrubbery and shallow-rooted forbs or grasses, with some active dunes. Qed3 is likely the youngest containing mostly active dunes, long narrow parabolics and hairpin parabolic dunes , with partially stabilized limbs and interdune areas. Wind rose in upper right (SFRU1– MesoWest station at Green River) and lower left (KHVE – MesoWest climate station at Hanksville) show relatively scaled abundance of threshold winds (> 6 m/s), generally WSW to SSW. Both stations align moderately well with general orientation of dune forms. Sample sites are located and identified on map.

4.2 Field investigation and sampling

Samples from 22 dune sites in SRDF were collected from across the project area to obtain a representative distribution of mapped dune units (n≥3 each unit) (Table 3.2; Figure 3.3). Sediment and soil descriptions including grain size, sorting, color, and texture were noted at each site. Samples for grain size, organic content and isotope geochemistry were collected at regular intervals (~20-30 cm) or where changes in physical properties were observed. Field observations and sediment descriptions were used to guide sample-selection for age control. Charcoal samples were sought for radiocarbon dating however none were identified at the sample sites. Samples for optically stimulated luminescence (OSL) dating were obtained following standard protocols for trench / natural exposure or for coring with a hand auger system (Nelson et al, 2015; 2019). Field sampling methodology is further detailed in Appendix A.

Biological soil crust development is abundant in the eolian sand sheets, which also contain linear sand ridges and coppice dunes. Dune sediment is mainly very fine to fine grained, sub-rounded to rounded, quartz sand grains, colored medium to dark red (typically Munsell 5 YR 5-6/8 to 5 YR 6-7/4-6) with minor amounts of feldspars, heavy minerals, and lag gravels. Very sparsely vegetated (i.e., grasses and forbs), ripple marked dunes occur throughout the project area, and are common on the west, south and northeast portions of the field area. Biological soil crusts occur where linear sand ridges and coppice dunes are the prevalent eolian deposits, and sage-steppe shrub vegetation is predominant. Field adjustments were made to pre-selected sample sites to ensure disturbance from vegetation was minimized and to avoid evidence of bioturbation (Bateman et al, 2007; Rink, et al, 2013).

Table 3.2. Sample site summary. San Rafael dune field

Site No.	Map Unit	USU No.	Latitude *(dd)*	Longitude *(dd)*	Elev *(km)*	Depth *(m)*	Site Description	Dune Type	Eolian Event
1	Qed1	USU 807	38.58708	-110.58181	1.55	0.55	above soil	parabolic	E0
2	Qed1	USU 2702	38.56081	-110.58202	1.62	1.10	arm of parabolic, veg, low relief, above soil	parabolic	E6
3	Qed3	USU 2676	38.558233	-110.58097	1.61	3.20	active dune at depth	parabolic	E6
4	Qed3	USU 808	38.58739	-110.56667	1.55	1.50	arm of +/- active parabolic	parabolic	E6
5	Qes2	USU 3236	38.52512	-110.55433	1.61	0.95	coppice dune	coppice?	E6
5	Qes2	USU 3237	38.52512	-110.55433	1.61	1.40	older dune, soil?	coppice?	E5
6	Qed1	USU 810	38.55248	-110.54861	1.58	1.00	Parabolic dune near 'L' bend 5-upper recent eolian	parabolic	E6
7	Qed3	USU 3240	38.59066	-110.53288	1.58	1.00	low relief, partially stabilized parabolic	parabolic	E6
7	Qed3	USU 3241	38.59066	-110.53288	1.58	1.50	low relief, partially stabilized parabolic	parabolic	E5
8	Qed3	USU 2678	38.585583	-110.52038	1.57	1.65	younger parabolic, crest	parabolic	E6
8	Qed3	USU 2679	38.585583	-110.52038	1.57	3.25	Sample below USU2678	parabolic	E6
9	Qes1	USU 3398	38.581	-110.51586	1.65	1.10	coppice dune, below biocrust	coppice	E2
10	Qes2	USU 2707	38.54462	-110.46273	1.62	2.40	arroyo cut through sand stripe	linear?	E6
10	Qes2	USU 2708	38.54462	-110.46273	1.62	3.40	below USU2707, deeper dune	linear?	E6
11	Qes1	USU 3395	38.58793	-110.46226	1.55	0.80	small "linear" dune, biocrust & shrub cover	coppice	E2
11	Qes1	USU 3396	38.58793	-110.46226	1.55	1.60	small "linear" dune, biocrust & shrub cover	coppice	E1
11	Qes1	USU 3397	38.58793	-110.46226	1.55	2.20	small "linear" dune, biocrust & shrub cover	coppice	E1
12	Qes2	USU 3239	38.53621	-110.44795	1.62	1.40	coppice dune, above soil	coppice	E6
13	Qes1	USU 2703	38.49733	-110.41688	1.74	0.95	soil under, linear sand stripe	linear	E0
14	Qes1	USU 3392	38.5013	-110.38125	1.70	0.80	thick coppice dune, thicker biocrust development	coppice	E5
14	Qes1	USU 3393	38.5013	-110.38125	1.70	1.33	thick coppice dune, thicker biocrust development	coppice	E4
14	Qes1	USU 3394	38.5013	-110.38125	1.70	2.20	thick coppice dune, thicker biocrust development	coppice	E4
15	Qed2	USU 3238	38.48519	-110.35120	1.69	1.10	abandoned older limb, active barchan dune field	barchanoid	E4
16	Qed2	USU 3003	38.48434	-110.34206	1.72	1.03	eolian (dune) sed above lag gravel-possible Bk?	barchanoid	E3
17	Qed1	USU 813	38.48576	-110.32910	1.65	0.60	e. linear ridge by barch field; spl below harder layer	barchanoid	E2
18	Qes1	USU 3232	38.46268	-110.28064	1.69	0.95	coppice dune	coppice	E6
19	Qes1	USU 2814	38.46957	-110.25683	1.58	1.75	heavily rooted dune -- coppice dune?	coppice	E6
19	Qes1	USU 2815	38.46959	-110.25683	1.58	1.88	Low relief dune, deflation surface	parabolic	E2
20	Qed2	USU 3235	38.57446	-110.23604	1.44	0.95	truncated parabolic limb	parabolic	E6
21	Qed3	USU 3233	38.56612	-110.22720	1.50	0.80	west limb, partially stabilized parabolic	parabolic	E6
21	Qed3	USU 3234	38.56612	-110.22720	1.50	1.40	west limb, partially stabilized parabolic	parabolic	E6
22	Qes1	USU 3390	38.51299	-110.19169	1.56	0.87	coppice dune, Qes	coppice	E6
22	Qes1	USU 3391	38.51299	-110.19169	1.56	1.40	coppice dune, Qes	coppice	E4

4.3 Analytical approach

Field observations and laboratory analysis were used in conjunction with OSL ages to develop a chronostratigraphy of the dune field record. Sediment samples were analyzed for grain size using a laser particle analyzer. Selected sediment samples were also analyzed for total organic content (TOC), percent carbon (%C), carbon isotope fractionation ($\delta^{13}C$) using an isotope ratio mass spectrometer (IRMS) that measures isotopic fraction. Select sediment samples were also analyzed for chemical composition using inductively coupled plasma mass spectrometry (ICP-MS). Analytical methods for sediment and chronology are further detailed in Appendix B.

From these analyses, individual sediment packages, paleosols and/or periods of partial dune stabilization separating episodes of dune reactivation were identified. Particle-size analyses were used in conjunction with field descriptions to identify fining upward sequences. Paleosols or periods of stabilization were identified using field observations and corroborated where possible with increased organic carbon content and/or reduced $\delta^{13}C$ values, and presence of ultrafine (< 63 mm) particles. Figure 3.4 shows the stratigraphic sequence graphed for Site 8, with particle size, color, $\delta^{13}C$ reflecting similar increases at a soil horizon above the lower OSL (dune) sample. Similar reconstructed stratigraphic columns depicting the graphical results of these analyses can be found in Appendix C.

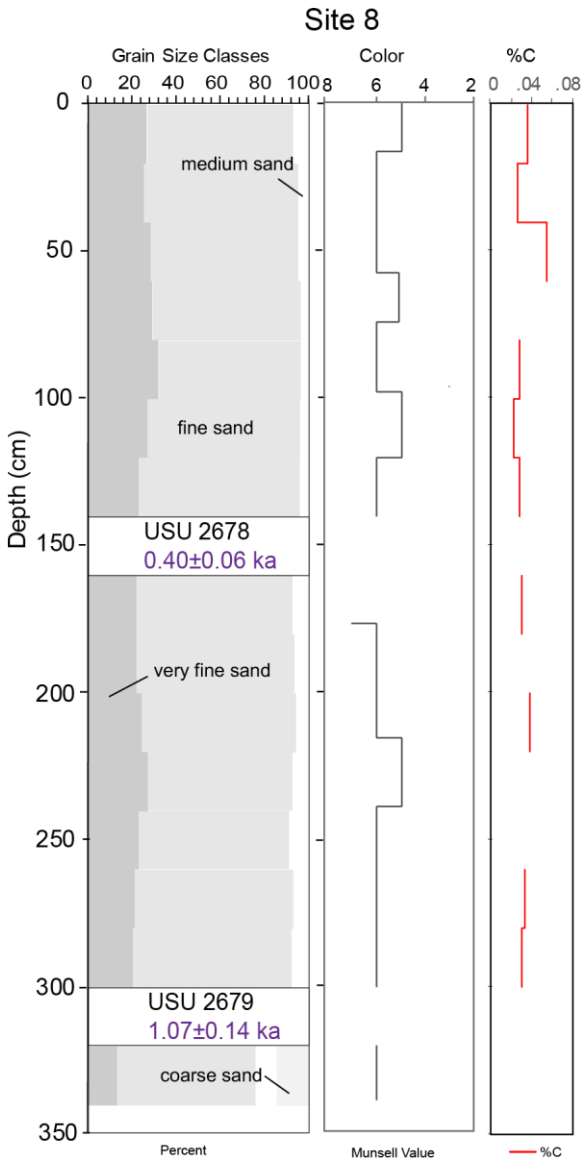

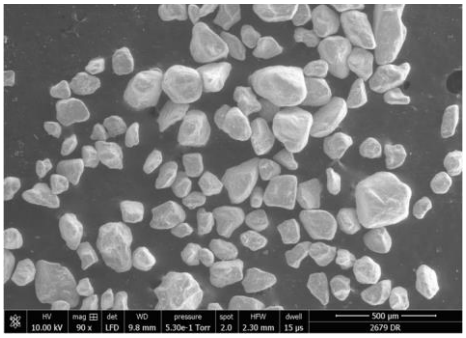

Figure 3.4. Site 8 – example chronostratigraphic record. Grain size profile shown as semi-logarithmic plot with varying distribution of very fine (medium gray), fine (light gray), medium (white) and coarse (very light gray) sand fractions. Upper and lower OSL sample locations with ages are shown, with SEM image of raw dune sand for lower sample (USU 2679) included to show typical dune sediment. Note: depths are from excavated auger platform, 25 cm below surface.

4.4 Age Control

Research in geomorphic processes and landscape evolution transformed with the application of luminescence dating to sedimentary deposits (Aitken, 1963; Huntley et al, 1985; Aitken, 1998; Rhodes, 2011). Luminescence dating determines the last time a mineral grain previously exposed to light or heat at Earth's surface, based on acquired charge post-burial.

Age control for San Rafael dune activity is obtained from optically stimulated luminescence (OSL) dating (Huntley et al, 1985). Thirty-four samples for OSL dating were collected from 22 sites, either using a soil auger with coring capability (n=20) or from natural exposure or trenches (n=14). Samples were processed and analyzed at the Utah State University Luminescence Laboratory for optically stimulated luminescence (OSL) dating.

Sediment cores and sample tubes were processed under dim amber light (~590 nm) to isolate the quartz mineral fraction. Outer sediment from the tubes and cores was discarded to remove grains potentially exposed to light, and remainder of each sample was wet-sieved to a target particle size between 75 and 150 μm (Appendix B). The sample was then treated with hydrochloric acid to dissolve carbonates, bleach to remove organic material, separated from higher density minerals using sodium polytungstate (2.7 g/cm^3), followed by concentrated hydrofluoric and hydrochloric acid treatments to remove feldspars, etch the outer surface of the grains, and prevent formation of fluorite precipitates (Wintle, 1997).

Representative subsamples of sediment were analyzed for dose-rate determination using ICP-MS and ICP-AES analyses for concentrations of radioelements K, Rb, Th, and U. *In-situ* gravimetric moisture content was measured on all samples (Appendix B). Due to drying effects of the current mega-drought and warm-season sampling the measured moisture values are interpreted to be minimum values in relationship to the mean conditions. An average of 5±2% was used as the moisture content in dose-rate calculations for all samples (e.g., Nelson and Rittenour, 2015). Dose-rate calculations include conversion factors from Aitken (1989) and Guérin et al. (2011), the influence of water attenuation, cosmic contribution by using sample depth, elevation, and longitude/latitude following Prescott and Hutton (1994), and uncertainty in elemental measurements.

Luminescence measurements were performed on two Risø TL/OSL Model DA-20 readers equipped with blue-green light emitting diodes (LED) (470±30 nm) (Bøtter-Jensen et al.,

2003). OSL ages were obtained from the quartz sand (75-150 μm) fraction using the small aliquot regenerative (SAR) dose protocol of Murray and Wintle (2000). Temperature settings for regenerative preheat (220° C) and test dose preheat (cutheat) (220° C) settings, and an optical bleach was used to remove remaining charge buildup between experiments (Wintle and Murray, 2006). Dose-response curves were fit within linear or saturating-exponential fits to calculate D_E values.

Cumulative D_E values were calculated using the central age model (CAM) of Galbraith and Roberts (2012), reported at 2-sigma standard error (Appendix B). Rejection criteria included evidence of feldspar contamination, recycling ratio <0.7 or >1.3, natural D_E greater than the highest regenerative dose given, large (>100%) D_E error and/or $D_E \leq 0$ Gy. Errors on ++age estimates are reported at 1-sigma standard error and include errors related to instrument calibration, and dose rate and equivalent dose calculations and were calculated in quadrature using the methods of Aitken and Alldred (1972) and Guerin et al. (2011).

5.0 Results

The San Rafael desert trends roughly southwest-northeast, generally aligned with the structural trend of the San Rafael Swell. Sand dunes within the desert are oriented approximately SSW-NNE. Active long parabolic dunes are predominant along the west side of the project area and along State Road 24. An active barchanoid dune field is located along W. Lower San Rafael Road ~17 km east of the Flat Tops.(see Figures 3.1 and 3.3). Five Quaternary eolian units are mapped, including two eolian sand sheets and three sand dune units. Seven periods of eolian activity were identified based on the chronostratigraphic record developed in this study.

5.1 Geomorphic mapping

Three dune units were mapped in the San Rafael dune field, identified as Qed1, Qed2 and Qed3 (Figure 3.3). Qed1 is interpreted as the oldest dune unit, with Qed2 and Qed3 likely similar in age based on evidence for modern activity. Linear sand ridges and coppice dunes are included in eolian sand sheets Qes1 and Qes2, older and younger respectively. Representative images of the five mapped eolian units are shown in Figure 3.5. Other map units include alluvial material, map unit Qal, which occurs along several streams and along canyon floors and Qea, mixed eolian and alluvial sediments, observed flanking bedrock exposures (unit Jbr) particularly in the central and eastern portions of the study area. Spring tufa deposits, unit Qst, are located along the north edge of the study site, and lacustrine deposits, Ql, are found in the northeast. Bedrock exposures are mapped as unit Jbr, after Doelling et al (2015) and contain Jurassic-age sedimentary units of the San Rafael Group (primarily Entrada, Summerville and Curtis Formations).

The (geomorphically) oldest dune unit mapped, Qed1, is characterized by stabilized long parabolic dunes from ~200 m – 1 km in length and ~2-4 m in height, sparsely vegetated with sagebrush (Artemesia arbuscula) and various grasses predominant. Relict parabolic limbs can reach ~ 2-2.5 km in length, and areas of biocrust are developed particularly in some interdune and covering relict limbs and other undisturbed (i.e., by grazing) areas. This unit is identified predominantly in the northwest quarter of the project area. Additional instances of this unit are found south of the main access road (W and E Lower San Rafael) in the center of the project area and in the northeast and southeast corners of the project area.

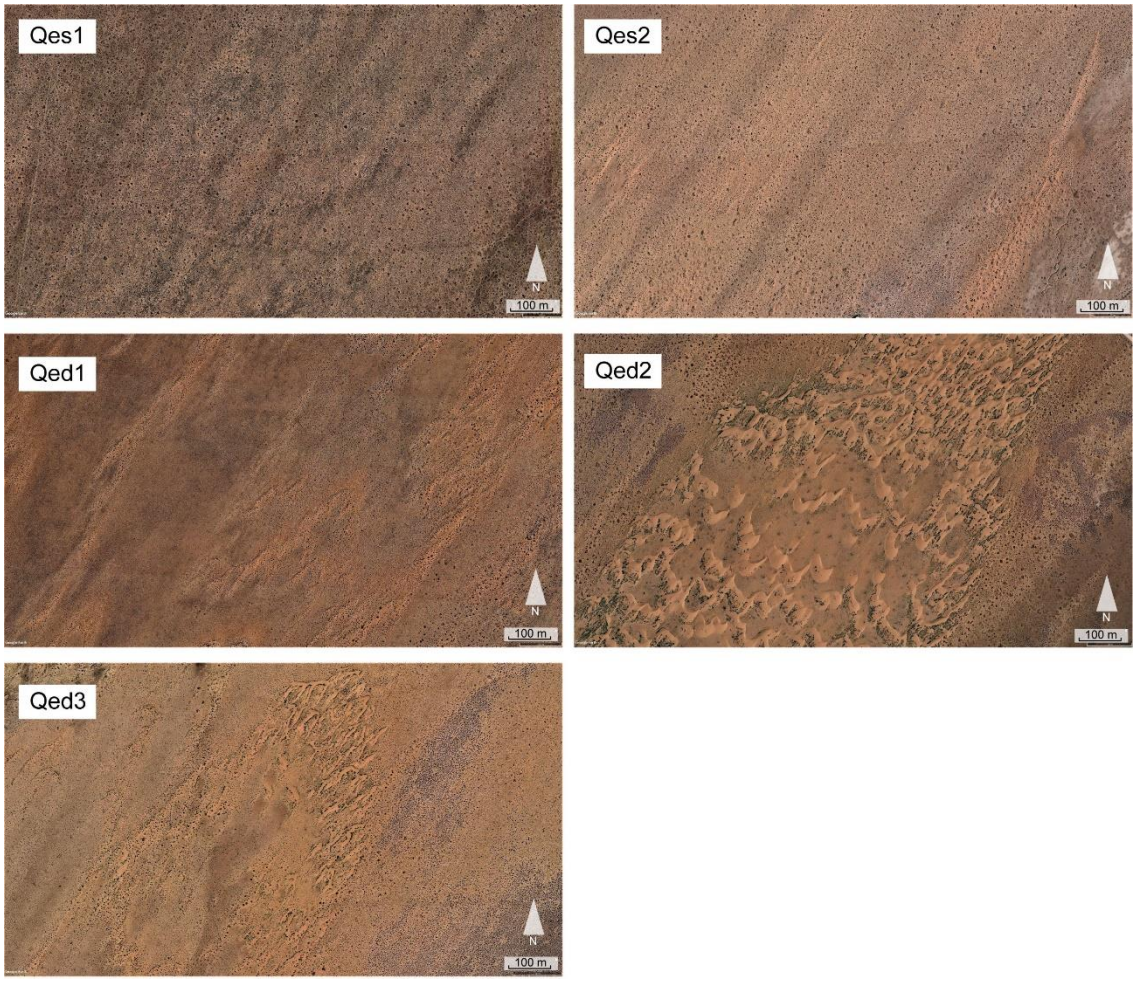

Figure 3.5. Example images of eolian units in SRDF. (Source: Google Earth, accessed 1/23/21). Units Qes1 (upper left) and Qes2 (upper right)are composed of mixed eolian sand and alluvial deposits. Qes1 is mostly stabilized with biocrust soil and vegetation. The Qes2 surface is covered by thin layers of partially active sand. Three dune units, Qed1, Qed2 and Qed3 are distinguished by the degree of stabilization and dune morphology. Qed1 contains linear sand ridges and long parabolic dunes, stabilized with biocrust soil and vegetation. Partially active and active barchan dunes and barchanoid ridges are mapped as Qed2. Unit Qed3 is characterized by partially active to active parabolic dunes.

Mapped dune unit Qed2 is comprised of partially active and active barchan dunes and barchanoid (transverse) ridges. This unit occurs as small individual groups of dunes across the project area both north and south of W/E Lower San Rafael Road, and north of the bedrock ridge exposures in the center of the dune field. Individual barchan dunes are typically ~ 30 – 40 m long, and ~30-50 m wide, and ~ 3-6 m in height. Individual dunes can reach ~70 m in length and coalescing ridges are ~100 – 400 m long. Individual dune fields within this unit are typically <2

km2 in area. Barchan dune crests contain little vegetative cover and dunes are formed around central stabilizing vegetation. Vegetation between dune limbs consists mostly of sage-steppe shrubs such as sagebrush, rabbitbrush and other xeriphytic shrubs.

Mapped dune unit Qed3 is comprised of partially active to active parabolic dunes. It is concentrated in a wide swath along SR 24, mapped in the west and northwest quarter of the project area. Other occurrences are found in the northcentral and northeastern parts of the project area, and along the east side of the bedrock exposures in the center of the project area. Dune fields mapped within of this unit are typically 1-10 km^2. Individual dunes are ~200 – 800 m in length, ~10 – 50 m wide, and ~ 2-4 m in height. Vegetation consists primarily of shallow rooted grasses and forbs, where the dunes are vegetated. Both map units Qed2 and Qed3 contain active dunes, visible in historical imagery (Google Earth) and observed during the period of study.

Eolian sand sheets, units Qes1 and Qes2, cover most of the SRDF. The sand sheets onlap bedrock exposures and merge with loose alluvial-colluvial debris shed from Jurassic bedrock (Br) exposures along the Lower San Rafael Road. They also onlap prominent ridges aligned southwest to northeast, in the southwestern portion of the study area (Figure 3.3). Qes1 is typically darker in hue on the imagery, with denser vegetation, and abundant areas capped with biological soil crust (Figure 3.5). Linear sediment ridges align with the general northeast trend of the other dune units, composed of mixed eolian alluvial sediments, locally underlain by shallow bedrock. Vegetation is predominantly sagebrush and Utah juniper with other common xeriphytic shrubs. Areas of coppice dunes are also common in this unit. Discontinuous relict limbs of parabolic dunes and mounds of dune sand, stabilized by vegetation or biological soil crusts also occur in this unit.

Qes2 is also characterized by linear sediment ridges, and contains similar relict dune forms. Vegetation in Qes2 is typically less dense overall and contains a greater proportion of grasses than in Qes1 (Figure 3.5). The linear sand ridges appear lighter in hue with little

vegetative cover and loose sand is often ripple-marked. Coppice dunes and biological soil crusts are less abundant than in Qes1.

5.2 Results of sediment analysis

Stratigraphic columns for sample sites containing analytical data for sediment and/or organic content analysis (particle size, color, $\delta^{13}C$, %C) are graphically compiled in Appendix C. Sediment mixing during the hand augering process obscured any sedimentary structures for these sites. Sediments are comprised predominantly of very fine to fine sand, with varying amounts of very coarse silt and finer particles also present at many sites. Where present, the silt and clay fraction (< 63 μ) typically increase with depth. Silt and clay fractions are typically associated with soil formation (e.g., Reheis et al, 2005; Ellwein et al, 2018) and interpreted to reflect periods of declining eolian activity and/or onset of dune stabilization.

Organic carbon content is generally less than 1% and is consistent with measurements in similar deposits (i.e., Muhs and Maat, 1993) using the Walkley Black method (Walkley and Black, 1934). Organic carbon content of San Rafael dune sediment measured in 27 sediment samples, spatially and temporally distributed across the dune field, ranged between 0.007% and 0.070%, with an error range of 16% to 38% of the reported value (±0.0036 – 0.0266%). Error for calibration of instrumentation is reported by the laboratory at ±0.5%. Analytical results are graphically depicted in Appendix C for all sites analyzed. Nitrogen content did not exceed 0.008%, with most samples registering instrumental baseline (0.0-0.002%) and therefore not used in further interpretation. Carbon isotope ($\delta^{13}C$) analysis results ranged between -36.16% and -24.08%, with calibrated standard deviation ranging from± 0.16% to 0.33%, adjusting for linearity and drift in instrumental measurements for individual runs. Error for calibration of instrumentation is reported by the laboratory at ±0.15%. Tabulated results of the TOC analyses are presented as Appendix D .

Stratigraphic control is developed from the sediment analyses, in conjunction with field observations, detailed in the following text and shown as stratigraphic columns in Appendix C. Sites 5 (map unit Qes2), 7 and 8 (map unit Qed3), and 11, 14, and 22 (map unit Qes1) contain stratigraphic evidence for multiple periods of dune activity. Evidence of hiatus is provided through a combination of field observations and sediment analysis. The primary indicator is a fining upward sequence (Glennie, 1970; Folk, 1971). Darker color (Munsell soil color) and higher $\delta^{13}C$ and/or %C and presence of a soil horizon or soil development also contribute evidence of a hiatus in the stratigraphic sequence.

Chronologic control is added using OSL ages. Figure 3.4 shows the graphical stratigraphic analysis for Site 8, where a depositional hiatus occurs. Dune activity is separated by 0. 7 ky and 1.6 m of sediment deposition. Using similar methods, evidence for depositional breaks occur at sites 5 and 7. At site 5 a stratigraphic break separates ages of the lower (1.2 m) and upper (0.95 m) age samples. A similar stratigraphic break at site 7 between the lower (1.5 m) the upper (1.0 m) sample occurs.

Sequences of three vertical samples were obtained from sites 11 and 14. Stratigraphic evidence (increased clay and silt content, color change and presence of calcified rootlets and/or calcite nodules) is observed between the middle and upper sample in each sequence, defining a hiatus in site 11 between 1.6 and 0.8 m and at site 14 between 1.33 and 0.8 m. At site 11, field observations of carbonate nodules >5mm at 1.9 m with an increased pulse of very fine and fine sand and deepened soil color value at 2.1 m suggest an additional hiatus in eolian activity between the lower (2.2 m) and middle (1.6 m) samples.

At site 22, on the eastern edge of the project area, a stratigraphic break occurs between the lower (1.4 m) and upper (0.9 m) sample ages, identified by increased silt and clay content, color change and development of calcite nodules. This is interpreted as a hiatus in eolian activity, marking a period of stabilization.

5.3 Results of age analysis

Age results from the OSL analyses are presented in Table 3.2 organized numerically by sample site as shown on the geomorphic maps (Figure 3.3) with additional information on dose rate chemistry and calculation available in Appendix B. Dune sediments typically respond well to OSL dating due to full sun exposure during transport and prior to deposition and burial. Equivalent dose radial plots are available in Appendix F with detailed summaries of OSL results by sample found in Table 3.2.

Ages are discussed here, organized by map eolian units, Qed1 to Qed3 followed by Qes1 and Qes2 and in approximate order of sample site west to east.

Table 3.3. Optically stimulated luminescence ages. San Rafael dune field.

Site No.	USU No.	Depth (m)	Num. of aliquots[1]	Dose rate (Gy/kyr)	Equivalent Dose[2] ± 2σ (Gy)	OSL age ± 1σ (ka)	Eolian Event
1	USU-807	0.55	16 (27)	1.61 ± 0.07	27.27 ± 2.19	**16.98 ± 1.76**	SR0
2	USU-2702	1.1	13 (26)	1.41 ± 0.07	1.27 ± 0.51	**0.90 ± 0.20**	SR6
3	USU 2676	3.2	16 (30)	1.39 ± 0.07	0.63 ± 0.19	**0.45 ± 0.08**	SR6
4	USU-808	1.5	14 (21)	1.17 ± 0.06	0.65 ± 0.17	**0.54 ± 0.09**	SR6
5	USU 3236	0.95	18 (26)	1.62 ± 0.06	0.65 ± 0.28	**0.40 ± 0.09**	SR6
5	USU 3237	1.4	17 (21)	1.61 ± 0.06	2.71 ± 0.40	**1.69 ± 0.19**	SR5
6	USU-810	1	12 (21)	1.30 ± 0.06	0.75 ± 0.44	**0.57 ± 0.18**	SR6
7	USU 3240	1	14 (20)	1.59 ± 0.06	0.72 ± 0.37	**0.45 ± 0.12**	SR6
7	USU 3241	1.5	19 (30)	1.76 ± 0.07	3.45 ± 0.71	**1.96 ± 0.25**	SR5
8	USU 2678	1.65	17 (34)	1.69 ± 0.07	0.68 ± 0.15	**0.40 ± 0.06**	SR6
8	USU 2679	3.25	17 (28)	1.66 ± 0.08	1.92 ± 0.37	**1.16 ± 0.16**	SR6
9	USU 3398	1.1	16 (26)	1.55 ± 0.06	13.25 ± 1.09	**8.57 ± 0.78**	SR2
10	USU-2707	2.4	16 (24)	2.35 ± 0.10	2.13 ± 0.17	**0.91 ± 0.09**	SR6
10	USU-2708	3.4	19 (32)	2.09 ± 0.08	2.17 ± 0.28	**1.04 ± 0.11**	SR6
11	USU 3395	0.8	19 (21)	2.95 ± 0.11	28.51 ± 2.06	**9.66 ± 0.84**	SR2
11	USU 3396	1.6	21 (24)	2.46 ± 0.09	27.46 ± 1.57	**11.17 ± 0.94**	SR1
11	USU 3397	2.2	20 (24)	2.19 ± 0.08	27.61 ± 2.10	**12.62 ± 1.11**	SR1
12	USU 3239	1.4	15 (17)	1.83 ± 0.07	1.36 ± 0.32	**0.74 ± 0.11**	SR6

Site No.	USU No.	Depth (m)	Num. of aliquots[1]	Dose rate (Gy/kyr)	Equivalent Dose[2] ± 2σ (Gy)	OSL age ± 1σ (ka)	Eolian Event
13	USU-2703	0.95	22 (29)	1.72 ± 0.08	27.79 ± 4.51	**16.19 ± 2.04**	SR0
14	USU 3392	0.8	20 (22)	2.07 ± 0.08	3.25 ± 0.37	**1.57 ± 0.15**	SR5
14	USU 3393	1.33	17 (22)	1.78 ± 0.07	5.11 ± 0.51	**2.87 ± 0.27**	SR4
14	USU 3394	2.2	19 (20)	1.96 ± 0.07	6.18 ± 0.43	**3.16 ± 0.27**	SR4
15	USU 3238	1.1	18 (21)	1.88 ± 0.07	6.32 ± 0.42	**3.36 ± 0.29**	SR4
16	USU-3003	1.03	20 (26)	1.74 ± 0.07	8.07 ± 0.59	**4.65 ± 0.41**	SR3
17	USU-813	0.6	18 (25)	1.89 ± 0.09	13.98 ± 1.71	**7.42 ± 0.84**	SR2
18	USU 3232	0.95	15 (20)	1.67 ± 0.07	0.85 ± 0.30	**0.51 ± 0.10**	SR 6
19	USU-2814	1.75	16 (27)	1.75 ± 0.07	1.07 ± 0.21	**0.61 ± 0.08**	SR6
19	USU-2815	1.88	22 (37)	1.65 ± 0.06	15.44 ± 1.27	**9.37 ± 0.84**	SR2
20	USU 3235	0.95	15 (23)	1.44 ± 0.06	1.26 ± 0.43	**0.87 ± 0.17**	SR6
21	USU 3233	0.8	18 (26)	1.41 ± 0.06	1.13 ± 0.34	**0.81 ± 0.14**	SR6
21	USU 3234	1.4	20 (27)	1.61 ± 0.06	1.09 ± 0.23	**0.68 ± 0.09**	SR6
22	USU 3390	0.87	15 (20)	2.13 ± 0.08	0.95 ± 0.33	**0.45 ± 0.09**	SR6
22	USU 3391	1.4	14 (20)	2.12 ± 0.08	5.30 ± 0.87	**2.50 ± 0.28**	SR4

[1] Number of aliquots used in age calculation and number of aliquots analyzed in parentheses.
[2] Dose rate is derived from radioelemental concentrations by conversion factors from Guérin et al. (2011). Radioelemental concentrations determined using ICP-MS and ICP-AES techniques. (SM 3.6 – Dose Rate Analysis)
[3] Equivalent dose (D_E) calculated using the Minimum Age Model (MAM) Galbraith and Roberts (2012).
[4] Optically stimulated luminescence (OSL) age analysis using the single-aliquot regenerative-dose procedure of Murray and Wintle (2000) on 2mm small-aliquots of quartz sand. Equivalent dose (D_E) calculated using the Central Age Model (CAM) Galbraith and Roberts (2012).

Four sites (Sites 1, 2, 6 and 17) in map unit Qed1 were sampled and described within the project area. OSL ages range from late Pleistocene (site 1 -17 ka) to mid-Holocene (site 17 – 7.4 ka) to latest Holocene (sites 2 and 6 – 0.9 - 0.6 ka) (Figure 3.3; Tables 3.2, 3.3). One sample was obtained from each site and depths ranged from 1.1 to 0.55 m. Two samples were obtained above apparent soil layers (Sites 1 and 2). One sample was collected below a partially cemented (calcium carbonate) layer ((Site 17) and one sample from an upper eolian layer, presumed young (Site 6).

Map unit Qed2 was sampled at three sites (Sites 15, 16 and 20). OSL ages span middle (4.7 and 3.4 ka at sites 15 and 16) to late Holocene (0.9 ka at site 20) (Figure 3.3; Tables 3.2,

3.3). One age is reported from each site, from sample depths between 0.95 and 1.1 m. A gravel lag was observed in the trench below the sample collected at Site 9.

Five sites were described (Sites 3, 4, 7, 8 and 21) and sampled from map unit Qed3 in the northwest side and northeast quadrant of the project area (Figure 3.3). OSL ages were obtained from eight samples, all late Holocene, ranging from 2 - 1.2 ka and 0.7 – 0.4 ka (Tables 3.2, 3.3). Sample depths range from 0.8 – 3.25 m and vertical sequences separated by 0.5-1.6 m of sediment were obtained from three sites (Sites 7, 8, 21). Two sediment packages are subtly distinguished, marking a stratigraphic break between the upper and lower samples at Site 8 (Appendix C). Field observations at Site 7 (change in Munsell color value, presence of Bk soil horizon) also support a stratigraphic break between the upper and lower age samples. No sedimentologic changes suggest a stratigraphic break between the upper and lower age at Site 21, however increased clear (noncoated, nonfrosted) coarse sand fraction with depth was observed at the site.

Map unit Qes1 is the most extensive eolian unit in the project area, and is interpreted as the oldest of the eolian geomorphic units in the San Rafael desert, characterized by low relief and relatively heavily vegetated or biocrust-covered surfaces. Seven sites (Sites 9, 11, 13, 14, 18, 19 and 22) were sampled and described from this map unit, with vertical sequences of two or more age samples obtained at four sites (Sites 9, 11, 14 and 22) (Figure 3.3; Tables 3.2, 3.3). Sites 9, 11, 14 and 22 are coppice dunes and site 13 is a linear sand ridge. OSL results reported here include one late Pleistocene age, corresponding to marine isotope stage (MIS) 2 (late glacial) (16.2±2.0 ka) (Site 13). Remaining ages range from earliest Holocene (12.6±1.1 ka) (Site 11, lowest) to latest Holocene (0.45±0.09 ka) (Site 22, upper). Evidence of a stratigraphic break (increased silt fraction, change in Munsell value) is observed at Site 22, separating a lower (1.4 m; 2.50±0.28 ka) and upper (0.9 m; 0.45±0.09 ka) samples. Similar stratigraphic evidence (changes in grain size and color) is observed separating the middle (1.6 m; 11.2±0.9 ka) and upper (0.8 m; 9.66±0.84 ka) age samples at Site 11 and at Site 14 the middle (1.3 m; 2.87±0.27

ka) and upper (0.8 m; 1.57±0.15 ka) age samples, marking horizons reflecting dune stabilization between eolian events (Tables 3.2, 3.3).

Map unit Qes2 is also extensive in the project area, with a range of eolian sediments similar to Qes1. The vegetation density is lower and there is less abundant biocrust development with thin sheets of non-stabilized sediment cover. These characteristics suggest that Qes2 is a younger unit, characterized by more recent eolian activity than Qes1. Three sites (Sites 5, 10 and 12) were sampled and described from this map unit, with vertical sequences of two or more OSL samples obtained at two sites (Sites 5 and 10) (Figure 3.3; Tables 3.2, 3.3). Sites 5 and 12 are coppice dunes, and site 10 is a linear sand ridge. Reported ages are all late Holocene, ranging from 1.69±0.19 ka to 0.40±0.09 ka. Evidence of stratigraphic break (increased silt fraction, change in Munsell value) is observed at Site 5 separating a lower (1.4 m; 1.69±0.19 ka) and upper (0.95 m; 0.40±0.09 ka) age samples.

6.0 Discussion

6.1 Temporal and spatial age distribution

Based on the chronostratigraphy developed for San Rafael dune field, seven episodes of eolian activity are defined (Figure 3.6). Temporal groupings were defined by identifying intervals with multiple dune activity records separated by temporal gaps of multi-centennial or greater duration that are spatially distributed within the dune field. Interpreted periods of stability (temporal gaps between grouped activity episodes) were confirmed by stratigraphic evidence of depositional hiatus between designated episodes (see Section 5.3). Individual sites with a vertical sequence of two or more age samples were used to constrain stratigraphic breaks between episodes, where obtained. Field observations and sediment analyses provided the evidence for periods of non-depositional hiatus within the dune, identified primarily by increased silt content and darker sediment color (Munsell soil color) (Appendix C).

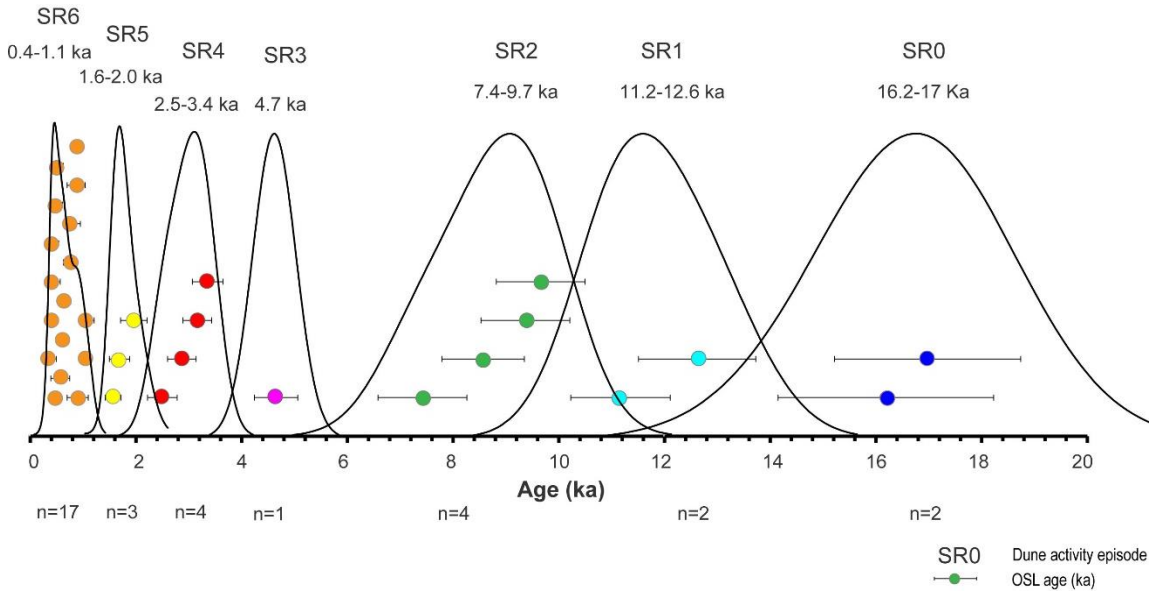

Figure 3.6. Chart of San Rafael eolian episodes. Initial eolian activity is late Pleistocene, SR0, at ~17-16.2 ka and earliest Holocene, SR1,~12.6-11.2 ka. Eolian events SR2 (~9.7-7.4 ka), SR3 (~4.7 ka), SR4 (~3.4-2.5 ka), SR5 (~1.6-2.0 ka) and SR6 (~1.1-0.4 ka) occur from early middle to latest Holocene.

Initial activation event SR0 (~17-16.2 ka) occurs in late Pleistocene, followed by SR1 at earliest Holocene (~12.6-11.2 ka). Holocene eolian events are identified as SR2 (~9.7-7.4 ka), SR3 (~4.7 ka), SR4 (~3.4-2.5 ka), SR5 (~2-1.6 ka) and SR6 (~1.1-0.4 ka). Spatial distribution for eolian activity events is shown in (Figure 3.7). Site locations, descriptions, sample depths and eolian events are summarized in Table 3.2, graphically depicted in SM 3.1 and further discussed here.

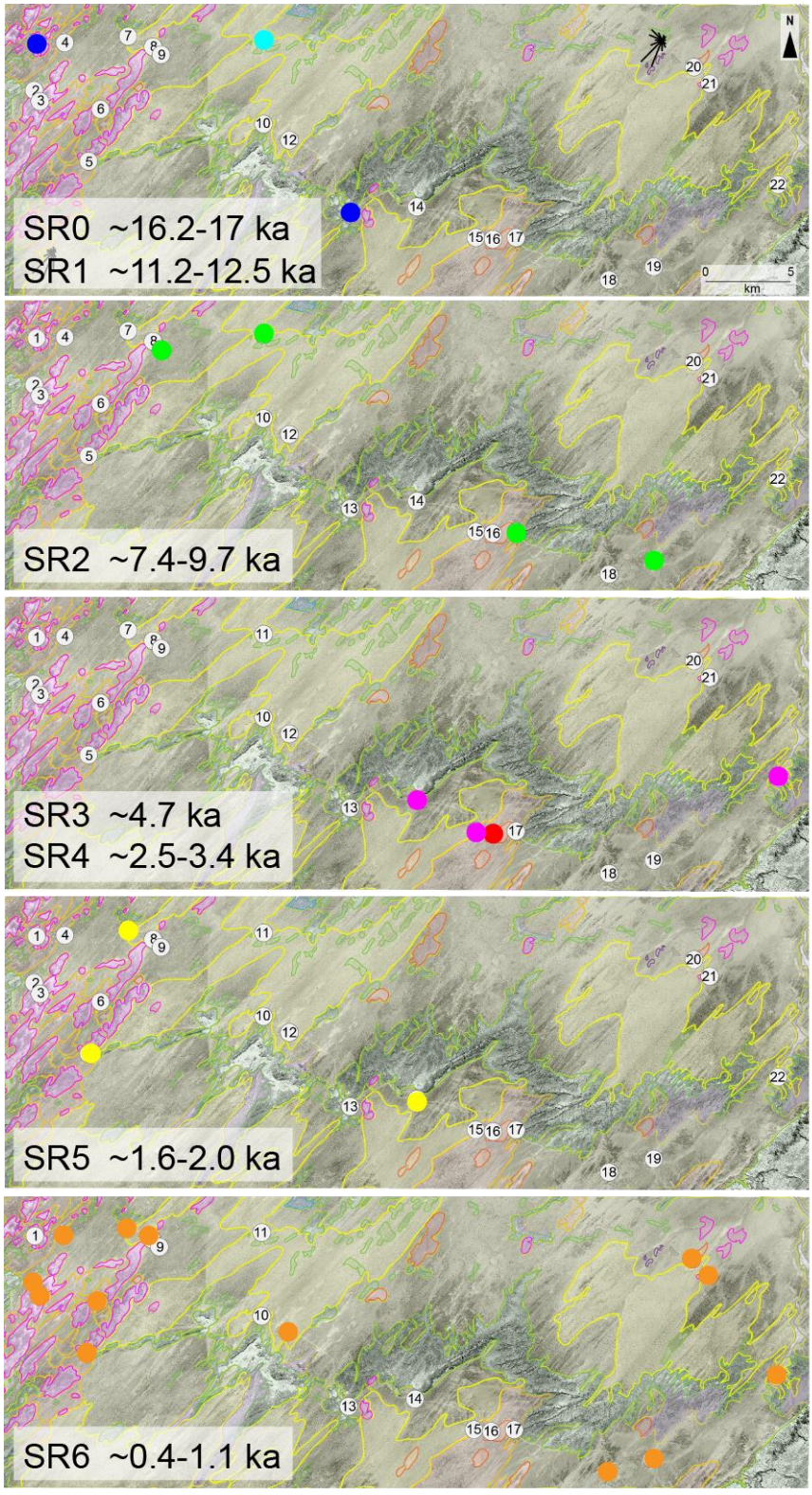

Figure 3.7. Spatial distribution of OSL ages, San Rafael dune field. Location of samples from individual dunes are shown for interpreted eolian events SR0, SR1, SR2, SR3, SR4, SR5 and SR6 to show spatial distribution within the dune field.

Eolian activity is broadly distributed across the study area, with some apparent spatial concentrations of different temporal groups. Sites from the northwestern corner (unit Qes1) (16.2±2.0 ka) and center (unit Qes1) (17.0±1.8 ka) of the dune field reveal late Pleistocene eolian activity, designated SR0. Preservation of stratigraphic records is inversely correlated with age, influenced by both geomorphic stasis and erosion (Sadler, 1981; Straub and Foreman, 2018). Given a relatively low preservation potential for Late Pleistocene eolian sediments in this highly erosive region with thin dune sediments, it seems likely these sites preserve deposits from more expansive eolian activity. However, they may simply reflect localized eolian activity in individual dunes captured in this study. The next younger period of dune activity, during the Greenlandian period (Walker et al, 2019) of the Holocene, SR1, is identified from a single site (11, Qes1) reporting sequential ages of eolian activity of (12.6±1.1 and 11.2±0.9 ka) separated by a millennium, located in the northcentral portion of the San Rafael project area (Figure 3.6). Decreased grain size and change in Munsell color above the lower sample (Appendix C) indicate discontinuity of eolian deposition between the lower and upper samples that define activity episode SR1. Additional sample sites might yield additional records of event SR1 but are less likely to be preserved than subsequent activity records (i.e., mid to late Holocene).

Evidence for late Greenlandian to Northgrippian (Walker et al, 2019) eolian activity (9.66±0.84 to 7.42±0.84 ka) was obtained at four individual dune sites distributed across the northcentral (map unit Qes1, sites 9, 11) and southwestern portions of the project area (map unit Qes1, site 19 and Qed1, site 17). These records are interpreted as widespread eolian activity in the field, extending ~2 millennia, identified as event SR2 (Figure 3.6). Stratigraphic evidence at site 11 between the middle (11.2 ±0.9 ka) and upper (9.66±0.84 ka) age sample documents a hiatus between SR1 and SR2 (Appendix C).

Evidence for a later mid-Holocene event (4.65±0.41 ka) is identified as SR3. It is located overlying a soil horizon at site 16 in map unit Qed2 in the southcentral project area (Figure 3.6) and is the only record obtained during a gap of ~4 kyr between events SR2 and SR4. SR3 is

denoted as an eolian event due to the extended temporal gap between these two events. Additional sampling would likely obtain additional records to further constrain this relatively young eolian activity, here identified in a single record although captured in other regional dune activity records (i.e., Wells et al, 1990; Reheis et al, 2005; Ford et al, 2010). Evidence for Meghalayan (early-late Holocene) (Walker et al, 2019) eolian activity, event SR4 (3.36±0.29 - 2.50±0.28 ka) is indicated by ages obtained at 3 sample sites. These sites are spatially distributed in map units Qes1 (site 14) and Qed2 (site 15) in the southcentral study area to map unit Qes1 in the west-central dune field project area (site 22) (Figure 3.6). Site 14 contains a vertical sequence with two ages (3.16±0.27 ka and 2.87±0.27 ka) indicating continuous eolian deposition.

Evidence for episode SR5 (1.96±0.25 to 1.57±0.15 ka) is supported by chronostratigraphy from three sites. These records are distributed in the west to central portions of the project area (map units Qed3 at site 7, Qes2 at site 5 and Qes1 at site 14) and are separated from SR4 by ~0.5 kyr, marking an interval of about 400 years of eolian activity (Figure 3.6). Evidence for a stratigraphic break between SR4 and SR5 is observed at site 14 with increased silt and change in Munsell color between the middle and upper age samples (Appendix C). The most recent eolian event, SR6, is identified in 17 eolian activity Meghalayan records (1.07±0.14 to 0.40±0.06 ka) at 14 sites (Figure 3.6). This episode is approximately 700 years long. Evidence of a stratigraphic break (depositional hiatus) between episodes SR5 and SR6 occurs at site 7, where increased silt and change in Munsell color are observed between the lower (SR5) and upper (SR6) age samples (Appendix C). The large numbers of deposits dated to this interval is likely due to the greater preservation potential of the more recent event.

Individual sites in the northwest SRDF provide evidence of early Pleistocene eolian activity ~17-16.2 ka identified as initial activation event SR0. A single site documents eolian activity at earliest Holocene (~12.6-11.2 ka), identified as SR1. Two eolian sediment packages are identified at this site (Appendix C). Holocene eolian events are identified as SR2 (~9.7-7.4 ka), SR4 (~3.4-2.5 ka), SR5 (~2-1.6 ka) and SR6 (~1.1-0.4 ka). One record obtained between

SR2 and SR4, an interval of ~4 ka, is denoted as SR3 (~4.7 ka) but is not interpreted as a full event. Periods lacking records of eolian activity in SRDF (this study) are ~16-12.5 ka, ~11-10 ka, ~7.4-5 ka, ~4.5-3.5 ka, ~2.5-2 ka and ~1.6-1.1 ka. Activity intervals decrease in duration through the Holocene from > 2 to ~0.7 ky. This study sought to focus on deeper time records, and restrict sediment sampling for age to depths ≥ 0.5 m. Modern dune activity was observed in the project area but is not linked with the latest Holocene event, SR6 in this study.

Of six Holocene eolian events identified, four (SR2, SR4, SR5 and SR6) are well constrained, millennial-scale events and are interpreted to reflect dune-field wide events at SRDF. Dune field-wide events, because of the aerial extent and number of dunes included, are more likely to reflect hydroclimate variability than eolian activity episodes identified in a single dune site within a dune field. Local conditions (i.e., fire or insect damage to vegetation) may act to destabilize an individual dune without initiating dune activation field-wide. However, the possibility that these dune field-wide events also reflect localized changes in hydroclimate, rather than a regional response, must be considered.

6.2 Eolian events in southern Utah dune fields

If dune activity episodes reflect a landscape response to hydroclimate (i.e., aridity) a reasonable expectation is that periods of eolian activity would be broadly coincident in dune fields within a physiographic region. The Kanab dune field (KDF), located southwest of SRDF and also part of the central Colorado Plateau region, was investigated using similar methods to this study. Five eolian events identified in KDF are compared to five Holocene eolian events identified in SRDF to evaluate common instances of temporally-shared dune activity. Interpreted eolian events for each field are shown in Figure 3.8.

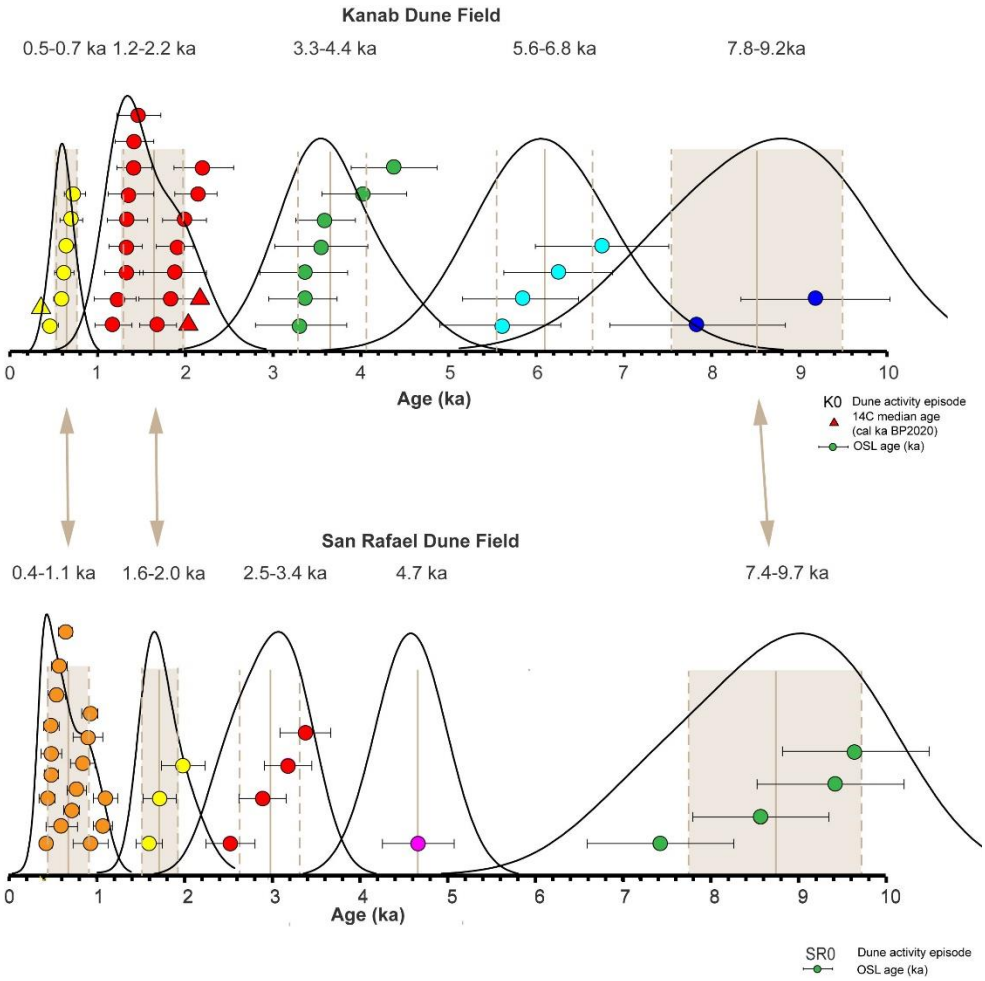

Figure 3.8. Holocene activity in Kanab and San Rafael dune fields. Individual records for eolian activity episodes in each dune field are plotted as dot-bar plots. Probability density function (PDF) plots are shown for each event that is constrained by chronostratigraphy, with mean (solid line) and standard deviation (dashed lines) are presented for each interval in each field. Three periods (shaded) likely reflect regional-scale periods of aridity, at ~7.5-9.5 ka, ~1.5-2 ka and ~0.5-1 ka. . Arrows indicate corresponding episodes of dune activity.

Individual eolian activity ages obtained from either OSL or ^{14}C dating are plotted, shown with probability density function (PDF) curves determined for each of the episodes. Temporal episodes were determined independently in each dune field, using similar analytical methods to determine the chronostratigraphic record of each dune field. That is, stratigraphic evidence was

used to identify breaks in dune activity between events (see Appendix C). The mean (solid line) and standard deviation (dashed lines) for each event is shown for both dune fields.

Overlap is apparent in many individual records between the dune fields, so clearly there are instances of concurrent individual dune activation in both dune fields throughout the past 10,000 years of the Holocene (0-10 ka). Individual dune activity, however, is not a useful index for coeval dune field-wide activity. The likelihood of dune field-wide activation is better represented by comparing the mean and standard deviation of each dune episode. There are three sets of episodes in which the mean (μ) and standard deviation (σ) values are closely aligned in the two dune fields (highlighted with orange shading, Figure 3.7). Co-eval events are suggested at SR2 (μ=8.76 kyr; σ=1.0 kyr) and K0 (μ=8.52 kyr; σ=0.95 kyr), SR5 (μ=1.74 kyr; σ=0.20 kyr) and K3 (μ=1.6 kyr; σ=0.34 kyr), and SR6 (μ=0.67 kyr; σ=0.22 kyr) and K4 (μ=0.62 kyr; σ=0.10 kyr). A confidence-interval test was used to compare the means of these paired events (Jaggia and Kelly, 2022). Results indicated that at a 95% confidence interval the means are statistically the same for events SR2 and K0, events SR5 and K3, and SR6 and K4. Thus, concurrent dune field-wide activation during these periods is likely.

Records of San Rafael dune activity during KDF event K1 (~5.6-6.8 ka) were not recovered in this study. Event K2 (~4.4-3.4 ka) is well documented in KDF, but is not matched by activity records in SRDF. The thinner dune deposits at SRDF seen in the stabilized parabolic and coppice dunes, as well as partially active and active parabolic dunes, reflect the highly erosive nature of the eolian activity in this dune field. Thicker sediments are observed only in active and partially active barchan dunes and barchanoid ridges. In contrast, thick parabolic dunes, some capped with coppice dunes, dominate KDF. Evidence of eolian activity in KDF is primarily surficial sand ripples less than a centimeter thick in most of the dune field. Much of KDF is stabilized with heavy vegetation, including abundant trees and large shrubs, while SRDF

is stabilized by biocrust and xeriphytic shrubs. In part these conditions reflect the cooler and drier mean annual climate in SRDF than KDF.

The overlap in age and number of records during three of the five events identified in each dune field, however, suggests both dune fields are likely responding to hydroclimate conditions during at least three periods, centered at ~ 8.6, 1.7 and 0.65 ka. In summary, comparison of SRDF and KDF records of eolian events suggest a millennial-scale, regional response to hydroclimate (i.e., aridity) during the early Holocene (~9-7 ka) and again during the late Holocene (~2-1.5 ka and ~1-0.5 ka). Events identified in this study likely reflect a lag from the actual onset of aridity in both dune fields. OSL ages are expected to reflect periods of greatest dune activation when packages of dune sediment are most fully mobilized. Further investigation of SRDF may be useful to better define the mid-Holocene record there and provide a more robust paleoclimate record.

6.3 Holocene hydroclimate in regional eolian records

To further assess the magnitude and regional extent of periods of Holocene eolian activity preserved in the San Rafael dune field, proximal regional studies of eolian activity were reviewed. Eolian records are shown, as well as suggested periods of dune activation reported for each study (Figure 3.9). Regional eolian events interpreted from this study are also indicated.

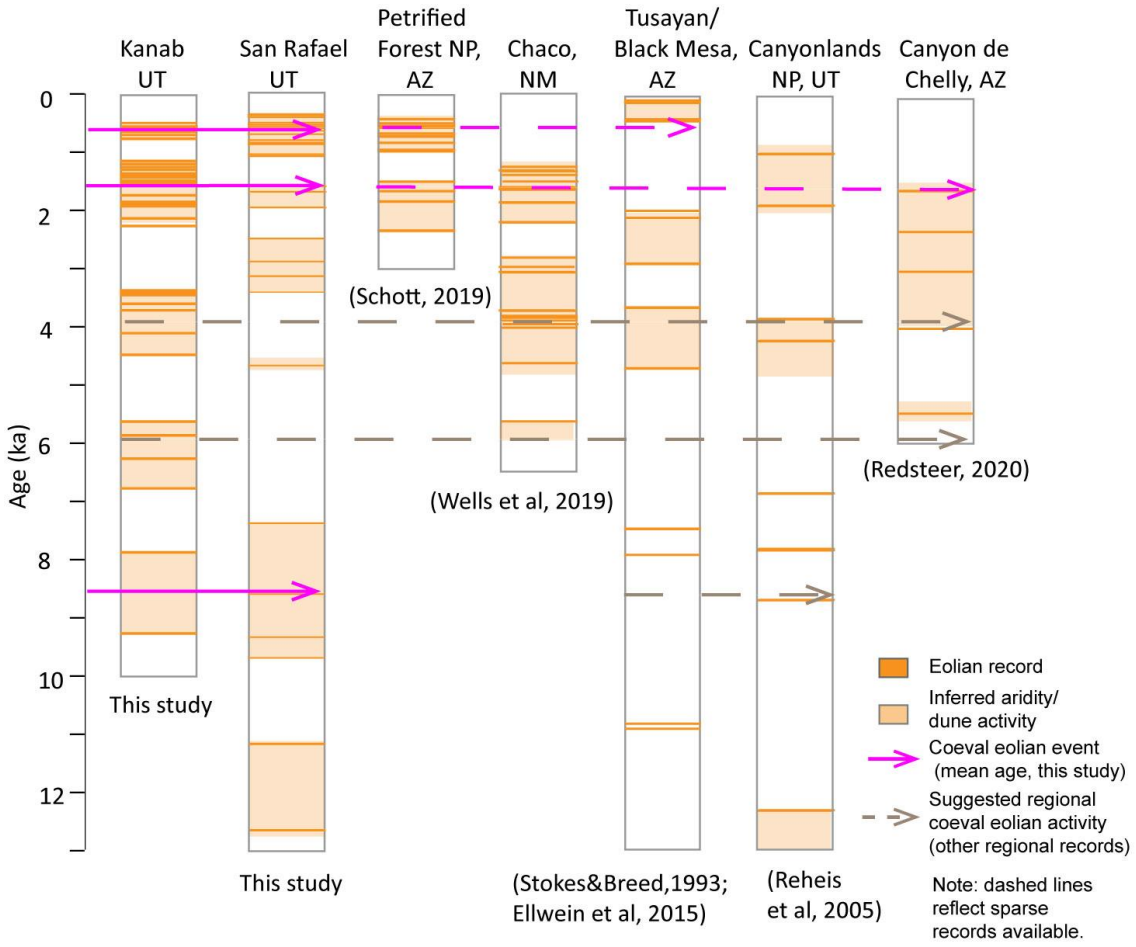

Figure 3.9. Selected eolian activity records. Mobile dune studies, Colorado Plateau and southwestern USA: Kanab dunes, UT (this study); San Rafael dunes, UT (this study); Canyonlands NP, UT (Reheis et al, 2005); Petrified Forest National Park (Schott et al, 2019); Canyon de Chelly (Redsteer, 2020); Chaco dune field (Wells, et al 1990); Tusayan dunes (Stokes and Breed, 1993) and Black Mesa dunes (Ellwein et al, 2015). Individual dune activity records and interpreted periods of aridity or dune activity are shown for each study. Solid arrows mark interpreted coeval eolian event (mean age of event shown, this study). Dashed arrows indicate suggested coeval eolian activity, from records of mobile dune activity at other Colorado Plateau locations.

Eolian activity in early Holocene, SRDF event SR2 (~ 9.7-7.4 ka) and KDF event K0 (~9.2-7.8 ka) is also reported in records between 10 and 7 ka ($n \leq 4$) in Canyonlands NP (Reheis et al, 2005) (Figure 3.8) and Black Mesa, AZ falling dunes (Ellwein et al, 2015) (Figure 3.9). Episodic eolian activity during wetter, cooler climate conditions were interpreted in the Canyonlands NP study, located approximately 60 km southeast of the project area (Reheis et al,

2005). In Black Mesa, researchers interpreted climate conditions likely favored dune stabilization, with episodic dune crest reworking, based on the concurrent records obtained at Polacca Wash dunes (Figure 3.8) (Ellwein et al, 2015). Chronostratigraphic records for SRDF and KDF both indicate decreasing fine sediment (silt and clay, with carbonaceous material) present during the earliest Holocene (≥ ~ 9 kyr). Younger sediments (≤ 9 kyr) are dominantly fine-medium (frosted) sand in both dune fields (Appendix C). This suggests that in southern Utah dune fields, hydroclimate conditions supported eolian activity during much of this interval. However, shifts of multi-decadal or greater duration in hydroclimate could have occurred during this period.

Evidence for early mid-Holocene eolian activity in San Rafael is limited to a single record at 4.7 ka, denoted as SR3, while regional records are more abundant. Records of dune activity (n≤4) occur in all other regional records (Kanab DF UT, Chaco dunes NM Tusayan and Black Mesa Dunes, Canyonlands NP, and Canyon de Chelly, AZ (Figure 3.9) except Petrified National Forest AZ which was preferentially sampled for records of dune farming during late Holocene. Limited record of eolian activity in SRDF during this time may be due to preservation bias. The consistency of records in Kanab and Chaco dune fields between ~ 4.5 and 3.4 ka suggest hydroclimate conditions supported continued eolian activity, however. Differences in the record preservation at individual dune fields may reflect spatial variability in threshold conditions (ie., winds, effective moisture and sediment supply) across the region. Such variability is likely, and has been reported elsewhere (i.e., Hesse and Simpson, 2006; Li and Yang, 2016; Hesse et al, 2017, Wolfe et al, 2017).

Eolian activity records at Canyon de Chelly, AZ (Redsteer, 2020), Chaco dune field, NM (Wells et al, 1990), and Tusayan dunes, AZ (Stokes and Breed, 1993) preserve records of dune activity coeval with eolian episode SR4 (~3.4-2.5 ka) in San Rafael dune field (Figure 3.9). However, records are sparse (n≤2) in all locations except Chaco dune field during this interval, which contains records compiled from multiple studies, primarily archaeological in focus.

Following a brief period of inferred stabilization, eolian activity resumes in SRDF at SR5 (~2-1.6 ka) and KDF at K3 (~2.2-1.2). A similar hiatus is reported at Chaco dune field (Wells et al, 1990). Eolian activity is documented (n≤4) in Canyonlands NP and Petrified Forest NP(Figure 3.8) . A final eolian activity episode, SR6 (~1.1-0.4 ka) in SRDF is widely distributed (n≤17), appears coeval with KDF event K4 (~0.7-0.5 ka) and records of eolian activity (n≤4) occur in Petrified National Forest, Arizona (Schott, 2019). Instances of dune activity in Tusayan dunes, Arizona (n=4) (Stokes and Breed, 1993) and Canyonlands NP (n=2) (Reheis et al, 2005) also fall within the SR6 period and were broadly interpreted in those studies as eolian activity that may extend into modern times. (Figure 3.9) Ongoing dune activity was observed at both San Rafael dune field and Kanab dune field during field investigations for the present study. Although the modern dune activity is suggestive, this study avoided sampling sediments likely to be modern. No samples younger than ~400 yr were obtained in either study dune field.

Records of dune activity from these sites on the Colorado Plateau support the interpretation of three episodes of regional eolian activity identified in this study of the Kanab and San Rafael dune fields in the central Colorado Plateau. Mean ages of these three episodes are ~8.6, 1.6, and 0.6 ka (Figure 3.9). Regional records also suggest regional eolian activity may have occurred during the K1 and K2 eolian episodes, ~6 and ~3.8 ka (Figure 3.9). The sparse number of available records is insufficient to constrain this eolian episode, but the coincidence of these records is acknowledged. If these suggested episodes were region-wide, it seems likely that additional records obtained through systematic approaches in these regional dune fields could constrain the temporal and spatial distribution of the activity.

6.4 Eolian activity records and dune morphology

Overlap between apparent dune stability or hiatal periods of dune activity with episodes of dune reactivation are evident in comparing these regional dune activity records. In addition to inherent sampling bias, dune morphology, as well as local physical conditions (i.e., relief, nature of vegetation, moisture conditions (P/PE)) can vary within dune fields. These factors may impact the eolian response of dune (or other source) sediments to changing threshold conditions (wind, soil moisture, sediment supply), which influence the local biogeomorphic response times to stabilize and to activate.

Dune morphology may affect preservation of eolian activity records. Falling dunes, for instance, such as in Canyon de Chelly and Black Mesa dunes, may contain a more complete record due to situational relief (i.e., less susceptible to erosion due to trapping in canyon or gully deposits) (Ellwein et al, 2015). Parabolic and barchan dunes may be more susceptible to destabilization and remobilization than coppice dunes, where soil formation may be enhanced, leading to increased moisture retention within the dune and increased resistance to destabilization (Redsteer, 2018; Halfen, 2016; Ellwein et al, 2015; Wolfe and Hugenholtz, 2005; and others).

In San Rafael dune field, seven eolian events were identified: SR0 (~17-16.2 ka), SR1 (~12.6-11.2 ka), SR2 (~ 9.7-7.4 ka), SR3 (~4.7 ka), SR4 (~3.4-2.5 ka), SR5 (~2-1.6 ka) and SR6 (~1.1-0.4 ka) (see Fig. 3.6 for temporal distribution and Fig. 3.7 for spatial distribution). Of these events, four are interpreted as dune-field-wide eolian events – SR2, SR4, SR5 and SR6. Event SR2 (early Holocene) records were distributed in three map units (Qes1, Qed1, Qed2) and three dune morphologies (two coppice dunes, one barchan dune and one parabolic dune). Event SR4 (mid-Holocene) records occurred in two map units (Qes1 and Qed2) and two dune morphologies, coppice and barchan. Event SR5 (late mid-Holocene) records are identified in three map units (Qes1, Qes2 and Qed3) and two dune morphologies (coppice and parabolic). Late Holocene dune activity event (SR6) records are widely distributed throughout the dune field, identified in all five eolian map units (Qes1, Qes2, Qed1, Qed2 and Qed3) and all dune morphologies (coppice, parabolic, linear (sand) ridge, and barchan).

Coppice dunes in SRDF are located in units Qes1 and Qes2. In addition to preserving records of these dune field-wide eolian events, early Holocene records (SR1) were preserved in coppice dunes. Vertical sample sequences in coppice dunes were collected at sites 5, 11, 14, and 22, from depths between 0.5 m and 2.20 m with age difference ranging from 1.05 ka to 2.96 ka, and contained records from SR1, SR2, SR4, SR5 and SR6 SRDF eolian events. These records suggest coppice dunes in SRDF may be preferentially aggradational, trapping eolian sands and preserving some of the oldest eolian activity records, rather than dominated by deflationary processes that are observed in SRDF crescentic dune deposits.

Late Pleistocene dune activity records also are preserved in unit Qes1, in a linear sand ridge below a soil layer(~ 0.95 m) and in unit Qed1 above a soil layer in a parabolic limb (~ 0.55 m). Units Qes1 and Qed1 were mapped as the oldest eolian and dune deposits respectively. The OSL ages support that geomorphic interpretation. The relatively shallow crests and thin dune deposits of the San Rafael dune field suggest a (sediment) supply-limited dune field that is highly erosive. Thin accretion layers found in the coppice dune chronostratigraphies also suggest a supply-limited dune field in SRDF (i.e., Hesp et al, 2021) (Appendix C – SM 3.1).

Eolian events identified as dune field-wide in Kanab dune field to the south and west are K1 (~6.8-5.6 ka), K2 (~4.4 – 3.3 ka), K3 (~2.2-1.2 ka) and K4 (~0.7-0.5 ka). These dune-field wide events are millennial in temporal spacing and reflect intervening periods of stability that are also approximately millennial in duration. All events in the Kanab dune field occur in parabolic dune morphologies. Records were obtained in generally thicker sequences of dune sediment that lacked visible evidence of soil development, in contrast to the typically thinner dune sediments of the parabolic and coppice dunes in SRDF (Appendix C). Several instances of vertically (temporally) continuous eolian activity in sediment samples separated by 1.0-1.5 m or more of sand, in spatially distinct dunes suggest whole dune migration within Kanab dune field. Evidence for limited sediment supply and preservation potential in San Rafael dune deposits contrasts with

an apparent ready source of sediment and greater record preservation of the millennial-scale eolian activity events observed in Kanab dune deposits.

Differences in initialization and cessation of dune field-wide events in San Rafael and Kanab may be related to differences in sediment supply and erosive processes reflected in the relative thickness and morphologies of stabilized (vegetated) dunes in each field. Differences in vegetation (amount, rate and continuity) are a potentially significant factor impacting biogeomorphic response in each dune field and, in turn, the absolute timing of eolian events in SRDF and KDF. Devegetation (destabilization) processes and timing impact sediment supply and susceptibility to erosion (Tsoar, 2005; Yizhaq and Ashkenazy, 2016; Hugenholtz and Barchyn, 2017). Although both dune fields are located in semi-arid climate regions, average annual precipitation and temperature conditions differ at the two fields. Precipitation at SRDF (144 mm) is less than half that of KDF (343 mm), and SRDF mean annual temperature is (12 ^{o}C) compared to KDF (21 ^{o}C) (this study, Ch. 2 and 3). Cooler, drier climate conditions are reflected in the different vegetative cover characteristic of each dune field. Lower effective moisture conditions at SRDF than KDF seen in modern instrumental records may reflect conditions seen throughout much of the Holocene, and, if so, may lead to the differential timing of dune field-wide activation in response to hydroclimate changes.

7.0 Conclusions

Sand dune records provide lower resolution paleoclimate records than some other sediment records, such as annual lake or speleothem deposits and are subject to biogeomorphic lag response to hydroclimate variability. However, sand dune deposits may also preserve records in regions lacking other paleoclimate records that extend the instrumental record into the

Holocene. Records of eolian activity records in SRDF were obtained by systematic investigation through geomorphic mapping to target representative sampling of the dune field.

Five eolian units were identified through geomorphic mapping. Thin parabolic dunes (Qed1 and Qed3), barchan dunes and barchanoid ridges (Qed2) are partially stabilized to active. Linear sand ridges and coppice (nebkha) dunes occur in two eolian sand sheet deposits (Qed1 and Qed2). Dunes are primarily stabilized with biocrust soil and xeriphytic vegetation. Dune morphology in SRDF is consistent with a sediment-limited, highly erosive eolian processes, and contrasts with KDF (see Ch. 2, this study) where thick parabolic dunes, stabilized with thicker vegetative cover and trees are predominant.

Multiple chronostratigraphic records obtained from individual sand dunes spatially distributed across the San Rafael dune field are used to identify seven millennial-scale eolian events (SR0, SR1, SR2 SR3, SR4, SR5 and SR6) from late Pleistocene through late Holocene. A tiered approach was used to identify eolian activity within individual dunes. Chronostratigraphy was developed to distinguish events. Stratigraphic breaks (hiatus or soil development) in eolian activity were identified using sediment analysis (grain size, chemistry and field observations) at each site. These records were then combined with site age records, obtained from OSL dating. Dune field-wide activation was interpreted using evidence of spatially distributed activity within the dune field for each chronostratigraphic unit. The full record includes late Pleistocene, SR0 (17.0±1.8 ka and 16.2±2.0 ka), Greenlandian, SR1 (12.6±1.1 ka and 11.2±0.9 ka), Northgrippian, SR2 (9.66±0.84-7.42±0.84 ka), Meghalayan, SR3 (4.65±0.41 ka) and SR4 (3.36±0.29-2.50±0.28 ka), and latest Holocene, SR5 (1.96±0.25 - 1.57±0.15 ka) and SR6 (1.07±0.14 - 0.04±0.06 ka) events.

Of five millennial events identified in Kanab dune field (KDF) using similar methods, three millennial eolian activity events in SRDF were determined to correspond statistically with three KDF events. Early Holocene eolian activity (~9-7 ka) is preserved in event K0 in KDF (two records) and in event SR2 in SRDF. Two events in each dune field during the late Holocene also

indicate coeval eolian activity. Events K3 (2.2-1.2 ka) and K4 (0.7-0.5 ka) in KDF coincide with events SR5 (2- 1.6 ka) and SR6 (1.1-0.4 ka) in SRDF. Differences in initiation and cessation of identified eolian events were recorded in the two dune fields.

Coincident, millennial-scale dune field-wide eolian activity is reported in San Rafael dune field, east-central Utah, and in Kanab dune field, southwest Utah, in early Holocene (~9-7 ka) and late Holocene (~2-1.6 ka and ~1-0.4 ka) with differences in onset and cessation of events observed. Eolian activity during these periods is likely to reflect a climate driver, rather than simultaneous influence by local forcing conditions. Hydroclimate conditions of prolonged periods of aridity likely occurred during these intervals. Spatial variability of onset and cessation of eolian events within each dune field is likely linked to climate zone variability and related local landscape processes and response. Reported records of dune activity suggest some coeval dune activity in other areas of the Colorado Plateau, with mean ages of ~ 8.6, 1.6 and 0.6 ka, concurrent with the three regional events identified in this study. Two additional periods of coeval eolian activity, suggested in other regional records, occur ~ 6 and ~3.8 ka. While important to acknowledge, additional records are needed to constrain these suggested regional episodes both temporally and spatially.

8.0 References

Aitken, M.J. 1998: An Introduction to Optical Dating: The dating of Quaternary sediments by the use of photon-stimulated luminescence. New York, Oxford University Press, 267 p.

Aitken, M.J., 1989. Luminescence dating: A guide for non-specialists. Archaeometry 31: 147-159

Aitken, M.J., 1983, (INVITED) Recent Advances in Thermoluminescence Dating, Radiation Protection Dosimetry, v. 6, i. 1-4, p. 181–183.

Aitken, M.J. and Alldred, J.C., 1972. The assessment of error limits in thermoluminescent dating. Archaeometry, 14(2), pp.257-267.

Allen, P.A., 2008. Time scales of tectonic landscapes and their sediment routing systems. Geological Society, London, Special Publications, 296(1), pp.7-28.

Arens, S.M. and Geelen, L.H.W.T., 2006. Dune landscape rejuvenation by intended destabilisation in the Amsterdam water supply dunes. Journal of coastal research, 22(5), pp.1094-1107.

Arens, S.M., Mulder, J.P., Slings, Q.L., Geelen, L.H. and Damsma, P., 2013. Dynamic dune management, integrating objectives of nature development and coastal safety: Examples from the Netherlands. Geomorphology, 199, pp.205-213.

Bagnold, RA, 1941. The physics of wind-blown sand and desert dunes. Methuen, London, 265 (10)

Bateman, M.D., Boulter, C.H., Carr, A.S., Frederick, C.D., Peter, D., Wilder, M., 2007. Detecting post-depositional sediment disturbance in sandy deposits using optical luminescence. Quat. Geochronol. 2, 57e64

Barchyn, T.E., and Hugenholtz, C.H., 2013, Reactivation of supply-limited dune fields from blowouts: A conceptual framework for state characterization: Geomorphology, v. 201, p. 172–182

Bøtter-Jensen, L., McKeever, S.W.S, and Wintle, A.G., 2003, Optically Stimulated Luminescence Dosimetry, Elsevier, 374 pp.

Bogle, R., Redsteer, M.H., and Vogel, J., 2015, Field measurement and analysis of climatic factors affecting dune mobility near Grand Falls on the Navajo Nation, southwestern United States: Geomorphology, v. 228

Bond, G., Showers, W., Cheseby, M., Lotti, R., Almasi, P., DeMenocal, P., Priore, P., Cullen, H., Hajdas, I. and Bonani, G., 1997, A pervasive millennial-scale cycle in North Atlantic Holocene and glacial climates. science, 278(5341), pp.1257-1266.

Bond, G., Kromer, B., Beer, J., Muscheler, R., Evans, M.N., Showers, W., Hoffmann, S., Lotti-Bond, R., Hajdas, I. and Bonani, G., 2001, Persistent solar influence on North Atlantic climate during the Holocene. Science, 294(5549), pp.2130-2136.

Bull, W.B., 1991, Geomorphic responses to climatic change.

Byers, D.A, 2013, The Dawson Site: A Paleoindian Camp in the San Rafael Desert. Utah Archaeologist, 25, 1-14.

Copeland, S.M., Bradford, J.B., Duniway, M.C. and Schuster, R.M., 2017. Potential impacts of overlapping land-use and climate in a sensitive dryland: a case study of the Colorado Plateau, USA. Ecosphere 8(5):K01823.10.1002/ecs2.1823

Cullinane Thomas, C., Koontz, L. and Cornachione, E., 2018. 2017 national park visitor spending effects: Economic contributions to local communities, states, and the nation. Natural Resource Report NPS/NRSS/EQD/NRR—2018/1616. National Park Service, Fort Collins, Colorado.

Davidson, D. W., Newmark, W. D., Sites, J. W., Shiozawa, D. K., Rickart, E. A., Harper, K. T., & Keiter, R. B., 1996. Selecting wilderness areas to conserve utah's biological diversity. The Great Basin Naturalist, 56(2), 95–118. http://www.jstor.org/stable/41716178

Doelling, H.H., Kuehne, P.A., Willis, G.C. and Ehler, J.B., 2015. Geologic map of the San Rafael Desert 30'x 60'quadrangle, Emery and Grand Counties, Utah. Utah Geological Survey.

Duller, G.A.T. 2008. Single-grain optical dating of Quaternary sediments: why aliquot size matters in luminescence dating. Boreas 37, 589–612

Duller, G.A.T., 2016, Challenges involved in obtaining luminescence ages for long records of aridity: Examples from the Arabian Peninsula: Quaternary International, v. 410, p. 69–74

Ellwein, A.L., Mahan, S.A. and McFadden, L.D., 2011, New optically stimulated luminescence ages provide evidence of MIS3 and MIS2 eolian activity on Black Mesa, northeastern Arizona, USA. Quaternary Research, 75(3), pp.395-398.

Ellwein, A.L, Mahan, S.A., and L. D. McFadden, 2015, Impacts of climate change on the formation and stability of late Quaternary sand sheets and falling dunes, Black Mesa region, southern Colorado Plateau, USA, Quaternary International 362 (2015) 87-107

Ellwein, A.L., McFadden, L.D., McAuliffe, J.A., and S.A. Mahan, 2018, Late Quaternary Soil Development Enhances Aeolian Landform Stability, Moenkopi Plateau, Southern Colorado Plateau, USA, Geosciences 2018, 8(5), p. 146

Finnegan, N.J., Schumer, R. and Finnegan, S., 2014. A signature of transience in bedrock river incision rates over timescales of 104–107 years. Nature, 505(7483), pp.391-394.

Fleck, J. and Castle, A., 2021. Green Light for Adaptive Policies on the Colorado River. Water, 14(1), p.2.

Folk, R.L., 1971, Longitudinal dunes of the northwestern edge of the Simpson desert, Northern Territory, Australia 1. Geomorphology and grain-size relationships. Sedimentology 16, 5-54

Forman, S.L., Oglesby, R., and Webb, R.S., 2001, Temporal and spatial patterns of Holocene dune activity on the Great Plains of North America: megadroughts and climate links: Global and Planetary Change, v. 29, p. 1–29

Forman, S.L.; Marin, L.; Gomez, J.; Pierson, J. 2008, Late Quaternary eolian sand depositional record for southwestern Kansas: Landscape sensitivity to droughts. Paleogeogr. Paleoclimatol. Paleoecol., 265,107–120.

Ford, R.L., Gilman, S.L., Wilkins, D.E., Clement, W.P. and Nicholl, K., 2010. Geology and Geomorphology of Coral Pink Sand Dunes State Park, Utah in Sprinkel, D.A, Chidsey, R.C. Jr., and Anderson, P.B., eds, Geology of Utah's Parks and Monuments, Utah Geological Association Publication 28 (3rd ed), p 371-398

Fossen, H., Schultz, R.A., and Torab, A., 2011, Conditions and implications for compaction band formation in the Navajo Sandstone, Utah, Journal of Structural Geology, v. 33: 10, pp. 1477-1490

Fryberger, S.G, 1979, Dune Forms and Wind Regimes. In A Study of Global Sand Seas; McKee, E.D., Ed.; U.S. Geological Survey: Reston, VA, USA, 1979; pp. 137–169

Fye, F.K., D.W. Stahle, and E.R. Cook, 2003: Paleoclimatic Analogs to Twentieth-Century Moisture Regimes Across the United States. Bull. Amer. Meteor. Soc., 84, 901–910

Galbraith, R.F. and Roberts, R.G., 2012. Statistical aspects of equivalent dose and error calculation and display in OSL dating: an overview and some recommendations. Quaternary Geochronology, 11, pp.1-27.

Glennie, K.W., 1970. Desert sedimentary environments. Developments in sedimentology, v. 14, 222 p., Amsterdam: Elsevier

Guérin, G., Mercier, N., and Adamiec, G., 2011, Dose-rate conversion factors: update, Ancient TL v. 29, n.1

Halfen, A.F., and Johnson, W.C., 2013, A review of Great Plains dune field chronologies: Aeolian Research, v. 10, p. 135–160

Halfen, A., Hesse, P., Roskin, J., Singhvi, A., Tsoar, H., Tripaldi, A., Yang, X., Zárate, M., 2016. The INQUA Dunes Atlas chronologic database, Quaternary International, v. 410, Part B, pp. 3-10

Halfen, A.F., Lancaster, N., Wolfe, S., 2016. Interpretations and common challenges in aeolian records from North American dune fields, Quaternary International, v. 410, 75-95.

Harris, J.G., 1983. A vascular flora of the San Rafael Swell, Utah. The Great Basin Naturalist, pp.79-87.

Hesp, P.A., Hernández-Calvento, L., Hernández-Cordero, A.I., Gallego-Fernández, J.B., Romero, L.G., da Silva, G.M. and Ruz, M.H., 2021. Nebkha development and sediment supply. Science of the Total Environment, 773, p.144815.

Hesse, P.P. and Simpson, R.L., 2006. Variable vegetation cover and episodic sand movement on longitudinal desert sand dunes. Geomorphology, 81(3-4), pp.276-291.

Hesse, P., 2016, How do longitudinal dunes respond to climate forcing? Insights from 25 years of luminescence dating in the Australian desert dunefields, Quaternary International, v. 410, 11-29

Hesse, P.P., Telfer, M.W. and Farebrother, W., 2017. Complexity confers stability: Climate variability, vegetation response and sand transport on longitudinal sand dunes in Australia's deserts. Aeolian research, 25, pp.45-61.

Hugenholtz, C.H., Wolfe, S.A., 2005a. Biogeomorphic model of dunefield activation and stabilization on the northern Great Plains. Geomorphology, 70(1), p 53-70.

Hugenholtz, C.H., Wolfe, S.A., 2005b. Recent stabilization of sand dunes on the Canadian prairies and relation to recent climate variations. Geomorphology, 68(2005), p 131-147.

Hugenholtz, C.H., Whitehead, K., Brown, O.W., Barchyn, T.E., Moorman, B.J., LeClair, A., Riddell, K. and Hamilton, T., 2013. Geomorphological mapping with a small unmanned

aircraft system (sUAS): Feature detection and accuracy assessment of a photogrammetrically-derived digital terrain model. Geomorphology, 194, pp.16-24.

Huntley, D.J., Godfrey-Smith, D.I., Thewalt, M.L.W., 1985. Optical dating of sediments. Nature 313: 105-107.

Kirby, M.E.C.; Patterson, W.P.; Lachniet, M.; Noblet, J.A.; Anderson, M.A.; Nichols, K.; and Avila, J., 2019, Pacific southwest United States Holocene droughts and pluvials inferred from sediment ^{18}O (calcite) and grain size data (Lake Elsinore, California), Frontiers Earth Sci. 7:74

Kocurek, G.; Lancaster, N., 1999, Aeolian system sediment state: Theory and Mojave Desert Kelso dune field example. Sedimentology, 46, 505–515.

Kocurek, G. and Ewing, R.C., 2005. Aeolian dune field self-organization–implications for the formation of simple versus complex dune-field patterns. Geomorphology, 72(1-4), pp.94-105.

Kocurek, G., Carr, M., Ewing, R., Havholm, K.G., Nagar, Y.C. and Singhvi, A.K., 2007. White Sands Dune Field, New Mexico: age, dune dynamics and recent accumulations. Sedimentary Geology, 197(3-4), pp.313-331.

Lancaster, N., 1988. Controls of eolian dune size and spacing. Geology, 16(11), pp.972-975.

Lancaster, N., 1992. Relations between dune generations in the Gran Desierto of Mexico. Sedimentology, 39(4), pp.631-644.

Lancaster, N., 1997, Response of eolian geomorphic systems to minor climate change: examples from the southern Californian deserts: Geomorphology, v. 19, p. 333–347

Lancaster, N., 2008, Desert dune dynamics and development: Insights from luminescence dating. Boreas, 37, 559–573.

Lancaster, N., Wolfe, S., Thomas, D., Bristow, C., Bubenzer, O., Burrough, S., Duller, G., Halfen, A., Hesse, P., Roskin, J., Singhvi, A., Tsoar, H., Tripaldi, A., Yang, X., Zárate, M., 2016, The INQUA Dunes Atlas chronologic database, Quaternary International, v. 410, Part B, pp. 3-10.

Li, H. and Yang, X., 2016, Spatial and temporal patterns of aeolian activities in the desert belt of northern China revealed by dune chronologies, Quaternary International, v. 410, 58-68

Li, X.R., Jia, X.H., Long, L.Q. and Zerbe, S., 2005. Effects of biological soil crusts on seed bank, germination and establishment of two annual plant species in the Tengger Desert (N China). Plant and soil, 277(1), pp.375-385.

Manning, J., 2010. OSL age information, Canyon de Chelly, Arizona, USGS-Flagstaff, NNLP, unpublished report, used with permission.

Mayer, J.H. and Mahan, S.A., 2004. Late Quaternary stratigraphy and geochronology of the western Killpecker Dunes, Wyoming, USA. Quaternary Research, 61(1), pp.72-84.

Metcalfe, S.E., Barron, J.A., Davies, S.J., 2015. The Holocene history of the North American Monsoon: 'known knowns' and 'known unknowns' in understanding its spatial and temporal complexity, Quaternary Science Reviews, v. 120, pp. 1-27

Muhs, D.R., 1985. Age and paleoclimatic significance of Holocene sand dunes in northeastern Colorado. Annals of the Association of American Geographers, 75(4), pp.566-582.

Muhs, D.R., Holliday, V.T., 1995. Evidence of active dune sand on the Great Plains in the 19th century from accounts of early explorers. Quat. Res., 43, 198–208

Muhs, D.R. and Maat, P.B., 1993. The potential response of eolian sands to greenhouse warming and precipitation reduction on the Great Plains of the USA, Journal of Arid Environments 25: 351-361.

Murray, A.S. and Wintle, A.G., 2000. Luminescence dating of quartz using an improved single-aliquot regenerative-dose protocol. Radiation measurements, 32(1), pp.57-73.

Nelson, M.S., Gray, H.J., Johnson, J.A., Rittenour, T.M., Feathers, J.K., and Mahan, S.A., 2015. User guide for luminescence sampling in archaeological and geological contexts, Advances in Archaeological Practice 3(2), 2015, pp. 166–177

Nelson, M., Rittenour, T. and Cornachione, H., 2019. Sampling methods for luminescence dating of subsurface deposits from cores. Methods and Protocols, 2(4), p.88.

Nield, J.M. and Baas, A.C., 2008. The influence of different environmental and climatic conditions on vegetated aeolian dune landscape development and response. Global and Planetary Change, 64(1-2), pp.76-92.

Overpeck, J.T. and Udall, B., 2020. Climate change and the aridification of North America. Proceedings of the national academy of sciences, 117(22), pp.11856-11858.

Prescott, J.R. and Hutton, J.T., 1994, Cosmic ray contributions to dose rates for luminescence and ESR dating: large depths and long-term time variations, Radiation Measurements, v. 23: 2–3, pp. 497-500

Redsteer, M. H., 2020, Sand Dunes, Modern and Ancient, on Southern Colorado Plateau Tribal Lands, Southwestern USA in Inland Dunes of North America ed. by Lancaster, N. and Hesp, P., pp. 287 – 310.

Reheis, M.C.; Reynolds, R.L.; Goldstein, H.; Roberts, H.M.; Yount, J.C.; Axford, Y.; Cummings, L.S.; Shearin, N., 2005, Late Quaternary eolian and alluvial response to paleoclimate, Canyonlands, southeastern Utah. GSA Bull., 117, 1051–1069

Reheis, M.C., Goldstein, H.L., Reynolds, R.L., Forman, S.L., Mahan, S.A. and Carrara, P.E., 2018. Late Quaternary loess and soils on uplands in the Canyonlands and Mesa Verde areas, Utah and Colorado. Quaternary Research, 89(3), pp.718-738.

Rhodes, E.J., 2011. Optically Stimulated Luminescence Dating of Sediments over the Past 200,000 Years, Annu. Rev. Earth Planet. Sci. 2011. 39:461–88

Rich, J., Rittenour, T.M., Nelson, M.S. and Owen, J., 2015. OSL chronology of middle to late Holocene aeolian activity in the St. Anthony dune field, southeastern Idaho, USA. Quaternary International, 362, pp.77-86.

Rink., W.J., Dunbar, J.S., Tschinkel, W.R., Kwapich, C., Repp, A., Stanton, W., Thulman, D., 2013. Subterranean transport and deposition of quartz by ants in sandy sites relevant to age overestimation in optical luminescence dating. Journal of Archaeological Science, 40: 2217-2226

Sadler, P.M., 1981. Sediment accumulation rates and the completeness of stratigraphic sections. The Journal of Geology, 89(5), pp.569-584.

Schott, A.F., 2019, Eolian Landscape History and Prehistoric Dune Farming in Petrified Forest National Park: A Geoarchaeological Approach to Understanding the Long-Term Use of a Marginal Landscape, downloaded, 10/30/2020, http://hdl.handle.net/10150/634273.

Schwinning, S., Belnap, J., Bowling, D.R. and Ehleringer, J.R., 2008. Sensitivity of the Colorado Plateau to change: climate, ecosystems, and society. Ecology and Society, 13(2).

Soil Survey Staff, Natural Resources Conservation Service, United States Department of Agriculture. Web Soil Survey. Available online at the following link: http://websoilsurvey.sc.egov.usda.gov/. Accessed [April/26/2021].

Steponaitis, E., Andrews, A., McGee, D., Quade, J., Hsieh, Y.T., Broecker, W.S., Shuman, B.N., Burns, S.J. and Cheng, H., 2015. Mid-Holocene drying of the US Great Basin recorded in Nevada speleothems. Quaternary Science Reviews, 127, pp.174-185.

Stokes, S.; Breed, C.S., 1993 A chronostratigraphic re-evaluation of the Tusayan Dunes, Moenkopi Plateau and southern Ward Terrace, northeastern Arizona. In The dynamics and Environmental Context of Aeolian Sedimentary Systems; Pye, K., Ed.; Geological Society: London, UK, 75–90

Tsoar, H., 2005. Sand dunes mobility and stability in relation to climate, Physica A: Statistical Mechanics and its Applications, v. 357 (1), pp. 50-56

Tsoar, H., Levin, N., Porat, N., Maia, L.P., Herrmann, H.J., Tatumi, S.H., and Claudino-Sales, V., 2009, The effect of climate change on the mobility and stability of coastal sand dunes in Ceará State (NE Brazil): Quaternary Research, v. 71, p. 217–226

Udall, B. and Overpeck, J., 2017. The twenty-first century Colorado River hot drought and implications for the future. Water Resources Research, 53(3), pp.2404-2418.

U.S. Bureau of Land Management, 2020, Site Visitor Satisfaction Survey 2019, https://www.blm.gov/policy/ib-2020-004

Vano, J.A., Udall, B., Cayan, D.R., Overpeck, J.T., Brekke, L.D., Das, T., Hartmann, H.C., Hidalgo, H.G., Hoerling, M., McCabe, G.J. and Morino, K., 2014. Understanding uncertainties in future Colorado River streamflow. Bulletin of the American Meteorological Society, 95(1), pp.59-78.

Viles, H.M., Naylor, L.A., Carter, N.E.A., Chaput, D., 2008, Biogeomorphological disturbance regimes: progress in linking ecological and geomorphological systems, Earth Surf. Process. Landforms 33, 1419-1435.

Wells, S.G., McFadden, L.D. and Schultz, J.D., 1990. Eolian landscape evolution and soil formation in the Chaco dune field, southern Colorado Plateau, New Mexico. In: P.L.K. Knuepfer and L.D. McFadden (Editors), Soils and Landscape Evolution. Geomorphology, 3:517-545.

Williams, A.P., Cook, B.I. and Smerdon, J.E., 2022. Rapid intensification of the emerging southwestern North American megadrought in 2020–2021. Nature Climate Change, 12(3), pp.232-234.

Wintle, A.G., 1997. Luminescence dating: laboratory procedures and protocols. Radiation measurements, 27(5-6), pp.769-817.

Murray, A.S. and Wintle, A.G., 2000. Luminescence dating of quartz using an improved single-aliquot regenerative-dose protocol. Radiation measurements, 32(1), pp.57-73.

Wintle, A.G. and Murray, A.S., 2006. A review of quartz optically stimulated luminescence characteristics and their relevance in single-aliquot regeneration dating protocols. Radiation measurements, 41(4), pp.369-391.

Wolfe, S.A., Huntley, D.J., David, P.P., Ollerhead, J., Sauchyn, D.J. and MacDonald, G.M., 2001. Late 18th century drought-induced sand dune activity, Great Sand Hills, Saskatchewan. Canadian Journal of Earth Sciences, 38(1), pp.105-117.

Wolfe, S.A. and Hugenholtz, C.H., 2009. Barchan dunes stabilized under recent climate warming on the northern Great Plains. Geology, 37(11), pp.1039-1042.

Wolfe, S.A., Lian, O.B., Hugenholtz, C.H. and Riches, J.R., 2017. Holocene eolian sand deposition linked to climatic variability, Northern Great Plains, Canada. The Holocene, 27(4), pp.579-593.

Xu, Z., Mason, J.A., Xu, C., Yi, S., Bathiany, S., Yizhaq, H., Zhou, Y., Cheng, J., Holmgren, M. and Lu, H., 2020. Critical transitions in Chinese dunes during the past 12,000 years. Science advances, 6(9), p.eaay8020.

Yizhaq, H. and Ashkenazy, Y., 2016, Periodic temporal oscillations in biocrust–vegetation dynamics on sand dunes, Aeolian Research, v. 20, pp. 35-44

CHAPTER 4

WIND AND GEOCHEMICAL DATA FROM THE KANAB AND SAN RAFAEL DUNE FIELDS

Abstract

Anemometer records from portable MesoWest climate stations in southern Utah were examined to determine wind regime with respect to eolian transport potential. Results were compared with dune orientation in two dune fields based on aerial imagery and suggest that modern wind records from these local stations provide a useful analog for Holocene winds.

Dune sediment and source rock geochemical records were evaluated using a simple and inexpensive method described by Muhs (2017). Ratios of K/Rb-K/Ba from feldspar grains in dune sediments have been used to distinguish the dune sediment provenance from potential source deposits. Selected sediment samples from each eolian event identified in Kanab (Chapter 2) and San Rafael (Chapter 3) dune fields were analyzed for temporal trends of K/Rb-K/Ba in the dune sediment to investigate source rock through time and geochemistry from all available dune field samples was also analyzed to determine statistically significant correlations within the data.

K/Rb-K/Ba values suggest provenance material for the Kanab dune field is sourced from the Jurassic Navajo Formation. The values in the dune sediment do not suggest a change in provenance through the Holocene time nor correlate statistically with eolian events. Sediment samples from the San Rafael dune field do not indicate any pattern linked to eolian events in the dune field. Values of K/Rb-K/Ba weakly overlap between the dune sediment and provenance material from the Jurassic Entrada Fm. A larger set of samples both of dune sediment and potential source material would be needed to clearly define the relationship between dune

sediments and source material using this method. The lack of change in source sediment supports a climate driver for eolian events.

1.0 Background

Sand dunes are a threshold geomorphic landform, with the potential to archive records of past climate conditions. Early studies of desert sand dunes identified three threshold properties that constrain sand dune mobility –adequate wind strength to entrain sand-sized particles (>6m/s), low soil moisture (< 0.4%) and available (loose) sediment supply (Bagnold, 1941; Logie, 1982). Analyzing wind regimes, and understanding the role of effective moisture is crucial to understanding the complex biogeomorphic responses of dunes to climate perturbations, observed as adjacent active and stabilized dunes in the Great Plains, Colorado Plateau and Great Basin dune fields (e.g., Barchan and Hugenholtz, 2013; Bogle et al, 2015; Lancaster, 2020; Lancaster and Hesp, 2020; Redsteer, 2020).

A useful tool to analyze wind regimes calculates sand transport (drift) potential (DP) by winds exceeding threshold velocity, described by Fryberger (1979). Wind analysis in the Great Basin linked late winter and spring-dominated cold fronts and extra-tropical cyclones to maximum DP using the Fryberger method, demonstrating the impact of seasonality on the role of wind in sand mobility (Jewell and Nicholl, 2011).

The state of dune stability, recognized as the amount of stabilizing vegetation on dunes, has also been linked to effective moisture, defined as the ratio of precipitation (P) to annual potential evaporation (PE) conditions (Lancaster, 1988). For regions with abundant winds capable of sand transport, P/PE may be a controlling factor of dune mobility (Lancaster, 1997, Tsoar, 2005; Barchyn and Hugenholtz, 2015; Redsteer, 2020). Dunes and dune fields on the southern Colorado Plateau were reported as approaching or exceeding observed effective moisture (P/PE) thresholds for mobility of 0.125 (Muhs and Holliday, 1995; Redsteer, 2020).

Available (loose) sediment supply is controlled by the amount and type of vegetation or other cover on sand dunes (i.e., Bagnold, 1941; Logie, 1982; Lancaster, 1988; Muhs and Holliday, 1995; Lancaster and Helm, 2000; Barchyn and Hugenholtz, 2015). In addition to sediment within the dune field, alluvial and playa systems can supply sediment to form dunes on the Colorado Plateau (Lancaster, 1997; Muhs, 2017; Redsteer, 2020). Bedrock erosion is also a significant sediment source. Rock strength is a first-order control on relief in fluvial systems (Sklar and Dietrich, 2001). Recent work suggests high rates of erosion from retreating escarpments during Holocene can be coupled with limited discharge rates to generate significant sediment supply (Riley et al, 2019).

Comparing the geochemistry of dune sediments to different potential sediment sources, previously detected through wind analysis, has allowed researchers to distinguish sediment sources for specific dune fields (i.e., Frahlick and Kronberg, 1997; Arbogast and Muhs, 2000; Muhs et al 2003; Muhs et al 2008; Liu and Wang, 2018; Chen et al, 2021). Muhs (2017) found K/Rb and K/Ba to be a robust indicator in sediment provenance studies that is inexpensive with reproducible results. Importantly, this method avoids introduction of bias from use of individual element concentrations that are subject to temporal change due to mineralogical maturity changes in dune field chemistry over time.

The primary objectives of this study are to examine the modern wind regime in comparison to the Holocene geomorphic record of dune orientation and to identify geochemical changes that have occurred during the Holocene in the study dune fields that may reflect temporal or spatial changes in sediment source.

2.0 Wind Analysis

2.1 Wind Records and Methods

To investigate wind regime, modern wind records from MesoWest climate stations were obtained from the Utah Climate Center for stations in southern Utah located near the Kanab and San Rafael dune fields and analyzed for (sand) drift potential (DP) and resultant drift direction (RDD). Results are compared to observed Holocene dune and dune field orientations from aerial imagery. Ten stations were identified for this study, based on proximity to the study sites of Kanab and San Rafael dune fields and a minimum continuous period of record of 10 years (Figure 4.1). Maximum length of record is 22 years, from 1997 – 2019, at the Buck Flat (BUKU1) and Canyonlands Field (KCNY) stations. All stations used a standard 10-m anemometer reference elevation wind velocity. For this study, number of records included all records with a measurement value ≥ 0. Calm periods were calculated using the "0" measurement. Record periods without a measurement were not used in the determination of time.

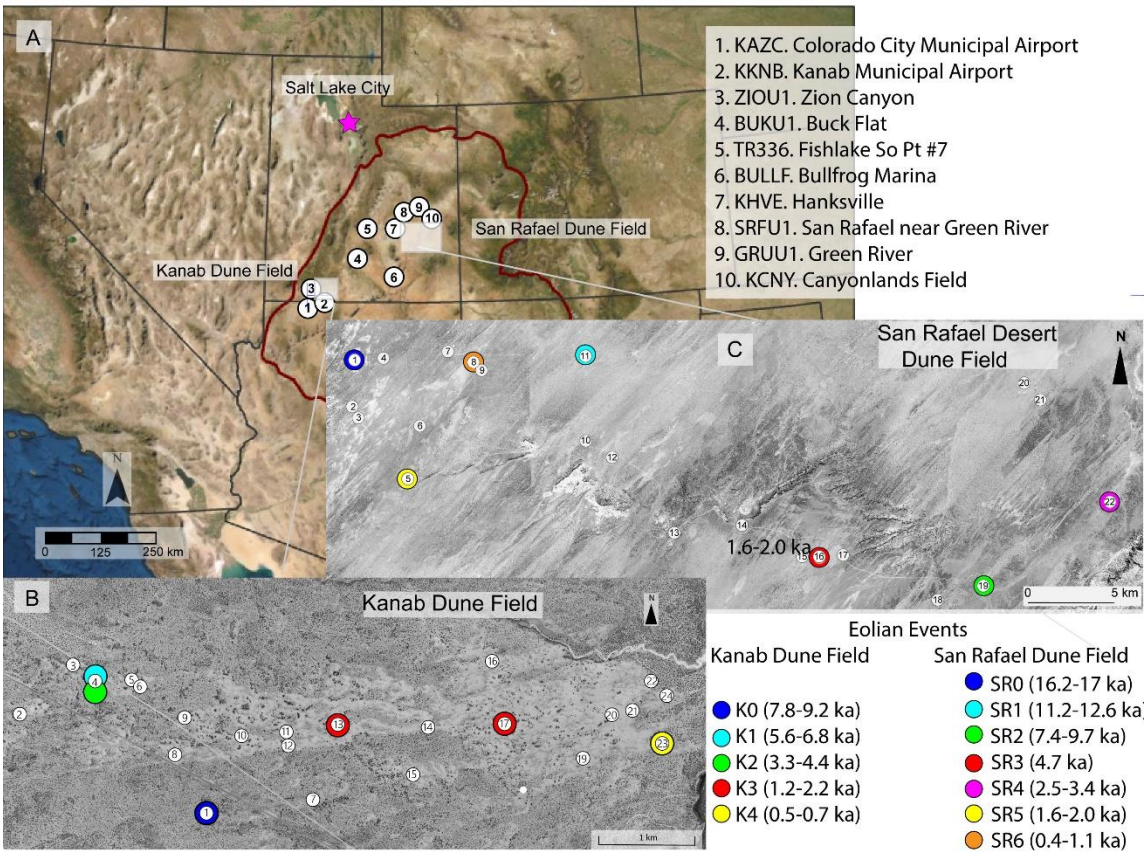

Figure 4.1 Project location map (A) – shows Kanab (KDF) and San Rafael dune field (SRDF) study areas in southwest and southeast Utah, within the central Colorado Plateau (brown outline). MesoWest wind stations are located (numbered white circles) and identified in the key (right side bar). Detailed locations and wind data are in Appendix G. Left inset image (B) shows expanded view of the Kanab DF project site. Right inset image (C) shows expanded view of San Rafael DF project area. Geochemistry sample locations are shown as colored, numbered circles representing different Holocene eolian events identified in site age sample. Key to eolian events is in lower right panel.

Sand drift potential was determined following the methods of Fryberger and Dean (1979). They defined the sand-moving capacity of wind as drift potential (DP), based on relative amount of sand migration produced by a wind velocity measured at standard height of 10 m, determined for 16 standard compass-based wind directions. This relationship is shown in Equation 1, below

$$DP = \sum q = \frac{u^2(u-u_t)}{100} t \qquad \text{(Eq 1)}$$

where DP is drift potential, q is the rate of sand drift, u is wind velocity (knots), u_t is threshold velocity (knots) and t is percent of time wind blew above threshold velocity (%) (Fryberger, 1979; Tsoar, 2005). Time and relative time for binned wind for compass direction is determined using the total number of records (counts) and number of records in each wind (compass) bin to determine relative time threshold winds were met or exceeded in each directional category. Sixteen (16) standard compass directions are used in the standard Fryberger method, and only winds between 11 and 40 knots are considered (Fryberger, 1979). Drift potential (DP) is calculated using units of knots for wind velocity, converted from the original MesoWest station wind records which are reported in either SI or British units. Wind speed in knots was used to ensure results are comparable with other studies (i.e., Bullard, 1997; Lancaster et al, 1997; Saqqua and Atallah, 2004; Wang et al, 2006; Jewell and Nicholl, 2011). Values over 40 knots are rare wind events, and introduce a significant skew that incorrectly weights those wind strengths, so were omitted from the drift potential calculations (Fryberger, 1979; Bullard, 1996; Allen, 1993). Drift potential is considered low for DP < 200, intermediate for 200 ≤ DP ≤ 400 and high for DP > 400. (Fryberger, 1979). Drift potential, rather than wind velocity, may better reflect conditions during dune activations, since vegetation cannot establish when sand is entrained (Siegal, 2013).

In addition to drift potential, resultant drift direction (RDD) and resultant drift potential (RDP) are determined for each wind station. RDD is the directional component of the vector sum of drift potential in each of the sixteen compass directions, and RDP is the magnitude of that vector sum. RDD expresses the net sand drift expected from these different winds, reported 180^{o} from the direction of the resultant vector sum to indicate the downwind direction of sand transport. Results of the wind calculations are typically diagrammed as a sand rose diagram. Sand rose diagrams are radial plots that display the drift potential as arms projecting radially from a unit circle, proportioned according to the DP magnitude binned to compass direction. The RDD is

plotted as an arrow, which points in the direction of net sand transport. The RDP is scaled as needed for reasonable map display, with scale factor reported on map.

2.2 Dune orientation and methods

Records of dune orientations in each dune field were obtained from aerial imagery for comparison with modern wind records of drift potential. Sites were selected to represent multiple examples from each mapped dune unit, and to be distributed spatially throughout each dune field. Dune orientations were measured axially, extending the line of measurement through the nose of the dune for parabolic dunes. For barchanoid ridges, the measurement was oriented perpendicular to the dune forms. For barchan dunes measurement extended centrally between the arms from the midpoint of the dune crest.

The dune orientation measurement dataset for Kanab dune field is comprised of seven sites, representing the four mapped dune units, Qed1, Qed2, Qed3 and Qed4 (Figure 4.2). All are parabolic dune forms, which appear to young eastward (downwind) (see Ch. 2, this study). Orientations are consistently northeast, ranging from 63-83^{o}NE, with a mean of 75 ^{o}NE. Resultant drift direction at the nearest wind station is 88 ^{o}NE, measured at Kanab Municipal Airport (KKNB), located approximately 13 km south of the dune field.

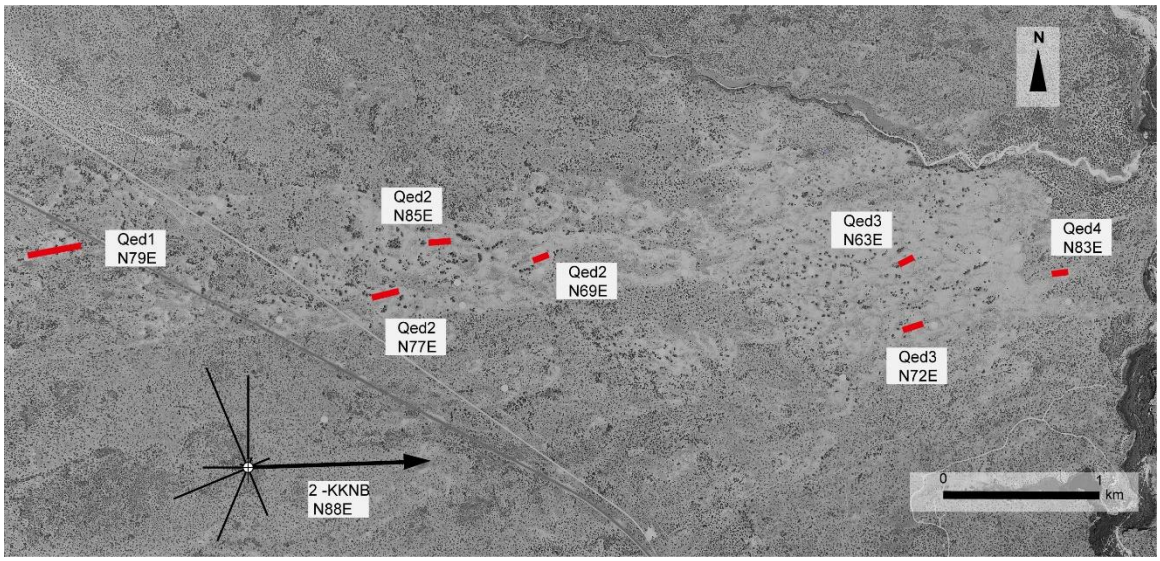

Figure 4.2. Dune orientation map, Kanab dune field. MesoWest wind station *2*-KKNB is plotted for reference, as the nearest station to the dune field. Actual location is south and west of the dune field (see Figure 4.1and Appendix G). Dune orientation measurement segments are shown in red, labelled with geomorphic map unit and bearing. Four dune units are mapped in Kanab dune field – Qed1, stabilized parabolic dunes, Qed2 – stabilized long parabolic dunes, Qed3, partially stabilized short parabolic dunes, Qed4 – partially active parabolic dunes

The San Rafael dune field geomorphic map includes three dune units, Qed1 (older) and Qed3 (younger) comprised primarily of stable and partially active to active parabolic dunes and Qed2, mapped as partially stabilized to active barchan dunes and transverse ridges. These mobile dunes are distributed throughout the project area with concentrations in the northwest, south central and northeastern portions. Bedrock exposures cross the central dune field and eolian sand sheets flank and overlap the bedrock. Dune units flank and overlie areas of lower relief (ie., valleys, arroyos, gullies) and are interspersed across the area with eolian sand sheets. Ten sites were selected to record dune orientations, representing the three mobile dune map units (Figure 4.3). Dunes are oriented downwind to the northeast, measuring 40-43^{o}NE, with a mean of 42^{o}NE. Resultant drift direction at the Hanksville weather station (KHVE) is 57^{o}NE, and at San Rafael at Green River (SRFU1) it is 34^{o}NE. KHVE is approximately 15 km southwest of the project area,

and SRFU1 is located about 20 km north of the dune field, with both stations on the western side of San Rafael dune field.

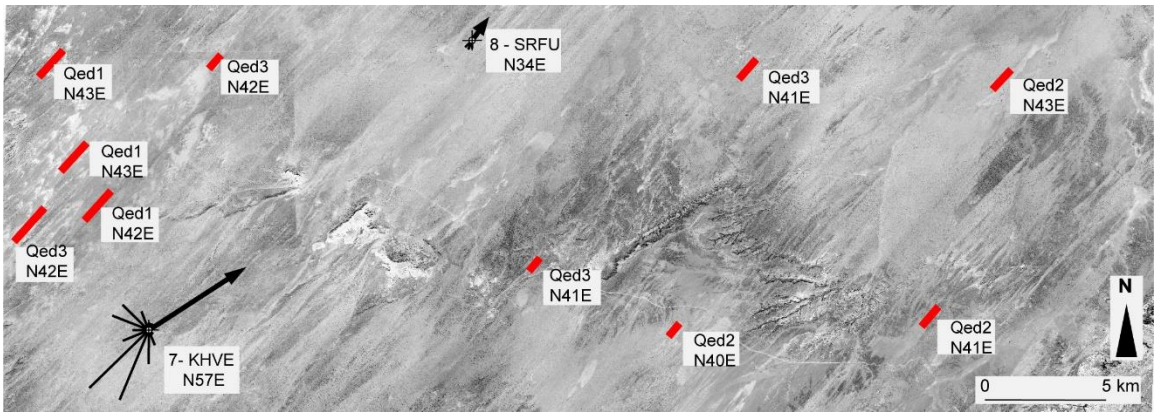

Figure 4.3. Dune orientation map, San Rafael dune field. MesoWest wind stations 7 – KHVE and 8 - SRFU are plotted for reference, as the nearest stations to the dune field. Actual location of KHVE is at Hanksville ~15 km southwest of the dune field and SRFU is near the San Rafael River about 25 km northwest (Figure 4.1). Dune orientation measurement segments are shown in red, labelled with geomorphic map unit and bearing. Three dune units are mapped in San Rafael, Qed1 – stabilized parabolic dunes, Qed2 – active or partially active barchan dunes and barchanoid ridges, and Qed 3 – active and partially active parabolic dunes

2.3 Wind summary

Station identification, location, period of record, number of records, and number of records exceeding threshold value of 6 m/s (11 knots) are provided in Table 4.1 (see Figure 4.1). Values for drift potential (DP), resultant drift potential (RDP), resultant drift direction (RDD) and the ratio of RDP/DP are also reported in Table 4.1 for each station. The ratio RDP/DP is a measure of the relative uniformity of winds capable of sand transport. Lower values of RDP/DP indicate greater directional variability for threshold winds. Sand rose diagrams for the study wind stations are plotted in Figure 4.4. Arrows mark the expected net sand transport direction (RDD) for each of the MesoWest stations. The RDD value at each station provides a comparison between observed / measured dune orientations (late Pleistocene to Holocene) and modern threshold winds (Figure 4.4). Significant deviations suggest that changes to threshold winds and drift potential have occurred through time.

Table 4.1 Summary of wind records. Results of drift potential calculations (methods after: Fryberger, 1979; calculations: dunes.py, Buie, 2021) (data source: MesoWest climate records, Utah Climate Center, M. Schroeder, 2019). Station locations are in Figure 4.1 and additional wind records are in Appendix G.

ID	Station Name	Record Period	Total Counts	Counts (>6m/s)	%	RDP *(vu)*	RDD *(° N)*	RDP/DP	DP *(vu)*
1	KAZC	2002-2019	125009	44603	35.7	600.9	74.8	0.4	1502
2	**KKNB**	**2003-2019**	**106184**	**51167**	**48.2**	**550**	**87.7**	**0.3**	**1833**
3	ZIOU1	2002-2019	135463	68514	50.6	2033.1	181.7	0.9	2259
4	BUKU1	1997-2019	162282	7298	4.5	5.7	1.3	0.2	29
5	TR336	2001-2013	32206	4401	13.7	72	137.9	0.4	180
6	BULLF	2003-2019	511378	137502	26.9	395.9	67.4	0.3	1320
7	**KHVE**	**2009-2019**	**132378**	**37476**	**28.3**	**1084.8**	**56.9**	**0.6**	**1808**
8	**SRFU1**	**2000-2019**	**263853**	**26431**	**10.0**	**135.1**	**34.2**	**0.7**	**193**
9	GRUU1	2008-2019	315010	44713	14.2	200.2	85.2	0.4	501
10	KCNY	1997-2019	423011	172738	40.8	1109.7	58.5	0.5	2219

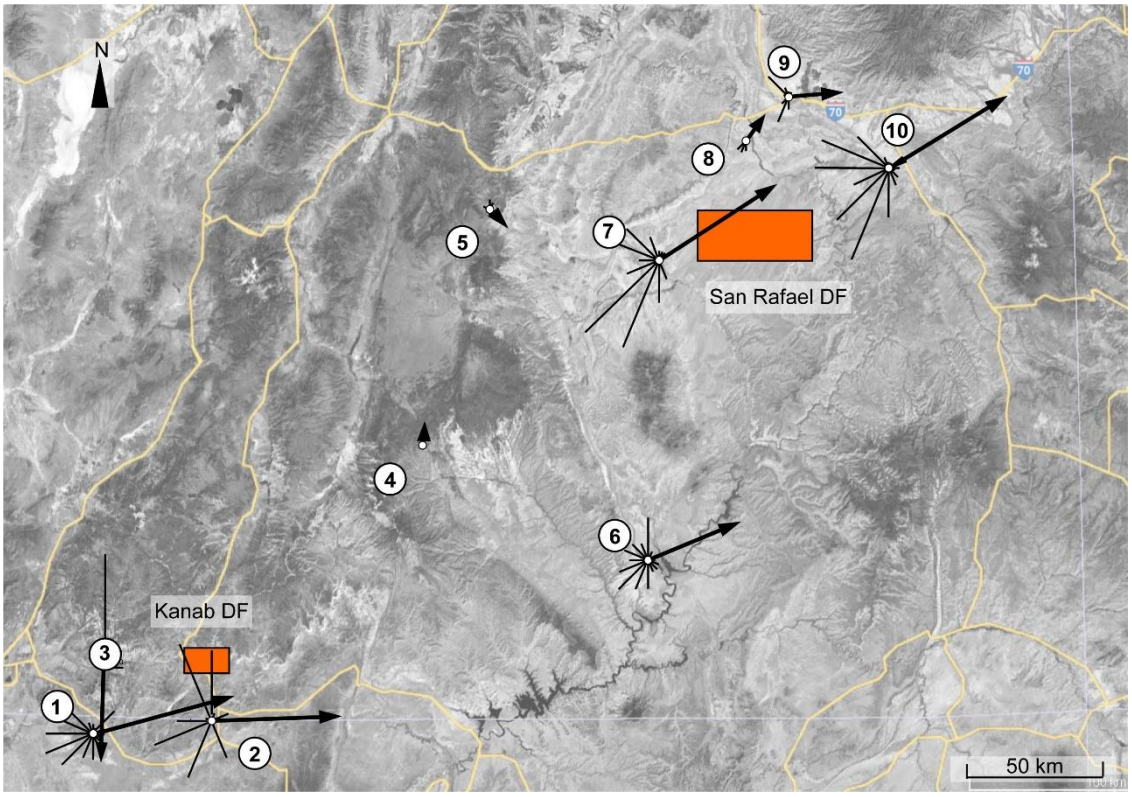

Figure 4.4. Drift potential diagrams, southern Utah MesoWest stations. Sand roses indicate drift potential binned to16 compass directions (data sources: MesoWest climate stations 1 – 10. Locations shown in Figure 4.1 and Appendix G). Data summarized in Table 4.1; wind records in Appendix G (methods: Fryberger, 1979). Arrow indicates resultant drift direction (RDD) for comparison with geomorphic record of dune orientations (Table 4.3) (stations 1-9: magnitude scaled by factor of 100, station 10: scale factor of 200).

2.4 Wind Discussion

Sand rose diagrams shown on Figure 4.4 demonstrate that resultant drift direction, while variable across southern Utah, suggests net sand transport to the east or northeast for seven of the ten modern climate stations studied. Sites 1 and 2 are located at small, rural airports, and indicate wind source is from the west to slightly southwest. They are located just south and west of the Kanab dune field project site, and indicate an expected sand transport approximately 75-90 degrees (Table 4.2, Figure 4.4). Dune orientations measured on aerial images of Kanab dune field range from N63^{o}E to N85^{o}E (Figure 4.2). Stabilized parabolic dunes to the west in Qed1 and Qed2, and in the youngest and partially active dune units, Qed 4 at the eastern side of the dune field fall within the RDD indicated at these nearby stations. Dune orientations in the central portion of the dune field, in map units Qed2 and Qed3, are oriented about 10 degrees northeast of this range. This slight deviation may result from impacts due to local escarpments or seasonal variability on drift potential in the center of the dune field.

Dune orientations measured in the San Rafael desert dune field range from about N40^{o}E to N43^{o}E in all three dune units, and do not appear to be influenced by an easterly net drift potential. Wind station 7, KHVE, located at Hanksville is the closest station to SRDF and is plotted on Figure 4.3 for ready comparison. RDD is N57^{o}E, suggesting the net sand drift is > 10^{o} east of the measured dune orientations. Station 8, located at San Rafael River at the north end of the dune field, indicates RDD N34^{o}E. Effectively the two stations appear to bracket the actual resulting sand drift observed, which is significant given that most of these dune units are at least partially active at this time. Standard wind anemometer measurements are made at 10m. The SRDF contains escarpments and buttes, and is flanked to the west by the San Rafael Swell, a monoclinal ridge. All of these structural features exceed 10 m elevation and may well impact anemometer measurements.

RDD calculated from wind records obtained at sites 3, 4 and 5 differ significantly from wind stations located near and downwind of the two dune fields (Figure 4.4). Wind directions

here indicate RDD that is nearly N-S (Table 4.2). Of these sites 4 and 5 have RDP/DP ratios of 0.2 and 0.4, indicating high to moderate directional variability of threshold winds. Also, the percent of threshold wind counts is less than 15%, and DP is in the low category (Fryberger, 1979). Site 3, Zion Canyon has high DP, and RDP/DP of 0.9. This suggests the station site is likely impacted by sharp contrasts in relief and other local characteristics that impact the wind velocity and direction. These three stations represent winds that deviate significantly from the dune orientations. It must be noted, however, that they are also separated by considerable distance and variable relief from the study dune fields. It seems likely that Kanab dune field, while proximal to station 3 with a strong northerly wind, may be impacted by the adjacent White Cliffs. This high-elevation bedrock bench of the Grand Staircase could disturb wind flow, effectively either blocking or diverting flow to the dune field from the wind. Seasonal shifts in wind flow were not investigated for this study, but may provide additional detail insight into the apparent inconsistencies between RDD and dune orientation.

Dune orientation measurements were obtained from all dune morphologies and dune units from geomorphic maps constructed as part of this project and discussed in Chapters 2 and 3. They are consistent with net sand transport direction suggested by the resultant drift directions calculated from the climate station records that are in closest proximity to the sand dune fields. Drift potential calculations for sites 1, 2, 6, 7, 9 and 10 fall into the high classification of Fryberger (1979). At sites 4, 5 and 8, DP is in the low classification. Of these, only site 8 has an RDD consistent with southwesterly wind source, similar to the measured San Rafael dune orientations (Table 4.2, Figure 4.4). Wind strength appears to meet or exceed threshold conditions required for dune activity based on these modern wind records in both Kanab and San Rafael dune fields.

In a study of wind regimes in the Great Basin, the coincidence of dune-field orientation on the western side of the basin with the largely westerly winds from the tropics as might be expected from zonal flow was observed (Jewell and Nicholl, 2011). In contrast, the eastern Great

Basins experiences a northerly and northeasterly wind flow as energy flows deviate around the southern end of the Sierra Nevada mountains from westerly low-pressure troughs that stall and strengthen along the range front (Shafer and Steenberg, 2008; Jewell and Nicholl, 2011). Dune fields in the eastern Great Basin exhibit dune orientations with northeasterly trends, reflecting local influence to upper atmospheric wind circulation patterns.

2.5 Wind Conclusions

Drift potential calculations from ten MesoWest climate station records from southern Utah following methods of Fryberger (1979) were compared with dune orientations measured on aerial imagery in two southern Utah dune fields. Wind records spanned a period of 10-22 years, from ~1997 – 2019. DP values indicate high wind environments occur across much of the region. Dune orientations in Kanab dune field and San Rafael dune field are largely consistent in each field with RDD determined from modern wind records, although some local deviation occurs. This may reflect the influence of local escarpments or seasonal variability. Dune activation in both fields has been dated from early to late Holocene. No systematic difference in dune orientation is evident based geomorphic map units from this study (see Chapters 2 and 3). The broad consistency in RDD and DP from modern wind records with Holocene dune directions suggests that modern wind records are a useful analog for Holocene winds. Wind records obtained for decadal and greater modern periods from portable units may also provide information about local physiographic conditions that impact local surficial processes in response to climate patterns. Further investigation of seasonal variability may provide additional detail on observed differences in dune orientation and apparent annual resultant drift direction.

3.0 Sediment Geochemistry Analysis

Dune activation requires a threshold supply of available (i.e., loose) sediment, in addition to meeting adequate wind velocity and low effective moisture conditions. Sediment source is a key factor in determining sediment availability for eolian transport. Weathering and erosion of bedrock exposures during warmer and wetter periods may generate sediment for transport during periods of aridity and alluvial deposits and lake sediments also provide ready sediment sources for eolian transport during periods of aridity. In recent decades, however, sediment source has been recognized as an important component for its role in the complex processes of dune activation and dune stabilization (i.e., Kocerak and Lancaster, 1999; Lancaster, 2008; Halfen and Lancaster, 2016). Increased silt deposition acts to hasten soil formation processes which can encourage or enhance soil vegetation leading to soil stabilization (i.e., Reheis et al, 1995; Tsoar, 2005; Hesp et al, 2021). Vegetated dunes may provide increased resistance to dune (re) activation (i.e., Yizhaq et al, 2019).

Geochemical trace elements have been used in sediment provenance studies, with mixed success (i.e., Frahlick and Kronberg, 1997; Arbogast and Muhs, 2000; Muhs, 2004; Hao et al, 2010; Wang et al, 2014; Chen et al, 2021). Using element ratios of K/Ba and K/Rb has proven successful in determining linkages between dune sediments and source sediments, particularly in differentiating alluvial source deposits (Muhs, 2017). Both mica and K-feldspar are potential source minerals that could contribute to K/Rb or K/Ba values in a sediment. Muhs argues that in K-feldspar is likely the single source of these elemental ratios in dune sediments, simply due to its greater crustal abundance. Moreover, K/Rb and K/Ba elemental ratios captured in dune sediment should be relatively insensitive to changing elemental concentration with increasing mineralogical maturity due to the chemical stability of K-feldspar (Muhs, 2017).

The provenance for dune sediments in southern Utah has been suggested as local bedrock exposures of Mesozoic sediments (e.g., Doelling et al, 2009, 2015; Ford et al, 2010). This

investigation seeks to determine whether sediment provenance has remained constant during the Holocene. If so, geochemical analysis should reveal consistent elemental ratios of K/Rb and K/Ba both temporally and spatially. A second goal is to determine whether local bedrock exposure is a potential source rock. If so, K/Ba and K/Rb ratios should be similar (i.e., demonstrate overlapping values) for dune sediments and for bedrock.

3.1 Sediment geochemistry records and methods

A sample for dose-rate determination is collected from the sediment surrounding each OSL sample. From these, representative samples of ~50-100 g weight were obtained using soil splitters at the USU Luminescence Laboratory, and sent to ALS Chemex Laboratories (Elko, Nevada and Vancouver, Canada) for geochemical analysis. Samples first were prepared in a four-acid digestion process using a combination of nitric, perchloric, and hydrofluoric acid with a final dissolution stage using hydrochloric acid. Following acid treatment, samples were analyzed using inductively coupled plasma mass spectrometry (ICP-MS) and inductively coupled plasma atomic emission spectroscopy (ICP-AES) protocols.

The following elemental analyses were obtained for each sediment sample: (Ag, Al*, As, Ba, Be, Bi, Ca*, Cd, Ce, Co, Cr, Cs, Cu, Fe*, Ga, Ge, Hf, In, K*, La, Li, Mg*, Mn, Mo, Na*, Nb, Ni, P, Pb, Rb, Re, S*, Sb, Sc, Se, Sn, Sr, Ta, Te, Th, Ti*, Tl, U, V, W, Y, Zn, Zr). Starred elements are reported in percent and the remainder in parts per million (ppm). Potential source rock samples from bedrock exposures of Jurassic Navajo Fm. (pink and white members), Jurassic Kayenta Fm., and Jurassic Entrada Fm., were submitted to the same lab for the same suite of geochemical analyses, to provide data for an investigation of dune sediment provenance.

To investigate changes in source rock geochemistry through the Holocene in Kanab and San Rafael dune fields, dose rate samples were selected from each eolian event and each geomorphic (dune) map unit to consider both temporal and spatial trends. Dune migration in

Kanab dune field occurs along a west-to-east trend, approximately coincident with the resultant drift direction determined from modern wind records (Figure 4.2). Identified eolian events indicate a similar general trend (Ch. 2). Dose rate samples were selected along an approximately west-to-east traverse from sites 1, 4, 13, 17 and 24 for this initial investigation (Figure 4.1). Holocene dune migration in San Rafael dune field generally follows a northeasterly trend, also similar to modern resultant drift direction seen in modern wind records in the proximity of SRDF (Figure 4.3). Eolian events are spatially distributed within the San Rafael dune field. Samples were selected to include different dune morphologies in addition to representing all identified eolian events and eolian map units. Dose rate samples are from sites 1, 5, 8, 11, 16, 19 and 22 (Figure 4.1).

3.2 Sediment geochemistry summary

This investigation from the selected samples for this preliminary investigation of source rock geochemical analysis Ratios of K/Ba and K/Rb were determined from the geochemical analyses (see Section 4.1). Surface characteristics were imaged using scanning electron microscopy and grain size distributions determined using laser particle analysis (Ch.2) to document physical characteristics of the sediments.

Results of the geochemistry and laser particle analysis for the selected samples are presented in Table 4.2. Six OSL samples representing the five eolian events (K0-K4) and five map units (Qes and Qed1-Qed4) are reported for Kanab dune field. This dataset includes two samples representing eolian event K3 obtained from two different map units (Qed2 and Qed3), and two samples from map unit Qed1, which are from two different eolian events (K1 and K2). Samples were selected along an approximate east-west (downwind) transect near the center of the dune field. Ratios of K/Ba range from 39-46 and K/Rb ranges from 267-301 ppm. The Kanab sediment samples lack clay or silt sized particles, predominantly fine to medium sand (Table 4.2).

The geochemistry dataset for San Rafael dune field is comprised of seven samples representing the seven eolian events identified (SR0-SR6) and from each of the mapped eolian units (sand sheets Qes1 and Qes2, and dune units Qed1-Qed3). Samples are spatially and temporally distributed across the project area.

Table 4.2 Summary of geochemistry records. Selected samples for source rock geochemistry preliminary investigation, Kanab and San Rafael dune fields. A) K/Ba and K/Rb and site location information. B) Grain size data from laser particle analyses (Ch. 2, 3).

Kanab DF						
Site	Sample ID	K/Ba	K/Rb	Eolian Event	Map Unit	Dune Type
1	USU-3331	42	290	K0	Qes	P
4	USU-3327	46	280	K1	Qed1	P
4	USU-3325	44	301	K2	Qed1	P
13	USU-2629	39	276	K3	Qed2	P
17	USU-2654	39	293	K3	Qed3	P
24	USU-2587	40	267	K4	Qed4	P
San Rafael DF						
Site	Sample ID	K/Ba	K/Rb	Eolian Event	Map Unit	Dune Type
1	USU-807	33	269	SR0	Qed1	P
11	USU-3397	40	307	SR1	Qes2	C
19	USU-2815	25	298	SR2	Qes1	P
16	USU-3003	23	297	SR3	Qed2	B
22	USU-3391	42	325	SR4	Qes1	C
5	USU-3237	36	301	SR5	Qes2	P
8	USU-2679	40	308	SR6	Qed3	C

Kanab DF								
Site	Sample ID	% clay	%silt	%vfsand	%fsand	%msand	%csand	%>1mm
1	USU-3331			12.7	62.6	24.6		
4	USU-3327			0.0	17.6	62.8	19.5	
4	USU-3325			0.0	18.7	68.0	13.4	
13	USU-2629			0.4	35.7	59.8	4.1	
17	USU-2654			1.9	47.2	49.4	1.5	
24	USU-2587			0.8	40.5	55.7	3.0	
San Rafael DF								
Site	USU#	% clay	%silt	%vfsand	%fsand	%msand	%csand	%>1mm
1	USU-807	n/a						
11	USU-3397	4.2	25.5	19.1	32.0	16.5	0.2	2.6
19	USU-2815	n/a						
16	USU-3003	n/a						
22	USU-3391	2.1	17.8	28.4	36.4	13.0	0.2	2.2
5	USU-3237	1.3	18.4	22.3	38.0	19.8	0.3	0.0
8	USU-2679	0.0		0.0	19.3	72.0	7.9	0.7

Photomicrographs of the sediment samples and histograms of the laser particle analysis provide a visual summary of the physical characteristics of the sediment for each geochemical sample (Figures 4.5 and 4.6). Lab analysis and field observations both indicate that Kanab dose rate sediments are rounded to well-rounded, well-sorted, and predominantly fine to medium sand. Histograms of laser particle analysis indicate medium sand fraction is predominant at site 4, in unit Qed1, fine sand predominates at site 1, in unit Qes, coarsening slightly at sites progressively more easterly in the dune field (shown as the lower row, sites 13, 17 and 24 in units Qed2, Qed3 and Qed4 respectively). SEM photographs in Figure 4.3 provide a detailed view of the particle size data, and a closer view of the rounding and sorting in the dune sediment (Figure 4.5).

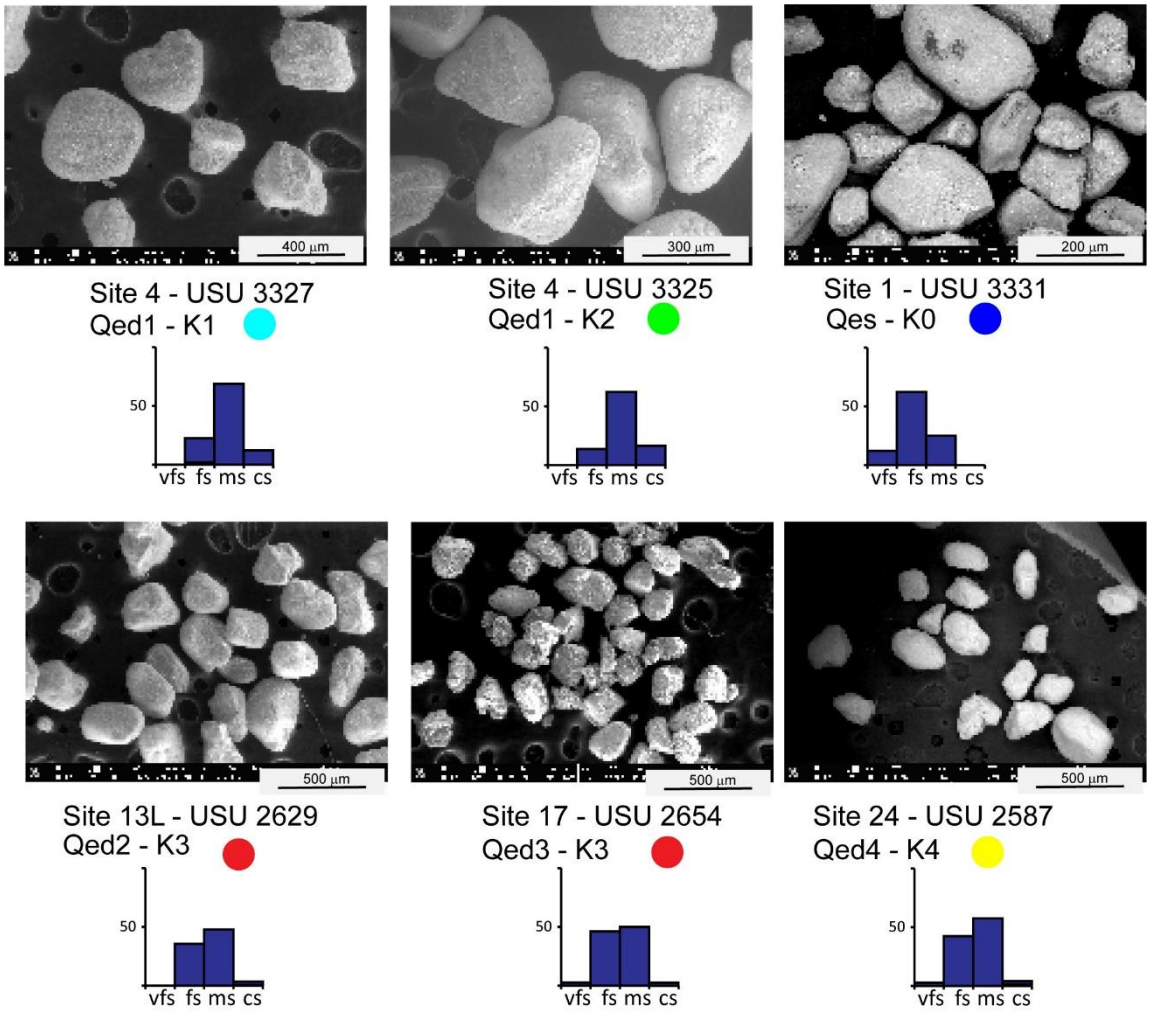

Figure 4.5. Geochemistry and physical characteristics, Kanab dune sediment. (Data from Table 4.2). SEM images are organized from west to east by sample location site in the dune field appear from left to right, upper to lower rows. Histograms show particle size distribution. Map unit and eolian events for each sample are indicated below the SEM images. Colors of eolian events key to colors in Figure 4.1.

Physical characteristics of dose rate sediments in San Rafael dune field are summarized graphically in Figure 4.6. San Rafael dose rate sediments are sub-rounded to rounded, mostly well-sorted, and comprised of very fine to fine sands. Silt fractions are significantly higher than in the Kanab dune field, with a minor coarse fraction (> 1mm) observed in samples from sites 11, 22 and 5 in units Qes2, Qes1 and Qes2, and eolian events SR1, SR4 and SR5 respectively. These samples are from coppice dunes. Histograms of laser particle analysis indicate medium sand

fraction is predominant at site 8, in unit Qed3, eolian event SR6, the most recent event, and is obtained from a parabolic dune.

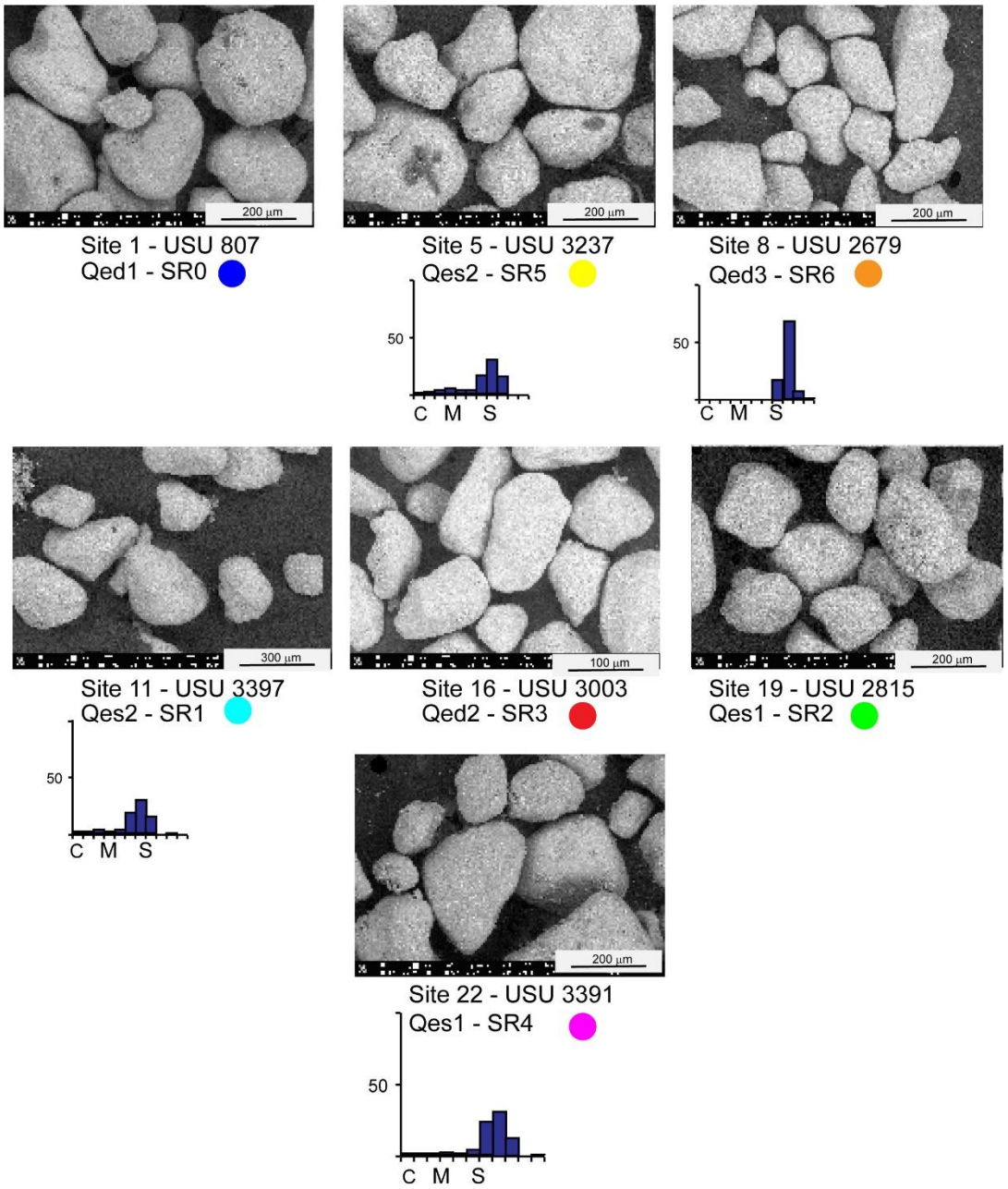

Figure 4.6. Geochemistry and physical characteristics, San Rafael dune sediment. (Data from Table 4.2). SEM photomicrographs are organized by sample location site in the dune field, numbered north to south and west to east, in upper to lower rows below. Histograms show particle size distribution. Map unit and eolian events for each sample are indicated below the SEM images. Colors of eolian events key to colors in Figure 4.1.

Samples of exposed bedrock were obtained during the field investigation in both dune fields for geochemical comparison with dune sediments to investigate as potential sediment sources. Five samples each were obtained from the Jurassic Navajo Formation White and Pink members, and four samples were obtained from the Jurassic Kayenta Formation to compare with Kanab dune sediment geochemistry. Samples were collected from outcrops surrounding the Kanab dune field to the north, west and south of the dune field. Five samples of Jurassic Entrada Formation were obtained for comparison with sediments from San Rafael dunes, within and near the San Rafael dune field, to the west and south. Plots of elemental ratios for K/Rb and K/Ba were compared for the selected dune sediment samples and for the source rock samples (Figure 4.7).

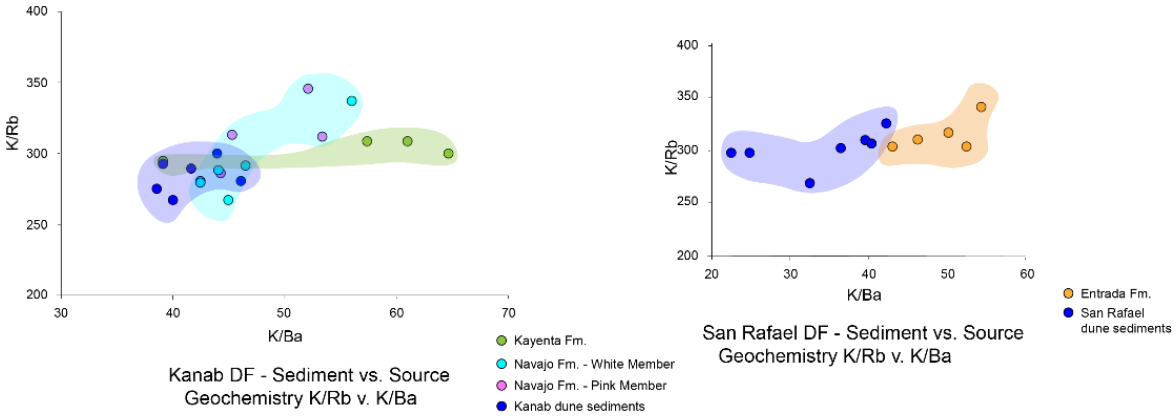

Figure 4.7. Dune sediment and source rock geochemistry K/Rb and K/Ba. Kanab (left) and San Rafael (right) dune fields. (Data from Appendix G). Dune sediment for each field is shown in dark purple shading. For Kanab dune field, the dune sediments overlap the Navajo Formation elemental ratios (here combined and shaded in blue). The Kayenta Formation (shaded green) lies outside the dune sediment region. The Entrada Formation, shaded orange, meets and slightly overlaps the dune sediments from San Rafael (dark blue, left plot).

The elemental ratio plot of K/Rb to K/Ba for Kanab dune field sediment and source rock materials supports the interpretation that Navajo Formation bedrock is sourcing the dune sediment, previously interpreted by Doelling et al (2008, 1989). The similar plot for San Rafael

suggests the Entrada Formation may contribute to the dune sediments there, but is not definitive. To further demonstrate the range of values for each dune field and examine the correlation with bedrock, sediment geochemistry for all samples within each dune field were constructed (Figure 4.8).

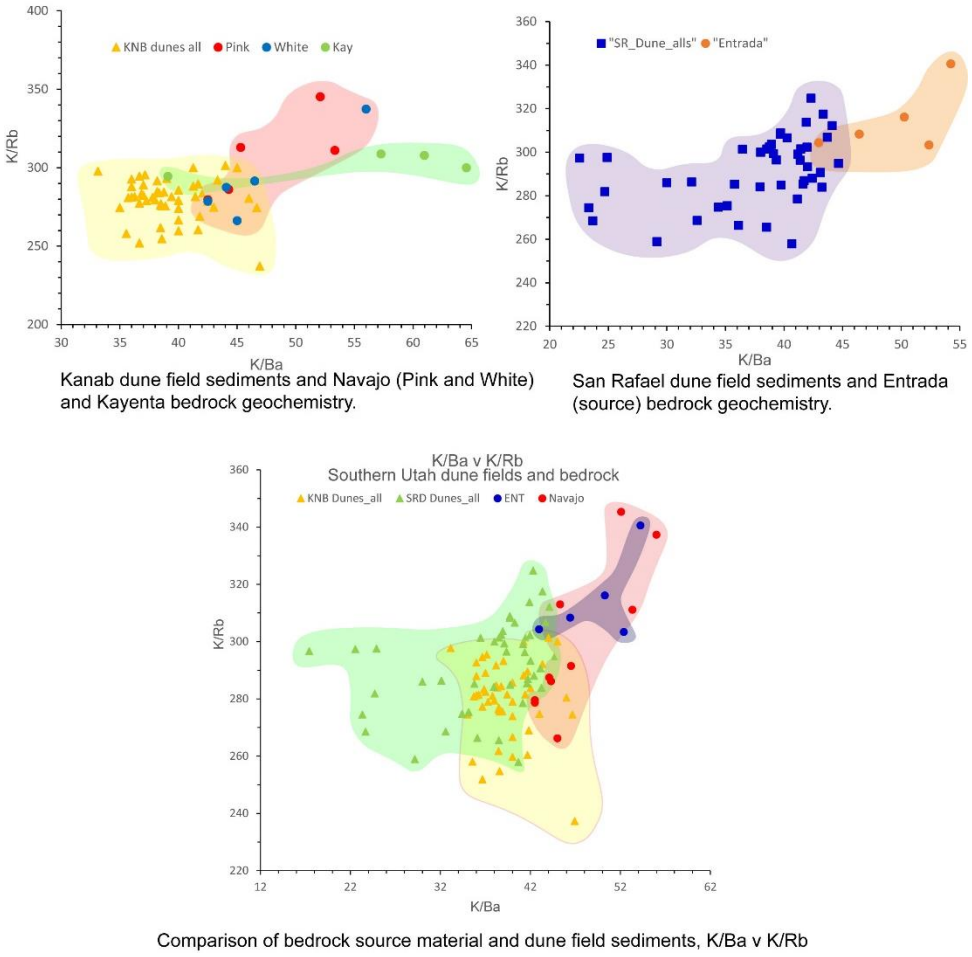

Figure 4.8. Dune sediment and source rock geochemistry, all samples. Kanab (left) and San Rafael (right) dune fields. (Data from Appendix G). Navajo Fm members are combined (red) for this correlation. Using the additional data slightly strengthens the overlap zone for source rock and sediment K/Rb, K/Ba values, suggesting a slightly stronger correlation than observed with the selected sample data. Lower diagram shows the significant overlapping zones of dune sediments and source rock.

Elemental ratios of K/Rb and K/Ba were generated for each dune field to investigate potential temporal and spatial trends in geochemistry during the Holocene (Table 4.2). Change in K/Rb and K/Ba is minor as shown in the data table, with a total difference ≤ 10% for each ratio. In Kanab dune field, there appears to be a slight concentration of higher K/Ba values on the western side of the dune field (sites 4 and 1) that is seen in the plots of eolian events and by geomorphic map unit (Figure 4.9). However, the trend is discontinuous to the east and younger map units and eolian events.

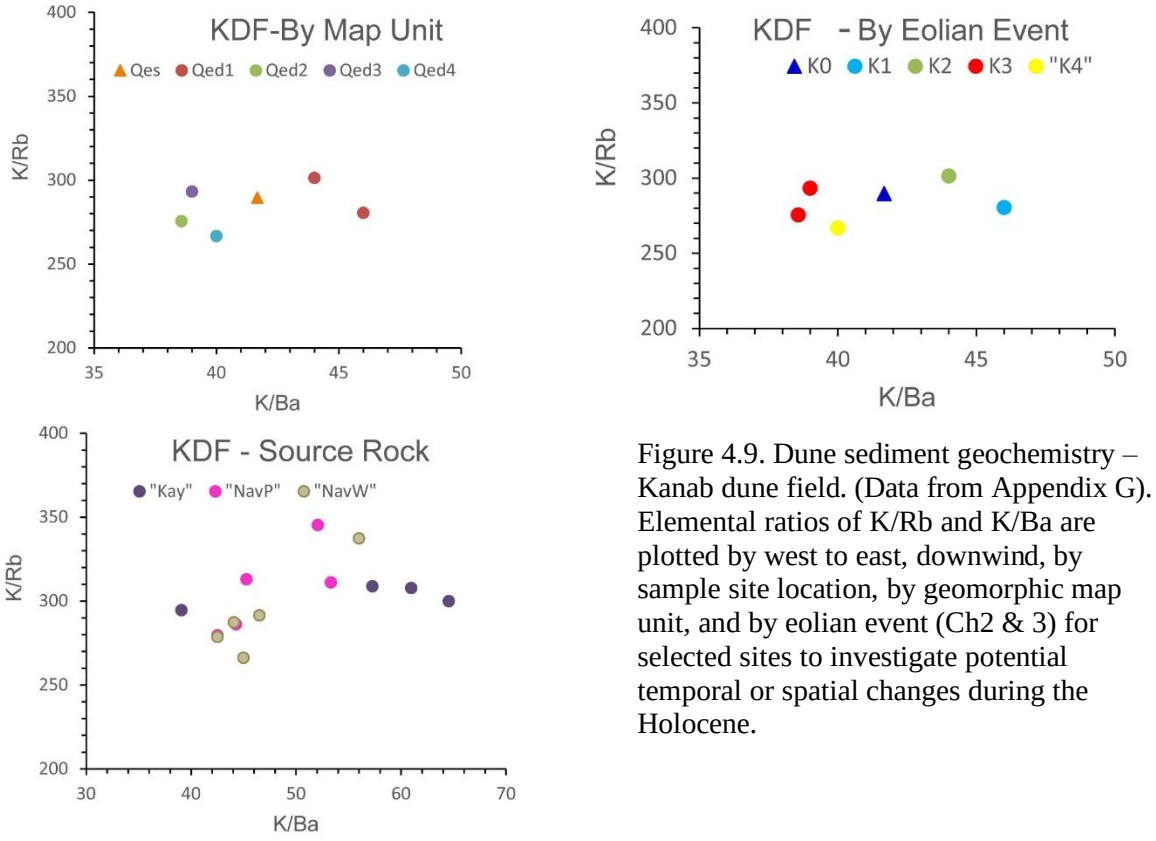

Figure 4.9. Dune sediment geochemistry – Kanab dune field. (Data from Appendix G). Elemental ratios of K/Rb and K/Ba are plotted by west to east, downwind, by sample site location, by geomorphic map unit, and by eolian event (Ch2 & 3) for selected sites to investigate potential temporal or spatial changes during the Holocene.

Values of K/Rb to K/Ba for the San Rafael selected samples (Figure 4.10) were plotted by map unit, eolian event and dune morphology. Map unit Qed1, corresponding with eolian event SR0, records the lowest K/Rb ratio. The other two mapped dune units, Qed2 (eolian event SR3) and Qed3 (eolian event SR6), both of which contain currently active dunes, have slightly higher

K/Rb values, than Qed1, the geomorphically older dune unit. The K/Ba do not exhibit any trend between these three samples, nor with either eolian unit or map unit. The samples from barchan dunes contain the highest K/Ba ratios. Coppice dune K/Ba and K/Rb ratios are widely dispersed. There is a slightly larger variability in both K/Rb and K/Ba in the San Rafael dune field than in the Kanab dune field (Table 4.2).

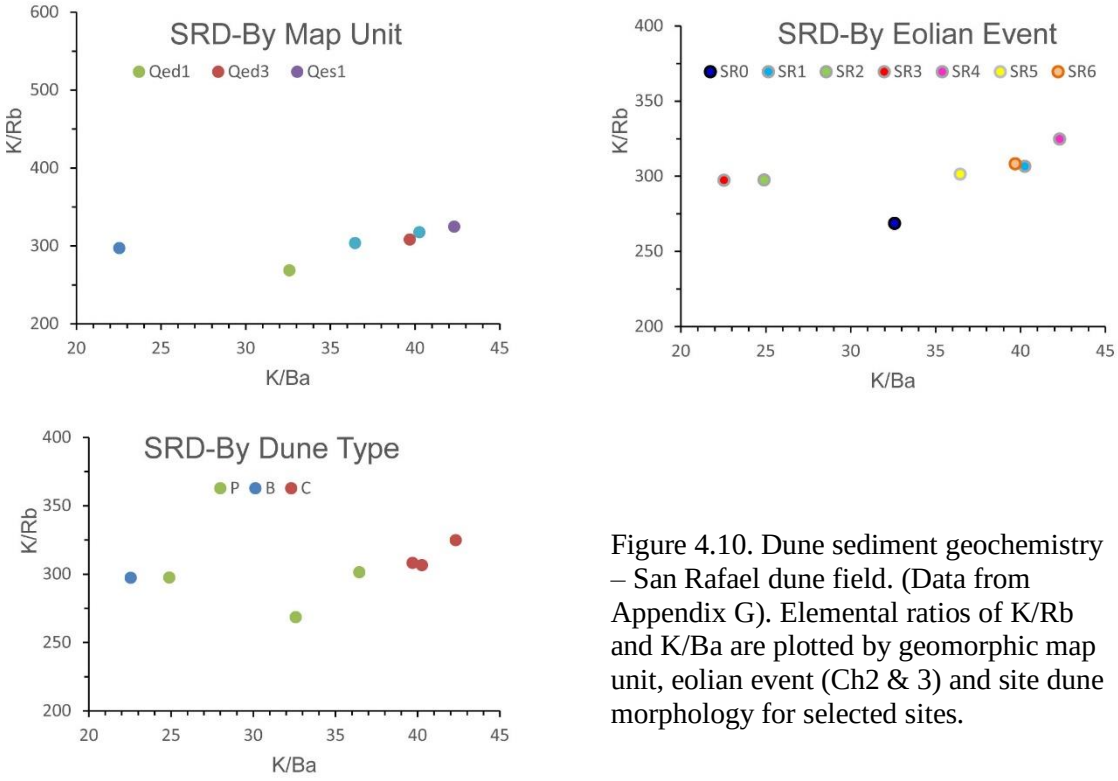

Figure 4.10. Dune sediment geochemistry – San Rafael dune field. (Data from Appendix G). Elemental ratios of K/Rb and K/Ba are plotted by geomorphic map unit, eolian event (Ch2 & 3) and site dune morphology for selected sites.

3.3 Discussion of sediment geochemistry

To examine the correlation of K/Rb and K/Ba within the dune sediments, a dataset of all geochemical records for each dune field was compiled and analyzed. Correlation diagrams were developed to compare individual elemental records (K, Ba, Rb) and ratios (K/Ba, K/Rb, K/Rb/K/Ba) for Navajo Formation source material (n=10), Kanab dune field sediments (n=50),

and San Rafael dune field sediments (n=45) (Figure 4.11). Spatial correlation was also considered for the dune field sediments, using latitude and longitude. Source material geochemistry for the Kayenta Formation (n=4) and Entrada Formation (n=5) was not included, due to the limited number of samples. The correlation diagrams are color-coded with blue shading indicating positive correlations (i.e., direct correlation) and red representing negative (i.e., inverse) correlations. Darker color represents stronger correlations and correlation value for paired arrays is provided in each square. Left side diagrams show all data, and right-side diagrams contain only significant values ($p < 0.1$).

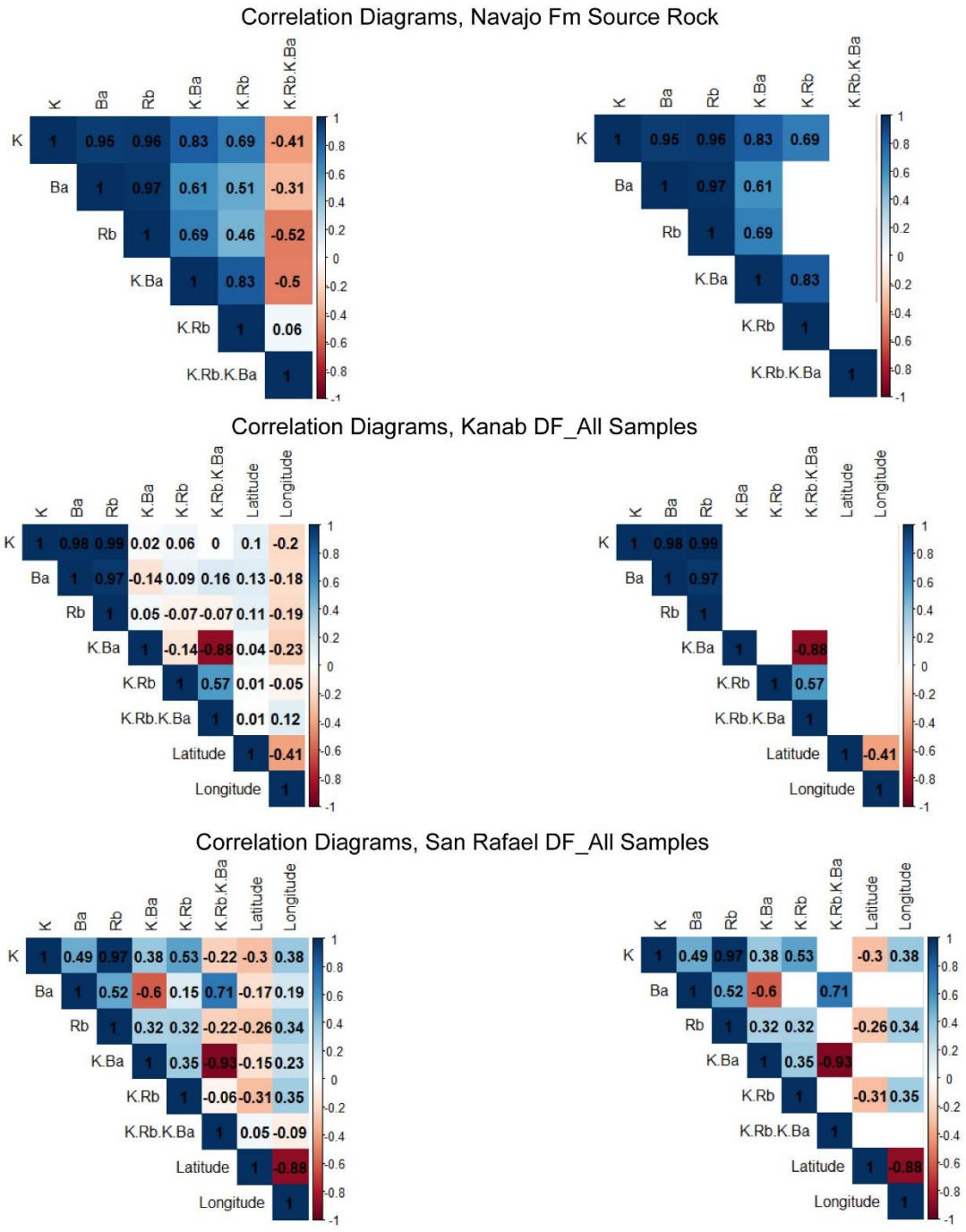

Correlation Diagrams, Geochemistry of Source Rock and Dune Sediments

Note: Significant values, plotted on left side, includes only correlations with p<0.1.

Figure 4.11. Correlation diagrams for sediment and source material geochemistry. Paired arrays. Left side diagrams indicate all paired correlations, and right-side diagrams omit correlations that are not statistically significant ($p<0.1$)

Correlation diagrams highlight differences in K/Ba and K/Rb values between bedrock samples and dune field sediments. Navajo Formation samples (n=10) indicate that K/Rb and K/Ba are strongly correlated (0.83). In contrast, correlation between K/Ba and K/Rb does not meet the test of significant value for the Kanab dune field sediments and is weakly correlated (0.35) for the San Rafael dune field sediments. This disconnect between the correlation strength is observed in the dune sediment and source rock plots of K/Rb and K/Ba (Figures 4.7 and 4.8) where there is limited overlap between the dune field data and the source material data.

To determine whether there is a change in source material through time, correlations between the three elemental ratios (K/Rb, K/Ba, and K/Rb/K/Ba) and two different spatial trends (latitude and longitude) are calculated (Figures 4.9 and 4.10). Kanab dune field exhibits a trend to younger map units and younger eolian activity events downwind, west to east (Ch. 2 and Figure 4.8). Weak negative correlation with longitude does not meet a p-test for significance. A similar value-range, weak positive correlation with latitude also fails a p-test. K/Ba shows a strong negative (-0.88) and K/Rb shows a moderately strong positive (0.57) correlation with the K/Rb/K/Ba ratio, but the K/Rb/K/Ba ratio does not correlate with either latitude or longitude. These results suggest that no change in source rock has occurred through the Holocene eolian activity recorded in the dune field, although some variability in both K/Ba and K/Rb occurs within the dune field.

San Rafael dune field correlations are visually stronger in most paired arrays than in the Kanab dune field. Notable exceptions are the moderate correlation value (0.49) for K and Ba, and Ba and Rb (0.52), much lower than the near-1 correlations seen for these elements in the Kanab dune field sediments. This may be due to additional sources of Ba in the San Rafael dune sediments. K/Ba exhibits a significant, strong negative correlation (-0.93) with K/Rb/K/Ba, similar to that shown in Kanab dune field data. If additional sources of Ba occur in the dune sediment, it may not impact the utilization of K/Ba as a geochemical marker. K/Rb does not correlate with K/Rb/K/Ba, and the latter does not correlate with either latitude or longitude. K/Rb

and K/Ba show a weak but statistically significant (0.35) correlation, absent in the Kanab dune field. There is a significant, weak negative correlation between K/Rb and latitude (distance south to north) and a significant weak positive correlation between K/Rb and longitude (distance west to east) in San Rafael dune sediments. Although correlation of the geochemical data is stronger than that observed in the Kanab dune sediments, it is insufficient to reflect a change in source material supplied to the dune field during the Holocene (Ch. 3 and Figure 4.9).

A graph of K/Rb and K/Ba for Kanab dune field and Navajo Fm bedrock source material with trend lines and R2 values (Figure 4.12) clearly demonstrates the strong correlation in the bedrock and the lack of correlation in the dune field sediments. A scatter plot of K/Rb/K/Ba with longitude for dune field sediment suggests a slight correlation in the trendline. Similar plots of K/Rb and K/Ba show there is no statistically significant correlation in distance west to east, downwind in the dune field.

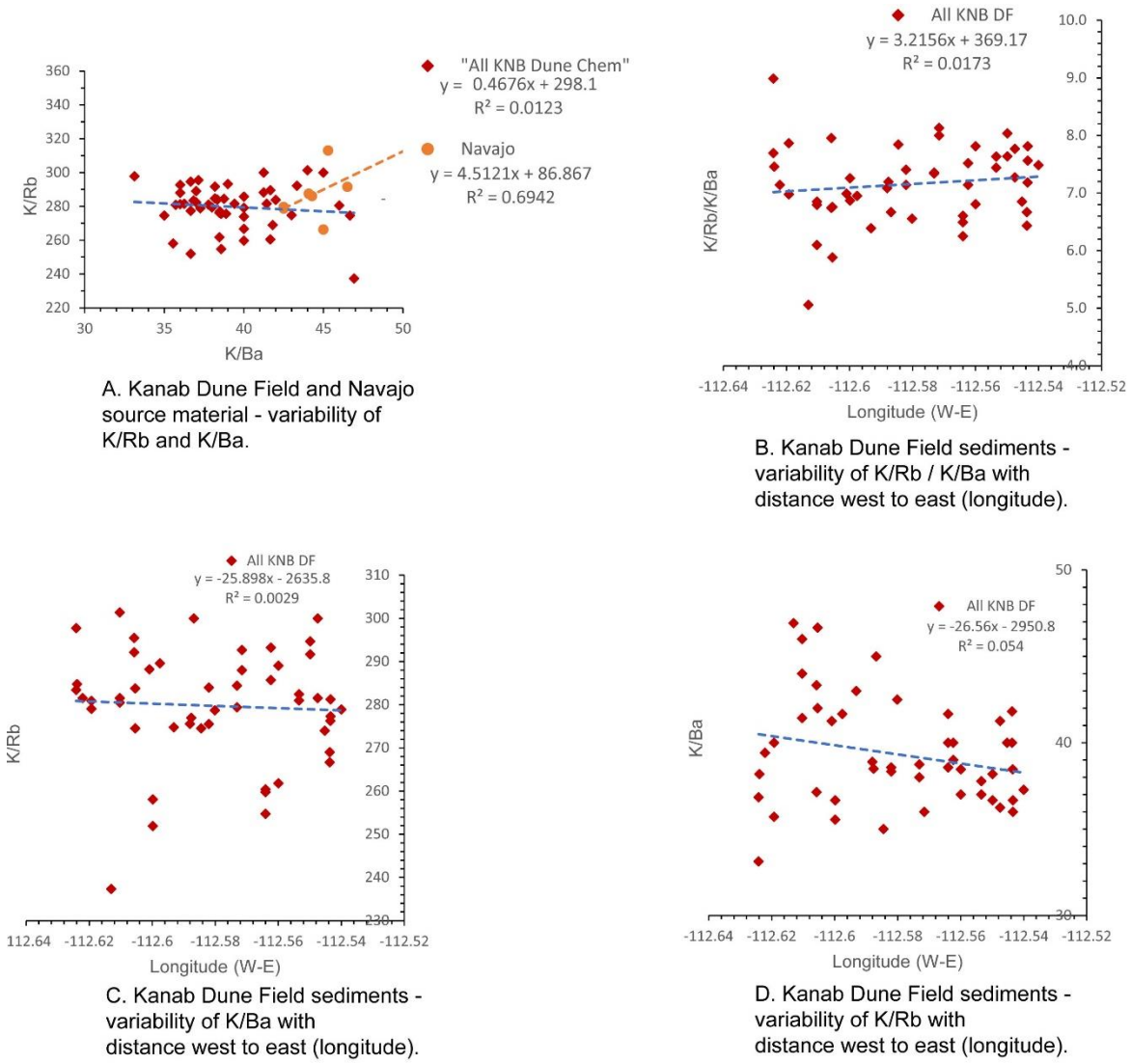

A. Kanab Dune Field and Navajo source material - variability of K/Rb and K/Ba.

B. Kanab Dune Field sediments - variability of K/Rb / K/Ba with distance west to east (longitude).

C. Kanab Dune Field sediments - variability of K/Ba with distance west to east (longitude).

D. Kanab Dune Field sediments - variability of K/Rb with distance west to east (longitude).

Figure 4.12. Dune sediment geochemistry – Kanab dune field. All samples (n=50), K/Rb and K/Ba. Upper left scatter plot shows dune sediment and Navajo Fm (n=10) bedrock source (data from both Pink and White members). Elemental ratios are further examined for correlation and trends with distance west to east, downwind.

A similar set of scatter plots was constructed for San Rafael dune sediments, with a single comparison plot showing the Entrada Fm bedrock geochemistry (K/Rb, K/Ba) (Figure 4.13). The trend for the bedrock source material, although limited (n=5) is moderately correlated (R2=0.4), while the dune field sediments correlate weakly (R2=0.1). Scatter plots of K/Rb and K/Ba with longitude (distance west to east) are not strongly correlated, as demonstrated by the trendline and

low R^2 values, which range from 0.02 to 0.12. Dune orientation is northeast, with downwind to the northeast. No evidence from the K/Rb and K/Ba geochemistry supports changing source material through time.

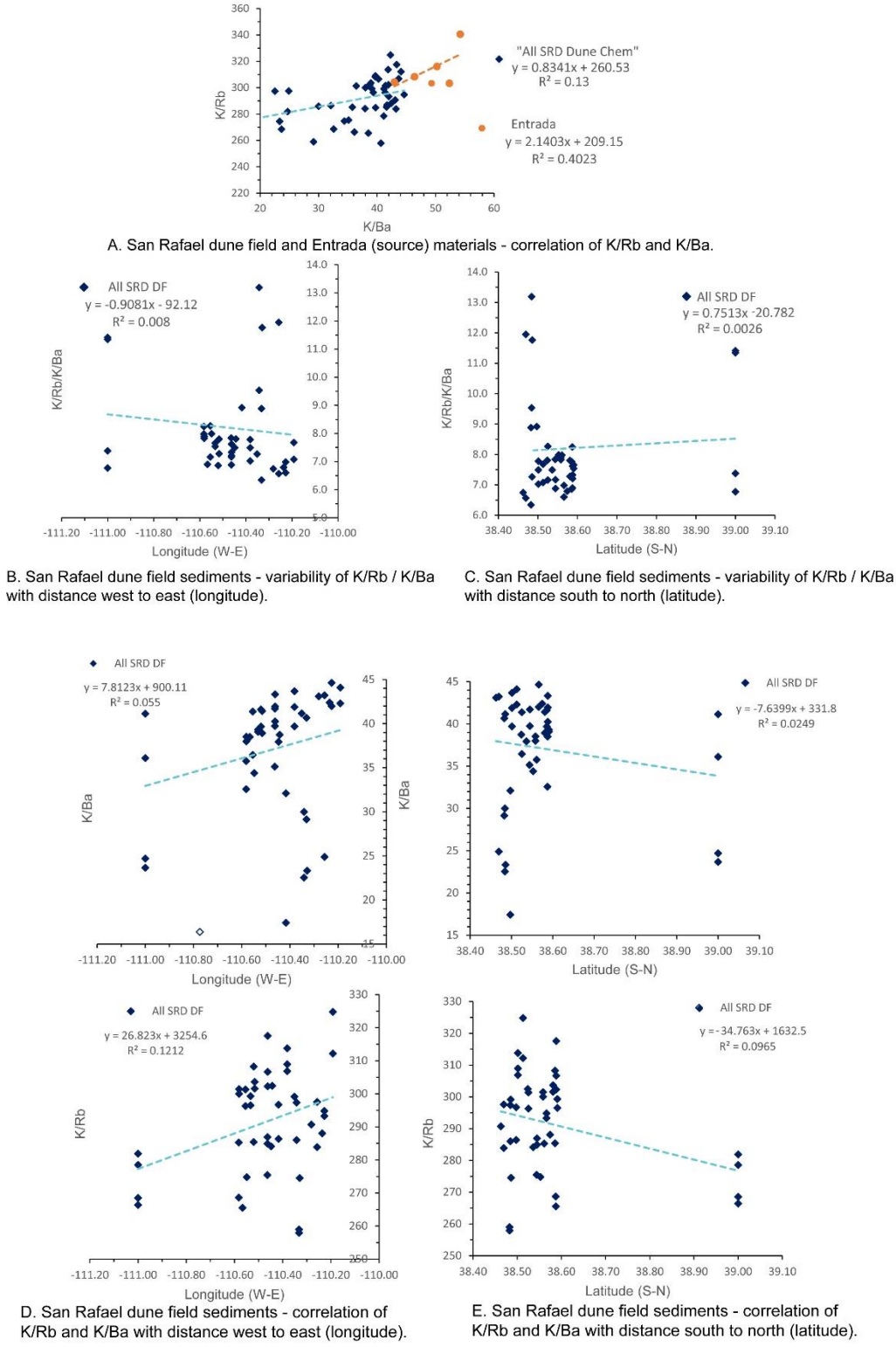

A. San Rafael dune field and Entrada (source) materials - correlation of K/Rb and K/Ba.

B. San Rafael dune field sediments - variability of K/Rb / K/Ba with distance west to east (longitude).

C. San Rafael dune field sediments - variability of K/Rb / K/Ba with distance south to north (latitude).

D. San Rafael dune field sediments - correlation of K/Rb and K/Ba with distance west to east (longitude).

E. San Rafael dune field sediments - correlation of K/Rb and K/Ba with distance south to north (latitude).

Figure 4.13. Dune sediment geochemistry – San Rafael dune field. All samples (n=45), K/Rb and K/Ba. Upper left scatter plot shows dune sediment and Entrada Fm (n=5) bedrock source. Elemental ratios are further examined for correlation and trends with distance west to east, and distance south to north.

3.4 Sediment geochemistry conclusions

Eolian events in Kanab dune field reflect demonstrate a slight trend to decreasing K/Rb-K/Ba ratios in sediment samples from a west-to-east transect near the center of the dune field (Figure 4.1 and 4.4; Table 4.2). In the larger, and shallower sand dunes of the San Rafael dune field there is no evident trend between K/Rb-K/Ba ratios and eolian events (Figures 4.1 and 4.3B; Table 4.2). Physical properties of the sediments are consistent across the Kanab dune field, which is mineralogically mature. In contrast, San Rafael dune field is characterized by a range of physical properties, including grain sizes that vary by dune morphology. Coppice dunes contain the widest range of particle sizes, with a well-defined silt fraction. Ratios of K/Rb-K/Ba appear higher and more consistent in the coppice dune sediments than the parabolic or barchan dune morphologies within the selected west-to-east site transect investigated in this study. A wider range of particle sizes that demonstrate greater angularity and less overall rounding in the coppice dune sediments suggests that these sediments are held within the coppice dune and thus may be less subject to abrasion than sediments in parabolic and barchan dunes. Any softer minerals including potassium feldspars (source of the Rb and Ba) are more likely to be preserved.

Samples of likely provenance rock were also investigated in this study for K/Rb-K/Ba characterization. There is a slight overlap between the San Rafael samples and the Entrada Fm. samples obtained from rock exposures within and south of the San Rafael dune field. The overlap is observed in some coppice dune samples. A scatter plot of all dune field sediment geochemistry (Figure 4.8) indicates a slightly increased overlapping region of similar K/Rb and K/Ba values than the selected samples (Figure 4.2). In Kanab dune field, values of K/Rb-K/Ba are most similar to the Navajo-White Member, with some overlap between the Navajo-Pink Member but due to the limited sample size, both members are grouped into a single Navajo Fm bedrock source material (Figure 4.8). The White Cliffs, which have extremely high erosion rates (Riley et al, 2021) may be a primary source of the dune field sediment.

K/Rb and K/Ba ratios may not be as useful in identifying unique bedrock sources for dune sediments as demonstrated for instances of alluvial deposit sources (Muhs, 2017). Significant overlap in both dune fields in this study, as well as limited overlap in bedrock source values suggests a limited correlation with the source rocks. Evidence from K/Rb and K/Ba ratios within the dune fields suggests there is no change (i.e., new sediment source) in dune sediment source through time. This suggests climate is the main driver of dune field activity or reactivation, rather than additional sediment supply.

4.0 Summary and conclusions

This study examined modern wind records obtained from MesoWest climate stations in southern Utah, provided by the Utah Climate Center, to determine sand drift potential and resultant drift direction. The results show strong correlation between wind stations near the dune fields with dune orientation measured from aerial imagery in Holocene dunes in both the Kanab and San Rafael dune fields of southern Utah (Figure 3.2). Results suggest modern winds are a useful analog for Holocene winds in characterizing eolian wind regimes in this region.

The geochemistry of dune sediments and potential source rock sediments was investigated using a simple, cost-effective technique using K/Rb – K/Ba ratios determined from available dose-rate geochemical data obtained for use in dating with optically stimulated luminescence (OSL). Dune sediments in Kanab dune field indicate a very minor decrease in K/Ba for the eastern and western portions of the dune field, but no evidence of a trend in K/Rb ratios. Elemental ratios for K/Rb and K/Ba were used to discern a bedrock source for the dune sediments in Kanab, from the Jurassic Navajo Formation, ruling out the Jurassic Kayenta Formation as a provenance material. This finding supports the interpretation that the White Cliffs may be a significant source for dune sediment in the dune field, previously suggested in Chapter 2 in part based on the high erosion rates determined for the White Cliffs (Riley et al, 2019). Further

investigation of winds, particularly seasonal variability, may provide additional information regarding this interpretation.

Neither San Rafael nor Kanab dune sediment geochemistry records or analysis indicate a change in source material for either dune field through the Holocene. The range of elemental values is larger in the San Rafael dune sediments, and analysis of the entire suite of geochemical samples may provide additional useful detail regarding potential temporal or spatial trends. A minor concentration of relatively higher K/Ba elemental ratios was observed in the barchan dune types. The higher amounts of silt observed in the dune sediment suggest that additional investigation of trace element markers may provide additional information on provenance material for this dune field.

5.0 References

Allen, J.R.L., 1993. Paleowind: geological criteria for direction and strength. Philosophical Transactions of the Royal Society of London B341, 235–242.

Arbogast, A.F. and Muhs, D.R., 2000. Geochemical and mineralogical evidence from eolian sediments for northwesterly mid-Holocene paleowinds, central Kansas, USA. *Quaternary International*, *67*(1), pp.107-118.

Bagnold, RA, 1941. The physics of wind-blown sand and desert dunes. Methuen, London, 265 (10)

Barchyn, T.E. and Hugenholtz, C.H., 2015. Predictability of dune activity in real dune fields under unidirectional wind regimes. Journal of Geophysical Research: Earth Surface, 120(2), pp.159-182.

Barchyn, T.E., and Hugenholtz, C.H., 2013, Reactivation of supply-limited dune fields from blowouts: A conceptual framework for state characterization: Geomorphology, v. 201, p. 172–182

Bogle, R., Redsteer, M.H. and Vogel, J., 2015. Field measurement and analysis of climatic factors affecting dune mobility near Grand Falls on the Navajo Nation, southwestern United States. Geomorphology, 228, pp.41-51.

Bullard, J.E., 1997. A note on the use of the “Fryberger Method” for evaluating potential sand transport by wind. Journal of Sedimentary Research 67, 499–501.

Bullard, J.E., Thomas, D.S.G., Livingston, I., Wiggs, G.F.S., 1996. Wind energy variations in the southwestern Kalahari Desert and implications for linear dune field activity. Earth Surface Processes and Landforms 21, 263–278.

Buggle et al., 2011. An evaluation of geochemical weathering indices in loess – paleosol studies: Quaternary International, v. 240, p. 12 – 21

Chen, G., Dong, Z., Li, C., Shi, W., Shao, T., Nan, W. and Yang, J., 2021. Provenance of Aeolian Sediments in the Ordos Deserts and Its Implication for Weathering, Sedimentary Processes. Frontiers in Earth Science, 9, p.544.

Doelling, H.H., Davis, F.D. and Brandt, C.J., 1989. The geology of Kane County, Utah: Geology, mineral resources, geologic hazards (Vol. 124). Utah Geological Survey.

Doelling, H.H., 2008. Geologic map of the Kanab 30'x60'quadrangle, Kane and Washington Counties, Utah, and Coconino and Mohave Counties, Arizona, 1: 100,000-scale: Utah Geological Survey. MP-08-2DM.

Doelling, H.H., Kuehne, P.A., Willis, G.C. and Ehler, J.B., 2015. Geologic map of the San Rafael Desert 30'x 60'quadrangle, Emery and Grand Counties, Utah. Utah Geological Survey.

Ford, R.L., Gillman, S.L., Wilkins, D.E., Clement, W.P., Nicoll, K., Sprinkel, D.A., Chidsey, T.C. and Anderson, P.B., 2010. Geology and geomorphology of Coral Pink Sand Dunes State Park, Utah. Geology of Utah's Parks and Monuments, Utah Geological Association, pp.379-406.

Fralick, P.W. and Kronberg, B.I., 1997. Geochemical discrimination of clastic sedimentary rock sources. Sedimentary Geology, 113(1-2), pp.111-124.

Fryberger, S.G.; 1979, Dune Forms and Wind Regimes. In A Study of Global Sand Seas; McKee, E.D., Ed.; U.S. Geological Survey: Reston, VA, USA, 1979; pp. 137–169

Halfen, A.F., Lancaster, N. and Wolfe, S., 2016. Interpretations and common challenges of aeolian records from North American dune fields. Quaternary International, 410, pp.75-95.

Hao, Q., Guo, Z., Qiao, Y., Xu, B. and Oldfield, F., 2010. Geochemical evidence for the provenance of middle Pleistocene loess deposits in southern China. Quaternary Science Reviews, 29(23-24), pp.3317-3326.

Hesp, P.A., Hernández-Calvento, L., Hernández-Cordero, A.I., Gallego-Fernández, J.B., Romero, L.G., da Silva, G.M. and Ruz, M.H., 2021. Nebkha development and sediment supply. Science of the Total Environment, 773, p.144815.

Jewell, P.W., and Nicoll, K., 2011, Wind regimes and aeolian transport in the Great Basin, U.S.A.: Geomorphology, v. 129, p. 1–13

Kocurek, G.; Lancaster, N., 1999, Aeolian system sediment state: Theory and Mojave Desert Kelso dune field example. Sedimentology, 46, 505–515.

Lancaster, N., 1988. Controls of eolian dune size and spacing. Geology, 16(11), pp.972-975

Lancaster, N., 1997, Response of eolian geomorphic systems to minor climate change: examples from the southern Californian deserts: Geomorphology, v. 19, p. 333–347

Lancaster, N.; Helm, P., 2000, A test of a climatic index of dune mobility using measurements from the southwestern United States. Earth Surf. Process. Landf., 25, 197–207.

Lancaster, N., 2008. Desert dune dynamics and development: insights from luminescence dating. Boreas, 37(4), pp.559-573.

Lancaster, N. and Hesp, P., 2020. Introduction to Inland Dunes of North America. In Inland Dunes of North America (pp. 1-10). Springer, Cham.

Lancaster, N., 2020. On the formation of desert loess. Quaternary Research, 96, pp.105-122.

Liu, J., Zhang, J., Liu, Z., Yin, C., Zhao, C., Li, Z., Yang, Z. and Dou, S., 2018. Geochemical and geochronological study on the Paleoproterozoic rock assemblage of the Xiuyan region: new constraints on an integrated rift-and-collision tectonic process involving the evolution of the Jiao-Liao-Ji Belt, North China Craton. Precambrian Research, 310, pp.179-197.

Logie, M, 1982. Influence of roughness elements and soil moisture on the resistance of sand to wind erosion. In Acidic soils and geomorphic processes: proc. International Conference International Society Soil Science Jerusalem Israel, Mar 19-Apr 4, 1981/DH Yaalon, ed.

Muhs, D.R., 2004. Mineralogical maturity in dunefields of North America, Africa and Australia. Geomorphology, 59(1-4), pp.247-269.

Muhs, D.R., 2017. Evaluation of simple geochemical indicators of aeolian sand provenance: Late Quaternary dune fields of North America revisited. Quaternary Science Reviews, 171, pp.260-296.

Muhs, D.R. and Holliday, V.T., 1995. Evidence of active dune sand on the Great Plains in the 19th century from accounts of early explorers. Quaternary Research, 43(2), pp.198-208.

Muhs, D.R., Ager, T.A., Bettis III, E.A., McGeehin, J., Been, J.M., Begét, J.E., Pavich, M.J., Stafford Jr, T.W. and De Anne, S.P., 2003. Stratigraphy and palaeoclimatic significance of Late Quaternary loess–palaeosol sequences of the Last Interglacial–Glacial cycle in central Alaska. Quaternary Science Reviews, 22(18-19), pp.1947-1986.

Muhs, D.R. and Budahn, J.R., 2019. New geochemical evidence for the origin of North America's largest dune field, the Nebraska Sand Hills, central Great Plains, USA. Geomorphology, 332, pp.188-212.

Nield, J.M. and Baas, A.C., 2008. The influence of different environmental and climatic conditions on vegetated aeolian dune landscape development and response. Global and Planetary Change, 64(1-2), pp.76-92.

Redsteer, M. H., 2020, Sand Dunes, Modern and Ancient, on Southern Colorado Plateau Tribal Lands, Southwestern USA in Inland Dunes of North America ed. by Lancaster, N. and Hesp, P., pp. 287 – 310.

Reheis, M.C., Kihl, R., 1995. Dust deposition in southern Nevada and California, 1984–989: relations to climate, source area, and source lithology. Journal of Geophysical Research 100, 8893–8918.

Reheis, M.C.; Goldstein, H.L.; Reynolds, R.L.; Forman, S.L.; Mahan, S.A.; and Carrara, P.A., 2018. Late Quaternary loess and soils on uplands in the Canyonlands and Mesa Verde areas, Utah and Colorado, Quaternary Research, 89, 718–738.

Riley, K.E., Rittenour, T.M., Pederson, J.L. and Belmont, P., 2019. Erosion rates and patterns in a transient landscape, Grand Staircase, southern Utah, USA. Geology, 47(9), pp.811-814.

Saqqa, W., Atallah, M., 2004. Characterization of the aeolian terrain facies in Wadi Araba Desert, southwestern Jordan. Geomorphology 62, 63–87.

Shafer, J.C. and Steenburgh, W.J., 2008. Climatology of strong intermountain cold fronts. Monthly Weather Review, 136(3), pp.784-807.

Siegal, Z., Tsoar, H. and Karnieli, A., 2013. Effects of prolonged drought on the vegetation cover of sand dunes in the NW Negev Desert: field survey, remote sensing and conceptual modeling. Aeolian Research, 9, pp.161-173.

Sklar, L. and Dietrich, W., 2001. Sediment and rock strength control on river incision into bedrock. Geology, 29, pp. 1087-1090.

Tsoar, H., 2005. Sand dunes mobility and stability in relation to climate, Physica A: Statistical Mechanics and its Applications, v. 357 (1), pp. 50-56

Wang, X., Chen, F. and Dong, Z., 2006. The relative role of climatic and human factors in desertification in semiarid China. Global environmental change, 16(1), pp.48-57.

Wang, C., Liang, X., Xie, Y., Tong, C., Pei, J., Zhou, Y., Jiang, Y., Fu, J., Dong, C. and Liu, P., 2014. Provenance of upper miocene to quaternary sediments in the Yinggehai-Song hong basin, south China sea: evidence from detrital zircon U–Pb ages. Marine Geology, 355, pp.202-217.

Yang, L., Wang, T., Long, H., and He, Z., 2017, Late Holocene dune mobilization in the Horqin dunefield of northern China: Journal of Asian Earth Sciences, v. 138, p. 136–147

Yizhaq, H. and Ashkenazy, Y., 2016, Periodic temporal oscillations in biocrust–vegetation dynamics on sand dunes, Aeolian Research, v. 20, pp. 35-44

CHAPTER 5
CONCLUSIONS AND RECOMMENDATIONS

Research for this dissertation focused on identifying and characterizing Holocene dune activity in two dune fields in southern Utah. A tiered approach to identify dune-field wide activity in each dune field, based on the temporal and spatial distribution of individual dune activity. The chronostratigraphic records were compared to sedimentological records to identify periods of regional dune-field activation. Results were compared with regional and global paleoclimate records to understand implications for natural hydroclimate variability in the drought-sensitive Colorado Plateau region.

In Chapter 2, geomorphic mapping identified study sites in the mostly stabilized, thick parabolic dunes of Kanab dune field. Sediment samples were obtained at regular intervals and analyzed to characterize dune-field stratigraphy and combined with age control from AMS radiocarbon and OSL dating to develop a chronostratigraphic record of dune (re) activation. Age control was obtained from three radiocarbon ages from charcoal samples and 34 OSL ages from 24 study sites. Five dune-field wide eolian events were identified through multiple contemporaneous, spatially distributed sites containing evidence for dune activation. These periods of dune-field reactivation are identified here as: K0 (~7.8-9.2 ka), K1 (~5.6-6.8 ka), K2 (~3.3-4.4 ka), K3 (~1.2-2.2 ka) and K4 (~0.5-0.7 ka). Eolian events identified in Kanab exhibit millennial duration and spacing, with decreased spacing between events in latest Holocene. Due to biogeomorphic response to climate perturbations, dune records may not align with higher resolution records of high-frequency climate variability. Drought occurring before or near the initiation of dune activity could be linked, but could not be tested due to the difference in resolution of the records. Because of this, dune-field wide activity at Kanab does not exhibit close correlation to periods of multi-decadal aridity identified in regional tree ring records. Comparison

with paleoclimate records suggests a connection with Bond events 5, 4, 2, 1 and 0 (Bond et al, 2001) as well as increased ENSO activity (Moy et al, 2002; Conroy et al, 2008) suggesting linkage with North Atlantic and Western Pacific warming.

Chapter 3 reports results of geomorphic mapping and dating of in San Rafael dune field which is characterized primarily by thin eolian deposits in stabilized and partially stabilized sand sheets and units of stabilized to active sand dunes. Sediment samples were collected from 22 study sites and used to develop a dune field stratigraphy and a Holocene chronology of dune activity using OSL dating of 33 age samples. Seven episodes of dune-field wide activity were identified using activity identified in multiple samples from coeval, spatially distributed sites. Periods of activity were identified as: SR0 (~16.2-17 ka), SR1 (~11.2-12.6 ka), SR2 (~7.4-9.7 ka), SR3 (~4.7 ka), SR4 (~2.5-3.4 ka), SR5 (~1.6-2 ka), and SR6 (~0.4-1.1) ka. Overlapping instances of dune-field wide activity in both San Rafael and Kanab dune fields was interpreted as region-wide dune activation and interpreted as a regional hydroclimate perturbation. The overlapping nature of the record, rather than coincidence to inception and cessation of events, suggests differential biogeomorphic response to climate perturbations occurs in the two dune fields. Dune activity at KDF and SRD was compared to regional mobile dune records. These records suggest as many as five region-wide episodes of dune activation may have occurred.

In Chapter 4, records from ten climate stations were analyzed using methods developed by Fryberger (1979) to characterize the modern wind potential for sand drift proximal to the study dune fields. Analytical results of the modern wind regime indicate similar threshold wind directions as identified in the Holocene dune forms. Chapter 4 also reviews geochemical records from the dose-rate geochemistry obtained for OSL dating. Ratios of K/Rb to K/Ba for samples of Kanab dune field were compared with those from rock samples obtained from proximal locations of the Jurassic Navajo Formation, Pink and White members, and the Jurassic Kayenta Formation. Results suggest the Navajo Formation, hypothesized here due to proximity of the White Cliffs to the Kanab dune field, is a consistent match with the dune sediments (Muhs, 2017). Similarly, the

Jurassic Entrada Formation may be a source for the San Rafael dune sediments. Using representative samples from each dune event in Kanab dune field, K/Rb-K/Ba ratios were reviewed to identify potential change in source rock through time. There is no discernable change in source rock through the Holocene time investigated for Kanab dune field. This may in part be due to the inherited mineralogical maturity (quartz-rich) of the dune sediment, from the Navajo Formation. Results were similar for the San Rafael dune field, with no evidence for change through Holocene time of the source rock for the dune sediment.

Results of this study suggest that a systematic, targeted approach to sampling a dune field is a useful tool to develop a record of dune activation within the dune field that may reduce the potential of sampling bias and improve the recovery of paleoclimate records from these ephemeral geomorphic landforms. Recovery of longer records can inform understanding of the relative impact of threshold conditions and may contribute to better understanding of the nature of the lag response in individual dune fields. In addition, modern wind data from localized climate stations, may provide insight into Holocene wind conditions and dune field activation.

The culmination of this research has revealed considerable information about the studied dunefields, but has also disclosed some additional avenues for future investigation. Future research directions could include systematic investigation of the Pleistocene dune activity preserved in the San Rafael dune fields, and detailed investigation of the soil development and coppice dune record preserved in the eolian sand sheets. Additional research questions might consider what is the seasonal variability in the wind regimes for Kanab and San Rafael dune fields and what are the implications for the predicted warming trends in this region? What are the different threshold controls in the Coral Pink and Kanab dune fields and do these two nearby dune fields share a Holocene or older history? How will predicted warming/aridity in the central Colorado Plateau impact dune stabilization and sediment supply? An important question is how ongoing human activities in dune fields with high drift potential (such as Kanab and San Rafael)

may impact dune stability due to ongoing anthropogenic climate change, and what that suggests for resource management of these lands.

More broadly, on a technical note, dune fields such as these are commonly challenging to access and frequently located in areas sensitive to disturbance because of archaeological records, sensitive ecological systems, or simply the risk of exacerbating destabilization. Additionally, due the upper loose sediment is always a contamination risk for obtaining pristine age samples for luminescence dating. Hand augering systems were used to obtain many of the sediments collected for dating and analysis in this study. Because the augering process destroys stratigraphic evidence, maintaining an accurate record of the depth from surface is particularly important to interpreting the stratigraphy. A collared hole is a simple, portable and cost-effective solution, and proved useful in this investigation. The collar also provides protection from surface winds or loose footing that causes contamination down the auger hole by surface sediments. Further details on this and other key information for sampling and of cores for luminescence are detailed by Nelson et al (2019).

Finally, luminescence dating has been an important tool to investigate the history of eolian systems, and to understand many geomorphic landscape processes. But not all quartz, even eolian-derived quartz, responds ideally. Additional work to compare the response in different grain size fractions from a low-sensitivity deposit such as Kanab dune sediments, and other lines of inquiry may develop early in a project. Pursuing questions that can enhance understanding of this important dating tool are also important lines of future research.

References

Bond, G., Showers, W., Cheseby, M., Lotti, R., Almasi, P., DeMenocal, P., Priore, P., Cullen, H., Hajdas, I. and Bonani, G., 1997. A pervasive millennial-scale cycle in North Atlantic Holocene and glacial climates. science, 278(5341), pp.1257-1266.

Conroy, J., Overpeck, J.T., Cole, J.E., Shanahan, T.M., Steinitz-Kannan, M., 2008. Holocene changes in eastern tropical Pacific climate inferred from a Galapagos Lake sediment record, Quaternary Science Reviews, 27, 1166-1180

Fryberger, S.G.; 1979, Dune Forms and Wind Regimes. In A Study of Global Sand Seas; McKee, E.D., Ed.; U.S. Geological Survey: Reston, VA, USA, 1979; pp. 137–169

Muhs, D.R., 2017. Evaluation of simple geochemical indicators of aeolian sand provenance: Late Quaternary dune fields of North America revisited, Quaternary Science Reviews, Volume 171, Pages 260-296.

Nelson, M., Rittenour, T., Cornachione, H, 2019. Sampling methods for luminescence dating of subsurface deposits from cores. Methods and Protocols 2, 88, doi:10.3390/mps2040088.

APPENDICES

APPENDIX A. SAMPLE COLLECTION METHODS

Appendix A. Sample Collection Methods.

Sediment Sampling

Map coordinates and surface elevation were obtained for each site using a hand-held Garmin Rino GPS, Model 520-530HCx, and the site location was described, sketched, and photographed. Sediment samples were obtained either by trench/natural exposure or by hand auger. Exposed surfaces were cleared of loose surficial debris and sediment using a shovel and / or trowel. Sediment samples were obtained at 20-cm intervals or as closely as possible based on exposure thickness, observed stratigraphic changes including but not limited to grain size, color and sedimentary structure. Field data collected for each sediment sample included grain size, color, sorting and rounding, and effervescence when exposed to HCl (10% solution). Other features noted were nature and presence of organic material and sedimentary structures.

A hand auger was used where natural exposures were not available and in sensitive areas of the dune field requiring minimally invasive sampling. Auger sediment samples were collected using an open face Edelman soil auger (6.8 cm x 20 cm). Sediment samples were obtained at 20 to 30-cm intervals and placed on a tarp for field description and bagged for particle size analysis (Nelson et al, 2019). To prevent contamination of samples by surface sediment, sites were prepared by removing loose surface sediment to prepare a hand-excavated platform or by emplacing a polyvinylchloride (PVC) collar that extended above the surface by 10 cm (Figure SM-2.1). The PVC collar provided a standard measuring platform to determine sample depth for auger samples.

Figure SM-2.1 Sediment sampling with auger. Row 1 shows extraction of sediment sample, moist dune soil, from cleared platform base, Kanab, UT: a) starting auger hole; b) measuring depth to sample; c) careful vertical extraction, avoiding sidewall disturbance; d) emplacing sediment sample for geologic description and sample collection. Row 2 shows use of PVC collar with cleared platform in dry dune soil conditions, San Rafael desert, UT: a) platform cleared, collar emplaced for measurement with duct tape; b) starting auger hole; c) measuring depth to sample.

Optically Stimulated Luminescence Sampling

Age control for dune activity is obtained primarily from optically stimulated luminescence (OSL) dating, a method first used in quartz grains (63-250 µm) by Huntley et al (1985). OSL provides reliable age estimates to 200,000 years or more in most settings (Rhodes, 2011). OSL dating is based on the loss of charge from traps in a mineral lattice with exposure to sunlight or heat (200-400^{o}C), termed “bleaching” or “zeroing”, and the gradual reacquisition of charge after the grain is buried and exposed to ionizing radiation in the surrounding sediments, referred to as the dose rate (Dr) (Aitken, 1998). An equivalent dose (De) measurement is made on individual aliquots or grains, stimulated by blue-green light-emitting diodes (LEDs) or green laser respectively, and calibrated to a laboratory dose of beta radiation (Aitken, 1989; Duller, 2006). The age of the sample is determined by dividing the average De in SI units of Grays (Gy, where 1 Gy = 1 J-kg-1) by the environmental dose rate (Gy yr-1) (Aitken, 1998).

Sample age (yr) = De (Gy) / dose rate (Gy yr-1) (Eq. 1)

Successful results from OSL dating are dependent on preserving sample integrity (i.e., avoiding exposure to light or heat, avoiding contamination through biological or mechanical processes such as bioturbation) and collecting representative surrounding sediment to determine dose rate and moisture content. Improved OSL characteristics are typically obtained from sediment deposited in environments that promote full bleaching prior to burial, such as exposure to full sun.

Samples for optically stimulated luminescence (OSL) dating were obtained following standard protocols for sediment samples as described in Nelson et al (2015). Specifically, sample collection tubes were 3.75 cm diameter x 20 cm length, plugged with a compressible foam wedge to help securely pack sediments in tube, and fitted with black vinyl end caps in the field. Separate, representative dose rate samples were collected from an approximately 30 cm diameter around each coring tube, as well as a representative moisture content sample compacted into an air-tight container. Water content was measured within a week of collection.

A hand auger was used where natural exposures were not available and in sensitive areas of the dune field requiring minimally invasive sampling. An AMS soil sampler (14.5 cm x 51 cm) with aluminum tube liner (5 cm x 20 cm), pre-packed with a foam wedge to ensure sediment packing in the tube, was used to collect OSL samples. Black vinyl caps were placed on each end of the OSL sample tube as it was extracted from the soil sampler to prevent exposure to light, and sealed with duct tape, following protocols from Nelson et al (2019). Sediment samples immediately above and below the OSL sample were collected for moisture content and dose rate analysis. Water content was analyzed within a week of collection.

Each exposure site was sampled for OSL based on the stratigraphy observed in the field, such as evidence for buried soils and changes in grain size, color and sorting. Thirty-four OSL samples were collected from 23 locations. Of these, six samples were collected from five sites

during a previous field investigation, but not previously analyzed. Samples were collected from natural exposures (n=1) and using a soil auger with coring capability (n=33).

Sampling for Radiocarbon Dating

Where encountered in stratigraphic context, charcoal samples were obtained for radiocarbon dating. Charcoal sample collection was conducted carefully, to avoid direct contact with other organic substances including skin, and stored in aluminum foil to avoid contamination and protect the sample from crushing. Samples were carefully removed from foil, and examined under a binocular microscope. Single charcoal pieces at least 1 mm in diameter were stored in glass vials and later sent for radiocarbon dating at the University of Georgia AMS Laboratory.

APPENDIX B. ANALYTICAL METHODS

Appendix B. Analytical Methods.

Laser Particle Size Analysis

Each sample was dried and sieved to capture the >1.0 mm fraction. The <1.0 mm fraction was analyzed using a Malvern Mastersizer 2000 laser particle size analyzer. Each homogenized sample was sub-sampled into 3 aliquots and added to the Malvern sample beaker of DI H_20 until ~10% laser obscuration was reached. Samples were then sonicated for 60s to ensure (aggregated) particles dispersed completely. Pump speed was set to 3000 rpm to ensure suspension of all particles and transport past the detection window. The instrument collected diffraction data over three, 30-second intervals and reported as separate data points. This was repeated for 3 aliquots of each sample, producing a total of 9 analyses per sample.

Total Organic Content Analysis

First, loss on ignition (LOI) was performed on 14 samples to obtain an estimate of the range of carbon content in the samples, at the USU Geochemistry Laboratory. A dry sediment sample mass of approximately 4 g was placed in a ceramic crucible of known mass. The filled crucible was then placed in a furnace at 550^{o}C and ignited for 2 hours. After 2 hours, the crucible was removed, cooled in a desiccator for 2 hours, then weighed. The crucible (with sample) was then returned to the furnace at 950^{o}C and ignited overnight. The following morning the filled crucible was removed from the furnace, cooled for 2 hours in a desiccator and then weighed. The total organic carbon was calculated using the ratio of the sample mass measured at 550^{o}C to the original sample mass. The total inorganic carbon was determined using the ratio of the difference between the sample mass after ignition at 550^{o}C and at 950^{o}C.

Next the sediment samples were analyzed for percent carbon and carbon isotope ratio (δ^{13}C). The USU Geochemistry-Stable Isotope lab uses a Costech 4010 Elemental Combustion Analyzer System (ECS) to obtain nitrogen and carbon content. The ECS is coupled to a Thermo-scientific Delta V isotope ratio mass spectrometer (IRMS) that measures isotopic fractions. The

coupled ECS-IRMS system allows the user to obtain measurements on both percent nitrogen and carbon, and $\delta^{15}N$ and $\delta^{13}C$ ratios in a single run. Percent nitrogen and carbon values are measured and calculated by a thermal conductivity detector (TCD) in the Costech ECS. From here, the gas stream is connected via an open-split connection to the Delta V IRMS. In the IRMS, the nitrogen peak elutes first, then a fast magnet jump to CO2 mass configuration is performed. Next, the carbon dioxide sample gas peak is eluted and integrated. The $\delta^{15}N$ ratios are determined from the peak amplitudes of masses 28 and 29 only and expressed in per mil notation (‰) as compared to the atmospheric AIR nitrogen standard. The $\delta^{13}C$ value is measured on CO_2 gas using amplitude of masses 44, 45, and 46 and expressed as a per mil (‰) value compared to the Vienna Pee Dee Belemnite (VPDB) isotope ratio standard.

Percent nitrogen and carbon values are calculated by the Costech TCD detector and calculated from the theoretical recovery of a lab acetanilide standard corrected for mass linearity. Precision of %N and %C is **±0.5 %.** Raw isotope data from this method is corrected for linearity and instrumental drift, and calibrated to lab working standards (calibrated annually to international reference standards). Lab working standards are a pair of Glycine powders (Glycine-normal and Glycine-13) having very different isotopic values and the international reference isotopic standards that we calibrate to for carbon and nitrogen are the **USGS 40** and **USGS 41** L-Glutamic acid standards. The isotope ratio precision reported is based on time-averaged L-Glutamic acid lab standard daily triplicate analysis. Precision for $\delta^{15}N$ values is **±0.20 ‰,** and the precision for $\delta^{13}C$ values is **±0.15 ‰.**

For this study, results of the LOI analysis guided the sample size, selection of standards, and specific modifications to the general laboratory procedure as described above, to better address the low organic content in the dune sediment samples. Sediment samples (n=114) were split to obtain a small packet of ~100 g for processing in the USU Geoscience Geochemistry lab on the ECS – IRMS coupled system. Sediment subsamples (~60 mg) and standard materials (acetanilide, glycine normal and glycine-13, low TOC soil) were weighed and encapsulated in tin

metal capsules prior to analysis. Due to the very low organic carbon content in the sediment samples, all standards were weighed at half-size to obtain lower N-and C-values for the calibration standards that more closely match the expected sample values. Multiple linearity standards were also weighed to account for super low and "high" carbon values. A modified sequence for low TOC materials was used for the IRMS analysis. This sequence changes the standard gas peak dilution and sample dilution to accommodate expected low carbon values from the study sediments.

Samples were dropped via an auto-sampler into the ECS and burned in presence of pure oxygen at 1,000°C. Combustion gasses were then passed over chromium oxide and silvered cobaltic/ous mixed oxides with a helium carrier gas stream to facilitate complete oxidation. The sample gas stream passed through a tube containing metallic copper at 850°C which removed excess oxygen and any nitrogen oxide species. Sample gasses then passed through a GC column at 50°C to separate nitrogen gas from carbon dioxide gas after passing through a trap to remove water gas.

Raw isotope data obtained for the study samples was then corrected for linearity and instrumental drift, and calibrated to the run standards. Percent nitrogen and carbon were obtained for each sample run. Although nitrogen content and isotopic ratios were obtained for the study samples, the values were at or below background and are not reported here.

Radiocarbon Analysis

Charcoal samples meeting a minimum 1 mm standard size (n=3) were radiocarbon-dated to provide additional independent age evidence of dune activity. Samples were processed using accelerated mass spectrometry (AMS) at the University of California – Berkely and the Center for Applied Isotope Studies at University of Georgia. The charcoal sample was treated with 5% HCl at the temperature 80°C for 1 hour, then washed with deionized water on the fiberglass filter and rinsed with diluted NaOH to remove possible contamination by humic acids. After that it was treated with diluted HCL again, washed with deionized water and dried at 60°C. For accelerator

mass spectrometry analysis, the cleaned samples were combusted at 900°C in evacuated / sealed ampoules in the presence of CuO. The resulting carbon dioxide was cryogenically purified from the other reaction products and catalytically converted to graphite using the method of Vogel *et al*. (1984) Nuclear Instruments and Methods in Physics Research B5, 289-293. Graphite 14C/13C ratios were measured using the CAIS 0.5 MeV accelerator mass spectrometer. The sample ratios were compared to the ratio measured from the Oxalic Acid I (NBS SRM 4990). The sample $^{13}C/^{12}C$ ratios were measured separately using a stable isotope ratio mass spectrometer and expressed as $\delta^{13}C$ with respect to PDB, with an error of less than 0.1‰. Uncalibrated dates are reported in radiocarbon years before 1950 (years BP), using the ^{14}C half-life of 5568 years. The error is quoted as one standard deviation and reflects both statistical and experimental errors. The date has been corrected for isotope fractionation.

Optically Stimulated Luminescence Analysis

Sample Processing

Thirty-four eolian sediment samples from twenty-three sites processed and analyzed at the Utah State University Luminescence Laboratory in Logan, Utah for optically stimulated luminescence (OSL) dating. Sediment cores and sample tubes were opened under dim amber light (~590 nm) and sieved to a narrow grain size target between 150 and 250 μm (see Table 1 for details). The outer 2.5 cm of sediment at the outer edges of each sample tube were discarded to remove any grains potentially exposed to light during sampling. The quartz mineral fraction was isolated by using 10-30% v/v hydrochloric acid to dissolve carbonates and bleach to remove organic material. Quartz grains were isolated from higher density minerals using sodium polytungstate (2.7 g/cm^3), followed by concentrated hydrofluoric and hydrochloric acid treatments to remove feldspars, etch the outer surface of the grains, and prevent formation of fluorite precipitates (Wintle, 1997). The samples were then dry sieved to remove the <75 μm

fraction of etched quartz and any partially dissolved feldspars. Purity of the samples was checked using infrared (IR) stimulation for all aliquots.

Dose Rate Processing and Calculation

Dose rate sample processing involved homogenizing the sediment and down-sampling to ~30 grams of sediment. For hand-augered OSL samples collected in core liners, 20 cm auger drives above and below the OSL sample. For tube samples, sediment for dose rate samples was uniformly collected within 15 cm of the OSL tube. Representative subsamples (~30 grams) of bulk sediment were analyzed using ICP-MS and ICP-AES analyses for concentrations of radioelements K, Rb, Th, and U. In-situ gravimetric moisture content was measured on all samples (Supplemental Data – Table 2.3). Given the variation in moisture conditions over the sampling seasons, an average of 5±2% was used as the moisture content in dose rate calculations for all samples (Nelson and Rittenour, 2015).

Dose-rate calculations include conversion factors from Aitken (1989) and Guérin et al. (2011), the influence of water attenuation, cosmic contribution by using sample depth, elevation, and longitude/latitude following Prescott and Hutton (1994), and uncertainty in elemental measurements.

Optical Measurements

Luminescence measurements were performed on two Risø TL/OSL Model DA-20 readers equipped with blue-green light emitting diodes (LED) (470±30 nm) and reader dose rates of 0.09-0.11 Gy/sec from a decaying ^{90}Sr beta radiation source (Bøtter-Jensen et al., 2003). The single-aliquot regenerative (SAR) dose protocol of Murray and Wintle (2000) was followed for OSL dating on quartz sand (150-250 μm) loaded onto 2 mm diameter small-aliquots (~20-40 grains per disk). Temperature (preheat) conditions were held constant at 220°C for 10 seconds prior to the natural, regenerative and test doses based on dose recovery data (Figure 2.4). A

220°C optical bleach (470 nm) was held for 40-60 seconds following each test dose OSL measurement to remove any remaining charge build up from the previous dosing cycle (Wintle and Murray, 2006). The luminescence signal was measured through 7.5-mm Hoya ultraviolet filters (U-340) over 40-52 seconds (250 channels) at 125°C with LED diodes at 70% power (30-35mW/cm^2 at the sample position, reader dependent) and calculated by subtracting the average of the last 5-6 seconds (220-250 channels: background signal) from the first 0.6-0.8 seconds (1-4 channels: peak signal) of the signal decay curve. Dose response curves were fit within linear or saturating-exponential fits to calculate D_E values.

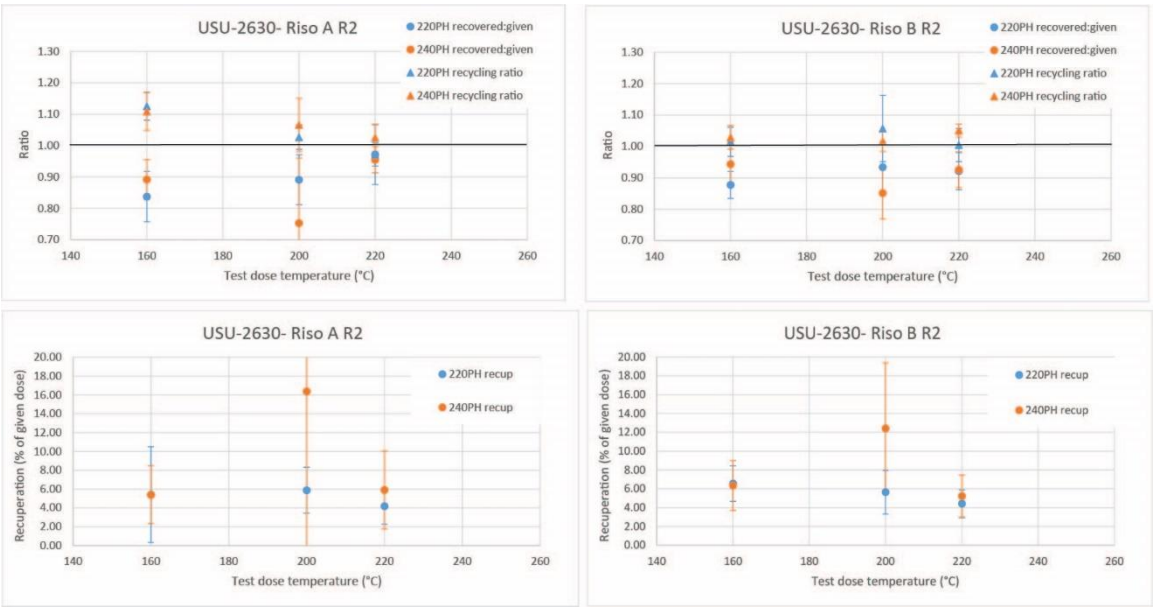

Figure 2.4. Dose recovery test results for USU-2630. Two readers were used for analyses: Riso A installed in 2006 and Riso B installed in 2009. The given beta dose for Riso A was 9.72 Gy and 9.48 Gy for Riso B. 'R' is regenerative dose number in SAR protocol, dose recovery D_E is fit with linear regression between the origin and R2. Beta doses: Riso A R2 = 19.45 Gy; Riso B R2 = 18.96 Gy. The ratio of recovered dose to given beta dose, and recycling ratio of repeat regenerative doses in the SAR protocol are shown in the upper plots. Temperature pairs (regen. preheat and test dose preheat [cutheat]) that produce results closest to 1.0 are 220°C PH and 220°C CH. Additionally, recuperation shown in bottom plots is lowest at the 220°C cutheat temperature. Recuperation in these tests is consistently >5% thus a 220°C optical bleach was added at the end of each SAR cycle to remove remaining charge build up during dosing and heating cycles.

Equivalent Dose (D_E) and Error Calculation

Cumulative D_E values were calculated using the central age model (CAM) of Galbraith and Roberts (2012) (Figure 2.4 and Supplemental Data – Table 2.4). Aliquots were rejected if they had evidence of feldspar contamination, recycling ratio <0.7 or >1.3, natural D_E greater than the highest regenerative dose given, large (>100%) D_E error and/or $D_E \leq 0$ Gy. Errors on D_E and age estimates are reported at 1-sigma standard error and include errors related to instrument calibration, and dose rate and equivalent dose calculations and were calculated in quadrature using the methods of Aitken and Alldred (1972) and Guerin et al. (2011).

APPENDIX C. GRAPHICAL CHRONOSTRATIGRAPHIC RECORDS

Appendix C. Kanab Dune Field, Utah. Graphical Chronostratigraphy (W-E)
Note: Stratigraphy ordered by geomorphic map unit / presumed age, older to younger.

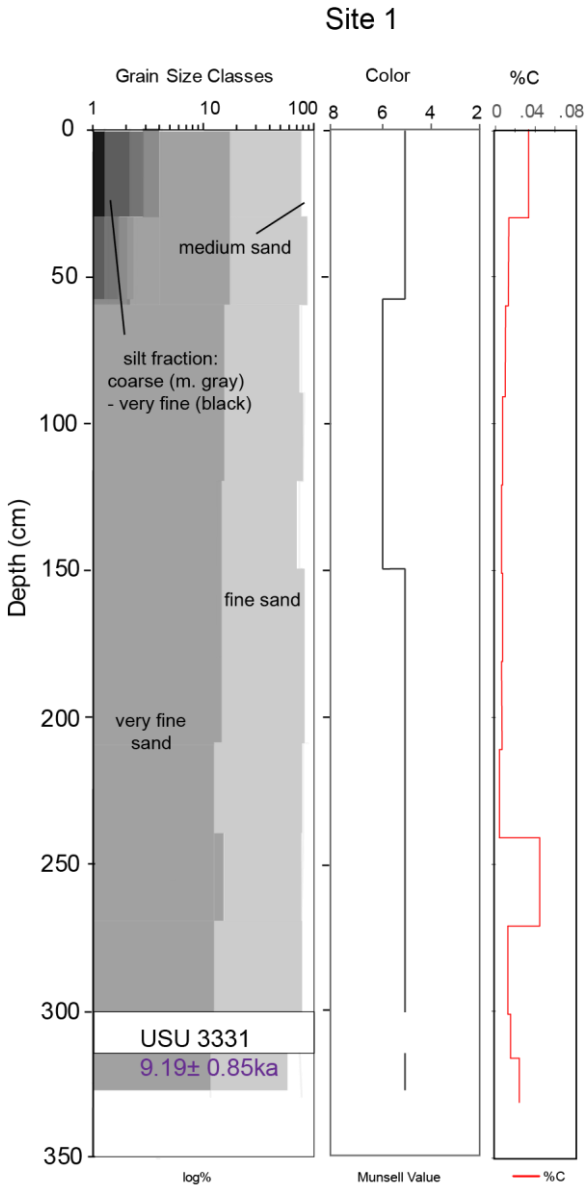

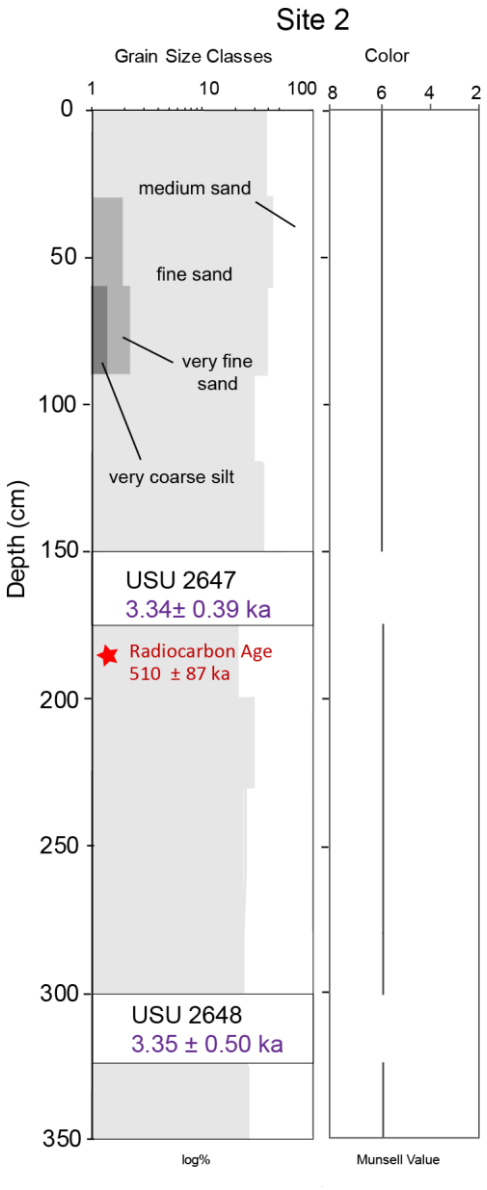
Site 2
Grain Size Classes
Color
1
10
100
8
6
4
2
0
50
100
150
200
250
300
350
Depth (cm)
medium sand
fine sand
very fine sand
very coarse silt
USU 2647
3.34± 0.39 ka
Radiocarbon Age
510 ± 87 ka
USU 2648
3.35 ± 0.50 ka
log%
Munsell Value

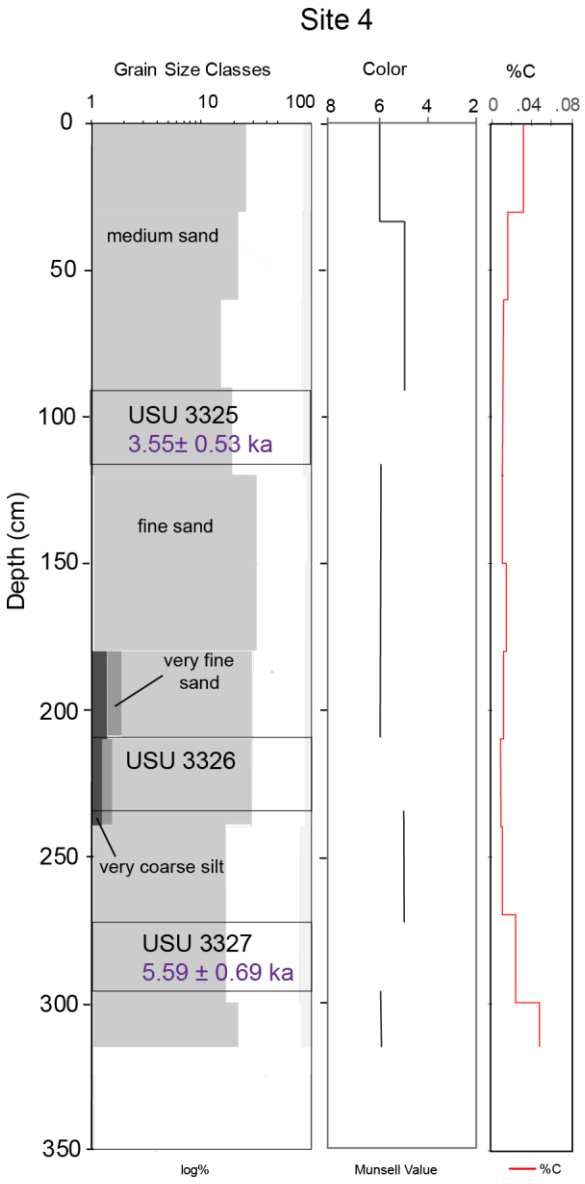
Site 4
Grain Size Classes
Color
%C
1
10
100
8
6
4
2
0
.04
.08
0
50
100
150
200
250
300
350
Depth (cm)
medium sand
USU 3325
3.55± 0.53 ka
fine sand
very fine sand
USU 3326
very coarse silt
USU 3327
5.59 ± 0.69 ka
log%
Munsell Value
%C

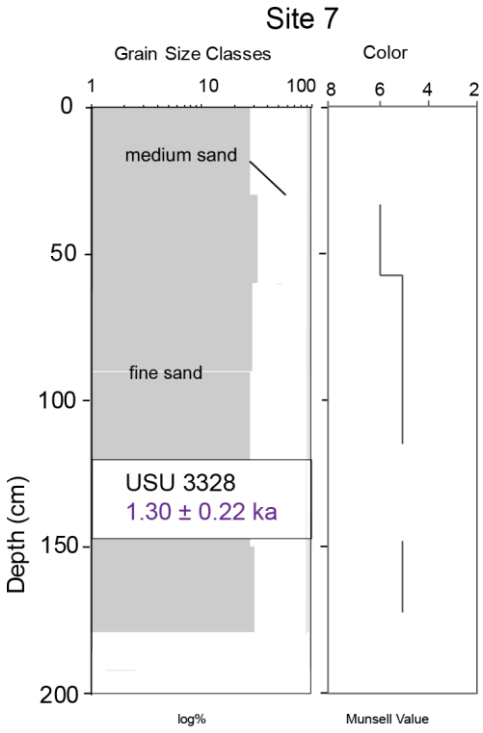
Site 7
Grain Size Classes
Color
1
10
100
8
6
4
2
0
50
100
150
200
Depth (cm)
medium sand
fine sand
USU 3328
1.30 ± 0.22 ka
log%
Munsell Value

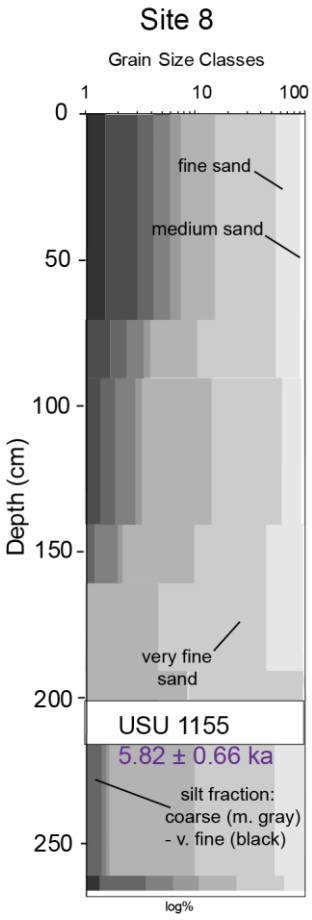
Site 8
Grain Size Classes
1
10
100
0
50
100
150
200
250
Depth (cm)
fine sand
medium sand
very fine sand
USU 1155
5.82 ± 0.66 ka
silt fraction:
coarse (m. gray)
- v. fine (black)
log%

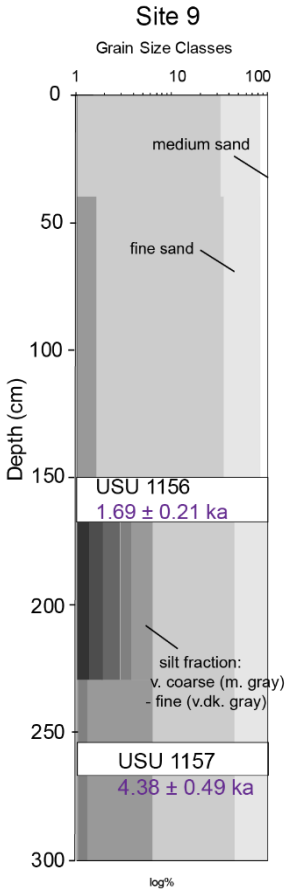
Site 9
Grain Size Classes
1
10
100
0
50
100
150
200
250
300
Depth (cm)
medium sand
fine sand
USU 1156
1.69 ± 0.21 ka
silt fraction:
v. coarse (m. gray)
- fine (v.dk. gray)
USU 1157
4.38 ± 0.49 ka
log%

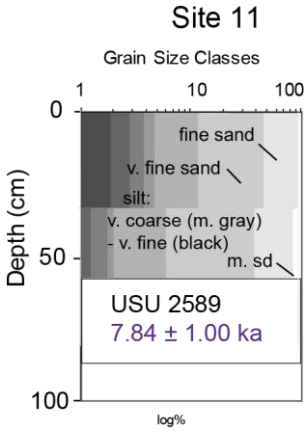
Site 11
Grain Size Classes
1
10
100
0
50
100
Depth (cm)
fine sand
v. fine sand
silt:
v. coarse (m. gray)
- v. fine (black)
m. sd
USU 2589
7.84 ± 1.00 ka
log%

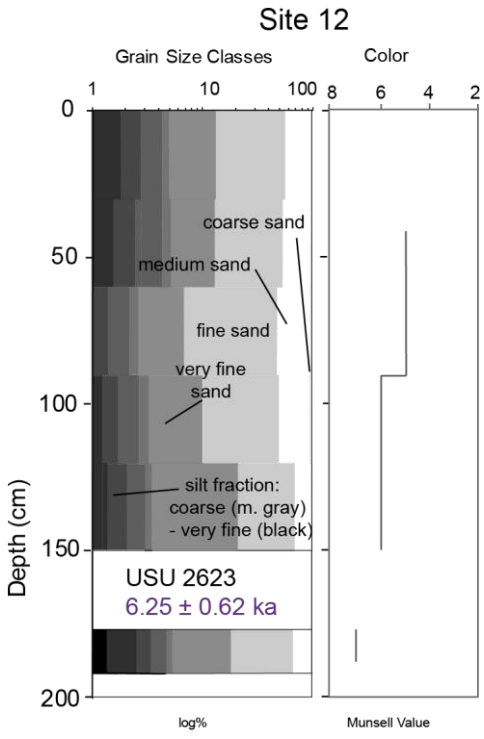
Site 12
Grain Size Classes
Color
1
10
100
8
6
4
2
0
50
100
150
200
Depth (cm)
coarse sand
medium sand
fine sand
very fine sand
silt fraction:
coarse (m. gray)
- very fine (black)
USU 2623
6.25 ± 0.62 ka
log%
Munsell Value

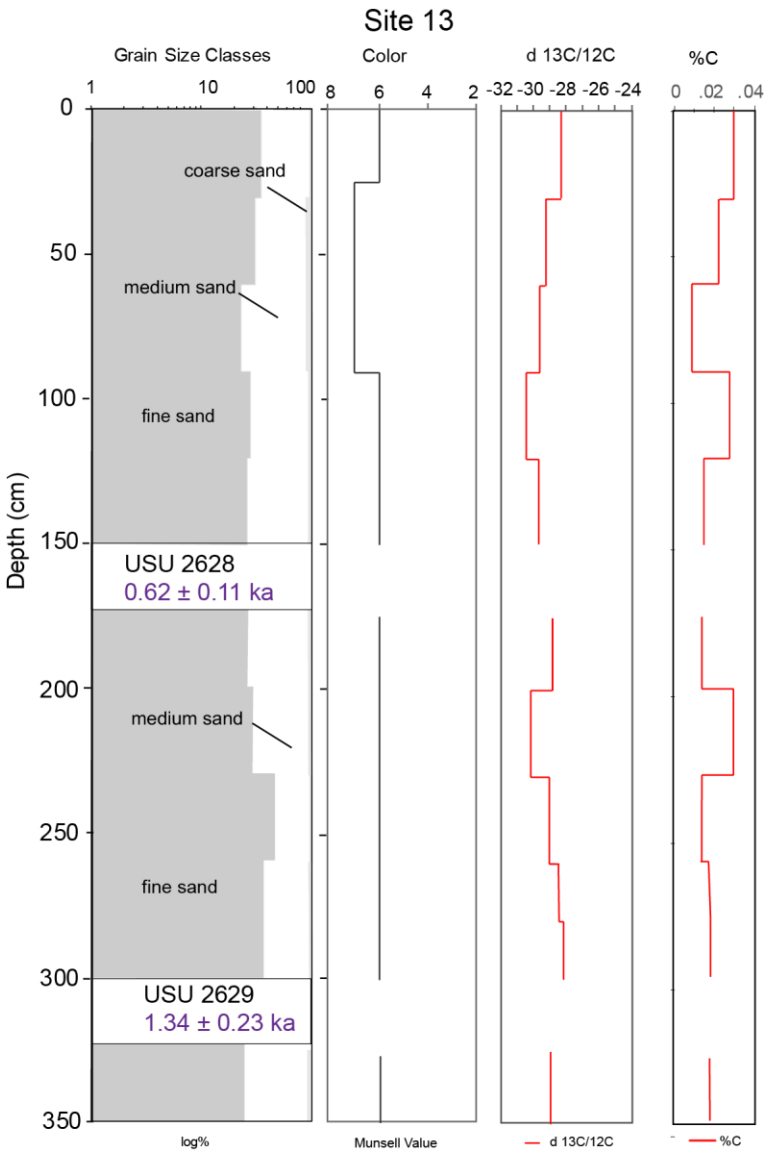
Site 13
Grain Size Classes
Color
d 13C/12C
%C
1
10
100
8
6
4
2
-32
-30
-28
-26
-24
0
.02
.04
0
50
100
150
200
250
300
350
Depth (cm)
coarse sand
medium sand
fine sand
USU 2628
0.62 ± 0.11 ka
medium sand
fine sand
USU 2629
1.34 ± 0.23 ka
log%
Munsell Value
d 13C/12C
%C

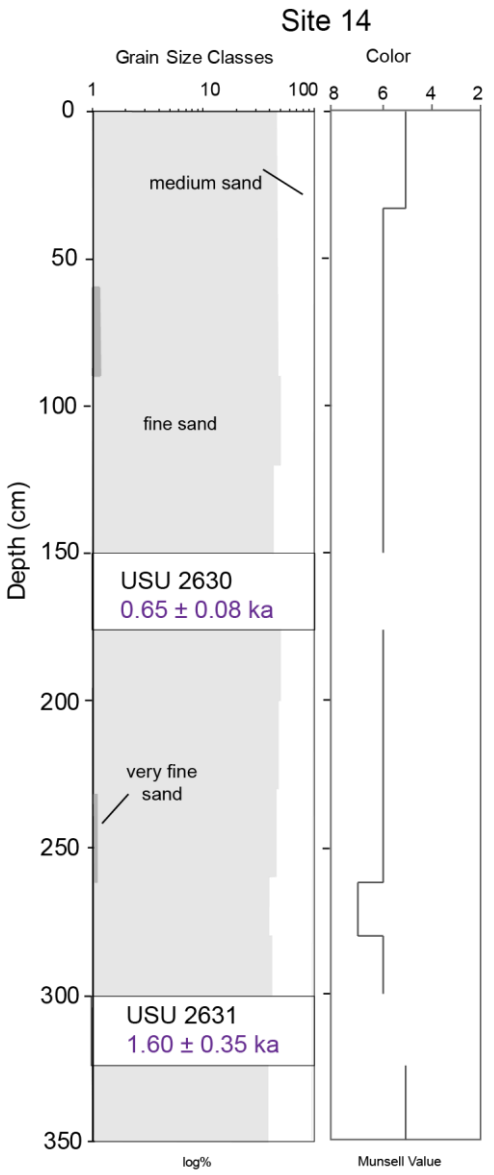
Site 14
Grain Size Classes
Color
1
10
100
8
6
4
2
0
50
100
150
200
250
300
350
Depth (cm)
medium sand
fine sand
very fine sand
USU 2630
0.65 ± 0.08 ka
USU 2631
1.60 ± 0.35 ka
log%
Munsell Value

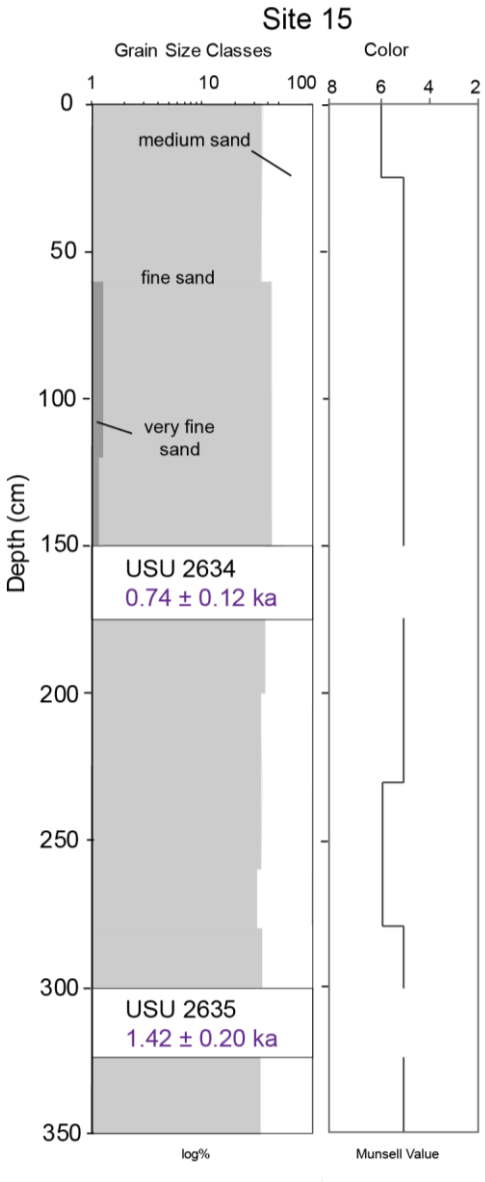
Site 15
Grain Size Classes
Color
1
10
100
8
6
4
2
0
50
100
150
200
250
300
350
Depth (cm)
medium sand
fine sand
very fine sand
USU 2634
0.74 ± 0.12 ka
USU 2635
1.42 ± 0.20 ka
log%
Munsell Value

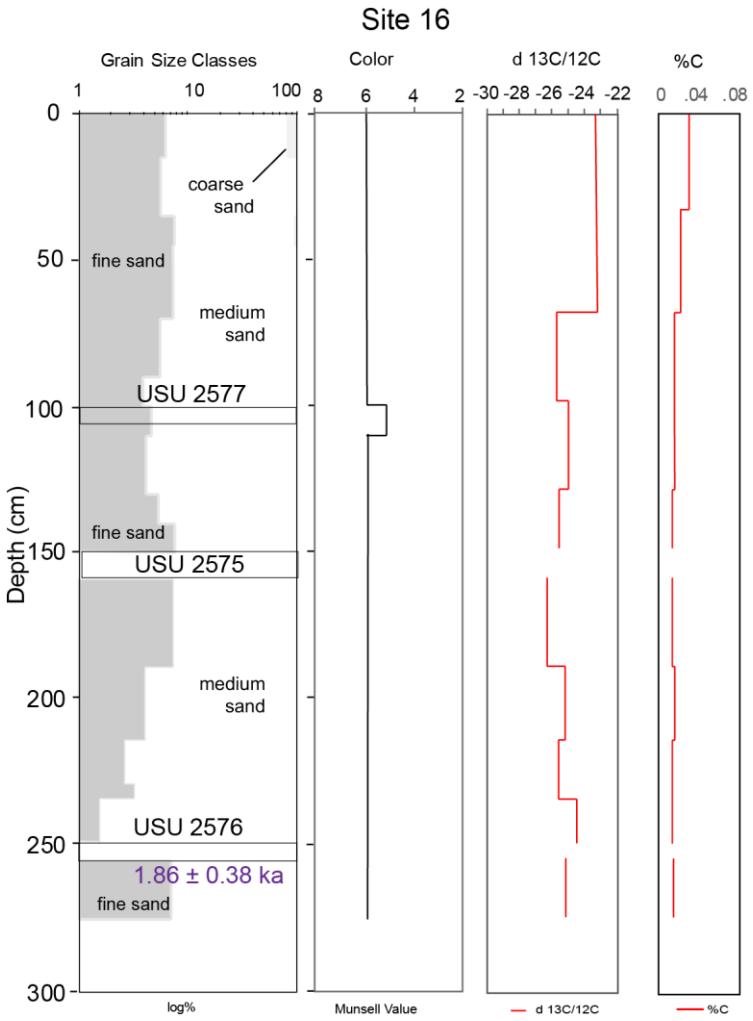
Site 16
Grain Size Classes
1
10
100
Color
8
6
4
2
d 13C/12C
-30 -28 -26 -24 -22
%C
0
.04
.08
Depth (cm)
0
50
100
150
200
250
300
coarse sand
fine sand
medium sand
USU 2577
fine sand
USU 2575
medium sand
USU 2576
1.86 ± 0.38 ka
fine sand
log%
Munsell Value
d 13C/12C
%C

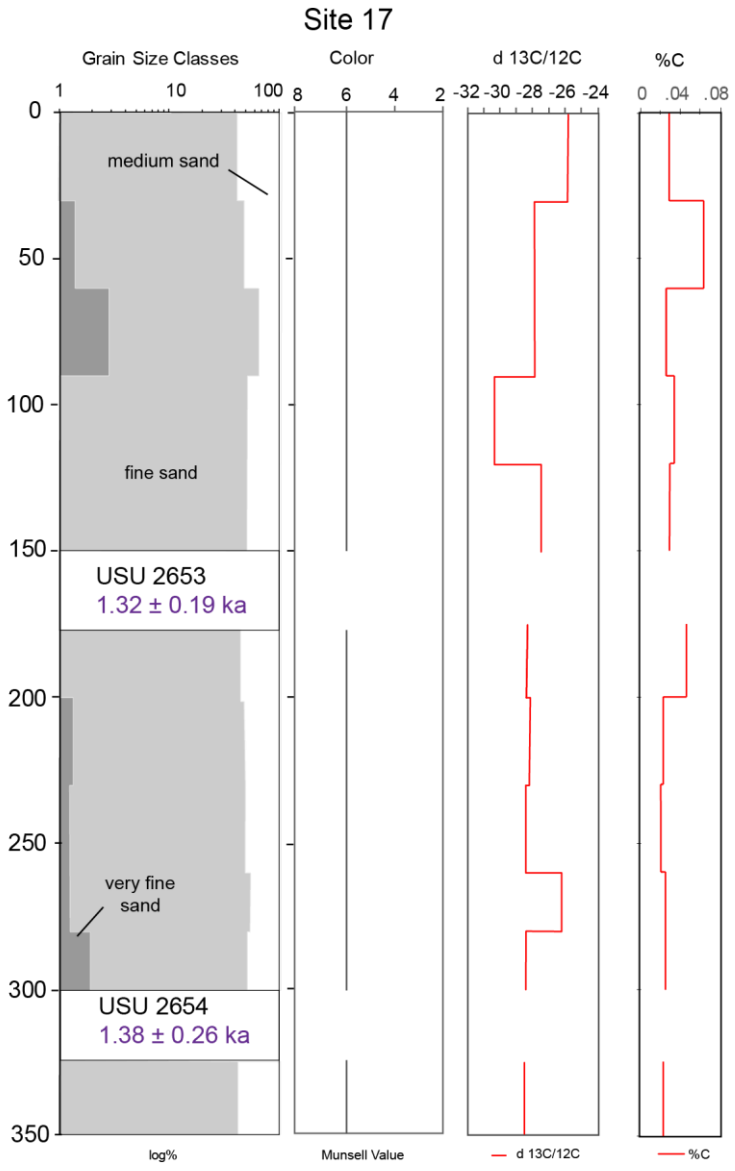
Site 17
Grain Size Classes
1
10
100
Color
8
6
4
2
d 13C/12C
-32 -30 -28 -26 -24
%C
0 .04 .08
0
50
100
150
200
250
300
350
medium sand
fine sand
USU 2653
1.32 ± 0.19 ka
very fine sand
USU 2654
1.38 ± 0.26 ka
log%
Munsell Value
d 13C/12C
%C

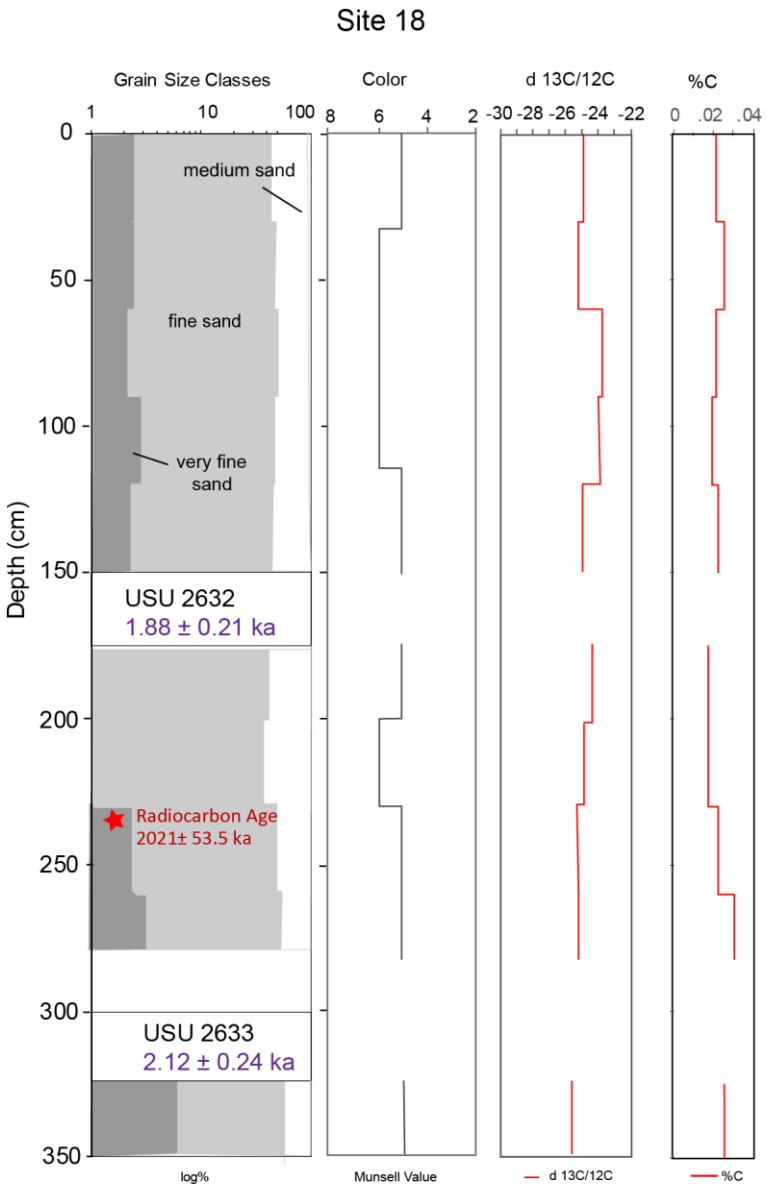
Site 18
Grain Size Classes
1
10
100
Color
8
6
4
2
d 13C/12C
-30 -28 -26 -24 -22
%C
0 .02 .04
Depth (cm)
0
50
100
150
200
250
300
350
medium sand
fine sand
very fine sand
USU 2632
1.88 ± 0.21 ka
Radiocarbon Age
2021± 53.5 ka
USU 2633
2.12 ± 0.24 ka
log%
Munsell Value
d 13C/12C
%C

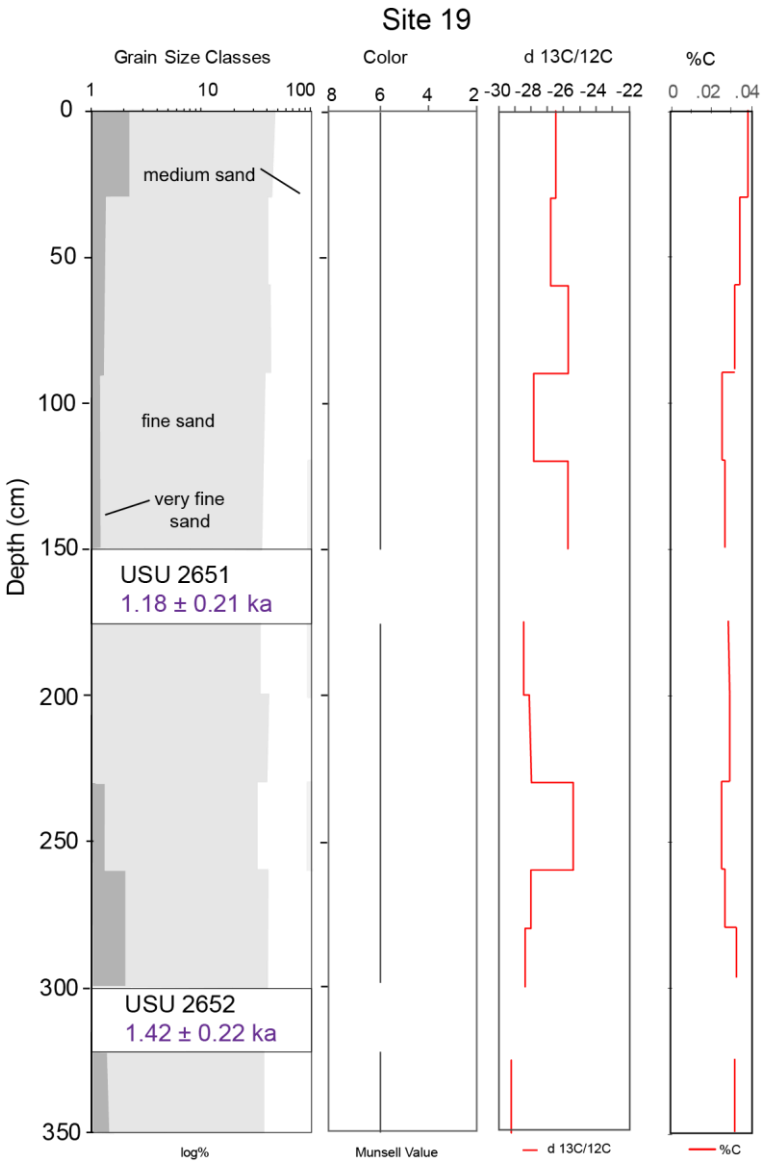
Site 19
Grain Size Classes
Color
d 13C/12C
%C
1
10
100
8
6
4
2
-30
-28
-26
-24
-22
0
.02
.04
0
50
100
150
200
250
300
350
Depth (cm)
medium sand
fine sand
very fine sand
USU 2651
1.18 ± 0.21 ka
USU 2652
1.42 ± 0.22 ka
log%
Munsell Value
d 13C/12C
%C

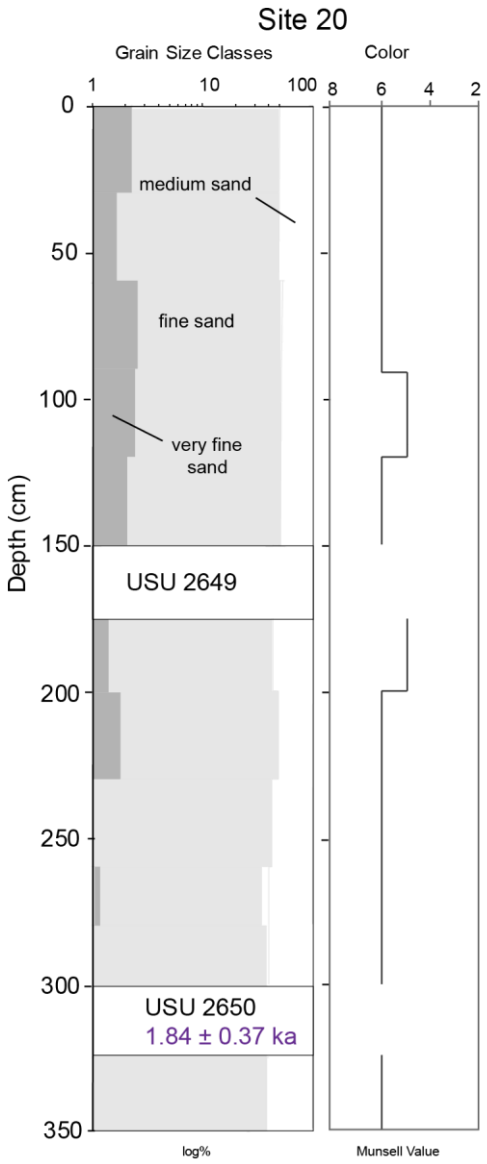
Site 20
Grain Size Classes
Color
1
10
100
8
6
4
2
0
50
100
150
200
250
300
350
Depth (cm)
medium sand
fine sand
very fine sand
USU 2649
USU 2650
1.84 ± 0.37 ka
log%
Munsell Value

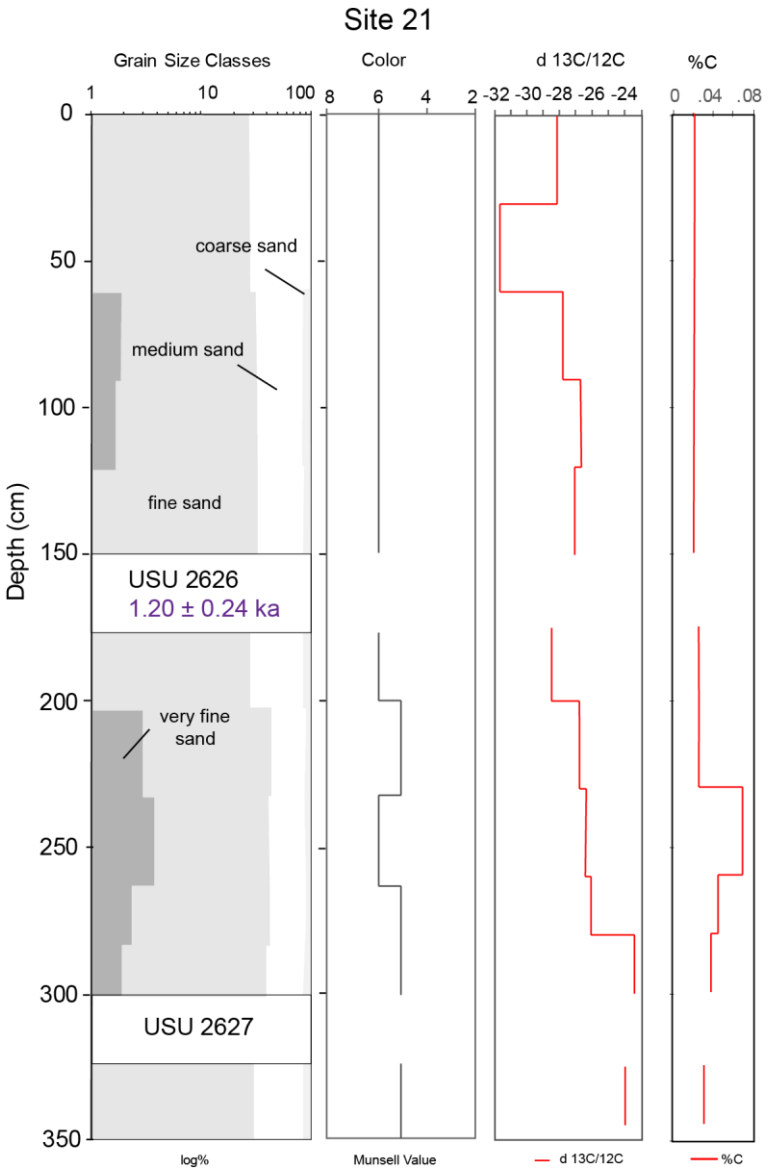
Site 21
Grain Size Classes
Color
d 13C/12C
%C
1
10
100
8
6
4
2
-32
-30
-28
-26
-24
0
.04
.08
Depth (cm)
0
50
100
150
200
250
300
350
coarse sand
medium sand
fine sand
USU 2626
1.20 ± 0.24 ka
very fine sand
USU 2627
log%
Munsell Value
d 13C/12C
%C

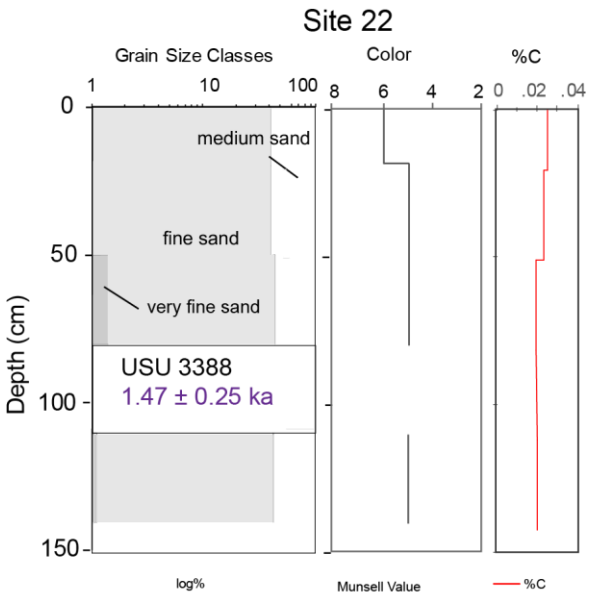
Site 22
Grain Size Classes
1
10
100
Color
8
6
4
2
%C
0
.02
.04
0
50
100
150
Depth (cm)
medium sand
fine sand
very fine sand
USU 3388
1.47 ± 0.25 ka
log%
Munsell Value
%C

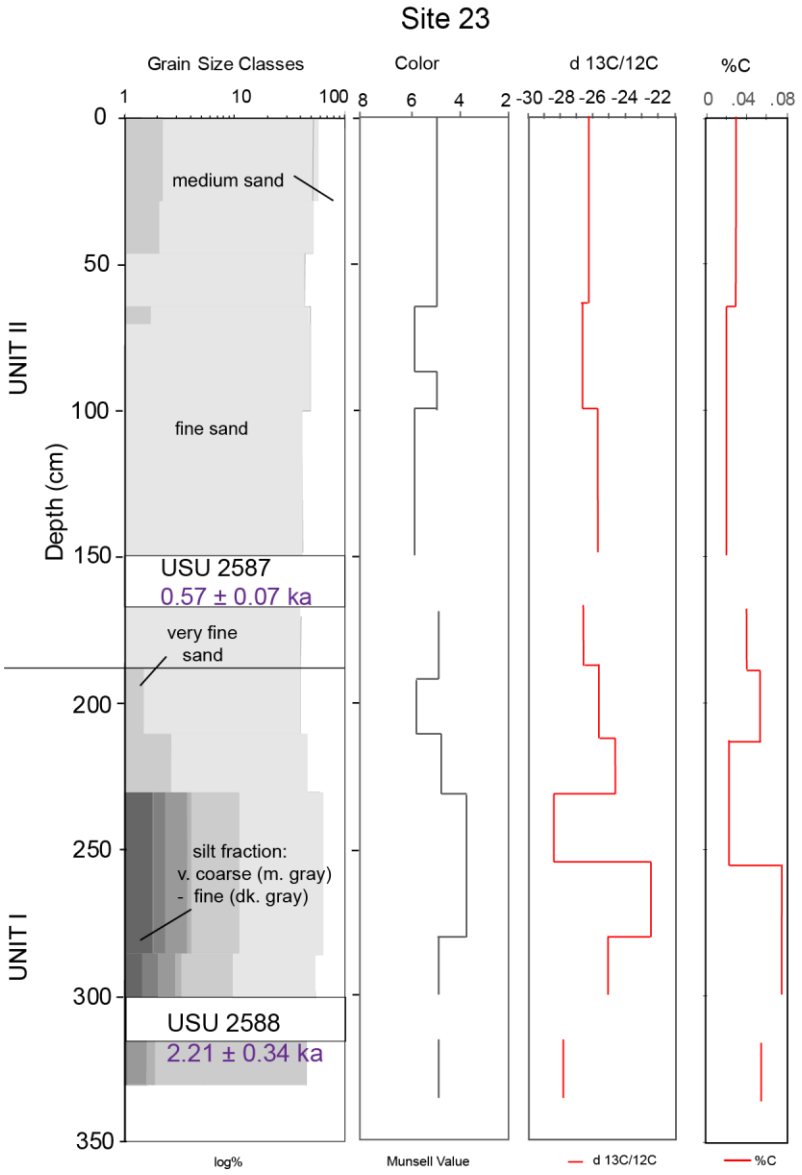
Site 23
Grain Size Classes
Color
d 13C/12C
%C
1
10
100
8
6
4
2
-30
-28
-26
-24
-22
0
.04
.08
0
50
100
150
200
250
300
350
Depth (cm)
UNIT II
UNIT I
medium sand
fine sand
USU 2587
0.57 ± 0.07 ka
very fine sand
silt fraction:
v. coarse (m. gray)
- fine (dk. gray)
USU 2588
2.21 ± 0.34 ka
log%
Munsell Value
d 13C/12C
%C

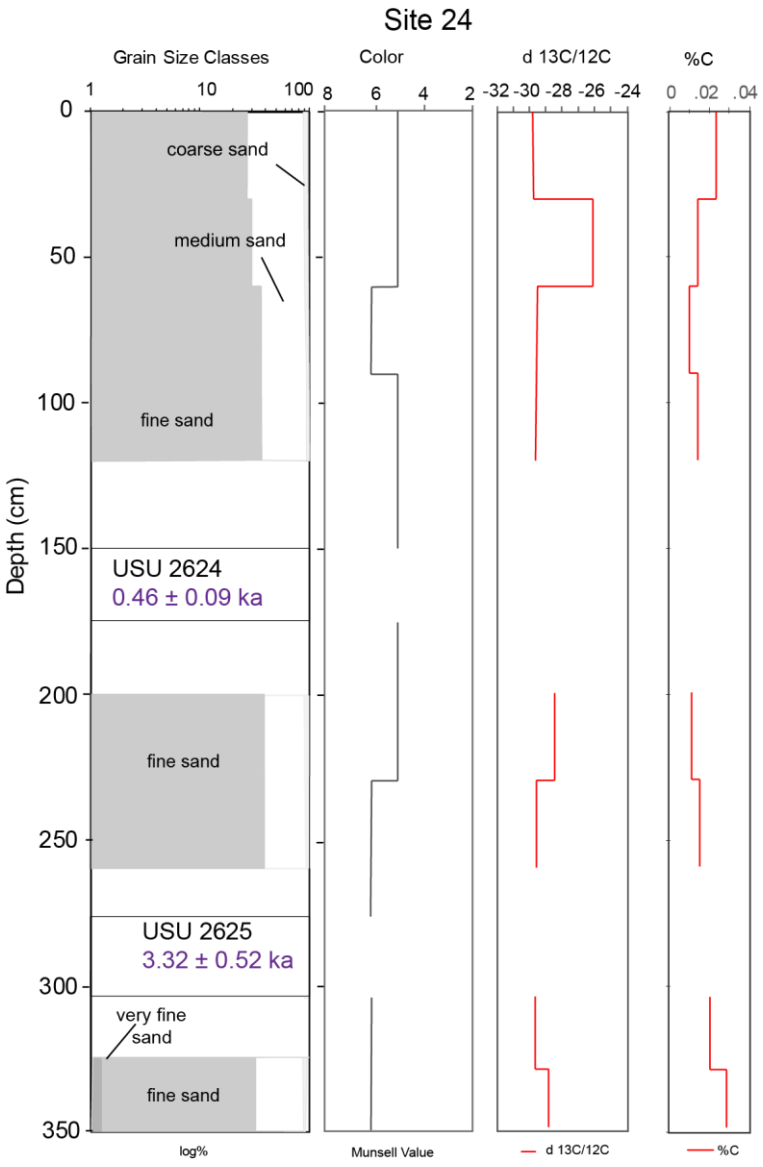
Site 24
Grain Size Classes
Color
d 13C/12C
%C
1
10
100
8
6
4
2
-32
-30
-28
-26
-24
0
.02
.04
Depth (cm)
0
50
100
150
200
250
300
350
coarse sand
medium sand
fine sand
USU 2624
0.46 ± 0.09 ka
fine sand
USU 2625
3.32 ± 0.52 ka
very fine sand
fine sand
log%
Munsell Value
d 13C/12C
%C

Appendix C. San Rafael Dune Field, Utah. Graphical Chronostratigraphy (W-E/N-S)

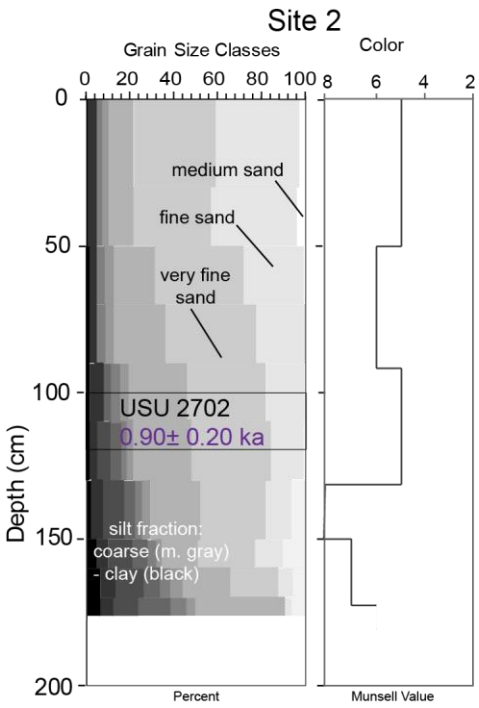

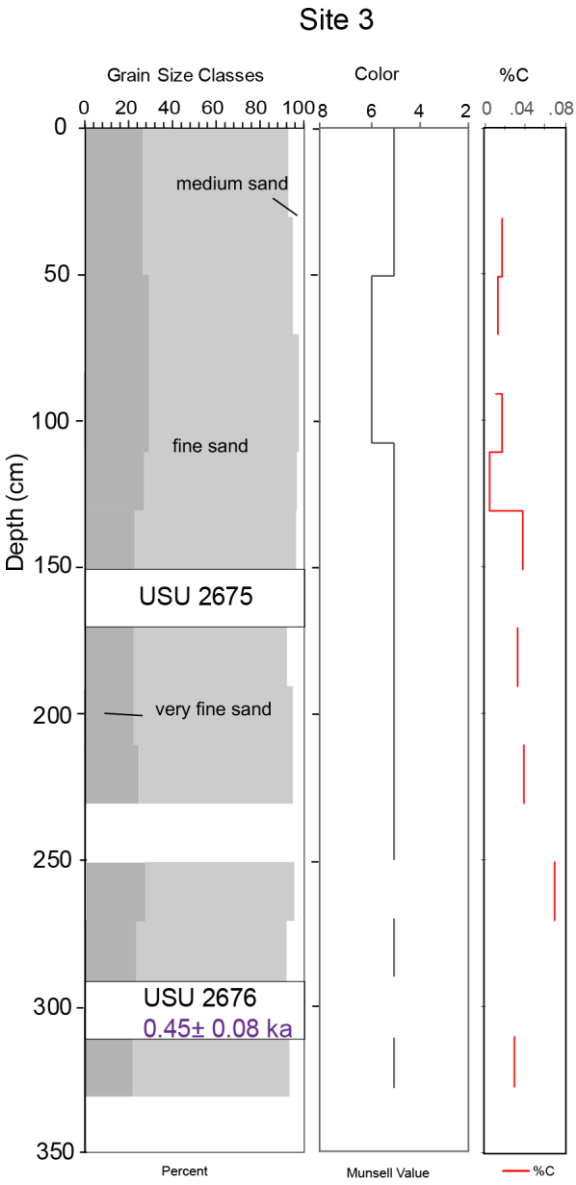

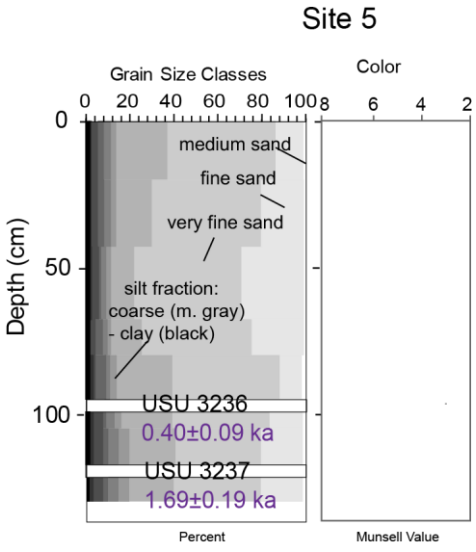

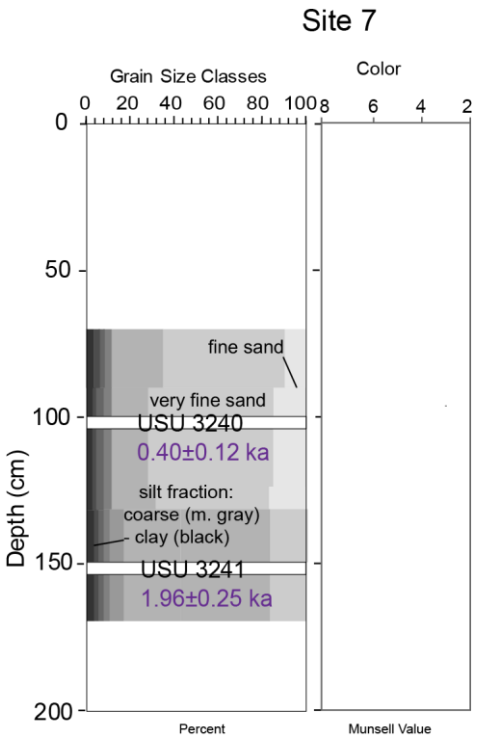
Site 7
Grain Size Classes
Color
0 20 40 60 80 100
8 6 4 2
0
50
100
150
200
Depth (cm)
fine sand
very fine sand
USU 3240
0.40±0.12 ka
silt fraction:
coarse (m. gray)
clay (black)
USU 3241
1.96±0.25 ka
Percent
Munsell Value

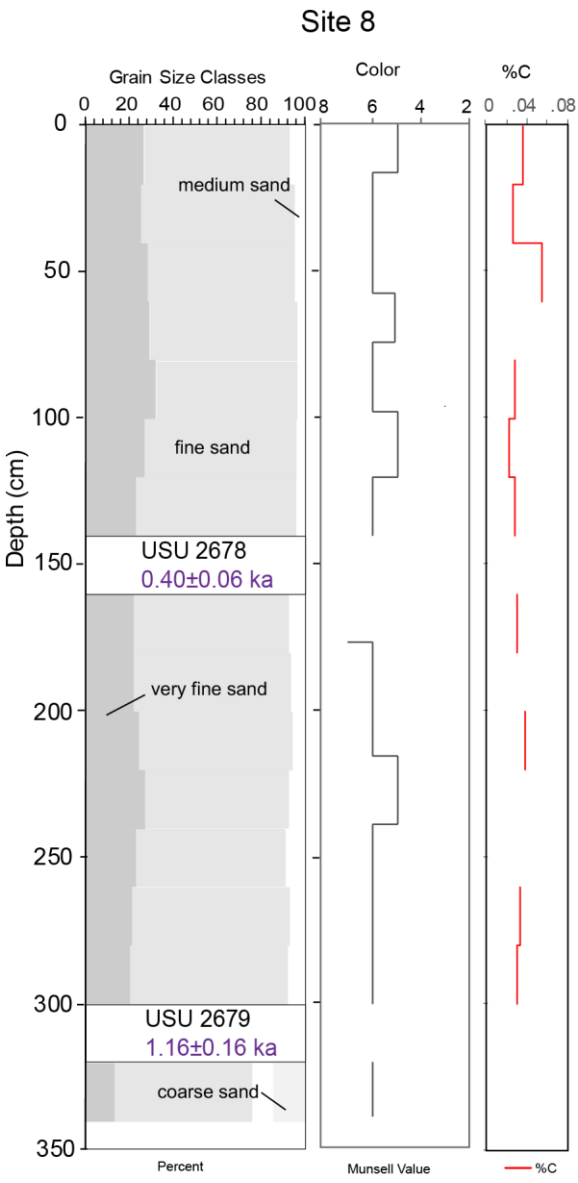
Site 8
Grain Size Classes
Color
%C
0 20 40 60 80 100
8 6 4 2
0 .04 .08
0
50
100
150
200
250
300
350
Depth (cm)
medium sand
fine sand
USU 2678
0.40±0.06 ka
very fine sand
USU 2679
1.16±0.16 ka
coarse sand
Percent
Munsell Value
%C

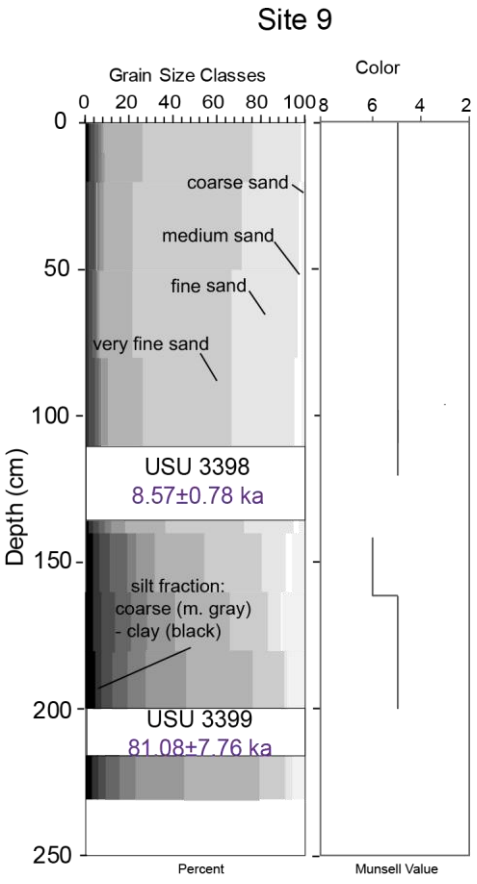
Site 9
Grain Size Classes
Color
0 20 40 60 80 100
8 6 4 2
0
50
100
150
200
250
Depth (cm)
coarse sand
medium sand
fine sand
very fine sand
USU 3398
8.57±0.78 ka
silt fraction:
coarse (m. gray)
- clay (black)
USU 3399
81.08±7.76 ka
Percent
Munsell Value

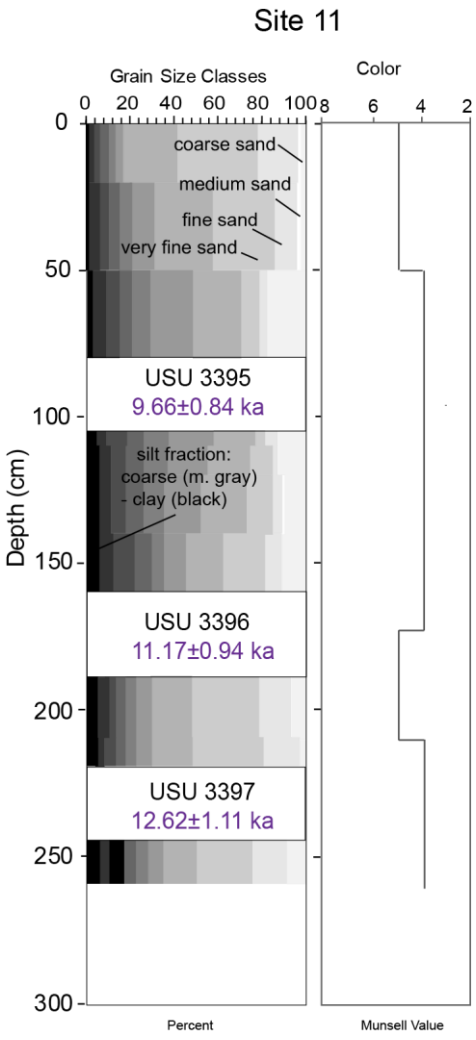
Site 11
Grain Size Classes
Color
0 20 40 60 80 100
8 6 4 2
coarse sand
medium sand
fine sand
very fine sand
USU 3395
9.66±0.84 ka
silt fraction:
coarse (m. gray)
- clay (black)
USU 3396
11.17±0.94 ka
USU 3397
12.62±1.11 ka
Depth (cm)
0
50
100
150
200
250
300
Percent
Munsell Value

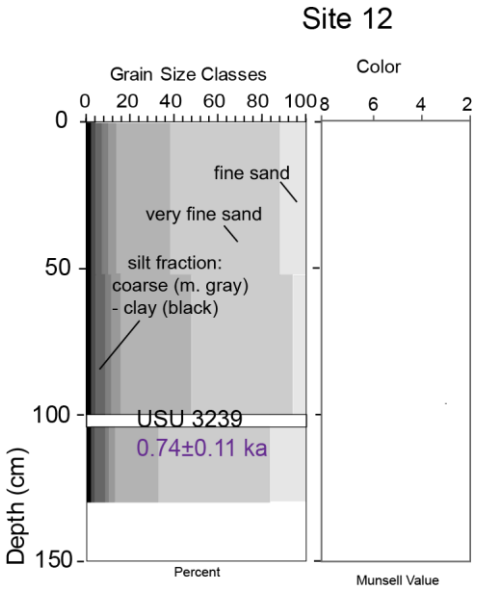
Site 12
Grain Size Classes
Color
0 20 40 60 80 100
8 6 4 2
fine sand
very fine sand
silt fraction:
coarse (m. gray)
- clay (black)
USU 3239
0.74±0.11 ka
Depth (cm)
0
50
100
150
Percent
Munsell Value

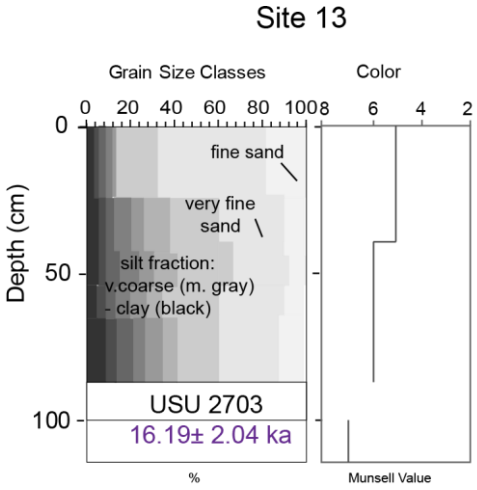
Site 13
Grain Size Classes
Color
0 20 40 60 80 100
8 6 4 2
fine sand
very fine
sand
silt fraction:
v.coarse (m. gray)
- clay (black)
USU 2703
16.19± 2.04 ka
Depth (cm)
0
50
100
%
Munsell Value

Site 14

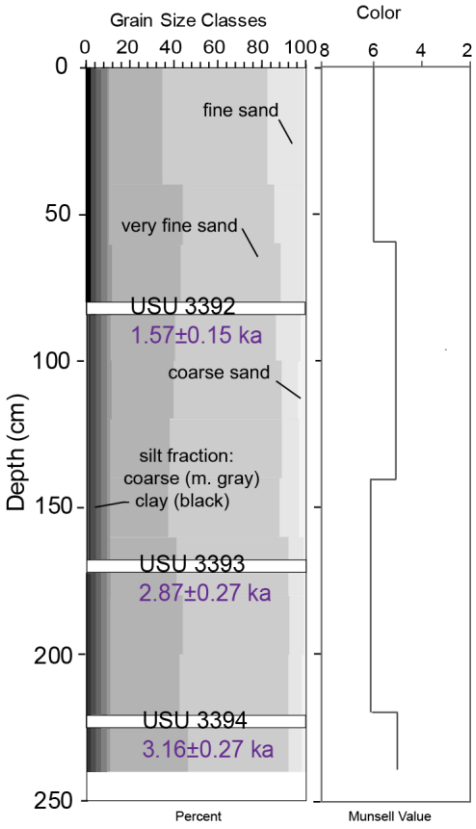

Site 15

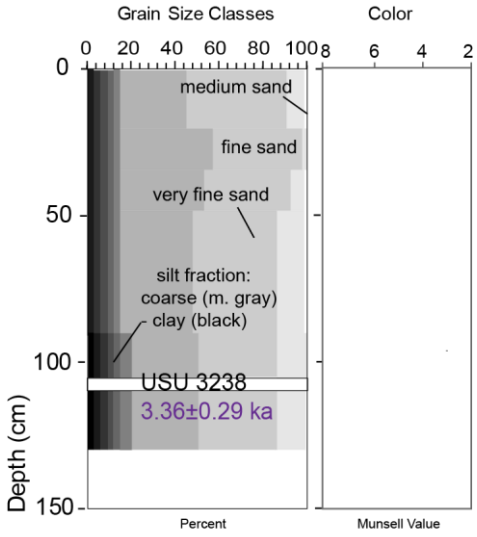

Site 20

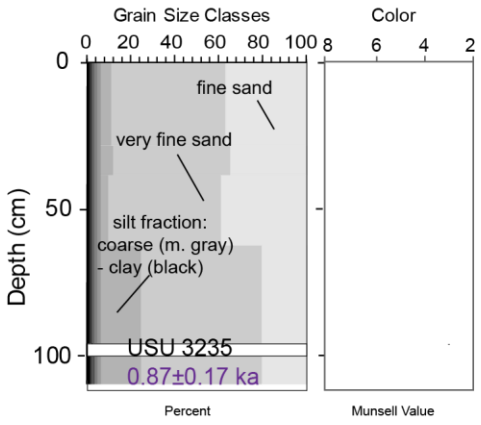

Site 22

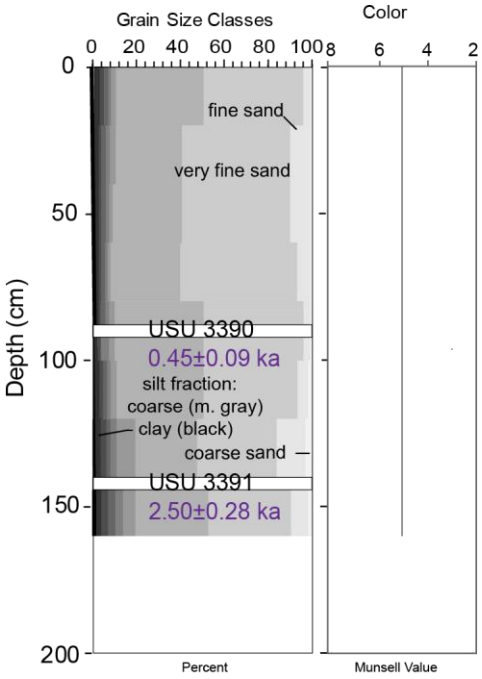

APPENDIX D. GEOCHEMICAL ANALYSES

Appendix D. Results of calibrated TOC and $\delta^{13}C$ analysis

1/23/2020

Site # 16	Depth (cm)	$\delta^{13}C$	%C
16	0-35	-23.33	0.03
16	35-70	-23.22	0.022
16	70-100	-25.42	0.016
16	100-130	-24.79	0.015
16	130-150	-25.29	0.014
16	160-190	-25.94	0.014
16	190-215	-24.97	0.015
16	215-235	-25.32	0.014
16	235-250	-24.34	0.014
16	255-275	-24.93	0.013
		±	±
Low TOC soil		0.59	0.007

12/20/19 & 1/23/20

Site # 23	Depth (cm)	$\delta^{13}C$	%C
23	0-64	-26.14	0.03
23	64-100	-26.45	0.023
23	100-148	-25.39	0.021
23	170-188	-26.40	0.041
23	188-210	-25.38	0.047
23	210-230	-24.38	0.025
23	230-255	-28.20	0.044
23	255-285	-22.63	0.075
23	285-315	-25.01	0.076
23	315-330	-27.62	0.046
		±	±
Low TOC soil	0-188 cm	0.59	
Low TOC soil	188-330 cm	1.07	

1/22/2020

Site # 24	Depth (cm)	$\delta^{13}C$	%C
24	0-30	-29.74	0.024
24	30-60	-26.10	0.015
24	60-90	-29.50	0.011
24	90-120	-29.63	0.015
24	200-230	-28.45	0.012
24	230-260	-29.58	0.016
24	305-330	-28.12	0.021
24	330-350	-27.30	0.029
		±	±
Low TOC soil		0.16	0.001

1/22/2020

Site # 13	Depth (cm)	$\delta^{13}C$	%C
13	0-30		
13	0-30a	-26.48	
13	0-30b	-28.18	0.03
13	30-60	-29.93	0.008
13	30-60b	-29.09	0.024
13	60-90	-29.49	0.009
13	90-120	-30.30	0.028
13	120-150	-29.56	0.015
13	175-200	-28.73	0.014
13	200-230	-30.04	0.03
13	230-260	-28.91	0.014
13	260-280	-28.49	0.016
13	280-300	-28.22	0.017
13	325-350	-28.84	0.018
		±	
Low TOC soil		0.16	Sample 0-30a
Low TOC soil		0.59	Samples 0-30b and 30-60b
Low TOC soil		0.40	
a	1/23/2020	Redo	
b	4/1/2020	Redo	

1/23/2020

Site # 18	Depth (cm)	$\delta^{13}C$	%C
18	0-30	-25.11	0.024
18	30-60	-25.42	0.028
18	60-90	-24.04	0.024
18	90-120	-24.26	0.022
18	120-150	-25.17	0.025
18	175-200	-24.62	0.02
18	200-230	-25.09	0.02
18	230-260	-25.49	0.025
18	260-280	-25.40	0.033
17	325-350	-25.78	0.028
		±	
Low TOC soil		0.59	

4/2/2020

Site # 21	Depth (cm)	$\delta^{13}C$	%C
21	0-30	-28.19	0.022
21	30-60	-31.80	0.022
21	60-90	-27.82	0.021
21	90-120	-26.70	0.022
21	120-150	-26.86	0.021
21	175-200	-28.54	0.026
21	200-230	-26.77	0.029
21	230-260	-26.55	0.069
21	260-280	-26.25	0.045
21	280-300	-23.28	0.038
21	325-350	-23.86	0.031
		±	
Low TOC soil		0.63	

4/1/2020			
Site # 19	Depth (cm)	$\delta^{13}C$	%C
19	0-30	-26.60	0.038
19	30-60	-26.89	0.033
19	60-90	-25.88	0.03
19	90-120	-27.87	0.023
19	120-150	-25.90	0.024
19	175-200	-28.45	0.026
19	200-230	-28.13	0.027
19	200-230c	-25.59	0.022
19	230-260	-28.04	0.024
19	260-280	-28.37	0.031
19	280-300	-29.17	0.03
19	325-350	-28.01	0.026
		±	
Low TOC soil		0.40	

4/1/2020			
Site # 17	Depth (cm)	$\delta^{13}C$	%C
17	0-30	-25.71	0.028
17	30-60	-27.85	0.062
17	60-90	-27.83	0.025
17	90-120		
17	90-120c	-30.27	0.033
17	120-150		
17	120-150c	-27.44	0.031
17	175-200	-28.27	0.045
17	200-230	-28.16	0.022
17	230-260	-28.38	0.02
17	260-280	-28.67	0.021
17	260-280c	-26.20	0.024
17	280-300	-28.36	0.024
17	325-350	-28.45	0.022
		±	
Low TOC soil		0.40	c-samples run 4/2/2020
Low TOC soil		0.63	

1/15/2021			
Site # 4	Depth (cm)	$\delta^{13}C$	%C

4	0-30	-26.39	0.032
4	30-60	-26.15	0.02
4	60-90	-34.96	0.017
4	90-120	-27.91	0.017
4	120-150	-29.70	0.016
4	150-180	-27.69	0.019
4	180-210	-26.04	0.017
4	210-240	-27.66	0.015
4	240-270	-26.44	0.016
4	270-300	-25.74	0.026
4	300-315	-26.88	0.044

	±	
Low TOC soil		0.78
Low TOC soil		2.0

1/15/2021

Site # 1	Depth (cm)	$\delta^{13}C$	%C
1	0-30	-20.36	0.034
1	30-60	-21.24	0.015
1	60-90	-25.23	0.012
1	90-120	-27.78	0.009
1	120-150	-28.07	0.008
1	150-180	-27.61	0.009
1	180-210	-28.63	0.008
1	210-240	-28.74	0.006
1	240-270	-27.80	0.04
1	270-300	-26.68	0.01
1	300-315	-28.06	0.02
1	315-330	-36.41	0.03
		±	
Low TOC soil		0.78	
		±	
Low TOC soil		2.0	

1/15/2021

Site # 22	Depth (cm)	$\delta^{13}C$	%C
22	0-20	-25.85	0.03
22	20-50	-25.59	0.02
22	50-80	-26.07	0.02
22	110-140	-24.99	0.02
	±	0.78	
	±	2.0	

Appendix D. Results of calibrated TOC and $\delta^{13}C$ analysis – San Rafael dune field

8/6/2020	& 8/18/2020		
Site	Depth (cm)	$\delta^{13}C$	%C
3	0-30	-25.75	N/A
3	30-50	-25.45	0.02
3	50-70	-25.44	0.02
3	70-90	-25.78	0.01
3	90-110	-25.45	0.02
3	110-130	-25.36	0.01
3	130-150	-25.90	0.04
3	170-190	-26.09	0.03
3	210-230	-26.54	0.04
3	250-270	-27.37	0.07
3	270-290	-36.05	
3	310-330	-25.92	0.03
		±	±
	Low TOC soil	0.16	0.38
	Low TOC soil	0.33	

8/18/2020	& 8/19/2020		
Site	Depth (cm)	$\delta^{13}C$	%C
8	0-20	-27.19	0.04
8	20-40	-26.06	0.03
8	40-60	-25.61	0.06
8	60-80	-36.16	
8	80-100	-25.95	0.03
8	100-120	-26.22	0.02
8	120-140	-25.37	0.03
8	160-180	-24.32	0.03
8	180-200	-24.08	0.04
8	200-220	-25.05	
8	220-240	-24.38	0.04
8	240-260	-24.55	0.03
8	260-280	-35.02	
8	280-300	-25.17	0.04
8	320-340	-34.76	
		±	±
	Low TOC soil	0.33	0.18

8/18/2020 & 8/19/2020

Site	Depth (cm)	d 13C/12C	%C
nr	0-20	-21.08	0.07
nr	20-40	-22.84	0.05
nr	40-60	-16.18	0.37
nr	60-80	-18.09	0.20
nr	80-90	-20.12	0.16
nr	100-120	-34.48	
nr	120-140	-21.85	0.06
nr	120-140	-37.17	
nr	140-160	-34.01	
nr	140-160	-26.83	
nr	160-180	-33.60	
nr	160-180	-26.83	
	±		
	Low TOC soil	0.33	

APPENDIX E. OPTICALLY STIMULATED LUMINESCENCE DOSE RATE VALUES

Appendix E. Dose rate information for OSL samples – Kanab dune field, Utah

Site	Map Unit	USU num.	Depth (m)	In-situ H_2O (%)[1]	Grain size (μm)	K (%)[2]	Rb (ppm)[2]	Th (ppm)[2]	U (ppm)[2]	Cosmic (Gy/ky)
1	Qes	USU-3331	3	3.25%	180-250	0.75±0.02	25.9±1.0	0.7±0.2	0.3±0.1	0.20±0.02
2	Qed1	USU-2647	1.8-2.05	2.23%	180-250	0.25±0.01	8.9±0.4	0.6±0.2	0.2±0.1	0.23±0.02
2	Qed1	USU-2648	3.3-3.55	2.93%	180-250	0.25±0.01	8.9±0.4	0.6±0.2	0.2±0.1	0.23±0.02
3	Qed1	USU-1530	0.80-1.00	-	180-250	0.61±0.02	25.7±1.0	1.5±0.2	0.4±0.1	0.27±0.03
4	Qed1	USU-3325	0.9	3.64%	180-250	0.22±0.01	7.3±0.3	0.6±0.2	0.2±0.1	0.26±0.03
4	Qed1	USU-3327	2.7	2.70%	180-250	0.23±0.01	8.2±0.3	0.7±0.2	0.2±0.1	0.21±0.02
5	Qed1	USU-1526	3.35	3.40%	150-250	0.26±0.01	8.8±0.4	0.6±0.2	0.2±0.1	0.19±0.02
6	Qed1	USU-1528	1.65-1.80	3.10%	180-250	0.21±0.01	7.4±0.3	0.6±0.2	0.2±0.1	0.24±0.02
7	Qed1	USU-3328	1.2	2.84%	180-250	0.28±0.01	10.2±0.4	0.6±0.2	0.2±0.1	0.25±0.03
8	Qed2	USU-1155	2.00-2.15	3.19%	90-150	0.66±0.02	22.9±0.7	0.8±0.2	0.2±0.1	0.23±0.02
9	Qed2	USU-1156	1.50-1.65	4.08%	90-180	0.33±0.01	13.1±0.5	0.7±0.2	0.2±0.1	0.24±0.02
9	Qed2	USU-1157	2.55-2.60	3.94%	90-180	0.32±0.01	12.4±0.5	0.7±0.2	0.3±0.1	0.21±0.02
10	Qed2	USU-2589	0.55-0.85	2.14%	180-250	0.35±0.01	12.7±0.5	0.6±0.2	0.2±0.1	0.28±0.03
11	Qed2	USU-2623	1.75-2.00	3.07%	150-250	0.77±0.02	27.8±1.1	1.3±0.2	0.3±0.1	0.23±0.02
12	Qed2	USU-2628	1.75-2.00	2.40%	180-250	0.23±0.01	8.1±0.3	0.5±0.2	0.2±0.1	0.23±0.02
12	Qed2	USU-2629	3.25-3.50	3.00%	180-250	0.27±0.01	9.8±0.4	0.6±0.2	0.2±0.1	0.19±0.02
13	Qed2	USU-2630	1.8-2.05	2.46%	180-250	0.36±0.01	12.5±0.5	0.6±0.2	0.2±0.1	0.23±0.02
13	Qed3	USU-2631	3.3-3.55	3.10%	180-250	0.36±0.01	12.3±0.5	0.6±0.2	0.2±0.1	0.19±0.02
14	Qed3	USU-2634	1.75-2.00	3.19%	180-250	0.38±0.01	13.6±0.5	0.6±0.2	0.2±0.1	0.23±0.02
14	Qed3	USU-2635	3.25-3.50	1.98%	180-250	0.31±0.01	10.9±0.4	0.6±0.2	0.2±0.1	0.19±0.02
15	Qed3	USU-2576	2.85-2.90	3.34%	150-250	0.20±0.01	7.7±0.3	0.7±0.2	0.2±0.1	0.20±0.02
16	Qed3	USU-2653	1.8-2.05	2.35%	180-250	0.36±0.01	12.6±0.5	0.6±0.2	0.2±0.1	0.23±0.02
16	Qed3	USU-2654	3.3-3.55	3.14%	180-250	0.39±0.01	13.3±0.5	0.6±0.2	0.2±0.1	0.19±0.02
17	Qed3	USU-2632	1.75-2.00	2.60%	180-250	0.37±0.01	12.8±0.8	0.6±0.2	0.2±0.1	0.23±0.02
17	Qed3	USU-2633	3.25-3.50	4.07%	180-250	0.50±0.01	19.1±0.8	0.7±0.2	0.2±0.1	0.19±0.02
18	Qed3	USU-2651	1.75-2.00	2.02%	180-250	0.34±0.01	12.1±0.5	0.6±0.2	0.2±0.1	0.23±0.02
18	Qed3	USU-2652	3.25-3.50	3.34%	180-250	0.37±0.01	13.1±0.5	0.6±0.2	0.2±0.1	0.19±0.02
19	Qed4	USU-2650	3.3-3.55	2.31%	180-250	0.33±0.01	11.2±0.4	0.6±0.2	0.2±0.1	0.19±0.02
20	Qed4	USU-2626	1.8-2.05	1.98%	180-250	0.29±0.01	10.3±0.4	0.6±0.2	0.2±0.1	0.23±0.02
21	Qed4	USU-3388	0.8	2.03%	180-250	0.40±0.01	14.6±0.6	0.7±0.2	0.2±0.1	0.26±0.03
22	Qed4	USU-2587	1.75	2.98%	150-250	0.36±0.01	13.5±0.5	0.6±0.2	0.2±0.1	0.24±0.02

Site	Map Unit	USU num.	Depth (m)	In-situ H_2O (%)[1]	Grain size (μm)	K (%)[2]	Rb (ppm)[2]	Th (ppm)[2]	U (ppm)[2]	Cosmic (Gy/ky)
22	Qed4	USU-2588	3.25	3.55%	150-250	0.46±0.01	17.1±0.7	0.7±0.2	0.2±0.1	0.20±0.02
23	Qed4	USU-2624	1.8-2.05	2.90%	150-250	0.36±0.01	12.8±0.5	0.9±0.2	0.2±0.1	0.22±0.02
23	Qed4	USU-2625	3.1-3.35	2.86%	180-250	0.33±0.01	11.9±0.5	0.7±0.2	0.2±0.1	0.19±0.02

[1] Assumed 5±2% for moisture content over burial history.
[2] Radioelemental concentrations determined using ICP-MS and ICP-AES techniques; dose rate is derived from concentrations by conversion factors from Guérin et al. (2011).

Appendix E – Dose Rate Information

Table 2. Dose Rate Information for OSL samples – San Rafael dune field project area

Site	Map Unit	USU No.	Depth (m)	In-situ H_2O (%)[1]	K (%)[2]	Rb (ppm)[2]	Th (ppm)[2]	U (ppm)[2]	Cosmic (Gy/kyr)
1	Qed1	USU 807	0.55	0.9	1.01±0.03	37.6±1.5	2.1±0.2	1.0±0.1	0.27±0.03
2	Qed1	USU 2702	1.1	1.1	0.93±0.02	32.6±1.3	1.6±0.2	0.7±0.1	0.25±0.02
3	Qed3	USU 2676	3.2	1.6	1.04±0.03	34.5±1.4	1.3±0.2	0.5±0.1	0.19±0.02
4	Qed3	USU 808	1.5	1.0	0.77±0.02	29.0±1.2	1.2±0.2	0.5±0.1	0.23±0.02
5	Qes2	USU 3236	0.95	0.7	1.20±0.03	40.5±1.6	1.5±0.2	0.5±0.1	0.25±0.03
5	Qes2	USU 3237	1.4	1.7	1.13±0.03	37.5±1.5	1.8±0.2	0.7±0.1	0.24±0.02
6	Qed1	USU 810	1.0	2.5	0.86±0.02	31.3±1.3	1.3±0.2	0.6±0.1	0.25±0.02
7	Qed3	USU 3240	1.0	0.5	1.18±0.03	39.8±1.6	1.3±0.2	0.5±0.1	0.25±0.02
7	Qed3	USU 3241	1.5	1.2	1.29±0.03	43.1±1.7	1.9±0.2	0.7±0.1	0.23±0.02
8	Qed3	USU 2678	1.65	1.1	1.29±0.03	45.2±1.8	1.6±0.2	0.5±0.1	0.23±0.02
8	Qed3	USU 2679	3.25	2.7	1.27±0.03	41.2±1.6	1.7±0.2	0.6±0.1	0.19±0.02
9	Qes1	USU 3398	1.1	1.6	1.09±0.03	35.9±1.4	1.7±0.2	0.6±0.1	0.25±0.02
9	Qes1	USU 3399	2.0	3.8	1.74±0.04	57.7±2.3	3.8±0.3	1.0±0.1	0.22±0.02
10	Qes2	USU 2707	2.4	-	1.71±0.04	59.6±2.4	3.0±0.3	1.3±0.1	0.21±0.02
10	Qes2	USU 2708	3.4	-	1.55±0.04	54.4±2.2	2.4±0.2	1.1±0.1	0.19±0.02
11	Qes1	USU 3395	0.8	5.4	2.08±0.05	65.5±2.6	5.0±0.5	1.6±0.1	0.25±0.03
11	Qes1	USU 3396	1.6	-	1.72±0.04	56.9±2.3	3.8±0.3	1.4±0.1	0.23±0.02
11	Qes1	USU 3397	2.2	3.5	1.57±0.04	51.2±2.0	3.2±0.3	1.1±0.1	0.21±0.02
12	Qes2	USU 3239	1.4	1.5	1.29±0.03	45.4±1.8	2.1±0.2	0.9±0.1	0.24±0.02

Site	Map Unit	USU No.	Depth (m)	In-situ H_2O (%)[1]	K (%)[2]	Rb (ppm)[2]	Th (ppm)[2]	U (ppm)[2]	Cosmic (Gy/kyr)
13	Qes1	USU 2703	0.95	2.6	1.15±0.03	39.5±1.6	2.0±0.2	1.0±0.1	0.26±0.03
14	Qes1	USU 3392	0.8	1.1	1.66±0.04	54.1±2.2	1.5±0.2	0.5±0.1	0.26±0.03
14	Qes1	USU 3393	1.33	0.7	1.35±0.03	43.7±1.7	1.5±0.2	0.6±0.1	0.24±0.02
14	Qes1	USU 3394	2.2	-	1.55±0.04	49.4±2.0	1.7±0.2	0.6±0.1	0.22±0.02
15	Qed2	USU 3238	1.1	1.9	1.40±0.04	46.8±1.9	1.9±0.2	0.7±0.1	0.25±0.03
16	Qed1	USU-3003	1.03	3.5	1.24±0.03	41.7±1.7	1.9±0.2	0.7±0.1	0.26±0.03
17	Qed1	USU 813	0.6	3.3	1.26±0.03	45.9±1.8	2.7±0.2	1.0±0.1	0.26±0.03
18	Qes1	USU 3232	0.95	1.1	1.25±0.03	43.0±1.7	1.4±0.2	0.5±0.1	0.26±0.03
19	Qes1	USU 2814	1.75	1.3	1.34±0.03	47.2±1.9	1.5±0.2	0.6±0.1	0.23±0.02
19	Qes1	USU 2815	1.88	1.7	1.22±0.03	41.0±1.6	1.7±0.2	0.6±0.1	0.22±0.02
20	Qed2	USU 3235	0.95	0.7	1.06±0.03	36.8±1.5	1.3±0.2	0.4±0.1	0.24±0.02
21	Qed3	USU 3233	0.8	0.5	1.05±0.03	35.8±1.4	1.1±0.2	0.3±0.1	0.25±0.03
21	Qed3	USU 3234	1.4	0.8	1.25±0.03	42.4±1.7	1.3±0.2	0.4±0.1	0.23±0.02
22	Qes1	USU 3390	0.87	0.7	1.72±0.04	55.1±2.2	1.6±0.2	0.5±0.1	0.25±0.03
22	Qes1	USU 3391	1.4	1.5	1.65±0.04	50.8±2.0	2.1±0.2	0.7±0.1	0.24±0.02

[1] Assumed 5.0±2.0% for samples as moisture content over burial history.

[2] Radioelemental concentrations determined using ICP-MS and ICP-AES techniques; dose rate is derived from concentrations by conversion factors from Guérin et al. (2011).

APPENDIX F. EQUIVALENT DOSE (D_E) RADIAL PLOTS

Equivalent Dose (D_E) Radial Plots

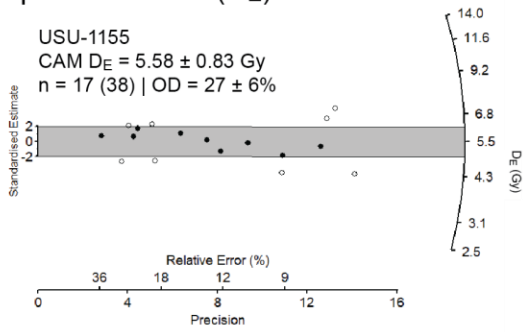

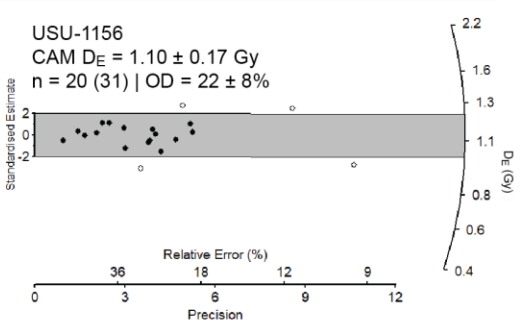

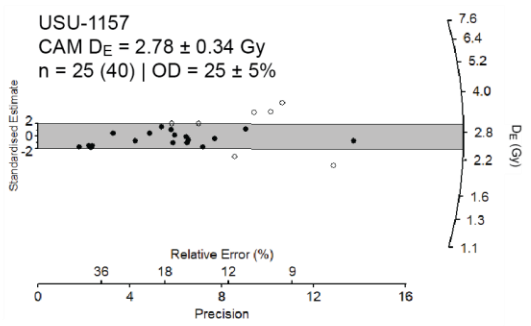

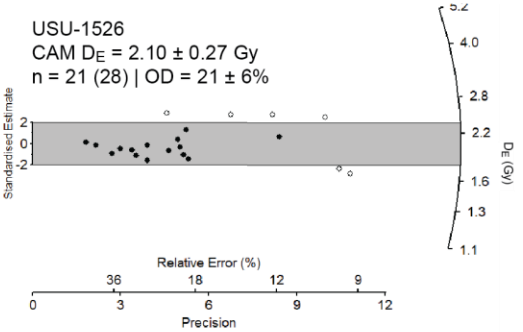

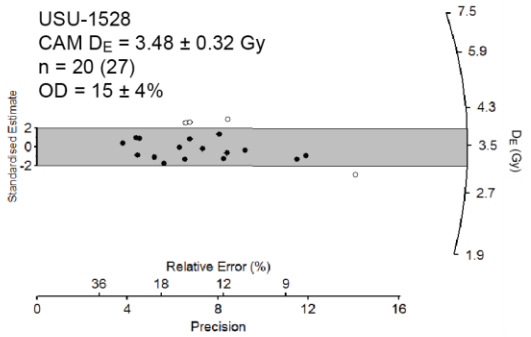

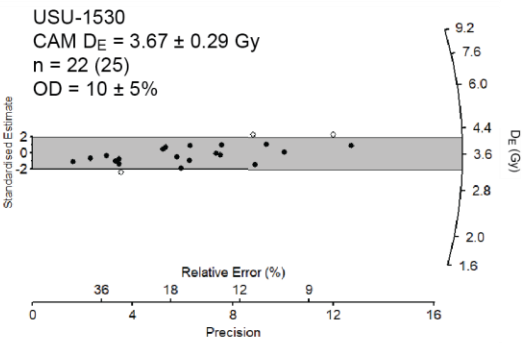

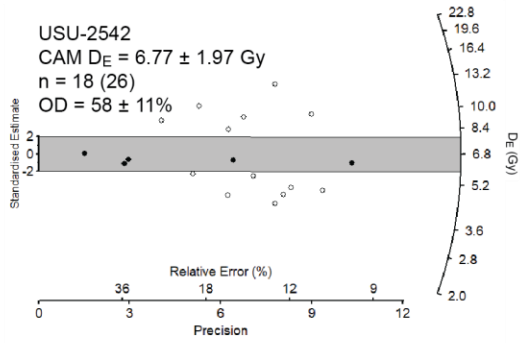

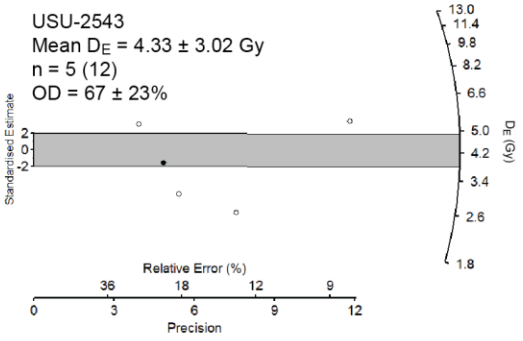

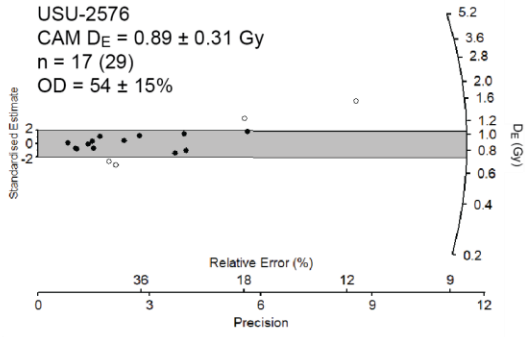

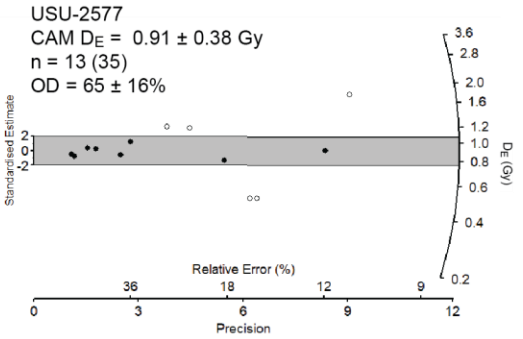

Equivalent Dose (D_E) Radial Plots

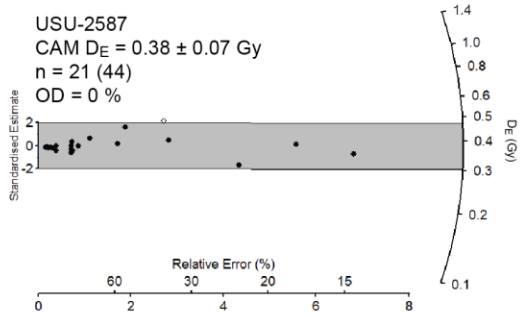

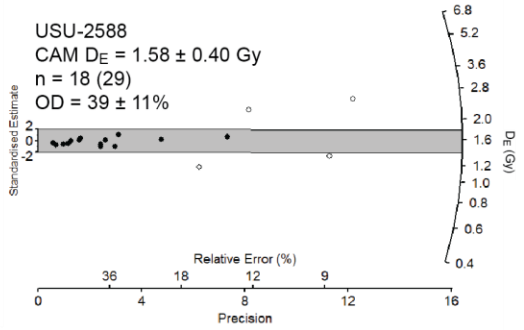

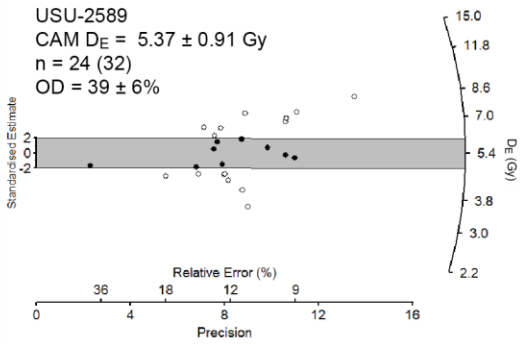

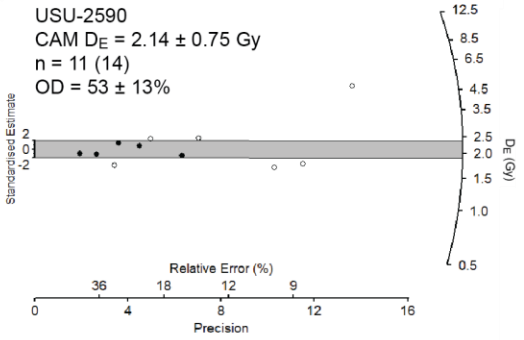

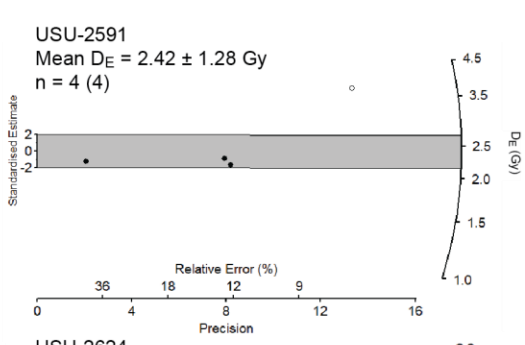

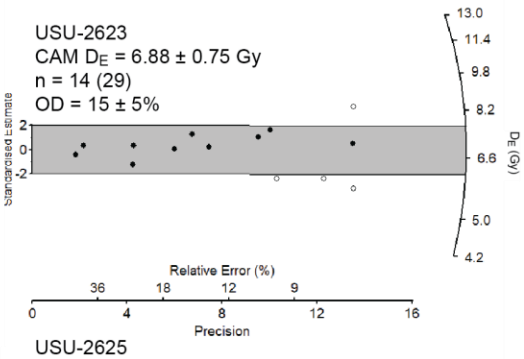

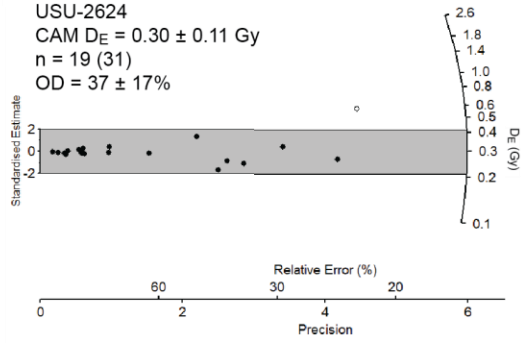

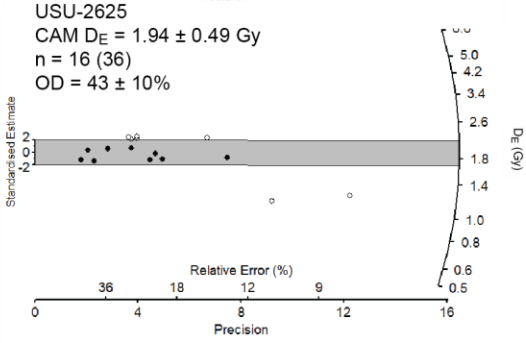

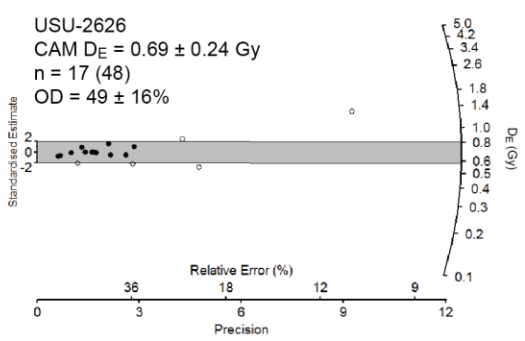

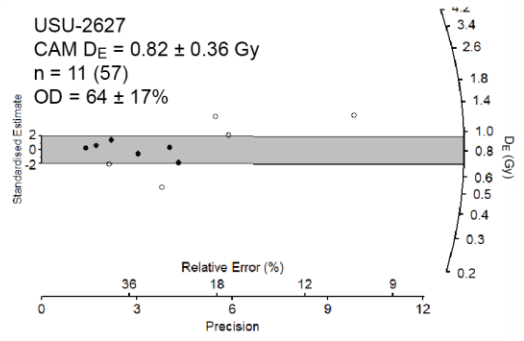

Equivalent Dose (D_E) Radial Plots

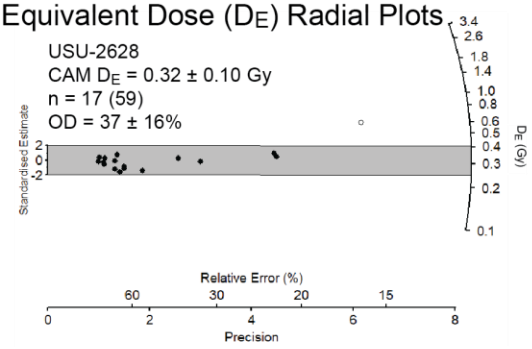

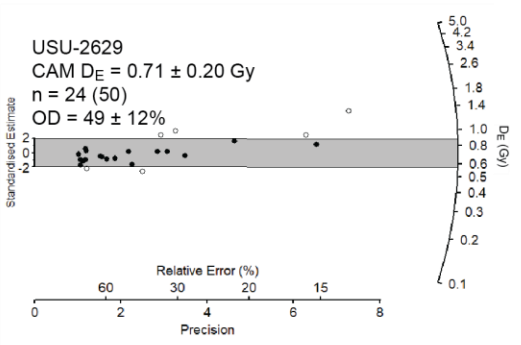

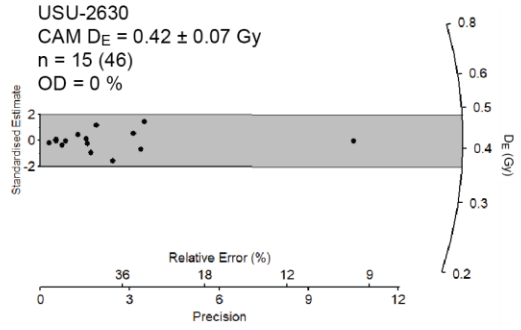

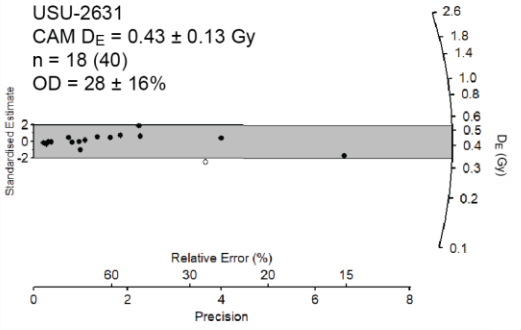

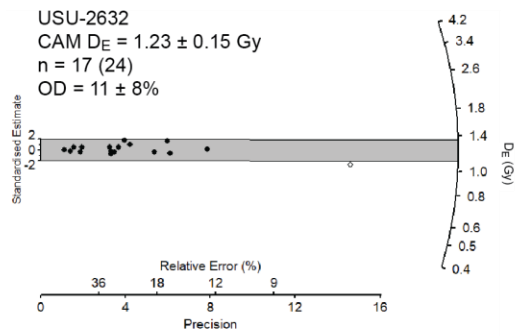

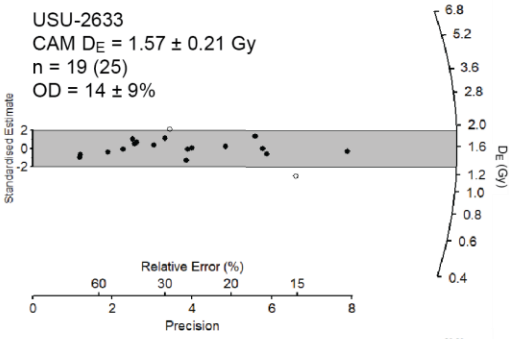

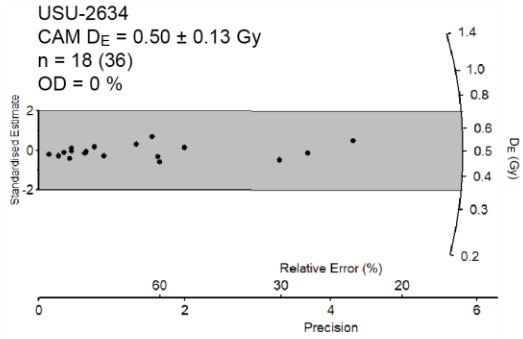

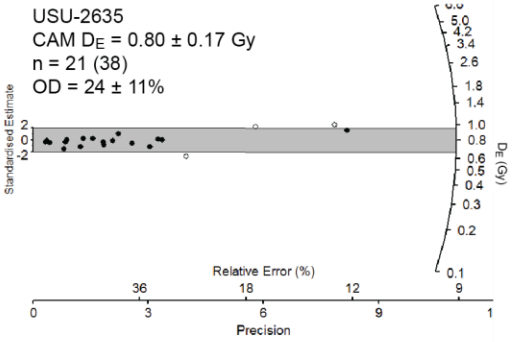

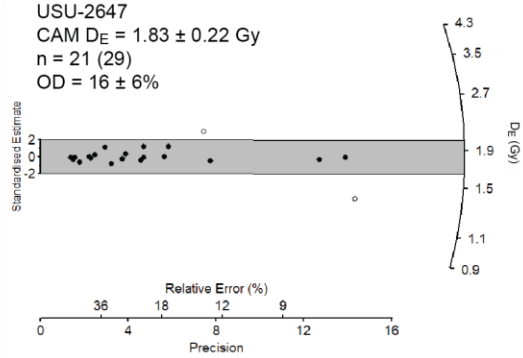

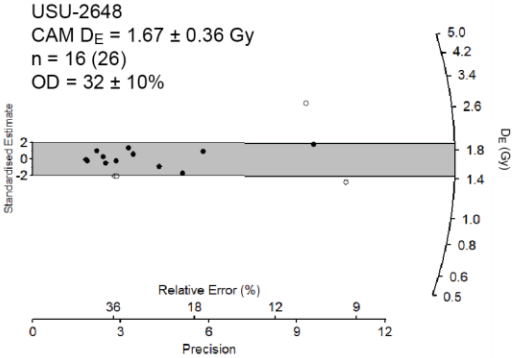

Equivalent Dose (D_E) Radial Plots

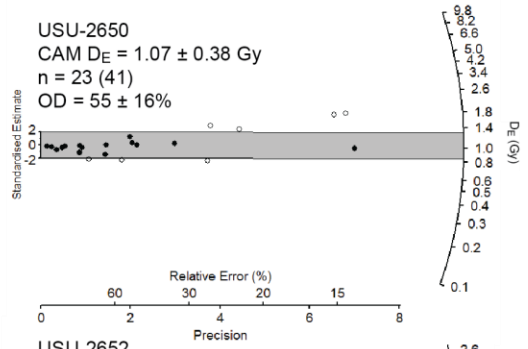

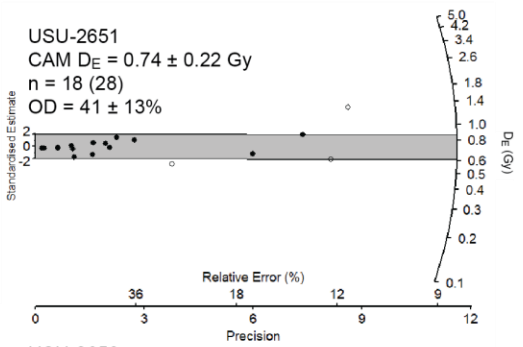

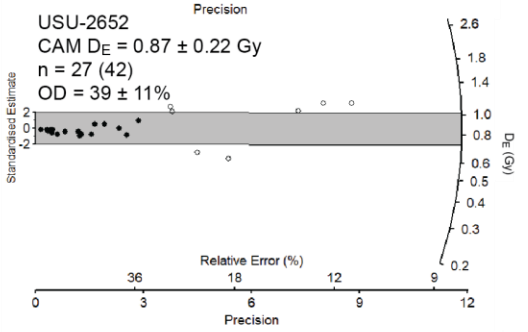

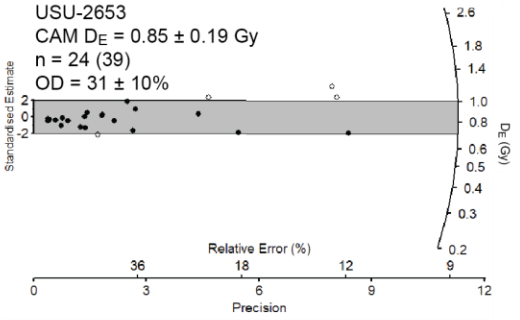

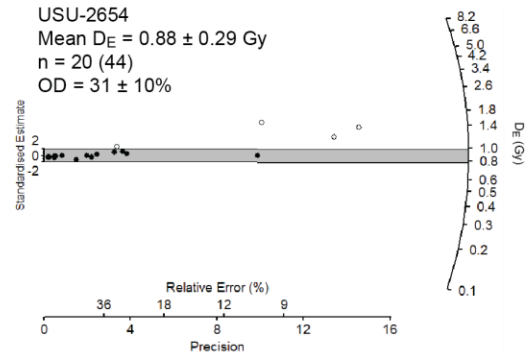

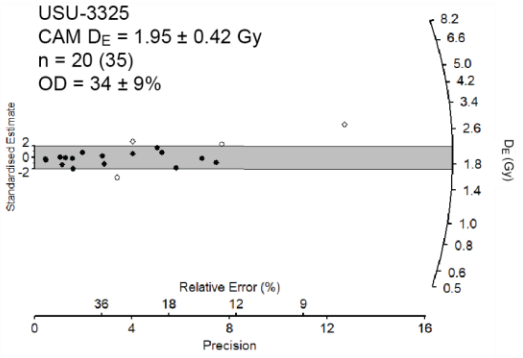

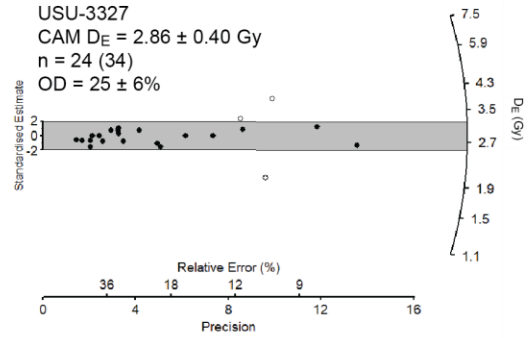

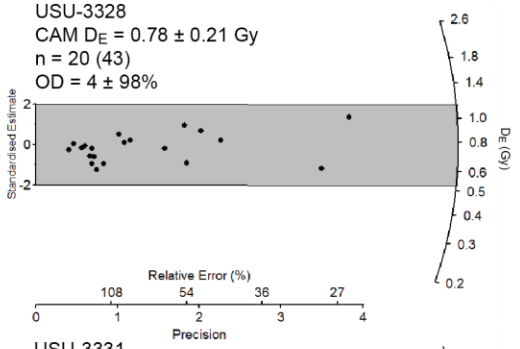

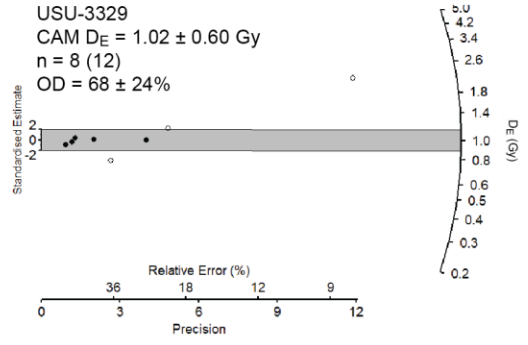

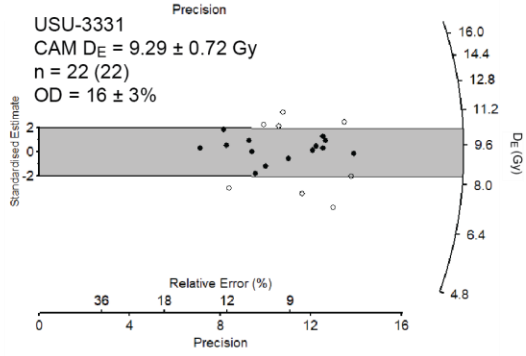

Equivalent Dose (D_E) Radial Plots

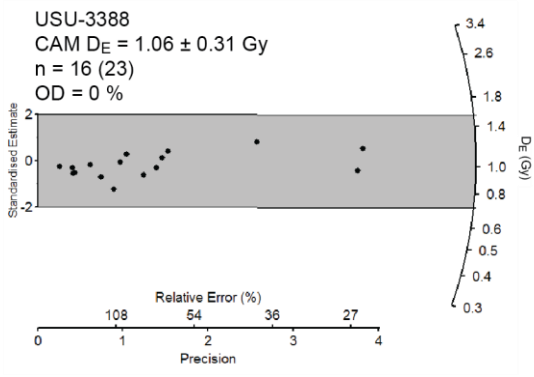

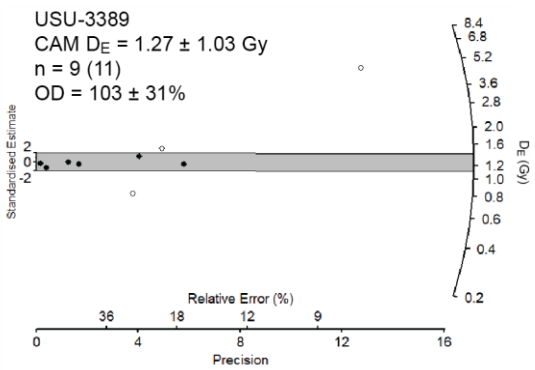

Equivalent Dose (D_E) Radial Plots

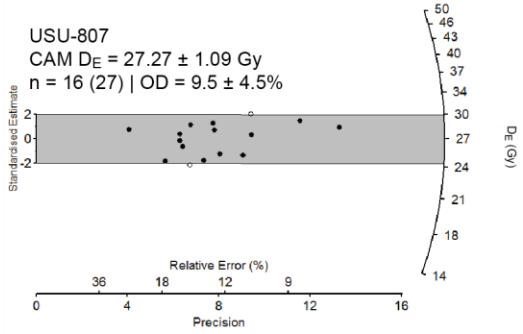

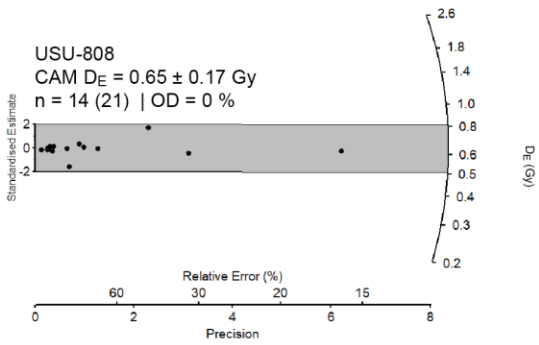

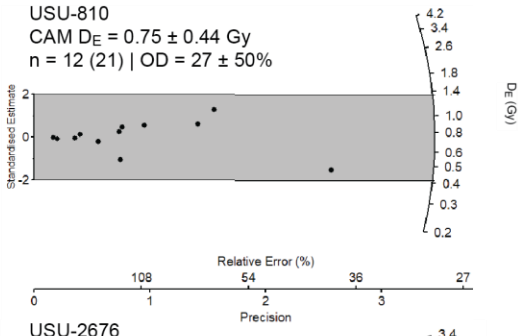

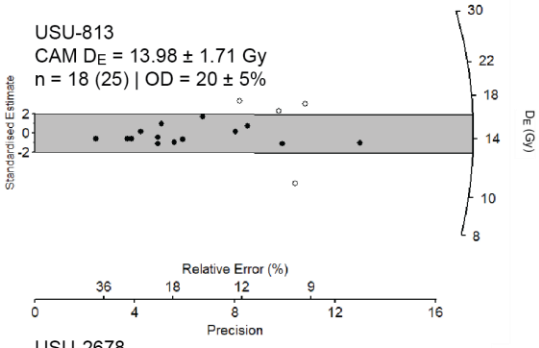

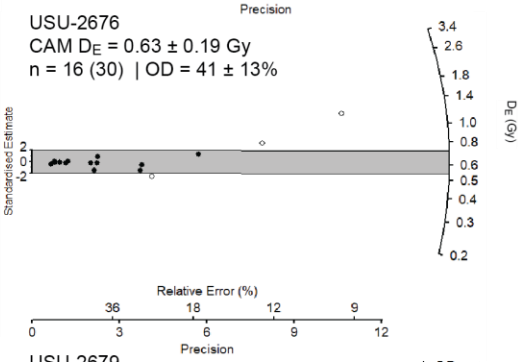

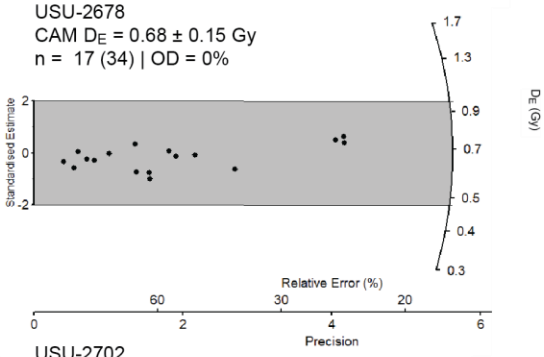

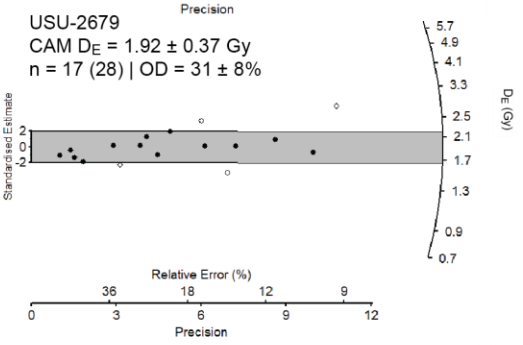

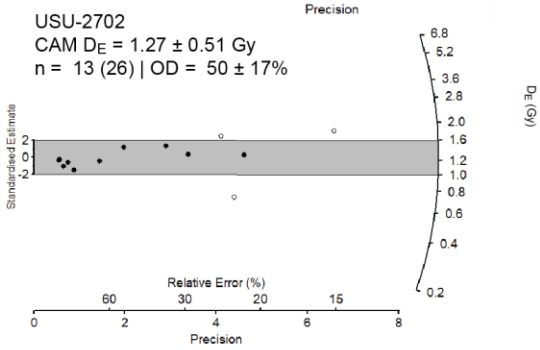

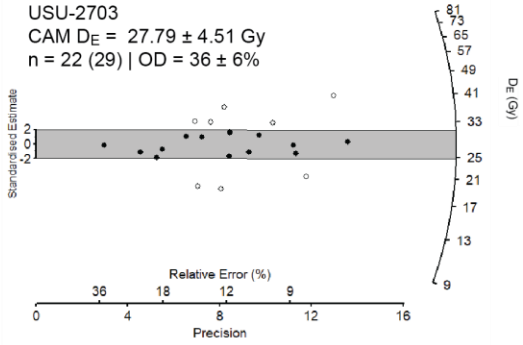

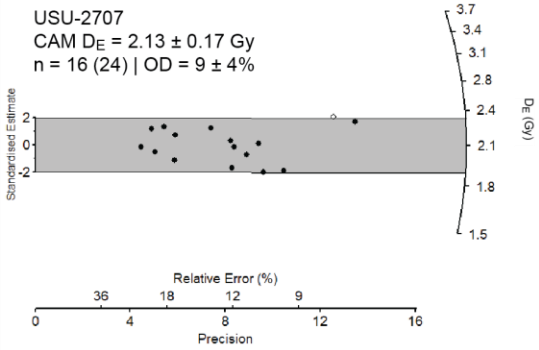

Equivalent Dose (D_E) Radial Plots

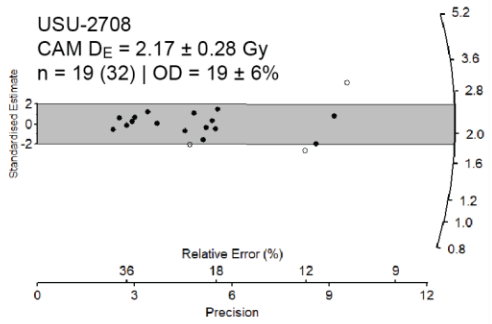

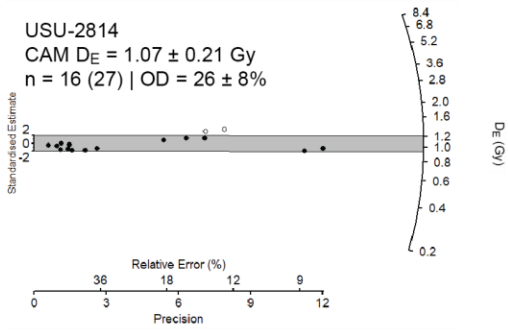

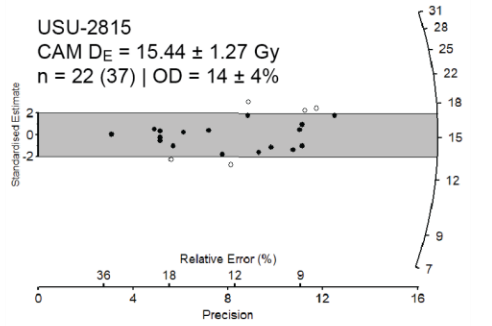

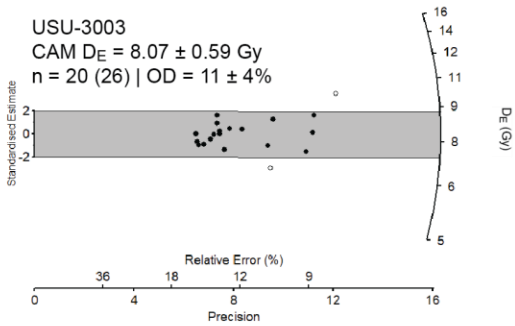

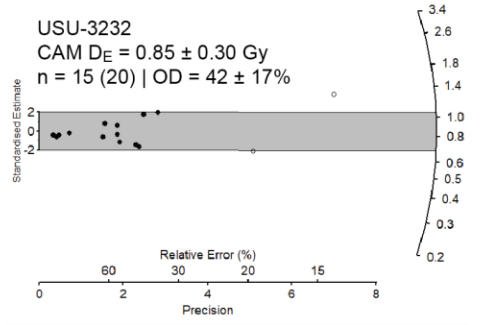

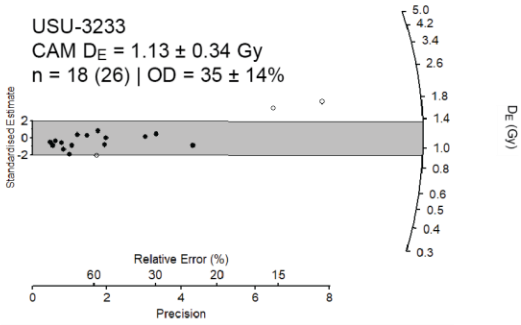

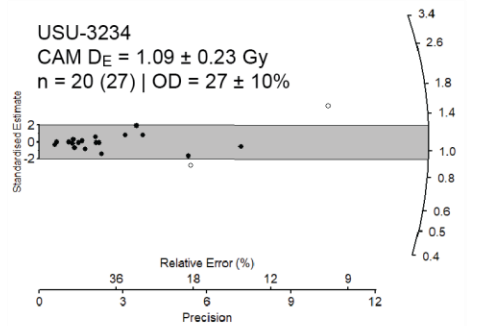

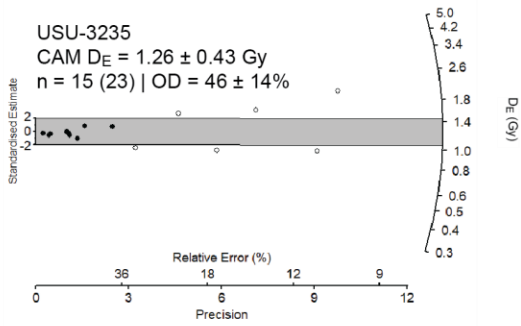

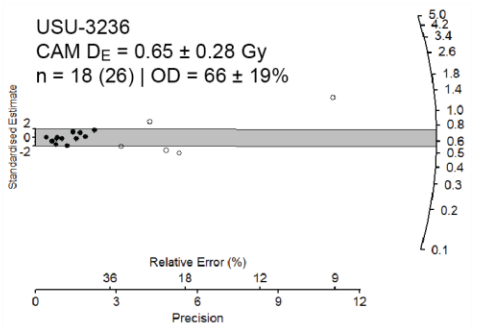

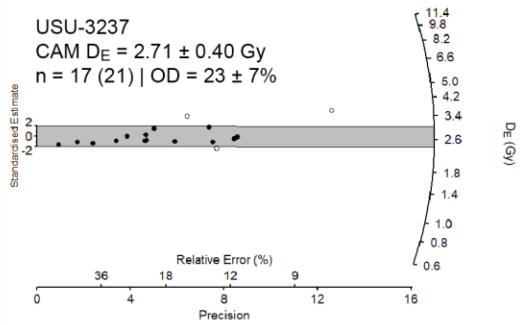

Equivalent Dose (D_E) Radial Plots

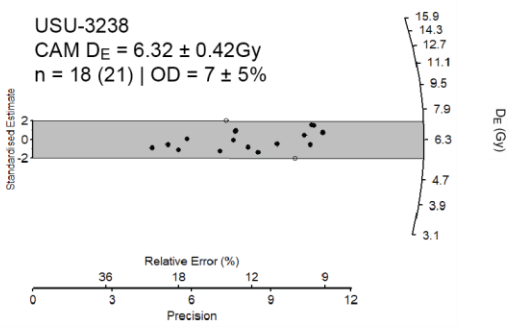

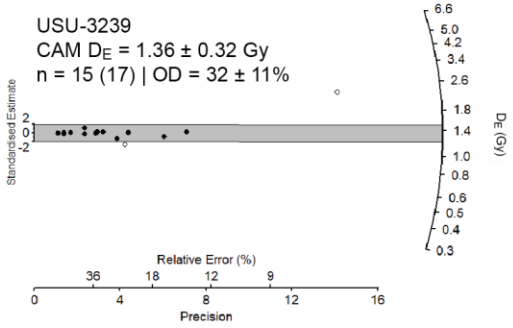

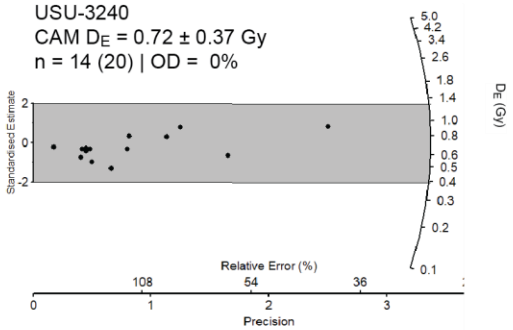

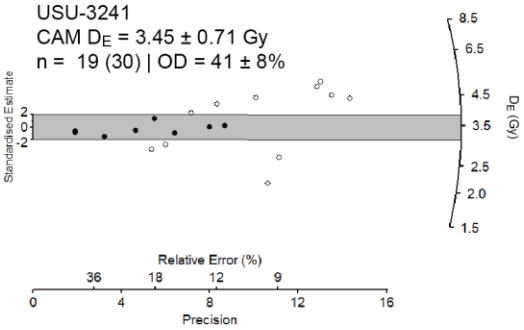

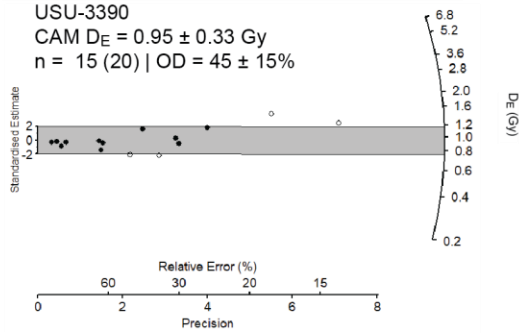

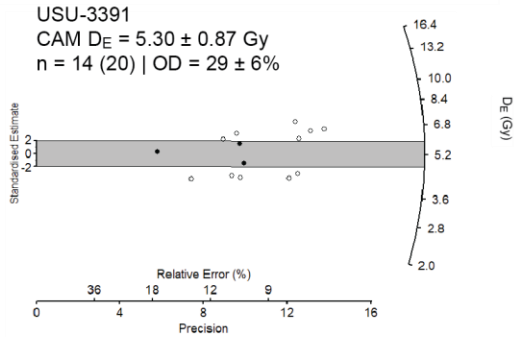

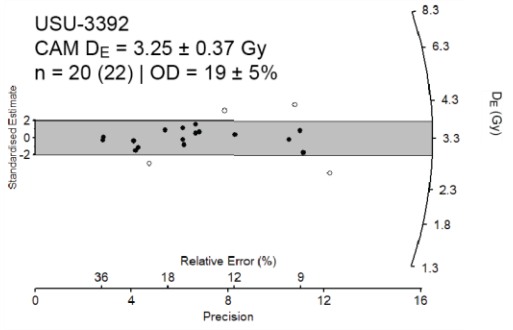

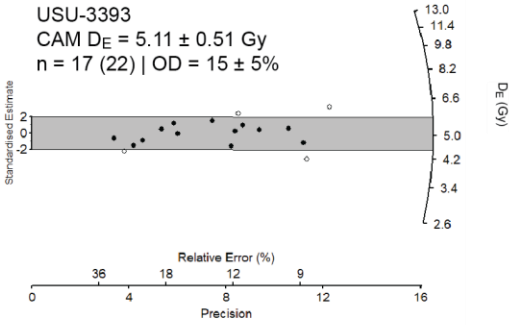

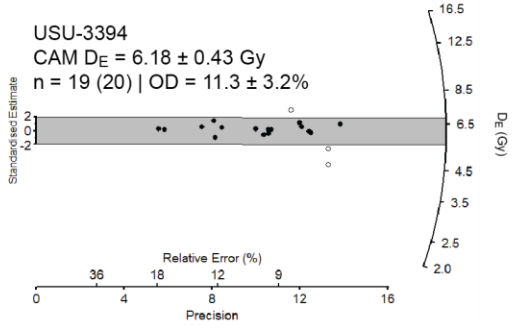

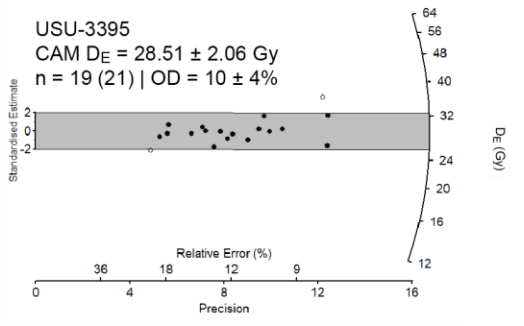

Equivalent Dose (D_E) Radial Plots

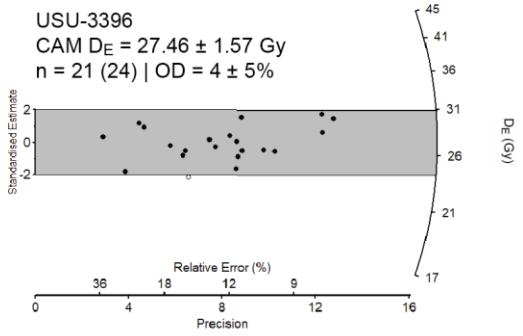

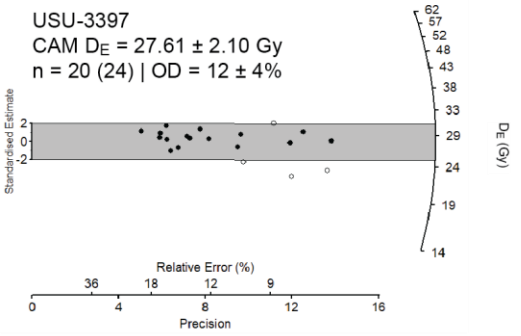

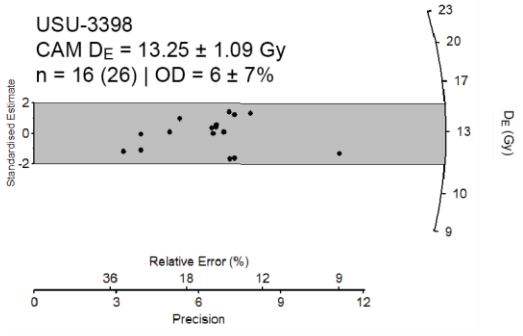

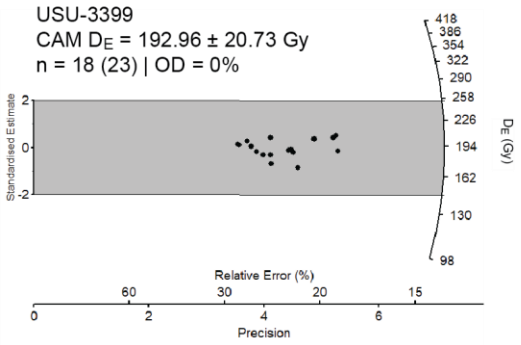

APPENDIX G. WIND AND GEOCHEMICAL DATA

Appendix G. Wind stations Appendix D. Results of calibrated TOC and $\delta^{13}C$ analysis

STATION: BUKU1
STATION NAME: BUCK FLAT
LATITUDE: 37.903408
LONGITUDE: -111.692361
ELEVATION [ft]: 8024
STATE: UT

STATION: BULLF
STATION NAME: Bullfrog Marina
LATITUDE: 37.5175
LONGITUDE: -110.7289
ELEVATION [ft]: 3700
STATE: UT

STATION: GRUU1
STATION NAME: GREEN RIVER
LATITUDE: 38.99722
LONGITUDE: -110.15778
ELEVATION [ft]: 4073
STATE: UT

STATION: KAZC
STATION NAME: Colorado City Municipal Airport
Colorado City
LATITUDE: 36.95
LONGITUDE: -113.00
ELEVATION [ft]: 4875
STATE: AZ

STATION: KCNY
STATION NAME: Canyonlands Field
Moab
LATITUDE: 38.76000
LONGITUDE: -109.74472
ELEVATION [ft]: 4554
STATE: UT

STATION: KHVE
STATION NAME: Hanksville
LATITUDE: 38.418037
LONGITUDE: -110.704038
ELEVATION [ft]: 4444
STATE: UT

STATION: KKNB
STATION NAME: KANAB MUNICIPAL AIRPORT
LATITUDE: 37.01
LONGITUDE: -112.53
ELEVATION [ft]: 4865
STATE: UT

STATION: SRFU1
STATION NAME: SAN RAFAEL RIVER NEAR GREEN RIVER 14SW
LATITUDE: 38.85833
LONGITUDE: -110.36944
ELEVATION [ft]: 4200
STATE: UT

STATION: TR336
STATION NAME: FISHLAKE SO PT #7
LATITUDE: 38.650472
LONGITUDE: -111.418497
ELEVATION [ft]: 8107
STATE: UT

STATION: ZIOU1
STATION NAME: ZION CANYON
LATITUDE: 37.204722
LONGITUDE: -112.977778
ELEVATION [ft]: 3999
STATE: UT

Appendix G. Summary wind data

Summary: DP-RDP-RDD-RDP/DP							
BUKU1				BULLF			
N	8.1	0		N	190.3	0	
NNE	0.2	22.5		NNE	44	22.5	
NE	0.2	45		NE	14.7	45	
ENE	0.2	67.5		ENE	15	67.5	
E	0.5	90		E	33.7	90	
ESE	0.2	112.5		ESE	51.8	112.5	
SE	0.2	135		SE	51.2	135	
SSE	3.6	157.5		SSE	111.3	157.5	
S	14.8	180		S	121.5	180	
SSW	0.2	202.5		SSW	136.1	202.5	
SW	0.2	225		SW	167.2	225	
WSW	0.2	247.5		WSW	138.5	247.5	
W	0.2	270		W	75.1	270	
WNW	0.2	292.5		WNW	104.1	292.5	
NW	0.2	315		NW	96.9	315	
NNW	4.6	337.5		NNW	75.5	337.5	
RDP	RDD	RDP/DP	DP	RDP	RDD	RDP/DP	DP
5.7	1.3	0.2	28.5	395.9	67.4	0.3	1319.667

GRUU1				KAZC			
N	16.9	0		N	3.3	0	
NNE	17.6	22.5		NNE	14.1	22.5	
NE	0.7	45		NE	104.3	45	
ENE	0.4	67.5		ENE	48.6	67.5	
E	0.4	90		E	49.7	90	
ESE	0.7	112.5		ESE	22.6	112.5	
SE	0.7	135		SE	34.2	135	
SSE	6.2	157.5		SSE	36.8	157.5	
S	50.5	180		S	106.9	180	
SSW	125.3	202.5		SSW	114.5	202.5	
SW	37.6	225		SW	178.4	225	
WSW	0.7	247.5		WSW	195.2	247.5	
W	4.3	270		W	189.2	270	
WNW	13.7	292.5		WNW	152.4	292.5	
NW	143.1	315		NW	163.8	315	
NNW	46.2	337.5		NNW	43.3	337.5	
RDP	RDD	RDP/DP	DP	RDP	RDD	RDP/DP	DP
200.2	85.2	0.4	500.5	601	75	0	1502

KCNY				KHVE			
N	15	0		N	39.7	0	
NNE	14.4	22.5		NNE	35.7	22.5	
NE	78.8	45		NE	33.2	45	
ENE	107.9	67.5		ENE	3.6	67.5	
E	50.6	90		E	3.6	90	
ESE	22.5	112.5		ESE	4.1	112.5	
SE	57.6	135		SE	18.2	135	
SSE	93.5	157.5		SSE	82.7	157.5	
S	201.3	180		S	176.7	180	
SSW	376.7	202.5		SSW	390.1	202.5	
SW	315.7	225		SW	425.2	225	
WSW	184.3	247.5		WSW	135	247.5	
W	304.9	270		W	93.9	270	
WNW	297.5	292.5		WNW	176	292.5	
NW	172.5	315		NW	187.4	315	
NNW	41.1	337.5		NNW	97.6	337.5	
RDP	RDD	RDP/DP	DP	RDP	RDD	RDP/DP	DP
1110	59	1	2219	1085	57	1	1808

KKNB				SRFU1			
N	275.7	0		N	5.9	0	
NNE	22.5	22.5		NNE	1	22.5	
NE	59.2	45		NE	0.3	45	
ENE	72.5	67.5		ENE	0.3	67.5	
E	57.1	90		E	0.3	90	
ESE	3.2	112.5		ESE	0.3	112.5	
SE	3.2	135		SE	0.3	135	
SSE	14.8	157.5		SSE	4.5	157.5	
S	218	180		S	37.9	180	
SSW	245.5	202.5		SSW	49.9	202.5	
SW	253.2	225		SW	49.6	225	
WSW	173	247.5		WSW	12.4	247.5	
W	133.6	270		W	4.2	270	
WNW	17	292.5		WNW	4.9	292.5	
NW	56.1	315		NW	4.9	315	
NNW	295.1	337.5		NNW	4.5	337.5	
RDP	RDD	RDP/DP	DP	RDP	RDD	RDP/DP	DP
550	88	0	1833	135	34	1	193

TR336				ZIOU1			
N	36.5	0		N	1967	0	
NNE	23.5	22.5		NNE	180.2	22.5	
NE	0.9	45		NE	7.5	45	
ENE	0.3	67.5		ENE	0.4	67.5	
E	0.3	90		E	0	90	
ESE	0.3	112.5		ESE	0	112.5	
SE	0.6	135		SE	1.3	135	
SSE	0.9	157.5		SSE	10.9	157.5	
S	24.3	180		S	58.4	180	
SSW	9.8	202.5		SSW	40.1	202.5	
SW	7.3	225		SW	2.5	225	
WSW	1.5	247.5		WSW	0.4	247.5	
W	5.5	270		W	0	270	
WNW	20.3	292.5		WNW	0	292.5	
NW	33.1	315		NW	0.4	315	
NNW	4	337.5		NNW	1.3	337.5	
RDP	RDD	RDP/DP	DP	RDP	RDD	RDP/DP	DP
72	138	0	180	2033	182	1	2259

Appendix G. Geochemical Data – Kanab dune field

SAMPLE	K	K	Ba		Rb			
Final OSL Set **Kanab Sand Dunes (n=50)**	(n=35)	**K0** (n=2)	**K1** (n=4)	**K2** (n=7)	**K3** (n=17)	**K4** (n=6)	**Event (Age)** Site No.	K/Rb/K/Ba
USU-1154 90-180 prefloat	0.860	8600	200	43	31	275	**10**	6.4
USU-1155	0.660	6600	160	41	23	288	**8**	7.0
USU-1156	0.330	3300	90	37	13	252	**9**	6.9
USU-1157	0.320	3200	90	36	12	258	**9**	7.3
USU-1526	0.260	2600	70	37	9	295	**5**	8.0
USU-1527	0.260	2600	60	43	9	292		6.7
USU-1528	0.210	2100	50	42	7	284	**6**	6.8
USU-1529	0.140	1400	30	47	5	275		5.9
USU-1530	0.610	6100	130	47	26	237	**3**	5.1
USU-2542	0.670	6700	170	39	24	282		7.1
USU-2543	0.840	8400	220	38	30	285		7.5
USU-2575	0.270	2700	70	39	11	255		6.6
USU-2576	0.200	2000	50	40	8	260	**16**	6.5
USU-2577	0.250	2500	60	42	10	260		6.3
USU-2587	0.360	3600	90	40	14	267	**23**	6.7
USU-2588	0.460	4600	110	42	17	269	**23**	6.4
USU-2589	0.350	3500	90	39	13	276	**11**	7.1
USU-2590	0.530	5300	160	33	18	298		9.0
USU-2591	0.700	7000	190	37	25	283		7.7
USU-2623	0.770	7700	200	39	28	277	**12**	7.2
USU-2624	0.360	3600	100	36	13	281	**24**	7.8
USU-2625	0.330	3300	90	37	12	277	**24**	7.6
USU-2626	0.290	2900	80	36	10	282	**21**	7.8
USU-2627	0.330	3300	80	41	11	300		7.3
USU-2628	0.230	2300	60	38	8	284	**13**	7.4
USU-2629	0.270	2700	70	39	10	276	**13**	7.1
USU-2630	0.360	3600	100	36	13	288	**14**	8.0
USU-2631	0.360	3600	100	36	12	293	**14**	8.1
USU-2632	0.370	3700	100	37	13	289	**18**	7.8
USU-2633	0.500	5000	130	38	19	262	**18**	6.8
USU-2634	0.380	3800	100	38	14	279	**15**	7.4
USU-2635	0.310	3100	80	39	11	284	**15**	7.3
USU-2647	0.250	2500	70	36	9	281	**2**	7.9
USU-2648	0.240	2400	60	40	9	279	**2**	7.0
USU-2649	0.420	4200	110	38	14	292		7.6
USU-2650	0.330	3300	90	37	11	295	**20**	8.0
USU-2651	0.340	3400	90	38	12	281	**19**	7.4
USU-2652	0.370	3700	100	37	13	282	**19**	7.6

USU-2653	0.360	3600	90	40	13	286	**17**	7.1
USU-2654	0.390	3900	100	39	13	293	**17**	7.5
USU-3325	0.220	2200	50	44	7	301	**4**	6.8
USU-3326	0.290	2900	70	41	10	282		6.8
USU-3327	0.230	2300	50	46	8	280	**4**	6.1
USU-3328	0.280	2800	80	35	10	275	**7**	7.8
USU-3329	0.170	1700	40	43	6	279		6.6
USU-3330	0.720	7200	160	45	24	300		6.7
USU-3331	0.750	7500	180	42	26	290	**1**	6.9
USU-3387	0.500	5000	130	38	18	276		7.2
USU-3388	0.400	4000	100	40	15	274	**22**	6.8
USU-3389	0.410	4100	110	37	15	279		7.5
mean	0.387	3867	99	39	14	280		7.2
std dev	0.170	1697	43	39	6	281		7.1

Appendix G. Geochemical Data – San Rafael dune field

SAMPLE	K	K	Ba		Rb			
DESCRIPTION	%	ppm	ppm	K/Ba	ppm	K/Rb	**Site No.**	K/Rb/K/Ba
Chondrite normalizing value								
Final OSL Dataset		**SR0**	**SR1**	**SR2**	**SR3**	**SR4**	**SR5**	**SR6**
San Rafael (n=45)	(n=33)	**(n=2)**	**(n=2(1))**	**(n=3)**	**(n=1)**	**(n=3(2))**	**(n=3)**	**(n=3)**
USU-806	1.160	11600	490	24	43	269		11.3
USU-807	1.010	10100	310	33	38	269	**1**	8.2
USU-808	0.770	7700	200	39	29	266	**4**	6.9
USU-809	1.440	14400	350	41	52	279		6.8
USU-810	0.860	8600	250	34	31	275	**6**	8.0
USU-811	0.840	8400	340	25	30	282		11.4
USU-812	0.650	6500	180	36	24	266		7.4
USU-813	1.260	12600	540	23	46	275	**17**	11.8
USU-2675	1.140	11400	300	38	38	300		7.9
USU-2676	1.040	10400	270	39	35	301	**3**	7.8
USU-2677	1.240	12400	320	39	41	302		7.8
USU-2678	1.290	12900	310	42	45	285	**8**	6.9
USU-2679	1.270	12700	320	40	41	308	**8**	7.8
USU-2702	0.930	9300	260	36	33	285	**2**	8.0
USU-2703a	1.220	12200	380	32	43	286	**13**	8.9
USU-2703b	1.080	10800	620	17	36	297		17.0
USU-2704	1.370	13700	470	29	53	259		8.9
USU-2705	1.220	12200	300	41	47	258		6.3
USU-2706	1.300	13000	370	35	47	275		7.8
USU-2707	1.710	17100	410	42	60	287	**10**	6.9
USU-2708	1.550	15500	390	40	54	285	**10**	7.2
USU-2814	1.340	13400	310	43	47	284	**19**	6.6
USU-2815	1.220	12200	490	25	41	298	**19**	12.0
USU-3003	1.240	12400	550	23	42	297	**16**	13.2
USU-3004	1.470	14700	490	30	51	286		9.5
USU-3232	1.250	12500	290	43	43	291	**18**	6.7
USU-3233	1.050	10500	250	42	36	293	**21**	7.0
USU-3234	1.250	12500	280	45	42	295	**21**	6.6
USU-3235	1.060	10600	250	42	37	288	**20**	6.8
USU-3236	1.200	12000	290	41	41	296	**5**	7.2
USU-3237	1.130	11300	310	36	38	301	**5**	8.3
USU-3238	1.400	14000	340	41	47	299	**15**	7.3
USU-3239	1.290	12900	340	38	45	284	**12**	7.5
USU-3240	1.180	11800	300	39	40	296	**7**	7.5
USU-3241	1.290	12900	330	39	43	299	**7**	7.7
USU-3390	1.720	17200	390	44	55	312	**22**	7.1
USU-3391	1.650	16500	390	42	51	325	**22**	7.7

USU-3392	1.660	16600	380	44	54	307	**14**	7.0
USU-3393	1.350	13500	340	40	44	309	**14**	7.8
USU-3394	1.550	15500	370	42	49	314	**14**	7.5
USU-3395	2.080	20800	480	43	66	318	**11**	7.3
USU-3396	1.720	17200	410	42	57	302	**11**	7.2
USU-3397	1.570	15700	390	40	51	307	**11**	7.6
USU-3398	1.090	10900	280	39	36	304	**9**	7.8
USU-3399	1.740	17400	420	41	58	302		7.3
mean	1.286	12856	357	36	44	292		8.1
std dev	0.285	2850	94	30	9	325		10.7

CURRICULUM VITAE
Harriet S. Cornachione

CAREER OBJECTIVE

My goals are to foster public understanding and use of scientific knowledge to inform evidence-based policy and decision-making, assist or lead efforts in strategic adaptation and mitigation planning for [adverse] impacts of climate change, and to assist, develop and mentor STEM and DEI in scientific communities.

EDUCATION AND PROFESSIONAL PREPARATION

PhD. in Geology; Utah State University, Logan, Utah. (8/22) Dissertation research: Holocene chronostratigraphy of dune fields in southern Utah – implications for natural moisture variability in the central Colorado Plateau; Advisor: Dr. Tammy Rittenour

Graduate studies in Environmental Engineering; Michigan Technological University, Houghton, MI (1990-92) Research emphasis: Changes in clay mineralogy in response to exposure to organic liquids; Advisor: Dr. John Gierke

M.S. in Geology; University of Texas at Dallas, Richardson, TX(8/84) Thesis research: Stratigraphy and sedimentology of the Sadlerochit Formation in the Arctic National Wildlife Refuge; Advisor: Dr. Ken Erickson

Graduate Studies in Geology; Colorado School of Mines, Golden, CO – (1974-75) Research emphasis: Geochemistry and Mineralogy of Skarn Deposits, Park City, Utah; Advisor: Dr. Samuel Romberger

B.S. in Earth Sciences; Western Michigan University, Kalamazoo, MI (8/74)

PROFESSIONAL EMPLOYMENT HISTORY

August, 2019 to Present
Lab Technician, USU Luminescence Lab, Utah State University, Logan

Sample processing and preparation for optically stimulated luminescence study; load and run experiments using Riso readers; supervise and train new students; laboratory operation and maintenance duties according to SOPs.

January, 2019 to May, 2019
Teaching Assistant, Department of Geology, Utah State University, Logan

Attend all classes for GEO 5690 – Geodynamics and GEO 3400 – Communicating Geoscience, provide tutoring and mentoring for students on presentations, projects, homework assignments and life. Grade regular lab / writing assignments.

August, 2017 to December, 2018
Research Assistant, Luminescence Lab, Utah State University, Logan

Assist with sample processing and preparation, routine laboratory operation and maintenance functions, assist with lab floats and supervise new students. Mentor/train undergraduate and graduate students conducting research as needed on laser particle analyzer and in sample processing and preparation for analysis, assist with OSL Short Course and other duties to support and promote Luminescence Lab.

May, 2015 to August, 2016
Retired Actively (Professor Emeritus, Civil Engineering Department, Oregon Institute of Technology-2010)

Independent, unaffiliated personal travel, tent-camping through Alaska and Canada. Co-teach (M. Cornachione) "Maji Safi" a workshop and training program in methods for water quality in remote regions lacking community water systems, at Hanga Vocational Technical Center, Songea, Ruvuma Region, Tanzania, leading team of students in additional community service and outreach.

August, 2014 to May, 2015
Adjunct Professor, Department of Physics and Geosciences, Texas A & M – Kingsville

Teach courses in World Geography, Earth Science, develop, manage and teach Geomorphology, Physical Geology, and Earth Science laboratories, supervise student Teaching Assistants, support recruitment and other departmental initiatives.

June, 2013 to July, 2014
Director of Communications, Coastal Bend Community Foundation, Texas

Development of marketing materials and IT management for non-profit foundation serving 7 county-area in Coastal Bend region of Texas.

January, 2013 to May, 2013
Visiting Assistant Professor, Department of Physics and Geosciences, Texas A&M – Kingsville

Teach courses in World Geography, Introduction to Meteorology, develop, manage and teach Physical Geology and Earth Science and laboratories, supervise student Teaching Assistants, support recruitment and other departmental initiatives.

January, 1985 to present
Geologist, Self-employed; Alaska, Nevada, Oregon, Washington

Provide geologic, geotechnical and environmental consulting services as requested. Successfully direct, manage and perform technical evaluations, assist with project and client marketing, develop positive working strategies with private interests and public agencies. Wide range of projects include resource evaluation (minerals exploration for coal, precious metals, oil & gas, geothermal), environmental & geotechnical site assessment studies in Alaska, Nevada, Oregon and Washington.

September, 1993 to June, 2010
Professor, Civil Engineering Department, Oregon Institute of Technology

Performed curriculum development, course and laboratory instruction with continuous program assessment and improvement (freshman programs, engineering geology, environmental engineering, senior design, and CAD). Developed and coordinated departmental advising program, provided student advising, managed and delivered recruitment/retention programs, initiated departmental grant program, provided departmental and institutional service including planning, budgeting, fiscal operations oversight, faculty policies, and grant management.

January, 1982 to December, 1984
Project Geologist, Placid Oil Company, Anchorage, Alaska

Developed offshore oil prospects especially in Norton Sound area of Bering Sea and performed economic analyses on various prospects for offshore lease sales. Investigated potential reserves in Arctic National Wildlife Refuge (ANWR), managed various field and office-based projects (including 2 successful field investigations in ANWR -- data gathered on time, under budget with no personnel, contractor or fiscal problems). Managed and mentored 4 geologists, managed presentations of prospects to potential partner companies (successfully obtained partnerships on all offshore lease prospects presented).

August, 1979 to December, 1981
Mining Engineer & Computer Geologist; Phillips Coal Company, Dallas, Texas

Developed life-of-mine and reclamation plans for lignite coal deposits; performed economic and technical feasibility studies for proposed mines to meet needs of proposed power generation plants. Optimized equipment and sequencing. Developed computer models of coal seams for deposits in East Texas lignite fields. Self-taught required mapping and modeling software package used by company on the job; successfully met initial project deadlines for first and all subsequent models.

September, 1977 to August, 1979
Staff Mining Engineer; Texas Utilities Generating Company, Dallas, Texas

Performed feasibility studies and generated life-of-mine-plans for lignite coal prospects tied to power generation. Coordinated projects with corporate staff and existing mine operations, provided technical support and management for equipment selection, mine plan revisions, developed reclamation plans and provided other environmental compliance for operating mines.

September, 1975 to August, 1977
Field Technician; U.S. Geological Survey, Lakewood, Colorado

Performed various geotechnical soils tests for coal resource evaluation of western federal lands, designed report forms and wrote lab reports analyzing the test results. Performed heavy mineral separates and other lab tests to support geo-hazard evaluations of Cascade Range and Hawaiian volcanoes.

PUBLICATIONS

Cornachione H., 2022, Holocene Chronostratigraphy of dune field in southern Utah: geomorphic record of past aridity in the central Colorado Plateau. Digital Commons: All theses and dissertations, Utah State University.

Nelson M., Rittenour T., Cornachione H., 2019, Sampling Methods for Luminescence Dating of Subsurface Deposits from Cores. Methods and Protocols: 2(4)88.

Cornachione, H.S., 2018. GSA 2018 – Kirk Bryan Field Trip – At the Edge of the Laurentide Ice Sheet: Stratigraphy and Chronology of Glacial Deposits in Central Indiana, GSA Online 06Dec18.

Lund, J., Boyd, T.L., Cornachione, H., Hiller Clark, A. and Marcus, S.A., 2009, Geothermal geology and utilization in Oregon: a field guide in O'Connor, J.E., Dorsey, R.J., and Madin, I.P., eds., Volcanoes to Vineyards: Geologic Field Trips through the Dynamic Landscape of the Pacific Northwest: Geological Society of America Field Guide 15, p. 583-598.

Cornachione, H., 2004, Transcription of General Land Office Survey Notes (GLO) for Upper Klamath Basin, Watershed Assessment/Action Plan Grant, Oregon Watershed Enhancement Board.

Cornachione, H., 2003, General Land Office Survey Notes Transcription for Riparian Records Project, Ecosystem Restoration Office Grant Final Report, U.S. Fish & Wildlife.

Cornachione, M., Cornachione H. and V. Vance, 2003 A Capstone Design Approach in Civil Engineering, Proceedings of the 2004 ASEE Annual Conference & Exposition, Salt Lake City.

Cornachione, H., 2003 Women in Science and Engineering at OIT, Strategic Post, October.

Cornachione, H.S. and Cornachione, M.A., 1998, Teaching the Business of Engineering in Proceedings of the American Society of Engineering Education (ASEE) Annual Conference, Environmental Section, 1998, St. Louis.

CONFERENCE PRESENTATIONS/POSTERS

Cornachione, H.S., Rittenour, T.M., and Nelson, M.S., 2019, Dune fields in southern Utah – an extended record of hydroclimate variability, Four Corners Science, Policy and Public Lands Symposium, Western Colorado University, 2019, Gunnison

Cornachione, H.S., Rittenour, T.M., and Nelson, M.S., 2019, Holocene dune activity – implications for multidecadal drought in the Colorado Plateau, USA, INQUA Annual Meeting – 2019, Dublin

Cornachione, H.S., Rittenour, T.M., and Nelson, M.S., 2019, Holocene dune activity in southern Utah, GSA Rocky Mountain Section Meeting – 2019, Manhattan

Cornachione, H.S., Rittenour, T.M., and Nelson, M.S., 2019, Using Holocene dune activity across southern Utah to predict future drought patterns in the central Colorado Plateau, USU Dept of Watershed Science, Spring Runoff Symposium

Cornachione, H.S., Rittenour, T.M., and Nelson, M.S., 2018, Chronostratigraphy of two dune fields in southern Utah - implications for drought patterns in the central Colorado Plateau, GSA Rocky Mountain Section Meeting – 2018, Flagstaff

Cornachione, H.S., Rittenour, T.M., and Nelson, M.S., 2018, Dry times in the central Colorado Plateau - prehistoric drought recorded in southern Utah dune fields, GSA Annual Meeting – 2018, Indianapolis

Cornachione, H.S., Rittenour, T.M., Nelson, M.S. and Townsend, K., 2017, Holocene chronostratigraphy and paleoclimate implications of dune fields across southern Utah, GSA Annual Meeting – 2017, Seattle

Cornachione, H., 2009, Role of Advising in Student Retention, CSSA Annual Conference, Feb. 4-5, Portland

Cornachione, H., et al, 2005, Technical Readers for WRI 227 Workshop, CCT Convocation Workshop, Fall 2005, Oregon Institute of Technology, Klamath Falls

Brower, T. and H. Cornachione, 2001, Women in Engineering Technology: Where are they? in Proceedings of the 2001 ASEE Annual Conference & Exposition, Albuquerque

Cornachione, H.S., J.S. Gierke, and S.D. McDowell "Fabric Changes in Clays Permeated with Organic Liquids," Clay Minerals Society 28th Annual Meeting, Houston, Texas, October 5-10.

TEACHING EXPERIENCE

Physical Geology (Michigan Tech Univ., 1990-91; Texas A&M-Kingsville, 2013-14)
Introduction to Civil Engineering (Oregon Institute of Technology, 1994-2009)
Computer-Aided Drafting (Oregon Institute of Technology, 1992-2009)
Engineering Geology (Oregon Institute of Technology, 1994-2009)
Environmental Engineering (Oregon Institute of Technology, 1995-2009)
Senior Environmental Design (Oregon Institute of Technology, 1995-2000)
Civil Engineering Senior Design (Oregon Institute of Technology, 2001-2009)
World Geography (Texas A&M-Kingsville, 2013-2015)
Earth Science (Texas A&M-Kingsville, 2013-2015)
Introduction to Meteorology (Texas A&M-Kingsville, 2013-2015)
Geomorphology (Texas A&M-Kingsville, 2013-2015)

FIELD EXPERIENCE

Site Investigations (professional projects)
Alaska, Washington, Oregon, Idaho, Nevada, Colorado
Texas (East Texas lignite mine and reclamation)

Research Field Investigations
Arctic National Wildlife Refuge, Alaska
Utah (Wasatch Mountains – Park City Mining District; San Rafael Desert, Kane County)

PROFESSIONAL MEMBERSHIPS & LICENSURE

Geological Society of America (GSA)
American Association of Petroleum Geologists (AAPG)
Association for Women Geoscientists (AWG)
Society for Sedimentary Geology (SEPM)
Licensed Geologist, #2899, State of Washington (status: inactive)
Registered Professional Geologist, #1408, State of Oregon (status: inactive)

SERVICE AND SYNERGISTIC ACTIVITIES (SELECTED)

Science News Intern, Utah Public Radio, Utah State University, Logan – 2020
Research, conduct interviews, write and record/produce audio news stories featuring science-related topics, with an emphasis on topics relevant to the listening audience (Utah and surrounding region), and other news as needed/assigned

Geosciences Congressional Visits Day, Representative, Geological Society of America, 2019, 2020
Applicants from Geological Society of American, American Geophysical Union and Soil Science Society of America meet congressional representatives to request legislative support

for geosciences. Includes pre-meeting training workshop, post-meeting session and continued contact as professional resource for each congressperson.

Science Communication Intern, Geological Society of America Annual Meeting, 2018, Indianapolis

Attend professional meeting, conduct interview with one or more speakers, and write article(s) for a public audience synthesizing the scientific research and its significance.

Advisory & educational work in Tanzania (Clean Water/Water Resources) 2009, 2010, 2014, 2015, 2017, 2021 (postponed from 2020 / covid_19)

Initiated as an Engineers Without Borders student club project for water well installation, advised by OIT Civil Engineering Department faculty Michael Cornachione and me, working in the remote Hanga and surrounding villages of the Songea, Ruvuma region. We have continued involvement through retirement, welcoming students and other interested volunteers too. Projects now focus on education and mentoring of students at the Hanga Vocational Technical Center, and providing technical assistance with specific water supply or water quality projects for NGO's and community water boards.

USU Ecology Center Speaker Selection Committee, member 2017, co-chair, 2017-2019

Speaker Selection Committee is a student-led volunteer group who ranks an annual pool of possible speakers, then invites, arranges schedules for and hosts the speakers at USU for monthly, two-day speaker series.

Native American Summer Mentorship Program, 2019, 2020

Provide week-long intensive individualized science laboratory experience in luminescence dating for two Native American students. 2019 – develop and teach on campus, field & laboratory; 2020 – develop and teach virtual session with site field component

Graduate Student Representative, USU Geosciences Department – 2018, 2019, 2020

College of Science Graduate Council, Geosciences Representative, 2018-20, Chair-2020

USU Geosciences & Student Council – contributor, Inclusivity and Fairness statements, 2020

USU Student Research Symposium, Judge, 2019

USU Geosciences Rock and Fossil Day, Museum - 2019, Stream Table – 2020

USU Geosciences Forster Lecture Series Co-Chair, 2017

USU AAPG Club, Treasurer and student mentor/resource – 2017, 2018, 2019

Member, Klamath County Solid Waste Advisory Board, 1997-2003

Member, Site Council, Roosevelt Elementary School, 2004-2007

Member, Site Council, Ponderosa Jr. High School, 2007-2008

Advising Coordinator, Civil Engineering Department, OIT, 1993-2009

Advisor, Engineers Without Borders (OIT Student Chapter); Tanzania Water Project 2007-2010

Advisor & mentor, Society of Women Engineers (OIT Student Chapter) 1992-2002

Coordinator/teacher, TWIST (Teen Women in Science and Technology), Civil Engr'g 1992-98

Coordinator/presenter, STE2M (Science, Technology, Engineering, Education & Mathematics) programming, 2002-2006

Youth coaching (soccer, volleyball, Destination Imagination teams) 1992-2004

PROFESSIONAL SKILLS / TRAINING (SELECTED)

Planning and Writing a Successful Grant Proposal, Utah State University, September, 2018

USU GrTs series:
Maintaining a Professional Presence Online, February, 2018
Best Practices for Conference Presentations, March, 2018
Tips for Successful Literature Reviews, October, 2018
Tips for Dealing with Conflict, November, 2018

"Know Your Audience" Online Workshop, Alan Alda Center Center for Communicating Science, Sept 2018

"A Guide to Speaking with Humans", Paul Sutter, Alan Alda Center for Communicating Science, Jan 2020

USU Scanning Electron Microscopy (SEM) Training, 2016

USU X-ray Diffraction and X-ray Fluorescence Training, 2016

USU Optically Stimulated Luminescence (OSL) Short Course, 2016

Utah State University, ArcGIS Pro, 2016

Texas A & M – Kingsville, Distance Education Certification Workshop, Blackboard 2015

Oregon Institute of Technology, Intro to Geographic Information Systems (ESRI software), 2009

Oregon Transportation Research Consortium, "Cutting Carbs Workshop", November 5, 2009

University of Wisconsin-Madison, Slope Stability and Landslides, Feb. 14-18, 2005

AutoCAD, AutoCAD Map, and Civil 3D Workshops, 2002, 2004, 2006, 2008, 2009

GRANTS AND AWARDS (SELECTED)

Graduate Researcher of the Year, Department of Geosciences, Utah State University 2021

"Desert dune field activations in southern Utah – implications for natural climate variability during the Holocene",Faruq El Baz Desert Research Award, Geological Society of America, 2020 - $2500

"Sand dune field activation and landscape response to climate change in southern Utah", USU Ecology Center Graduate Student Award, $5000

"Chronostratigraphy of dune fields in southern Utah - implications for Holocene drought patterns of the southwestern Colorado Plateau", Geological Society of America Student Research Grant, 2017 - $1488, Colorado Society Student Research Grant, 2017 - $990

Graduate Research Travel Award, Association of Women Geoscientists, 2017 - $1000

USU Seeley-Hinkley Scholarship, 2019-2020

Peter R. McKillop Scholarship, USU Geosciences, 2017, 2018

J. Stewart Williams Scholarship, USU Geosciences, 2019

USU Research Travel Grant, 2017, 2018, 2019, 2020

Service Honor Award & Ceremony, Hanga Vocational Technical Center, 2015
(for 3-week "Maji Safi" course and certification of training)

Oregon Institute of Technology, Professor Emeritus, 2009

Student Evaluations: ≥4.5/5.0 average annual rating, 1996 through 2009

Best Paper Award, ASEE Environmental Section, 1998